SEISMIC PERFORMANCE OF REINFORCED CONCRETE NONCONFORMING COLUMNS

Farah Dameh

A THESIS SUBMITTED TO THE FACULTY OF GRADUATE STUDIES IN PARTIAL FULFILLMENT OF THE REQUIREMENTS FOR THE DEGREE OF MASTER OF APPLIED SCIENCE

GRADUATE PROGRAM IN CIVIL ENGINEERING
YORK UNIVERSITY
TORONTO, ONTARIO

September 2021

ABSTRACT

The estimation of deformation indices and strength capacities of reinforced concrete structural members is neither a simple nor a systematic unique approach. Several analytical models for such estimations have evolved over the years (Park and Paulay (1975), Lehman et al. (1998), Panagiotakos and Fardis (2001), FEMA 273 (1997), Priestley et al. (1996)) and some are an essential part of today's Seismic Codes of Assessment in the form of acceptance criteria (e.g. EC8-III 2020, ASCE/SEI 41-17). However, significant dispersion still exists between experimental data and code-based analytical estimates, especially when assessing structures built prior to the consolidation of capacity-design provisions in international codes (before the 1980's). These structures -referred to as nonconforming - consist primarily of structural members that possess deficiencies in the quality of concrete and steel, and in the transverse and/or longitudinal reinforcement detailing. Deficiencies in longitudinal detailing consists of presence of lap splice at the base of the column or inadequate development lengths, and sparse and poorly anchored transverse reinforcement. In the present work a comparative study was conducted using advanced nonlinear finite element simulations (using software ATENA, https://www.cervenka.cz/) for a benchmark set of columns modelling older detailing practices. Pushover analyses were conducted on the column models in order to determine the parametric sensitivity of the deformation indices, failure mode and associated strength of these benchmark cases to their basic design properties (such as longitudinal and transverse reinforcement ratios and arrangement, axial load ratio and anchorage/lap-splice geometries). It was found that deformation capacities of columns deteriorate significantly in the presence of lap splice or insufficient anchorage length in critical regions. Stirrup yielding and shear failure are suppressed in the case of adequate confinement and may only appear with higher axial compression. Yield penetration and pull out failure dominates the failure mechanism at low axial loads limiting the deformation capacity significantly in the absence of good confinement. The analytical results are calibrated against the design expressions used in the assessment codes illustrating the limits of the applicability and the discord between the different approaches used by current codes to define the so-called acceptance criteria in the seismic assessment practice. The simulation results are also used to vet the various assumptions that underlie the simple mechanistic models used in deriving seismic design expressions for yield and

ultimate deformation capacities, shear strength and the rate of its degradation with increasing ductility.

ACKNOWLEDGMENTS

First and most importantly, I would like to extend my deepest gratitude to my supervisor Professor S.J. Pantazopoulou for her guidance, support and encouragement throughout the two years of research in this project. Without her guidance the completion of this thesis would not have been possible.

Special thanks to York University for their financial assistance through out my research study. Many thanks to Rob for providing the technical assistance that contributed in the numerical conclusion of this thesis. Thanks are also extended to my graduate colleagues, Konstantinos Tsiotsias and Nicolas Al Joukhadar for their patience in providing the support in the knowledge regarding the numerical simulation conducted in this thesis. Special thanks as well to all the professors who I had the honour to learn from them.

To my parents, Falah and Nihad, thanks for always being there, supporting me emotionally, supporting my decisions, and teaching me to work hard for my goals.

To all, I dedicate this thesis.

TABLE OF CONTENTS

List of Tables

List of Figures

List of Symbols

A_b	cross sectional area of one longitudinal bar
A_g	cross-sectional area of the column
A_{hs}	total area of bars developed or headed (ACI 319M 2019)
A_{sl}	total area of the longitudinal reinforcement
A_{st}	transverse reinforcement area
A_{tt}	total area of stirrups or tie parallel to the developed headed bar (ACI 319M 2019)
A_{ws}	area of the transverse reinforcement bar
b	Cross Section Width
b_c	concrete core section width from center to center of transverse reinforcement.
c	$C_{min} + 0.5d_b$ (ACI- 408R-2003)
c_b	least of the half centre to centre of the longitudinal reinforcement spacing and the closest distance from the concrete edge to the centre of the longitudinal reinforcement. (ACI-2019)
c_{clear}	maximum spacing between the ribs on bar reinforcement. (fib Model Code 2010)
C_{max}	maximum of (c_b, C_s). (ACI 408R-2003)
C_{min}	minimum of (c_b, C_s). (ACI 408R-2003)
C_s	is the least of the clear cover and one-half of the clear spacing of the longitudinal reinforcement + $0.25in$ (ACI 408R-2003)
d_b	longitudinal reinforcement bar diameter
d_c	depth of core
d_{cs}	represents the confinement provided by the cover of the section. It is the least of the half

	centre to centre of the longitudinal reinforcement spacing and the closest distance from the concrete edge to the centre of the longitudinal reinforcement.
d_f	is equal to the depth of the section h for columns with span to depth ratios less than 1.0 or equal to the effective depth for columns with span to depth ratios higher than 1.0 to 1.5
E_c	uncracked Young's Modulus.
$E_{ijij}^{\prime cr}$	crack stiffness (Cervenka et al. 2020)
f_c	Concrete Compressive Strength
f_{c1}	stress in concrete in the second (compressive) principal direction
f_{c2}	stress in concrete in the second (compressive) principal direction
f_{ck}	characteristic compressive strength of concrete.
f_{cm}	mean concrete cylinder compressive strength MPa
f_{stm}	maximum estimated bar stress (mean value) MPa.
f_{yl}	yield strength of the longitudinal reinforcement
$f_{y,tr}$	yield strength of transverse reinforcement
$f(p_{i-1})$	is the vector of total internal joint forces at a previous loading point. (Cervenka et al 2020)
g	ratio of the strain at the core edge to the core edge strain at axial or shear failure.
G	is the elastic shear modulus after cracking (Cervenka et al. 2020).
G_F	energy fracture (Cervenka et al. 2020)

G_c	uncracked elastic shear modulus. (Cervenka et al. 2020)
G_t	tangent shear Modulus. (Cervenka et al. 2020)
h	depth of the gross cross section
h_c	concrete core section depth from center to center of transverse reinforcement
j_e	depth of the core
K_1	factor representing the bar location and is equal to 1.3 for when 300 mm or more of fresh concrete is placed under the development length and 1.0 for other cases. (CSA A23. 2014)
K_2	coating factor that equals to 1.5 for epoxy-coated reinforcement if the clear cover is less than $3d_b$ or clear spacing between bars being developed is less than $6d_b$. (CSA A23. 2014)
K_3	concrete density factor, and it is equal to 1.3 for structural low-density concrete and 1.2 for structural semi-low-density concrete and to 1.0 for normal-density concrete. (CSA A23. 2014)
K_4	bar size factor, and it is 0.8 for 20M and smaller bars and deformed wires and 1.0 for 25M and larger bars. (CSA A23. 2014)
K_e	effectiveness coefficient of the confinement pressure produced from the transverse reinforcement. (CSA A23. 2014)
k_{sh}	$1+\sqrt{\frac{200}{d}} \leq 2.0$ and the effective depth d is in mm. (EN 1 Part 1-1992)
K_{tr}	confinement of a section provided from the transverse reinforcement. (ACI 318-2019)
$K(p_{i-1})$	stiffness matrix at a previous loading point. (Cervenka et al. 2020)
L	clear length of the column

L_c	crush band size (Bazant and Oh 1983)
L_t	crack band size (Bazant and Oh 1983)
L_{ch}^c	characteristic length in compression. (Cervenka et al. 2020)
L_{ch}^t	characteristic length in tension (Cervenka et al. 2020)
l_o	avaible lapped length. (EC 8 III-2005)
$l_{ou,min}$	minimum required length at ultimate
$l_{oy,min}$	required developed length at yielding in accordance to (EC 8 III-2005)
m	Shear span-depth ratio.
n_b	number of anchored bars on a potential splitting plane. (EC 8 III-2005)
n_{restr}	number of lapped bars restrained by a stirrup corner or a cross tie. (EC 8 III-2005)
n_{tot}	total number of lapped bars along the cross-section perimeter. (EC 8 III-2005)
P	axial load.
r	s_s/ε_s
s	longitudinal stirrup spacing
s_1	slip in the longitudinal bars at the maximum bond stress representig the beginning of the plateau region. (fib Model Code 2010)
s_2	slip at the maximum bond stress representing the end of the platue region. (fib Model Code 2010)
s_3	slip at the beginning of the residual strength region(fib Model Code 2010)
s_h	stirrup spacing (ACI 408R 2003)
t_d	$0.78d_b + 0.22$ (ACI 408R 2003)
u_e	elastic bond stress

u_e	plastic bond stress
v_{max}	column shear stress at shear failure.
V_n	lateral column strength provided from the contribution of concrete, transverse stirrups and axial load
V_p	shear demand here refers to the shear force that creates plastic hinges at critical column sections due to the yielding in the longitudinal reinforcement
w	$(0.1C_{max}/C_{min}) + 0.9 \leq 1.25$ in. (ACI 408R 2003)
x_u	depth of the compression zone at ultimate.
x_y	depth of the compression zone at yielding
z	length of the internal lever arm which is equal to *d-d'* for components with rectangular sections
Z	descending slope of stress strain relation of concrete proposed by Kent and Park (1971)
δ_2	$= \left(\frac{d_2}{d}\right)$ where d_2 is the distance of the extreme compression fiber to the centroid of compression reinforcement.
Ψ_c	factor accounts for concrete compressive strength and is 1.0 for concrete strength larger or equal to 6000 psi (48 MPa) and is taken

	equal to (f_c/48) +1 for concrete strength less than 48 MPa. (ACI-318-2019)
Ψ_o	1.0 for headed bars if the developed bars end inside the column core with a cover larger than 2.5 in. or a cover larger than $6d_b$. 1.25 for other cases. . (ACI-318-2019)
Ψ_p	1.0 for longitudinal reinforcement bars No. 11 and smaller with $A_{tt} \geq 0.3A_{hs}$ or $s\geq 6d_b$, where s is the spacing of headed bars from center to center. 1.6 for other cases. (ACI-318-2019)
Ψ_c	0.7 for hook No. 36 and smaller with a clear cover equal or larger than 65 mm or 90-degree hook and the cover beyond the hook is 50 mm or larger and 1.0 for other cases. (ACI-318-2019)
Ψ_e	accounts for epoxy coating of bar and is equal to 1 for the case of uncoated reinforcement. (ACI-318-2019)
Ψ_r	0.8 for the case of 90-degree hooks of No. 36 or smaller bars confined with stirrups or ties with a spacing of $3d_b$ or less. Ψ_r is also taken 0.8 for 180-degree hooks of No. 36 or smaller bars if the confining transverse reinforcement is spaced not more than $3d_b$ along the developed bar. Ψ_r is 1.0 for other cases. (ACI-318-2019)
Ψ_s	factor accounts for bar diameter smaller and larger than 19 mm and equals 0.8 and 1 respectively. (ACI-318-2019)
Ψ_t	represents casting conditions and is equal to 1.3 when less then 300 mm of fresh concrete is cast below the development length, and 1 for other concrete casting conditions. (ACI-318-2019).

η_1	1.75 and 0.9 for ribbed and smooth bars respectively (fib Model Code 2010)
η_2	=1, when good bonding conditions are present.
η_3	=(25/ d_b)$^{0.3}$ and is taken 1.0 for $d_b \leq$ 25 mm (ACI 408R)
η_3	represents the bar diameter reduction factor for bar diameters more then 25 mm (fib design code) (fib Model Code 2010)
η_4	factor is used to adjust the yield strength of longitudinal reinforcement and is calculated from $(500/f_{yk})^{0.82}$ (fib Model Code 2010)
Θ	is the angle that forms between the critical sliding crack and the member cross section (i.e., the crack angle at which axial failure occurs)
θ_c	cracking angle (Eq.2.9)
θ_y	yield rotation
θ_{fPlmax}	plastic rotation component of $\theta_{ftotmax}$
$\theta_{ftotmax}$	is the column flexural rotation at shear failure initiation measured over a hinge length h excluding bar-slip–induced rotations
$\theta_{totPlmax}$	plastic rotation component of θ_{totmax}
ε_1^f	tensile strain tensor at the finite element integration points (Cervenka et al. 2020).
ε_2^P	compressive strain tensor at integration point(Cervenka et al. 2020).
ε_c	$1.8f_c/E_c$ (Panagiotakos and Fardis (2001))
$\varepsilon_{c,o}$	strain at peak strength.
$\varepsilon_{c,u}$	strain of the concrete at 15 % reduction in maximum strength on the post peak concrete stress strain curve.
$\varepsilon_{c,y}$	0.75 of $\varepsilon_{c,o}$
ε_{cp}	core strain corresponding to maximum concrete stress.

ε_c^p	strain corresponding to the maximum compressive stress
ε_d	strain at a compressive strength of 0 (the last point on the softening branch of the concrete stress-strain curve that intersects with the x-axis) (Cervenka et al. 2020).
ε_{loc}^P	localized compressive strain and corresponds to the strain corresponding to the maximum compressive strength after subtracting the linear portion. (Cervenka et al. 2020).
ε_{loc}^f	localized tension strain (Cervenka et al. 2020).
ε_s	reinforcement steel strain
ε_t	concrete maximum tensile strain
ρ_1	longitudinal tension reinforcement ratio (EC 8 III 2005)
ρ_2	longitudinal compression reinforcement ratio (EC 8 III 2005)
ρ_d	steel ratio of diagonal reinforcement. (EC 8 III 2005)
$\rho_{s,tr}$	volumetric transverse reinforcement ratio. (EC 8 III 2005)
ρ_{sx}	= $A_{sx}/b_w s_h$ is the ratio of transverse steel parallel to the direction of the loading. (EC 8 III 2005)
ρ_{sy}	transverse reinforcement ratio parallel to the direction of loading (y). (EC 8 III 2005)
ρ_t	ratio of area of distributed transverse reinforcement to gross concrete area perpendicular to that reinforcement = *Av/(bd).* ASCE SEI 41-17)
ρ_{tot}	total longitudinal reinforcement ratio (Chapter 6).
ρ_v	distributed longitudinal reinforcement along the web of the member. (EC 8 III 2005)

φ_y	yield curvatures
$\emptyset$	angle of inclination of the compression field related to the vertical web reinforcement.
Δp_i	deformation increments due to increasing load increments at the current loading point. (Cervenka et al. 2020).
α_t	is the bar size adjustment factor, which equals 0.5 for bars up to and including size 25 mm. (fib 2010 Model Code)
γ_{cb}	material safety factor for concrete.
γ_{st}	shear deformation for diagonal tension shear failure
γ_{sc}	shear deformation for diagonal compression shear failure
σ_c	concrete maximum stress and strain
σ_{cp}	$= N_{Ed}/ A_c \leq 0.2f_{cd}$ [MPa]. N_{Ed} is the axial force subjected to the cross section [in N]. (EN I PART 1 1992)
τ	Chapter 2 , shear stress at shear failure. Chapter 3, Bond stress
τ_1	reduced bond stress that is given by the user and ranges between the maximum bond strength and the residual bond strength (Cervenka et al. 2020)
τ_{bf}	residual bond stress. (Cervenka et al. 2020)
τ_{bmax}	bond strength when pullout failure is assumed. (Cervenka et al. 2020)
$\tau_{u,split}^{1}$	maximum bond stress when splitting failure is assumed with high transverse confinement. (Cervenka et al. 2020)
$\tau_{u,split}^{2}$	maximum bond stress when splitting failure is assumed with low transverse confinement. (Cervenka et al. 2020)

λ	accounts for concrete weight, and is equal to 1 and 0.75 for normal and light weight concrete respectively
ϕ	strength reduction factor
ν	is the axial load ratio
ω'	mechanical longitudinal reinforcement ratios in compression. (EC 8 III 2005)
ω	mechanical longitudinal reinforcement ratios in tension. (EC 8 III 2005)
ξ_y	normalized depth of compression zone at yielding
ξ_u	normalized depth of compression zone at ultimate

1. Introduction

1.1 Background

It has been observed in reconnaissance reports following previous strong ground motion events that many structural components constructed prior to the introduction of modern seismic design concepts (e.g. before the 1980's in the Western world) exhibit premature failures. These Premature failures prevent these components from developing their intended full deformation capacity and strength (Pantazopoulou 2003). Structural deficiencies may be associated with substandard detailing and dimensioning that was mainly based on allowable stress design with no emphasis on the confining function of adequately anchored or closely spaced transverse reinforcement. Therefore, substandard R.C buildings may collapse due to localization of failure in few locations of the building prior to redistribution of stresses (Lang et al. 2011, Augenti et al. 2010, Mehrabian et al. 2005, Dogangun et al. 2004, Jeong et al. 2004, Varum 2003). Premature mechanisms leading to localized failures may include buckling of compression reinforcement, slip of longitudinal reinforcement due to the presence of poorly confined lap splices in the plastic hinge zone region - which was a common practice 40 years ago-, crushing of concrete in the web of the member, etc.). Those types of structural components which do not comply to modern seismic provisions are labelled henceforth nonconforming members (Chasioti et al. 2010). Nonconforming members represent a large percentage of structures across Canada. They are a result of older methods of construction prior to the 1980's when the earthquake engineering community worldwide had reached a thorough depth of understanding regarding the mechanics of seismic resistance of RC. By not meeting the current standards these may be deemed deficient in terms of seismic resistance, and eventually, providing compromised safety to the occupants (NRC 1995). It has been estimated that financial losses between 15-30 billion dollars can result even from a small earthquake (Mitchell 2007). Compounding over time are the deficiencies in more modern structural systems due to evolving time-dependent effects such as corrosion which, practically, has similar implications (i.e., reduction of stirrup cross section, loss of bond, loss of concrete strength due to carbonation). Therefore, there is a need for improved understanding of the critical mechanisms governing the deformation capacity and strength of RC structures, their relationship to the available reinforcement details and member geometry (e.g. aspect ratio).

The study of the effect of different design variables on the deformation capacity estimates in reinforced concrete columns is a complicated procedure considering the available database of the experimental columns. The differences in testing methods and material properties presented in the experimental database, for example, may alter the response of two columns with the same longitudinal reinforcement ratio.

Understanding the behavior of reinforced concrete columns subjected to monotonic or cyclic loading is not the only concern. The current international assessment codes categorize components into limit states (EC8-III 2005) or acceptance criteria (ASCE-SEI 41/17) based on their performance level. The deformation capacities of reinforced concrete columns are anticipated from analytical equations developed through linear regression analysis of experimental data (Elwood et al. 2007). Based on the performance level of each component the retrofit design strategy is selected. The dispersion between the experimental and analytical deformation capacities for columns with premature failure (i.e., nonconforming columns-columns not developing their full intended capacities) form a sourse of uncertainty in the selected retrofit design strategy. Moreover, uncertainties may arise as well from the different available approaches for the code-based calculations for deformation capacities. The deformation capacity calculations require sectional analysis, thus, the multiple available tools for curvatures and sectional property estimations form another sourse of uncertainty.

The majority of experimental analysis of columns are represented in literature are as cantilever sticks swaying laterally. This representation stems from the static similarity between the cantilever column and the full-scale column presented in real frame structures. In the last 20 years, researchers have shifted towards the full-scale column in their experimental studies abandoning the laterally swaying cantilever. This is because of the differences in the boundary condition of the two cases (i.e., half and full scale columns) which causes another sourse of uncertainty in deformation capacity estimation.

This thesis addresses these challenges through detailed nonlinear finite element simulations going back to the underlying assumptions of pseudostatic experimental tests done on column specimens in the lab and considering in detail the important parameters that govern the mechanistic problem.

1.2 Proposed Study and Research Objectives

The research aimed to study:

1- The Deformation capacities for a group of reinforced concrete (RC) columns were obtained using advanced nonlinear finite element models (using ATENA Engineering 3D/ https://www.cervenka.cz/) in order to be compared with the deformability estimates obtained after using the prevalent assessment framework in North America, specified in the ASCE-SEI 41/17 standard. Of particular interest is in the determination of the ultimate displacement capacity and the governing mode of failure of axially loaded columns with a rectangular cross-section, as well as the effective yield displacement and stiffness to yield of the components. Finite element modelling pursued in the present work focused particularly in the explicit representation of bar – concrete interaction, through the use of distributed interfacial bond springs. Bond strength slip relations adopted from the fib Model Code (2010) were quantified with reference to the amount and placement of transverse reinforcement and cover, in order to account for the slip behavior and the resulting lumped rotation contribution to drift capacity resulting from slip, both along the anchorage but also along the shear span of the member. Bond failure here was anticipated also in the lap splice zones adjacent to the footing support of the column element (based on the traditional construction method that used starter bars) on account of the low confinement pressure provided from the cover and transverse reinforcement of the columns. Moreover, in order to capture the effect of confinement on deformation capacities of the columns studied, concrete stress strain relations effected by the confinement of the cover and transverse reinforcement were considered, through the application of appropriate softening expressions for the unconfined cover and the confined zones. A database for deformation and strength capacities was created for several benchmark RC column examples that represent a range of practical cases in older structures. The database is used to study the effect of the following design parameters on the deformation capacities and strength of RC columns:

1- Geometric Properties: aspect ratio of columns was controlled by altering the effective cross-sectional depth (400 mm and 700 mm)
2- Longitudinal detailing: the effect of bar anchorage at the base of the column including lap-splicing along starter bars, and various forms of bar anchorage inside the footing.

3- Axial load ratios: Column with applied axial loads of 10%, 35% and 50% of compression crushing were studied $\left(\frac{P}{A_g f_c}\right)$.

4- Transverse reinforcement spacing: Columns with longitudinal spacing of 200 mm and 100 mm were studied.

5- Longitudinal reinforcement ratios: ratios ranging between ρ_l = [0.405-0.81] % were considered.

2- The relevance of the cantilever column simulation that is used in experimental practice in order to model the shear span of a laterally swaying full column, as well as the contribution of P-Δ effects in the macroscopically observed reduction of shear resistance in RC members with increasing ductility demand.

3- The degree of correlation between analytical deformation capacities code-based estimation and the deformation capacities from finite element analysis. Discussions on the differences between approaches used to estimate deformation capacities is presented in detail.

4- The efficiency of the finite element models in estimating the deformation and shear strength, the resistance curves of analytical models were correlated against the resistance curves of experimental specimens

To conclude, upon completion of this research, resistance curves were provided for a set of cantilever columns with monotonic and cyclic loading representing different cases of nonconforming structures (different combinations of longitudinal reinforcement, stirrup spacing and axial load ratios). Moreover, the response curves of full swaying columns were modelled, and results were obtained and compared to half column models to quantify the effectiveness of the experimental test setups (that mostly used cantilever models of the shear span of swaying columns) in reproducing the failure modes of full column under true seismic conditions. Data from models were calibrated against deformation estimations which were calculated analytically through existing assessment codes and. Therefore, a complete understanding of source of uncertainties in deformation estimations were established and the effect of different shapes of substandard detailing on the strength and deformation capacity will be provided.

1.3 Research Significance

Several analytical models for deformation estimations have evolved over the years (Park and Paulay 1975, Lehman et al. (1998), Panagiotakos and Fardis (2001), FEMA 273 (1997), Priestley et al. (1996)). Some of these models are an essential part of today's Codes of Seismic Assessment in the form of acceptance criteria (e.g. EC8-III 2020 , ASCE/SEI 41-17). The deformations in most of these models depend on using a cantilever model swaying laterally where its length represents half the length of the full column (shear span). It has been shown in several models that the total deformation a member undergoes is a contribution of added shear, flexural and slip deformation (Syntzirma et al. 2010) as shown in Figure 1.1. This approach was tested against hundreds of specimens collected from the literature in databases. From this correlation it has been found that significant dispersion still exists between experimental data and code-based analytical estimates, especially when assessing nonconforming, older structures.

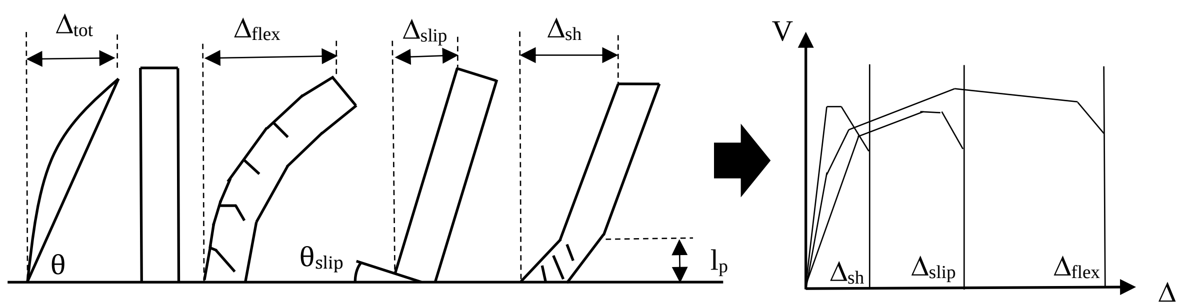

Figure 1.1: Various Response Mechanisms (Modified from Chasioti et al. 2010)

Current Seismic Codes provide empirical limits for the milestone points of the idealized response curve of members - which can be used in modelling of seismic response through nonlinear analysis software. However persistent scatter exists between experimental and theoretical values - an illustrative example was a prediction contest of a simple full-scale reinforced concrete bridge column with a concentrated mass at the top, subjected to six ground motions (Fajfar 2018). Each entry estimated several response indices of the structure such as peak displacement and acceleration demands. Despite the fact that the input properties of the structural component and the ground excitation were known, large differences in the displacement estimate were found between the 41 contestants from different countries (Terzic et al. 2015). This thesis aims to study the uncertainties that may arise when computing the deformation capacities theoretically using code-based estimates and the effect of detailing and geometry aspects on the strength and deformation capacities of column using detailed nonlinear finite element analysis.

An extensive parametric comparative study for different columns with combinations of longitudinal reinforcement, stirrup spacing and axial load ratio was completed using advanced finite element modelling. The comparative study aimed to investigate the mechanisms limiting the deformation capacities and the effect of various important design variables on column's behaviour. This included the axial load ratio, and the longitudinal (including lap-splice) and transverse detailing. Member resistance curves from pushover analysis of nonconforming columns were produced in order to determine, the structural performance in terms of expected damage and collapse potential in the event of a future, credible earthquake loading.

1.4 Thesis Outline

This Thesis is organized into eight chapters. This section will introduce the main topics of each chapter.

Chapter One: This chapter introduces the important issues related to the study of the seismic deformability and strength of concrete columns. The proposed study and research objectives are also presented in this chapter.

Chapter Two: This chapter introduces the previous work of researchers in the field of seismic deformability of reinforced concrete columns. The chapter provides a summary of the definition of nonconforming columns. The type of columns based on their failure modes are presented in this chapter as well. Several experimental full scaled columns from previous research is introduced. Analytical shear, flexure and slip deformation capacity models and their degree of correlation to experimental data is also presented in this chapter. The analytical deformation capacities of columns at axial and shear failure from famous research work is also introduced.

Chapter Three: This chapter provides the steps for preparing a set of benchmark columns for finite element analysis. The material properties and the column sectional geometry are the main topics discussed in this chapter. The study variables are presented. The concrete constitutive algorithms used in the finite element program (using software ATENA, https://www.cervenka.cz/) are explained in detail. Concrete stress strain models from Kent and Park (Kent et al. 1971) and

Modified Kent and Park (Park et al. 1982) used in defining the concrete constitutive material are presented. This chapter also presents the available estimation of bond stress-slip relation provided from several codes such as ACI 318M-11,14 and 19, CSA A23.3-14, fib Model Code 2010 and ACI 408R-03. The steel reinforcement properties are also presented. Solution parameters, mesh and boundary conditions for the finite element analysis are also explained in detail.

Chapter Four: The results of the columns presented in Chapter Three are discussed in this chapter. The deformation capacities at yielding and ultimate and base shear are presented. The modes of failure and the effect of each study variable is presented in detail. A comparison between the bond failure for columns against the expected mode of failure suggested by the codes (ACI 318-19, ACI 408R) are also presented.

Chapter Five: In this chapter the validity of the assumption of cantilever columns to represent the full columns is discussed. Full scaled columns of 16 cantilever columns are presented in Chapter Three are modelled with similar material properties. The differences in deformation, strength and longitudinal reinforcement strains between the two columns (full and half) are studied and addressed in detail.

Chapter Six: In this chapter detailed investigation of the correlation between the deformation capacities from the modelled columns and the calculated from two major international assessment codes (ASCE SEI-41/17, EUROCODE 8 Part III) is introduced. The uncertainties that arise from the issues discussed in Section 1.1 of this chapter is presented.

Chapter Seven: In this chapter the analytical program (ATENA, https://www.cervenka.cz/) used for this study is used to model three experimental columns (Sokoli et al. 2016) under reversed cyclic loading. This chapter addresses the difference in the column response under application of monotonic and cyclic loading. The crack models and the concrete program parameters are studied and the correlation between the experimental and analytical investigation is presented.

Chapter Eight: This chapter presents the conclusion of the thesis. The nonconforming columns premature failures are summarized, and the effect of each study variable is addressed. The efficiency of the code in predicting the deformation capacity of columns with premature failure are summarized as well. Recommended future studies are also presented.

2. Literature Review

This literature review starts with an introduction to seismic assessment of reinforced concrete columns and a background to the current open questions in the affiliated research field. The introduction is followed by a background review of the various types of columns based on their behaviour under monotonic and reversed cyclic loading. This will be followed by the section that lays out the definition and characteristics of nonconforming structural components designed and detailed according with older practices. This literature review will also provide a summary of experimental tests of columns under reversed cyclic loading and the research efforts in developing analytical models for shear and axial failure. The developed analytical models for shear and axial failure can be used to consistently calibrate the experimental evidence and can therefore be used for seismic assessment of older structures.

2.1 Introduction and Background

Understanding the response of prismatic reinforced concrete members under cyclic loads has been at the center of Earthquake Engineering development since its inception. This is because the prismatic element encapsulates all the basic principles of structural mechanics in a relatively straightforward manner: the key kinematic assumption of plane sections remaining plane after deformation, which is used to relate stress and strain even in the nonlinear region is generally acceptable particularly in slender members such as beams and columns. Prismatic elements also are the typical member of frame structures, which is the most rudimentary structural system to provide seismic resistance.

Columns, in particular, have been the subject of extensive experimental research, owing to their significant contribution to structural load bearing capacity and safety. Columns support the overbearing gravity of the floors above, and it is therefore of principal importance that they do not fail during lateral swaying motion of the building as a result of the earthquake action.

Column actions during lateral displacement comprise axial load, N, shear force V which is constant along the height, and a linearly varying flexural moment (with zero value occurring at midheight, where the curvature changes signs, known as point of inflection). The actual location of the point of inflection occurs closer to one of the two column ends, i.e., towards the more rotationally compliant end. Despite the perceived simplicity of the problem, the experimental evidence shows great variability and dispersion of results in terms of the governing strength and deformation capacity of columns. The uncertainty that this reflects, underscores that there is a gap of knowledge regarding our current understanding and ability to quantify the important response indices that would enable estimation of the seismic resistance of the column.

The scope and detail of experimental studies has been evolving with the increased understanding that has been gained over the years. A database of tests conducted on columns has been assembled in order to provide sufficient scope and critical mass of experimental evidence regarding the role of important design variables. Specimens in the database include those tested by Lynn (2001), Sezen (2002), Lam et al. (2003), Elwood (2007), Matchulat (2009), Sokoli and Ghannoum (2016), and many more. Collective evaluation of the database has been used to correlate predictive expressions for characteristic response indices. Response indices are one of the following: yield drift, ultimate drift capacity, drift at loss of shear strength, drift at loss of load bearing resistance, all being critical parameters for the performance based methods of assessment and retrofit. However, these expressions are persistently marked by large dispersions. In response to this, several researchers have considered subsets of the database looking for more consistent, selective groups of data that could shed some specific light in areas of stronger uncertainty. For example the magnitude of shear strength and its dependence on the intensity of the applied drift, the role of overbearing load, and the effect of some details such as lap splicing and stirrup arrangement in the critical regions. Another aspect of the evolution of the more recent experimental research is the continuous improvement and correction of experimental features that may be considered to contribute to the uncertainty. Typical specimen form that represents the majority of the tests in the database is the cantilever type column, which extends to half the length of the actual column being studied. The cantilever length extends from the critical section to the mid-height of the actual column. The relevance between these two situations is merely static similarity, i.e., under lateral sway they are both under constant shear, they have the same shear span, aspect ratio and axial load. The implicit assumption is that the two will show the same deformation capacity.

Although the two cases are statically equivalent, the question of whether the cantilever is an accurate representation of a full column has concerned researchers. Therefore, in the past twenty years several simulations have been conducted that involve full columns – i.e., abandoning the cantilever scheme despite the increased complexity of the test setups of full column testing. Size is another parameter that has prevailed as a major concern in recent experimental studies. With the explicit recognition of shear being dependent on size, there has been a shift of late to test larger – closer to full scale specimens. This is done in order to populate that range of the database where most of the older specimens did not extend to, i.e. columns with cross section sizes that resemble actual construction. Other aspects have also been considered with greater emphasis in recent years. Foe example such trend that prevails in the experimental literature is the attention to structural details that represent older practices. Rightly so from the point of view of performance-based assessment since in this time and age, several old structures constructed with pre-1980's details are in full use throughout the world (in fact, more than 2/3 of the inventory of existing structures).

From among the multitude of the experimental evidence some tests have made striking illustrations of parameters and phenomena or have helped illuminate open issues that today occupy much of the relevant research. One such example is the definition of a lateral drift limit beyond which the column is said to lose its vertical load bearing strength. In the following sections, some of these important experimental studies are reviewed with an interest to provide the context and the open questions that drive research in the area of seismic response and assessment of columns and piers in reinforced concrete structures.

Researchers have also placed emphasis on developing analytical models to estimate the deformation capacity of a structural component at axial and shear failure. Others have attempted to employ these analytical modes in nonlinear analysis programs such as *OpenSees* (PEER 2006) in order to verify its validity against available experimental analysis. The development of the analytical models is presented in the following sections.

2.2 Type of Columns Based on Failure Modes

The experimental database of concrete columns consists of columns subjected to a loading protocol of successive reversed cycles with increasing the target displacement in each cycle (Matchulat 2009). After the column has reached its ultimate lateral load resisting capacity, flexural/shear cracks develop, leading to degradation in the column's lateral and axial capacities, and eventually to an axial failure (Elwood 2004). In most of the databases, and in order to provide a rational comparative investigation of the effect of column detailing- longitudinal and transverse- on the deformation capacities, the lateral displacement at the column point of loading is divided by the length of the column. This results in a deformation index named drift ratio (Matchulat 2009).

Matamoros (2006) classified the columns based on the controlling mechanism to: shear-critical columns, flexure-shear critical columns and flexure critical columns. An illustrative representation of the modes of failure are depicted in Figure 2.1 (Matchulat 2009). The ratio between the nominal shear strength V_n (the lateral column strength provided from the contribution of concrete, transverse stirrups and axial load) and the shear demand V_p (the shear demand here refers to the shear force that creates plastic hinges at critical column sections due to the yielding in the longitudinal reinforcement) is the main factor for determining the expected failure type of the columns (Matchulat 2009).

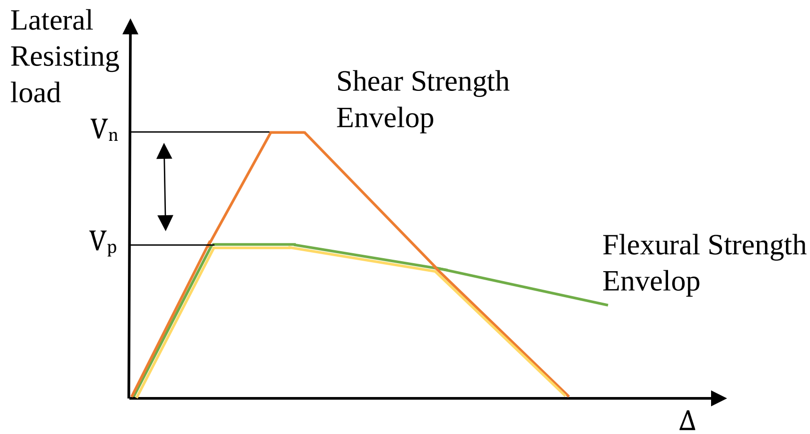

Figure 2.1: Lateral Resistance Curves for Columns with Governing Failure Type (Modified from Matchulat 2009)

For columns to be controlled by shear, the ratio of V_p/V_n ought to be greater than 1.0 (Elwood et al. 2007). The main trait of these types of columns is that they possess small percentages of transverse reinforcement ratios or large percentages of longitudinal reinforcement ratios. This makes them vulnerable to inclined shear cracking and therefore rapidly developing axial failure simultaneously, or directly after shear failure (Matamoros 2006). Thus, these types of columns are the least preferrable. If the ratio of V_p/V_n is less than 0.6, the column is deemed “flexure-critical” (Elwood et al. 2007). These types of columns develop mostly horizontal flexural cracks particularly near the critical section, initiating from the tension face of the column. Flexure-critical columns provide greater warning to impeding collapse and high deformation capacities with less to no degradation in shear strength before axial failure. In fact, these columns have high potential to fail due P-Δ effects before developing any signs of shear failure (Matchulat 2009). The axial load bearing capacity of the flexure-critical columns starts to degrade after developing post yield strains in the longitudinal reinforcement followed by cover spalling (Matchulat 2009). For flexure-shear (combined) failure, the ratio of V_p/V_n ranges between 0.6-1.0 according to Elwood et al. (2007). These types of columns experience three phases of damage: flexure, shear and axial failure. For the first phase, flexural horizontal cracks develop with yielding in the longitudinal reinforcement. With the increase in lateral loading, the cracks become deeper and start rotating towards the neutral axis, which triggers the column to enter the shear failure phase. According to Elwood (2005), the onset of shear failure is identified as the point in the post-peak resistance envelope at 20% reduction in the lateral load capacity whereas the complete axial failure is identified with the complete loss of lateral resistance.

2.3 Nonconforming Structures

Shear-critical/flexural-shear critical columns form a large percentage of column members in RC frame structures across Canada, the US, but also in the rest of the world where reinforced concrete was used in construction (NRC 1995). Columns that have been constructed prior to the 1980's are significantly compromised in terms of modern seismic detailing and are referred to according to FEMA 356 2000, as nonconforming components. These components were built in accordance with design codes and guidelines that did not place proper emphasis on the detailing of transverse reinforcement, while the cross-sectional dimensions of the components were designed considering allowable stresses (Pantazopoulou 2003).

The characteristics of nonconforming components that are linked to the occurrence of significant damage or collapse of structures. This is associated with material properties, detailing of longitudinal and transverse reinforcement and design principles that did not consider a capacity-based hierarchy of strengths (Pantazopoulou 2003). The material strengths were also low compared to the strengths used today. The concrete strength was in the range 160 – 250 kg/cm^2 (Pantazopoulou 2003). For steel reinforcement, it was found that some structures build prior to 1960's have smooth bars instead of ribbed (Pantazopoulou 2003).

The spacing of transverse reinforcement was placed in older construction for reasons such as to prevent buckling, resist a small portion of the design shear or for torsion (Pantazopoulou 2003). No emphasis was placed on transverse reinforcement for the sake of confinement. Additionally, deficiencies in the detailing of longitudinal reinforcement were present in structures built prior to the 1970's. For example, insufficient anchorage lengths of longitudinal reinforcement into the joint or the presence of lap splice with short lap length and no confinement at the critical section of the component were common occurrences (Pantazopoulou 2003). Such detailing poses a threat to the seismic deformation capacity of the lateral resisting components in a frame. Research in the 1980's through the joint US-Japan project (Wight et al. 1984) placed emphasis on the need to improve the anchorage pattern and stirrup spacing in code specifications (Pantazopoulou 2003).

2.4 Experimental Analysis of Reinforced Concrete Columns

Researchers have assembled databases of several experiments conducted on nonconforming reinforced concrete columns. This was done to illustrate the collapse behaviour and to support the development of an improved assessment procedure that may be used for retrofit design (Sezen 2002, Lynn 2001, Lam et al. 2003, Matchulat 2009, Henkhaus 2010, Goodnight et al. 2013, Sokoli et al. 2016). These experiments were carried out on single column specimens under lateral displacement reversals causing double curvature on the member. Therefore, reproducing the deformation patterns occurring in a column constructed as part of a lateral resisting frame under the lateral sway generated by the earthquake. The force redistribution in the column and its interaction with the surrounding frame components were not considered in these isolated column tests. Very few studies have been published on the redistribution of loads in a lateral load resisting reinforced concrete frames, by conducting such experiments under simulated earthquake action on shake tables (Elwood 2007, Shin 2011, Yavari 2011, Ghannoum et al. 2012). The frames were tested under scaled ground excitation simulating real earthquakes. This section will summarize the findings of both types of experimental studies with the objective to highlight the basis of calibration and the knowledge gaps in modern seismic assessment codes (ASCE/SEI 2017 and EC8-3 2005).

2.4.1 Single Column Tests

Due to the scarcity of data from large scale experiments on nonconforming columns, Lynn (2001) and Sezen (2002) developed an experimental program to fill-in the knowledge gap in the international database of shear-critical columns. Both researchers used the same setup and general specimen geometry as depicted in Figure 2.2. The experimental program was carried out at the University of California, Berkeley. The columns were subjected to axial loading and followed by cyclic lateral displacement until axial failure. The authors concluded that the drift ratio at which axial failure occurs decreases with the increase of the axial load and the transverse reinforcement spacing (Elwood et al. 2005).

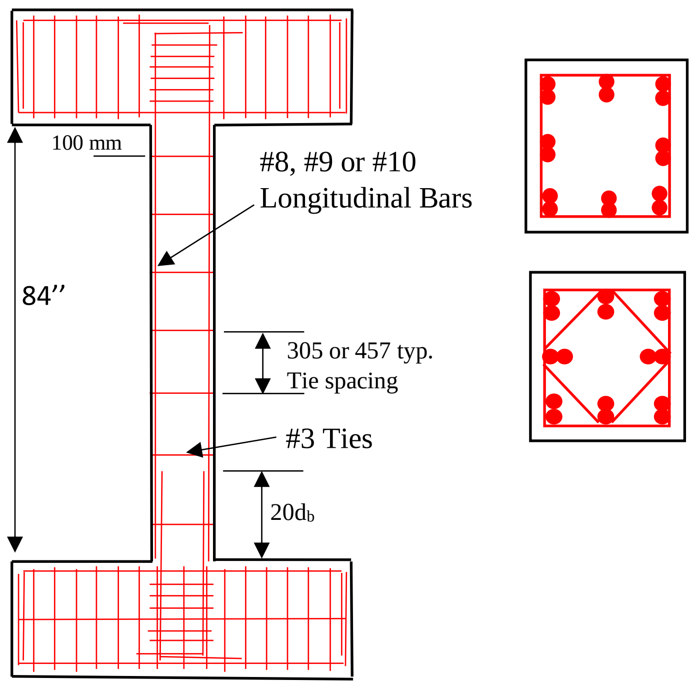

Figure 2.2: Typical Column Specimen Lynn (2001) and Sezen (2002) (Modified from Elwood 2005)

Another set of shear critical full-scale columns representing column detailing of the pre mid 1970's era was tested by Matchulat (2009). She attempted to reproduce the column's behaviour as reported in Lynn (2001) and Sezen's (2002) database. This test aimed to identify the drifts ratios where axial and shear failure occur. The test also aimed to identify the column cases that experience simultaneous axial and shear failure. Two full length columns were constructed and were tested under two different magnitudes of axial loading. The dimensions and reinforcement detailing are shown in Figure 2.3. All transverse reinforcement along the length of the column were spaced at 18 in. and closed with a 90° hook with a $5d_b$ bar extension. The Author reported the 28-day concrete compressive strengths were 5010 psi and 4700 psi for specimen 1 and 2 respectively. From tensile tests performed on steel reinforcement coupons, the longitudinal and transverse yield strength were 64 ksi and 54 ksi, respectively. The columns were subjected to cyclic lateral displacement reversals.

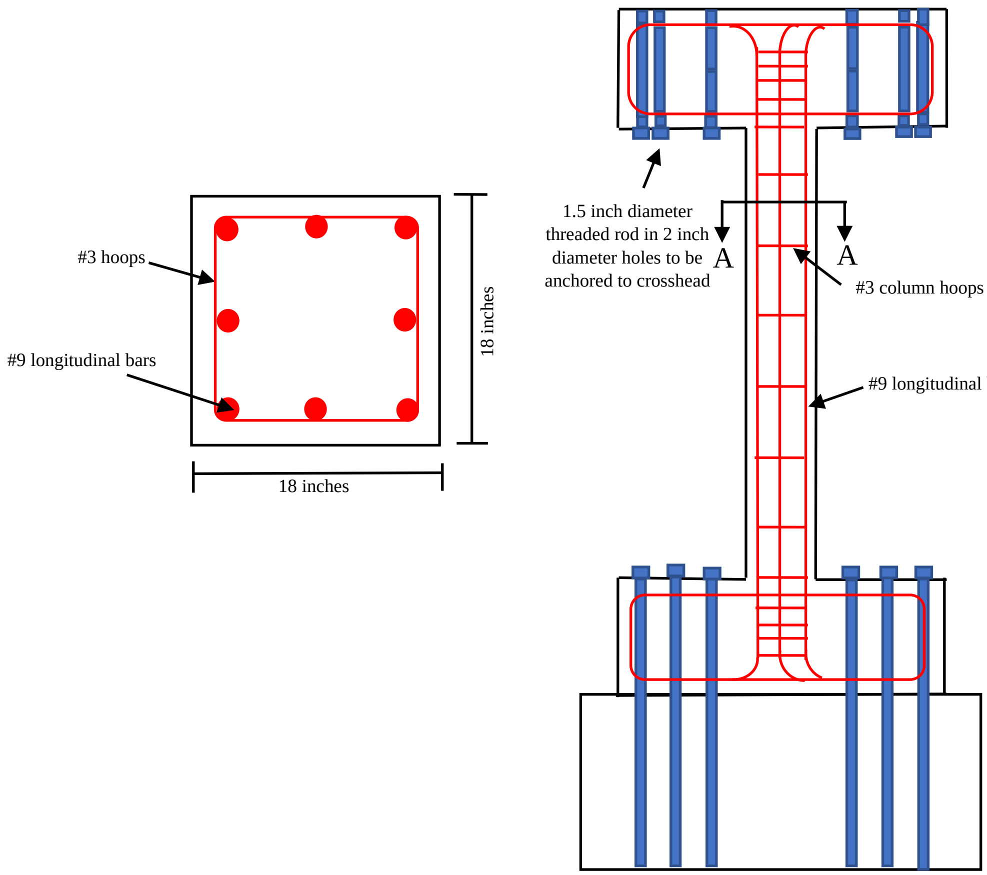

Figure 2.3: Typical Column Specimen and Testing Configuration (Modified from Matchulat 2009)

The findings from Matchulat (2009) were compatible with those of Lynn's (2001) and Sezen's (2002) tests. The authors concluded that the axial failure occurs at an earlier stage when axial loading is increased. Axial failure in first specimen which was subjected to higher axial load, occurred at a negative peak displacement in the first cycle at 1.0% drift ratio. Shear and axial failure occurred in this specimen simultaneously. For Specimen 2, which is the specimen with less axial load, the axial failure occurred at a positive peak displacement for the first cycle at a drift ratio of 1.25%. It was concluded that the occurrence of axial failure in both specimens was a result of shear degradation. It was also found that even though the columns sustained axial failure accompanied with significant damage they still retained some residual axial capacity.

Lam, Wu, Wong, Wang, Liu and Li (2003) also tested shear critical columns. The test was carried out in Harbin Institute of Technology in China. The columns in this experimental program possess low lateral confinement, high axial loads, and high longitudinal reinforcement ratios similar to columns that were build prior to the mid 1970’s. The database contained nine columns. The geometry and the reinforcement detailing of the specimens are shown in Figure 2.4. Two configurations of transverse reinforcement anchorage were studied, i.e., with 90° and 135° hooks. The columns were loaded axially in the first loading stage. For lateral loading, the displacement (U) at the onset of yielding, was recorded. The columns were subjected to two complete reversed cycles at U, 2U, 3U, etc.

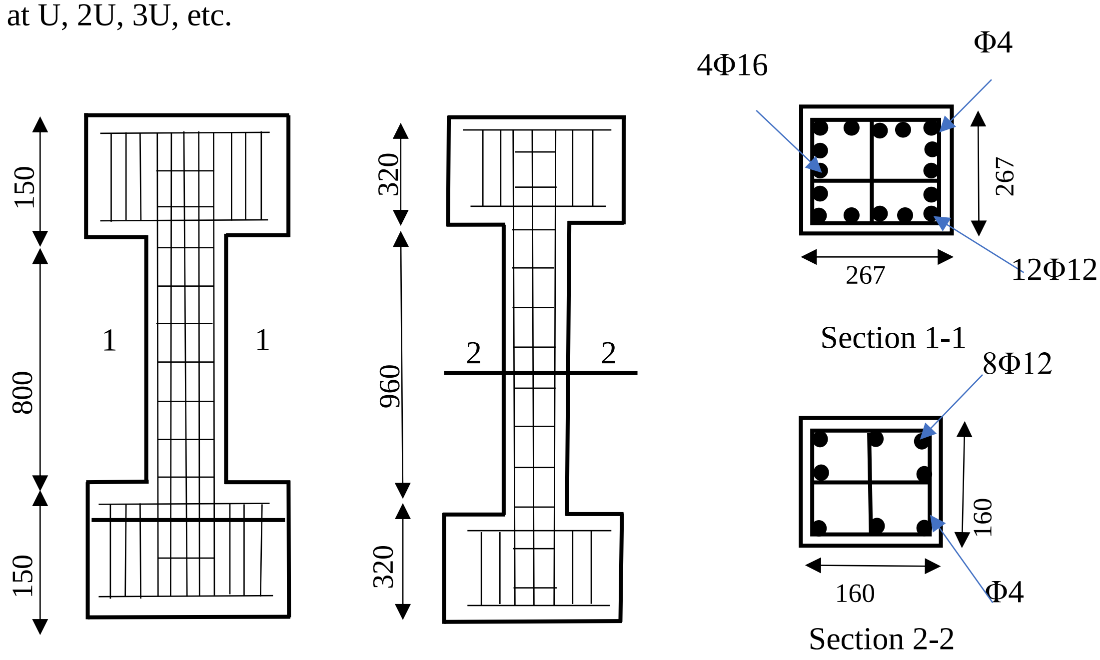

Figure 2.4: The Geometry and the Reinforcement Detailing of the Specimens Modified from Lam, Wu, Wong, Wang, Liu and Li (2003)

The monotonic loading envelopes are shown in Figure 2.5. It was concluded that columns with low shear span aspect ratio, L_s/h = 1.5 and low amount of lateral confinement fail in a shear-brittle manner (for example Column X-9 shown in Figure 2.5). The effect of confinement on the ultimate drift ratio was found significant. It was concluded that an increase in the transverse reinforcement ratio from 0.001 to 0.003 may increase the ultimate drift ratio by 100%. It was also concluded that placing a transverse reinforcement with a hook angle of 90° rather than 135° can reduce the ultimate strength to 40% (for example Column X-6 opposed to X-7 and Column X-8 as opposed to Column X-9 from Figure 2.5). The monotonic envelopes were corrected for P-Δ effects.

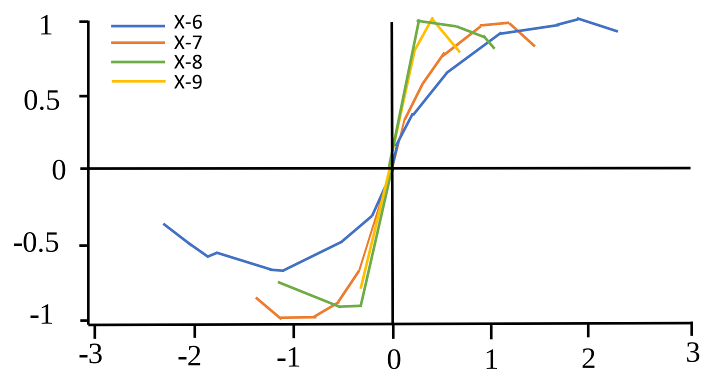

Figure 2.5: Monotonic Resistance Envelop for Four Specimens Modified from Lam, Wu, Wong, Wang, Liu and Li (2003).

The performance limit state for circular cross sections were also investigated in Goodnight, Kowalsky and Nau (2013). The column cross section details is shown in Figure 2.6. The aim of this experimental program was to study the effect of load histories and the design variables on the relationship between strain and displacement. The database contained twelve specimens which consisted of variables that are sensitive to reinforcement buckling such as the loading history, ratio of spiral transverse reinforcement and amount of axial load.

Figure 2.6: Column Cross Sectional Properties Modified from Goodnight et al. 2013

It was concluded in the study, that bar buckling is affected by the load history subjected to the column. It was found that the severity of buckling increased in the case of the symmetric three-cycle-set load history relative to real earthquakes when evaluated to the same peak displacement. This is because of an increase in the amount of inelastic cyclic loading. The fracture of a previously buckled bar occurs at a displacement equal to or less than the previously achieved buckling displacement. The authors state that the displacement when steel fractures for a previously buckled column is difficult to determine because it mainly depends on the extent of buckling damage.

Henkhaus (2010) conducted tests to study the behavior of eight full scale columns under reversed cyclic displacement reversals until axial failure. The findings were combined with findings in other experimental studies such as Matchulat (2009), Woods (2010), Lynn (2001) and Sezen (2002) with a total of 76 columns. This collection was analyzed to study the degree of reliability of columns with stirrup spacing larger than d/2, where d is the column cross-section’s effective depth and 90° hook arrangement of stirrups to resist the lateral load. It was concluded from the study that the difference between drift ratio at axial failure and the drift ratio at shear failure was approximately 0.5% for columns with axial load ratios larger than 0.2, and can be as low as zero (i.e. simultaneous shear and axial load failure).

Matamoros and Woods (2010), using simpler test series than Henkhaus (2010), studied the collapse failure of columns with low transverse reinforcement ratios and high axial loading. It was concluded that for such type of columns, the collapse is controlled by buckling mechanisms in the longitudinal reinforcement.

The study of column behaviour in literature was not limited to old type construction. Sokoli and Ghannoum (2016) studied the mode of failures in seismically detailed columns. The aim of this study was to investigate bonding and shear transfer mechanisms for columns with high steel strength. The study includes the failure type of three different columns with identical flexural strengths and therefore the mode of failures and drift ratios of these columns were comparable. The column's longitudinal detailing and elevation are shown in Figure 2.7. The columns were named, CS60, CS80 and CS100 with longitudinal reinforcement yield strength of grade 60, 80 and 100 respectively. To produce columns with equal column flexural strengths, the bar diameters were changed.

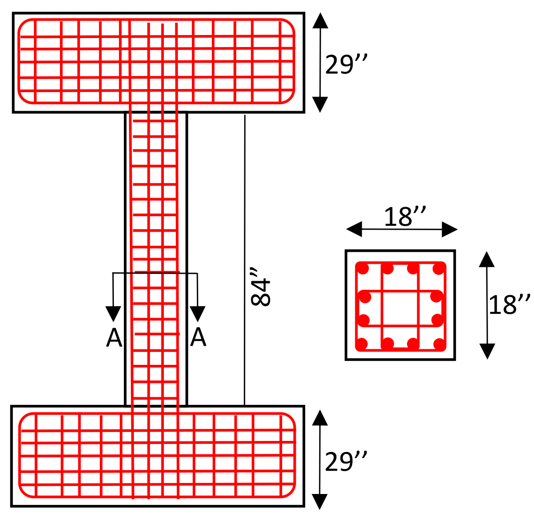

Figure 2.7: Vertical Section of Column Specimens. (Modified from Sokoli and Ghannoum 2016)

It should be noted as well that the transverse reinforcement in the columns CS60 and CS80 were designed to meet shear stress requirements and not confinement requirements of lateral resisting frames. Column CS100 met the shear and confinement requirements for lateral resisting frames according to the ACI 318M-14. It was concluded that columns CS60 and CS80 showed similar lateral load-drift ratio curves. Both columns sustained shear and axial failures at approximately same drift ratios. Moreover, the integrity of shear transfer was maintained using the two steel reinforcement grades.

Even though the columns had identical flexural strengths, higher steel strengths demanded higher bond slip, therefore, the lateral load degradation in Column CS100 was controlled by reinforcement slip. Additionally, no initiation of axial failure was observed, and the test was stopped due to the limited displacement the actuator can provide. It was also found that prior to bond failure at a drift ratio of 1.5%, the strains in the longitudinal reinforcement were double the strain in the longitudinal reinforcement in column CS60. After bond failure the strains were released throughout the height of the column.

2.4.2 Shake Table Tests

Shake tables were designed to observe the dynamic response of columns under shear and axial failure when an alternative path is available for load redistribution (Elwood 2007). Ghannoum and Moehle (2012) have developed old type experimental columns cast in a one-third scale, three bay, three storey, planner reinforced concrete frame. The frame configuration is shown in Figure 2.9. The frame consisted of two older type columns and two well detailed columns to slow the collapse failure of older type columns and to facilitate monitoring the collapse mechanism. The old type columns in this experiment were designed as flexure-shear critical columns (Column A and B as shown in Figure 2.8). The frame was subjected to 4 tests, half yielding, test 1, test 2 and test 3. Each test was subjected to different amplitude of ground excitation.

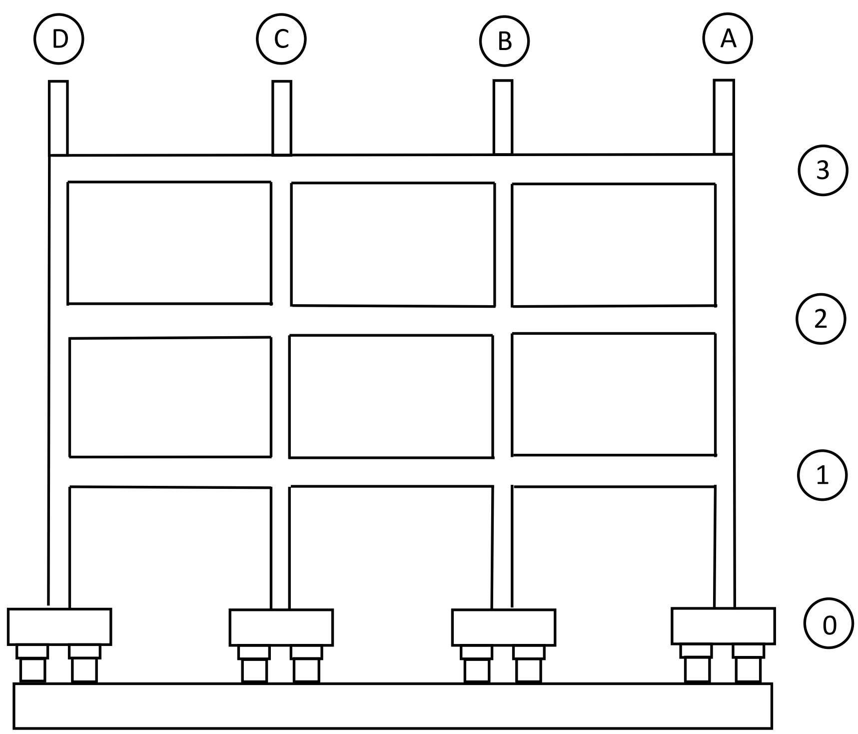

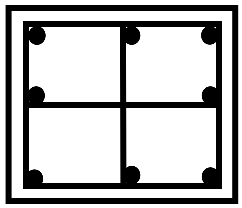

Ductile Column Section
8#2 Longitudinal Bars
3/16 in diameter wire ties
(For all floors)- Column C and D

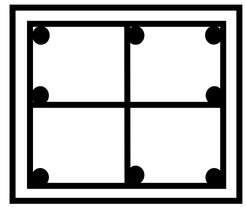

Non-Conforming Column Section
8#3 Longitudinal Bars
1/8 in diameter wire ties
(For all floors)-Columns A and B

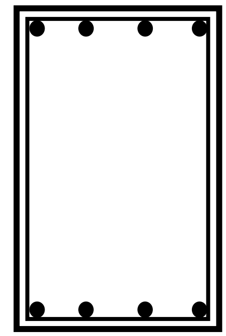

Beam Section
8#3 Longitudinal Bars
3/18 in diameter wire ties
(Typical All Beams)

Figure 2.8: Typical Cross Section and Frame Elevation for Columns (Modified from Ghannoum et al. 2007)

During test 1, the frame was subjected to Llolleo ground motion from March 1985, Chile earthquake (Llolleo Station Component 100). The ground motion was scaled to $1/\sqrt{3}$. It was concluded that B1 and A1 resist same lateral loading during the first half cycle. For the second half cycle Column B1 experienced shear distress followed by axial load failure. For Column A1, lower shear forces were sustained in the second half cycle (negative loading) which was attributed to the reduced axial load occurring from framing actions. This resulted in lower stiffness and moment strength in column A1.

The designed older type columns that are on the second floor (Column A2 and B2) did not sustain shear or axial failure during test 2 at an interstorey drift ratio of 0.047 (which is equal to the interstorey drift for shear failure of the column on the first floor) . This was attributed to two reasons: 1) due to the lower axial load on the columns compared to the columns on the first floor, the shear demand V_p, is reduced, 2) an important reason lies in the difference in the end connections between the columns on the first and second floor. For example, the columns on the first floor are connected to rigid end foundations, which required the column to experience extreme flexural deformations to undergo the applied drifts. However, the columns on the second floor are connected to beam-column joints which rotate and deform, granting flexibility to the column ends and therefore they undergo less flexural deformations at the same applied drift.

Elwood (2007) has also conducted shake table tests on a 2D frame with three scaled columns connected to a top beam. The column’s cross section is shown in Figure 2.9. The central column was designed to fail in shear (shear-critical column) and designed as one-half scale of Sezen (2002) column. For the first test specimen the central column carried an axial load of $0.1f_cA_g$ and the second specimen carried an axial load of $0.24f_cA_g$. The aim of this study was to investigate the load distribution which occurs when the system is redundant, after shear failure of the central column.

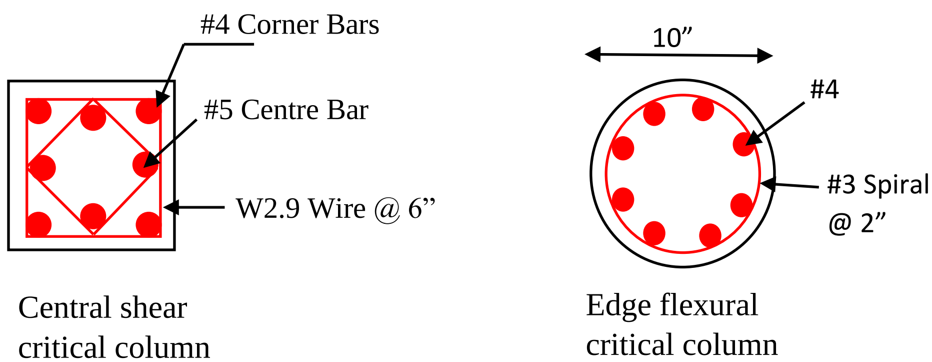

Figure 2.9: Test Configuration of (Modified from Elwood 2007) Shake Table Test

It was found from Elwood's (2007) tests that when the central column was subjected to higher axial load, shear failure occurred at lower drift ratios compared to the specimen with lower axial load. The results of the test also indicated that when the central column was subjected to a low axial load, most of its initial share of overbearing axial load was maintained and not redistributed. The author also concluded that the main cause of shortening in the column when axial failure is initiated is attributed to larger pulses that suddenly increase the vertical displacement when critical drift ratio was reached. Another reason for column shortening when axial failure occurs is due to the smaller oscillations that appear to cause collapse of the shear-failure plane. During axial failure of the central column larger load transfer occurred to the outside columns.

Shin (2007) conducted shake table tests on a single- storey, single bay reinforced concrete frame with a rigid top beam. The two columns forming the single bay are either both ductile to achieve a ductile frame response, or one ductile and one shear-critical to provide a gradual shear degradation response, or two shear critical columns, where very low shear strength is achieved. The design of the shear critical columns are prototypes from Lynn (2001) and Sezen (2002) single column tests. Two axial loads were applied ($0.1f_cA_g$ and $0.24f_cA_g$) to each combination of columns. The test configuration is shown in Figure 2.10. The column was built at 1/3 scale.

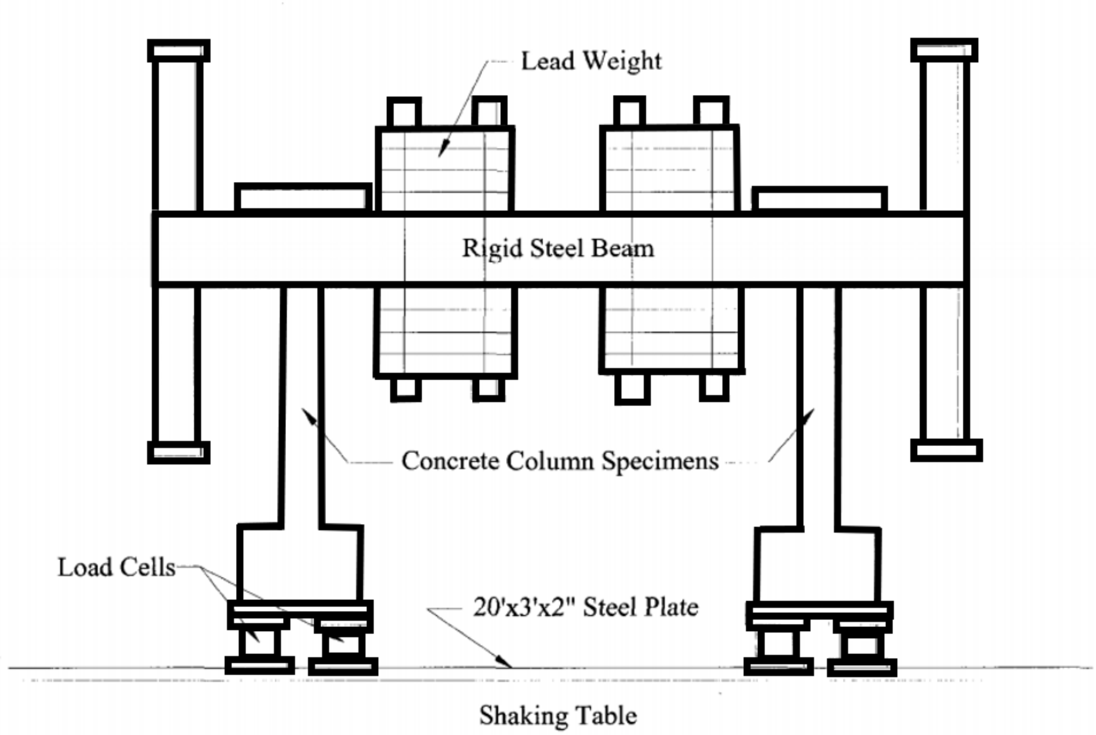

Figure 2.10: Test Configuration of (Modified from Shin 2007) Shake Table Test

The frame was subjected to two real ground motion records from Chile (1985) and Kobe (1995) earthquake. The Chile (1985) earthquake is a long duration and low velocity ground motion while Kobe (1995) is a short duration and high velocity ground motion. The test showed that shear degradation to the different ground motion tests were not similar. The strength degraded from cycle to cycle when the frame was subjected to Chile (1985) ground motion inputs. However, the frames subjected to Kobe (1995) earthquake had a monotonic in-cycle shear degradation. The drift demands for the frames subjected to Kobe were higher. As was concluded from the previous test, increasing the axial load caused a rapid axial load failure. However, contrary to observations in some of the previous studies, axial failure initiation did not necessarily occur when shear capacity degraded to approximately zero.

Yavari (2011) studied the behaviour of lightly reinforced concrete columns up to collapse under scaled ground motion excitation. His experimental study consisted of four two-bay and two-story frames. The geometries and details were selected to be representative of elements used in an existing six-story hospital building in Taiwan. The influence of unconfined joints on the collapse behaviour of the frame was also investigated.

The author tested four specimens with varying axial load, joint confinement and column's modes of failure (either flexure-critical columns or shear-flexure-critical). As concluded from previous tests, the behaviour of the column was controlled by the amount of axial load. It was found that the gap between the flexure and shear failure decreases with an increase in the axial load. The shortening after axial failure for the specimen with higher axial loads occurs at a higher pace compared to the specimens that were subjected to lower axial loads. This caused different damage patterns and collapse modes for the two specimens. Opening and closing of cracks at first-story joints for the frames with unconfined joints were observed. The unconfined joints did not allow shear to be fully developed in first-story columns by accommodating much of the deformation demands and reducing the moment at the top of the columns.

Wu et al. (2008) conducted reversed cyclic shake table tests on half scaled planar frames. The author subjected the frames to lateral loading using a recorded earthquake ground excitation from (1999) Chi-Chi Tiawan eqarthquake. Three of the frames consisted of two short columns and one consisited three short columns with a central nonductile column and two outside flexure-critical columns. Flexural columns were added to the frame to allow for gradual vertical and lateral failure in order to monitor the collapse of the frame. From the three-column frame tests it was confirmed that vertical load redistribution exists. The diagonal crack on the columns after shear failure were in an average of 60° angle with respect to the transverse axis. The authors also concluded that the existing models used to estimate shear strength underestimate the shear strength of ductile columns.

2.5 Analytical Models for Deformation Capacity and Shear Strength

The total lateral displacement of a cantilever column under reversed cyclic loading can be modelled analytically in a series of springs simulating its flexure, shear and slip deformation contributions to its response (Shoraka et al. 2013). In this section the efforts placed on simulations of the columns analytically using *OpenSees* (PEER 2006) will be reviewed. This section will also present proposed models for estimating shear and axial failure rotations which were calibrated from assembled experimental column databases.

2.5.1 Flexure Response of Columns

The flexural behaviour of the columns were simulated using force formulations of the classical fibre-section element (Shoraka et al. 2013 , Ghannoumn et al. 2012). This methodology used for simulating flexure in a column has shown high fidelity when calibrated against experimental data. Moreover, this methodology has been known for its ease in application as it only requires the input of the section geometry and material properties.

Examples of fibre section analysis was found in Shoraka and Elwood (2013) in efforts to develop a sufficient and noncomplex computational model through *OpenSees* (PEER 2006) and verify its validity from cyclic resistance curves of columns obtained experimentally. The flexural behaviour was derived from the moment curvature analysis of fiber cross-sectional model using appropriate material models. The authors employed Modified Park and Kent (1982) model for describing the uniaxial stress-strain relationship for concrete in compression, and the Giuffré-Menegotto-Pinto Model for the reinforcement steel. The column was modelled as a flexural sub element using nonlinear fibre elements, where the length was divided into five sections for the moment-axial load interaction (Spacone et al. 1996). The sectional forces in the column were found from the integration of forces at the column ends (flexibility method). The sectional deformations were than found from the sectional forces which were than integrated over the length of the column to find the deformation at the column end sections. The authors attempted to reproduce experimental columns using the proposed model. The experimental database was collected from Mostafaei et al. (2009), Henkhaus, (2010), Matamoros and Woods (2010) and Sezen and Moehle (2006). The combined deformations (flexure, shear and slip) showed good correlation with the experimental models until the point of shear failure.

Ghannoum and Moehle (2012) also attempted to replicate their experimental planar three bay, three storey frame response through nonlinear analysis using OpenSees (reviewed in Section 2.4.2). The authors also used fibre section elements to simulate the cyclic flexure behaviour including concrete cracking, steel yielding and concrete crushing. Ghannoum and Moehle (2012) used three sub elements per column. The top and bottom sub elements consisted of two fibre elements, one fibre element at each end of the sub element (with a length (h) between the two fibre sections, where h is the depth of the column cross section in the direction of loading). The middle sub element consisted of five fibre elements with a distance of h between two consecutive fibre elements. The plastic hinge length in this study was taken equal to h/2 for simplicity. In this discretization, most of the inelastic deformations occur at the column's ends. The model was capable of simulating the important aspects of the measured dynamic response from low deformation levels to well beyond flexural yielding.

2.5.2 Shear Response of Columns

The flexural and bar slip reponse are predicted accurately by current models whereas the shear degradation response of columns with inelastic flexural deformation needs further development. This section will summarize one of the latest improvements in the shear behaviour of previous proposed models used proposed by Shoraka and Elwood (2013).

Shoraka and Elwood (2013) provide an improved update on Elwood et al. (2005) model using concepts from the displacement-based analysis method which studies the interaction between axial-shear- flexural response (Mostafaei et al. 2009). Moreover, this model is based on physical mechanics rather than empirical equations. This model also presents the capacity of columns with different type of failure modes with acceptable accuracy (Shorakra et al. 2013).

Shoraka and Elwood (2013) have developed a model to estimate the shear resistance curves for columns. The authors divided the shear response into three phases and developed analytical models from the available in the literature. The first phase, which is the pre-peak phase of the response, before the column reaches its shear strength, is modelled using the Modified Compression Theory (MCFT) developed by Vecchio and Collins (1986). The second phase, which is the peak shear strength of the column, is modelled using analytical models from Mostafaei et al. (2009). For the final phase, which corresponds to the descending branch of the shear reponse, the authors used a developed model from Elwood and Moehle (2005) for the drift ratio at axial failure.

The MCFT relates average stresses to average strains in a cracked reinforced concrete element. From MCFT (Vecchio and Collins 1986) the axial strains are related to the longitudinal strains (ε_x along the centroidal axis and φ the sectional curvature). Shear strain is obtained from longitudinal and transverse sectional strains using Eq. 2.1. The strains in the second principal direction (in compression) are evaluated using Eq. 2.2 from sectional analysis. The strains in the first principal direction are calculated in accordance with Eq. 2.3 according to MCFT. Finally, the transverse strains are calculated using strain compatibility from Eq. 2.4

[2.1] $\gamma_s = 2\sqrt{(\varepsilon_x - \varepsilon_2)\left(\varepsilon_y - \varepsilon_2\right)}$

[2.2] $\varepsilon_2 = \varepsilon_x + \frac{\varphi\,(h-0.85c)}{2}$

[2.3] $\varepsilon_1 = (\,\varepsilon_x - \varepsilon_2)\frac{f_{c1}-f_{cx}}{f_{c1}+f_{y,tr}\rho_{sy}} + \varepsilon_x$

[2.4] $\varepsilon_y = \varepsilon_1 + \varepsilon_2 - \varepsilon_x$

where,

γ_s is the shear deformation, ε_2 is the principal compressive strain, c is the depth of the compression block, f_{c1} is the stress in the concrete in the first principal direction (tension). The strains ε_2, $\varepsilon_1, \varepsilon_y$ are found according to Eq. 2.2, 2.3 and 2.4 respectively, they are substituted into Eq. 2.1 for shear deformations prior to peak shear strength.

The displacement-based analysis proposed by Mostafaei et al. (2009) was used for estimating the point of shear failure. The point of shear failure is defined by one of the following mechanisms: 1) diagonal tension failure which happens when insufficient amount of shear reinforcement is placed in the column which produces columns uncapable of restricting crack width opening in the web, 2) diagonal compression failure which happens in columns with high axial load when the principal compressive stress exceeds the strength of concrete in the direction of the compressive strut of the column (Kuo et al. 2006). Equation 2.5 and 2.6 developed by Collins and Mitchell (1991), define the limit of shear stress when diagonal tension failure occurs, and diagonal compression shear failure occurs respectively:

[2.5] $\tau = \frac{V}{bd_f} \geq \tau_i + f_{syt}\rho_{sy}\,cot\,\theta_c$

[2.6] $\tau = \frac{V}{bd_f} \geq \frac{f_{c1} - f_{c2}}{(tan\,\theta_c + 1/\,tan\,\theta_c)}$

where τ_{i} is calculated in accordance with Walraven's equation (Walraven 1981). d_f is equal to the depth of the section h for columns with span to depth ratios less than 1.0 or equal to the effective depth for columns with span to depth ratios higher than 1.0 to 1.5 (Mostafaei et al. 2009). Angle θ_c is the cracking angle, which is the angle formed between the inclined crack and the vertical axis). f_{c2} is the stress in concrete in the second (compressive) principal direction and τ is the shear stress at shear failure. Other symbols were defined in Eq. 2.1-2.4. In this model the concrete principal compressive strain and the longitudinal strain are calculated from Eq.2.7 and 2.8 respectively. These equations were developed based on average values of the concrete uniaxial compression and longitudinal strains corresponding to the resultant forces of the concrete stress block.

[2.7] $$\varepsilon_2 = \frac{\varepsilon_{2i} + \varepsilon_{2i+1}}{2}$$

[2.8] $$\varepsilon_x = \frac{\varepsilon_{xci} + \varepsilon_{xci+1}}{2}$$

Where ε_{xci} and ε_{2i+1} are calculated from sectional analysis. The cracking angle is found based on Mohr's circle found in Eq. 2.9.

[2.9] $$cot\theta_c = \frac{\gamma_s}{2(\varepsilon_x - \varepsilon_2)}$$

The shear deformation for diagonal tension shear failure and diagonal compression shear failure are found by combining Eq.2.9 and Eq. 2.5 or 2.6 (Mostafaei et al. 2009) and are shown in Eq. 2.10 and 2.11 respectively.

[2.10] $$\gamma_s \leq \gamma_{st} = \frac{\frac{V}{bd_f} - t_i}{f_{syt}\rho_{sy}}\, 2(\varepsilon_x - \varepsilon_2)$$

[2.11] $$\gamma_s \geq \gamma_{sc} = (\varepsilon_x - \varepsilon_2)\left[\frac{(f_{c1} - f_{c2})bd_f}{V} + \sqrt{\left[\frac{(f_{c1} - f_{c2})bd_f}{V}\right]^2 - 4}\right]$$

The shear friction model for the descending part of the shear resistance response curve, developed by Elwood and Moehle (2005) is used to model the descending branch in the Shoraka and Elwood (2013) model. The shear friction model is extended to provide an estimation of the degrading slope after shear failure. The authors developed this model to reproduce the shear behaviors of columns from the Sezen and Moehle (2006) database which was discussed in Section 2.3.5. Combining Equation 2.29 and 2.30 (equation of equilibrium of forces along the inclined shear crack) from Section 2.3.5 results in Eq. 2.12.

$$[2.12]\ V = \frac{A_{st} f_{y,tr} d_c}{s} 2.1 - P\left(\frac{25\frac{\Delta}{L}}{5.6 - 53.5\frac{\Delta}{L}}\right)$$

Where P is the axial load, A_{st} is the transverse reinforcement area, $f_{y,tr}$ is the transverse reinforcement yield strength and L is the clear length of the column, s is the longitudinal stirrup spacing and d_c is the depth of core (centerline to centerline of ties).

By differentiating Eq. 2.12 and combining it with Eq. 2.34 in Section 2.3.5 the degrading slope of the shear drift backbone in terms of axial load and transverse reinforcement ratio is derived, as shown in Eq. 2.13.

$$[2.13]\quad \frac{dV}{d\left(\frac{\Delta}{L}\right)} = -4.5P\left(\frac{A_{st} f_{y,tr} d_c}{P s_h} 4.6 + 1\right)^2$$

This shear response was calibrated against a database of experimental resistance curves from Mostafaei et al. (2009), Henkhaus (2010), Matamoros and Woods (2010), and Sezen and Moehle, (2006). It was concluded that the post peak branch of the curves needed improvement, however, the estimates are more reasonable when the failure is controlled by diagonal compression shear failure. The shear mechanism was modelled using a spring that was translational in the transverse direction; this was connected to a rotational spring at the base of the clear span to account for pullout slip, and zero length axial load springs in series.

Ghannoum and Moehle (2012) simulated the shear response using a spring with a shear stiffness of (5/6)GA_g/(L/2). This shear model produced discrepancy when calibrated against the experimental column in the frames tested by the same authors at the point of shear failure and the post peak shear reponse. Therefore, no shear model has been developed to be capable of accurately representing the shear response of the column after shear failure.

2.5.3 Slip Response of Columns

When the bar is under tensile stresses, additional required length is needed to transfer the stress to the anchored portion of the reinforcement. Thus, slip in the longitudinal bar is produced as a result of bar elongation due to the present strains in the anchored portion of the bar (Ghannoum 2007). This accumulates towards the loaded end, causing rigid body rotation that is not accounted for in the flexure response of the column (Shoraka et al. 2013). Bar slip accounts for almost 40% of the lateral deformation (Sezen and Moehle 2006).

The first bond slip model was developed by Otani and Sozen (1972) which assumes a constant bond stress along the anchored reinforcement. Eligehausen et al. (1983) and Ciampi et al. (1982) developed a more detailed bond slip relation, depending on the concrete strength, confinement and interface geometry. Sezen and Setzler (2008) developed uniform stress models depending on whether the reinforcement yields or not. The moment and bar slip relationship using Sezen and Setzlers (2008) model depends on the column's cross section, ratio of longitudinal and transverse reinforcement, axial external load, and material properties.

Lehman and Moehle (2000) studied the stress bond relation for lightly confined circular columns. This model assumes constant elastic bond stress before yielding and after yielding, with values of $12\sqrt{f_c}$ (psi) and $6\sqrt{f_c}$ (psi). Figure 2.11 depicts the strain profile and the bond stress along reinforcement embedment. As shown in Figure 2.11 the bond stress profile can be linearized without loss of accuracy (Ghannoum et al. 2007). Assuming a bi-uniform bar stress, the slip in the longitudinal reinforcement is the result of integrating strain profiles along the anchorage length as shown in Eq. 2.14 and 2.15.

[2.14] $S_y = \frac{\varepsilon_y f_{yl} d_b}{8u_e} \ if \ \varepsilon_s \leq \ \varepsilon_y$

[2.15] $S_s = \frac{\varepsilon_y f_{yl} d_b}{8u_e} + \frac{(\varepsilon_y + \varepsilon_y)(f_s - f_y) d_b}{8u_p} \ if \ \varepsilon_s > \ \varepsilon_y$

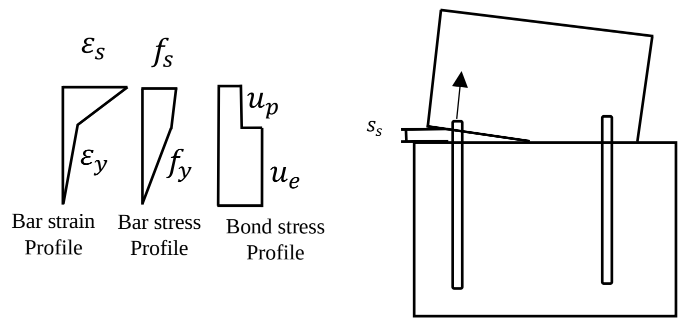

Figure 2.11: Bar Strain and Bond Stress Profile for Bar Slip (Modified from Ghannoum and Moehle 2012)

Berry (2006) worked on linearizing the parabolic relation of the bar slip to steel reinforcement stress ratio when using bilinear steel stress-strain relation. Zhao and Sritharan (2007) derived bar stress and bar slip relations from calibration against experimental data. Therefore, the bond -steel stress relations was not a required step to estimate bar slip.

Ghannoum and Moehle (2012) developed improvements to the Berry (2006) and Zhao and Sritharan (2007) models. Berry (2006) and Zhao and Sritharan (2007) models assumed discontinuous steel stress and neutral axis location between the bar slip and the adjacent fibre section. To eliminate discontinuity, the rotations due to bar slip are calculated according to Eq. 2.16. The curvature of the adjacent fibre section is given in Eq. 2.17.

[2.16] $\theta_{bs} = s_s/(d-c)$

[2.17] $\varphi = \varepsilon_s/(d-c)$

Where, c is the depth of the compression block, s_s is the slip along the bar and ε_s is the reinforcement steel strain. From combining Eq. 2.16 and 2.17, the bar slip values are related to the concrete strains through a ratio r = s_s/ε_s and the rotation due to bar pullout can be modelled according to Eq.2.18.

[2.18] $\theta_{bs} = \varphi\left(\frac{s_s}{\varepsilon_s}\right)$

In Eq.2.18 the concrete strains in the fibre of the bar slip fibre section is related to the concrete strains in in frame element fibres through the ratio r. This avoids discontinuity in steel stress and neutral axis location between the bar and adjacent fibre section. The elastic bond stress values, u_e, assumed by Lehman and Moehle (2000) showed adequate correlation when calibrating the analytical values of slip rotation against experimentally measured rotations due to slip, in Ghannoum and Moehle (2012).

2.5.4 Shear Deformation Capacity Models

Shear rotation capacity is defined in multiple ways in research. Some researchers agree that the rotation at shear failure should be determined at a point when diagonal shear cracking develops. Other researchers assume that the shear rotation capacity is determined at 20% reduction in the lateral load resisting curve. This section will provide shear deformation capacity models based on a specific shear rotation capacity definition.

Elwood (2004) proposed an equation to calculate the deformation capacity at which shear failure occurred as shown in Eq. 2.19.

[2.19] $$\frac{\Delta_s}{L} = \frac{3}{100} + 4\rho_{sy} - \frac{1}{40}\frac{\nu}{\sqrt{f_c}} - \frac{1}{40}\frac{P}{A_g f_c} \geq \frac{1}{100}$$

Where, ν is the axial load ratio, ρ_{sy} is the transverse reinforcement ratio.

This drift ratio is at a shear degradation of more than 20% of the maximum shear strength. When implementing this model in *Opensees* (PEER 2006) for a database of columns tested experimentally, it was found that this model correlates well only to columns with similar properties of those that had been used by Elwood (2004) to derive the empirical form of Eq. 2.19. The database columns considered were flexural-shear columns.

Kato and Ohnishi (2002) proposed a model to calculate the drift ratio at shear failure as shown in Eq.2.20, 2.21 and 2.22. The model accounts for the maximum edge strain of the concrete core, axial load ratio and the cross-sectional dimensions. A shown from Eq. 2.20 the model is a sum of the drift ratio at yielding and the plastic rotation. The shear failure is defined at a drop of 20% of shear strength.

[2.20] $$\frac{\Delta_s}{L} = \frac{\Delta_y}{L} + \frac{\Delta_p}{L}$$

[2.21] $$\frac{\Delta_p}{L} = h\left(\frac{g\varepsilon_{cp}}{j_e}\right)\left(\frac{2}{3e_n}\right), 0 < e_n < \frac{1}{3}$$

[2.22] $\frac{\Delta_p}{L} = h\left(\frac{g\varepsilon_{cp}}{j_e}\right)\left(\frac{2/3}{5e_n - \frac{4}{3}}\right), \frac{1}{3}, \leq e_n < \frac{2}{3}$

In the above equations, h is the depth of the gross cross section, j_e is the depth of the core, ε_{cp} is the core strain corresponding to maximum concrete stress. g is the ratio of the strain at the core edge to the core edge strain at axial or shear failure. e_n is the equivalent axial load ratio. This model showed close estimations when compared to the column specimens of Ghannoum and Moehle (2012).

Pujol et al. (1999) proposed a model to define the drift ratio at shear failure for columns based on a database containing 92 columns. The model is shown in Eq.2.23.

[2.23] $\frac{\Delta_{max}}{L}(100) = \left(\frac{\rho_t f_{y,tr}}{v_{max}}\right)\frac{a}{d} \leq \frac{a}{d}, 4$

Here the shear failure is defined at 80% of the maximum shear strength. Term v_{max} is the column shear stress at shear failure and is equal to the ratio of the applied shear force at failure divided by $b_w d$. This model is based on the observation that the drift ratio at shear failure increases with the increase in the aspect ratio $\frac{a}{d}$ and transverse reinforcement index $\frac{\rho_t f_{y,tr}}{v_{max}}$. This model showed conservative estimations when compared to columns from Ghannoum and Moehle (2012).

Sasani (2007) proposed a model to estimate the drift ratio at shear failure as shown in Eq.2.24. This model was developed from the observation that the drift ratio at shear failure increases with the increase of the volumetric transverse reinforcement ratio and shear span section height ratio and decreased with the increase in the magnitude of the axial load.

[2.24] $\theta_{sh,fail} = \lambda {\rho_{s,tr}}^{0.74} \nu^{-0.18} \frac{a}{h}$

λ equals 1 for columns with single curvature and 0.85 for column bent in double curvature, a is the shear span length, ν is the axial load ratio and $\rho_{s,tr}$ is the volumetric transverse reinforcement ratio. Shear failure is defined at 80% of the maximum strength on the post peak curve.

Ghannoum and Moehle (2012) also proposed a model to calculate the drift at which shear failure occurs. The model was derived based on 56 laboratory tests from Sezen and Moehle (2006), Lynn (2001), Ohue et al. (1985), Esaki (1996), Li et al. (1991), Saatcioglu and Ozcebe (1989), Yalcin and Saatcioglu (2000), (Ikeda (1968), Umemura and Endo (1976), Kokusho (1964), Kokusho and Fukuhara (1965)) all as reported in Masaya (1973), Wight and Sozen (1973), Elwood and Moehle (2005), Ghannoum (2007) and Yoshimura et al. (2003). The model assumes that the shear strength of a column at shear failure *(V_n)* is a function of concrete compressive strength, concrete maximum tensile strain ε_t, concrete maximum stress and strain (σ_c and ε_c) and transverse reinforcement strength and ratio ρ_t, $f_{y,tr}$ as shown in Eq. 2.25

$$[2.25]\quad V_n = V_{max} = f(\frac{s}{d}, \rho_t, f_{y,tr}, f_c, \varepsilon_t, \sigma_c, \varepsilon_c)$$

Using forward stepwise linear regression, it was found that the total end rotations are most sensitive to the parameters s_h/d, $P/A_g f_c$ and $v_{max}/\sqrt{f_c}$. Equation 2.26 was developed with the constants b_o, b_1 and b_2 found using iterative reweighted least square algorithms. The constants found for b for different maximum rotations indices are shown in Table 2.1.

$$[2.26]\quad \theta_{max} = b_o + b_1\left(\frac{s}{d}\right) + \ b_2\left(\frac{P}{A_g f_c}\right) + b_3\left(\frac{v}{\sqrt{f_c}}\right)$$

Table 2.1 Column Rotation Model Regression Parameter (Ghannoum and Moehle 2012)

	θ_{totmax}	$\theta_{ftotmax}$	$\theta_{totPlmax}$	θ_{fPlmax}
b_o	0.0437	0.0210	0.0317	0.0149
b_1	-0.0171	-0.0077	-0.0138	-0.0067
b_2	-0.0211	-0.0088	-0.0165	-0.0065
b_3	-0.024	-0.013	-0.019	-0.0010

Where θ_{totmax} is the total rotation at the initiation of shear failure (δ_{max}, V_{max}) measured over hinge length h and including bar-slip–induced rotations. $\theta_{ftotmax}$ is the column flexural rotation at shear failure initiation measured over a hinge length h excluding bar-slip–induced rotations. $\theta_{totPlmax}$ plastic rotation component of θ_{totmax} and θ_{fPlmax} is the plastic rotation component of $\theta_{ftotmax}$.

More empirical equations for the ultimate drift rotation were proposed by Lam , Wu, Wong, Wang, Liu and Li six (2003) from a database comprising 107 columns from Taylor et al. (1997). The columns in the database possessed low amounts of lateral confinement, high axial load ratios and moderate to low shear span ratios. Several mathematical equations were studied, and the influence of the shear span and the axial load is introduced in the expression for the ultimate rotations through a non-dimensional parameter α shown in Eq. 2.26.

[2.26] $\alpha = (1+m)\left(1-\sqrt{v}\right)\sqrt{\frac{\rho_{s,tr} f_{y,tr}}{f_c}}$

Where m is the shear span to depth ratio and v is the ratio of the axial load to the axial load carrying capacity. The ultimate drift rotation for experimental data was plotted against α to provide a parabolic relation shown in Eq. 2.27.

[2.27] $\frac{\theta}{100} = 0.564 + 8.459\alpha - 7.804\alpha^2$

The ductility of the columns with a transverse reinforcement detailing with a 90° hooks is related to the ductility of well tied columns (stirrups anchored with 135° hooks) from Eq.2.28.

[2.28] $\mu_{90} = 1 + (\mu_{135} - 1)R$

R= 0.65 for columns with a shear span to depth ratio of 3.0 and 0.33 when the shear span- depth ratio is reduced to 1.5.

2.5.5 Drift Capacity at Axial Failure Models

Elwood and Moehle (2005) developed an analytical model to relate the drift ratio of a column at axial failure with the axial load and the transverse reinforcement spacing. The authors derived the relation based on shear friction which is the mechanism responsible for transferring the axial load across a shear crack in a column exhibiting shear failure. The free body diagram of forces the shear crack are shown in Figure 2.12. Equations 2.29 and 2.30 are derived from equilibrium of forces across the shear crack in the horizontal and vertical directions. The two equations were derived from free body equilibrium considering that the column has no residual shear strength when the axial failure occurs (V=0) and the dowel action of the longitudinal reinforcement is ignored due to the large stirrup spacing (V_d=0).

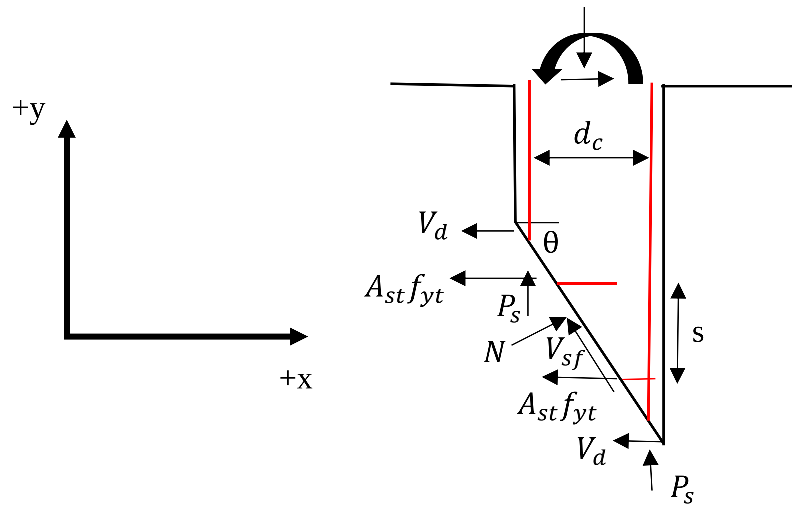

Figure 2.12: Free Body Diagram of Forces along a Shear Crack (Modified from Elwood et al. 2005)

Equilibrium of forces in the x direction:

[2.29] $Nsin\Theta + V_{sf}\cos\Theta = +\frac{A_{st}f_{yt}d_c}{s}tan\Theta$

Equilibrium of forces in the y direction:

[2.30] $P = Ncos\Theta + V_{sf}sin\Theta + n_{bars}P_s$

In the above equations, Θ is the angle that forms between the critical sliding crack and the member cross section (i.e., the crack angle at which axial failure occurs). The authors found that this angle correlates to the linear relation shown in Eq. 2.31 calibrated with critical angles in the experimental database of Lynn (2001) and Sezen (2002). The average critical angle is 65°.

[2.31] $\Theta = 55 + 35P/P_o$

With reference to Fig. 2.9, P is the axial load acting on the cross section, and P_o is the axial crushing load of the column cross section, taken equal to $0.85f_c(A_g - A_{sl}) + f_{yl}A_{sl}$ (here, A_{sl} and f_{yl} is the area and strength of the longitudinal reinforcement).

Traditional models of shear friction found in AC1 318 (1977) assume the shear crack as a flat surface and the shear capacity is product of the axial force acting along the crack and the coefficient of friction μ (i.e., V= Nμ). Substituting Eq. 2.29 and 2.30 into this formula, it is possible to solve for the axial load capacity of the column from Eq. 2.32.

$$[2.32]\quad P = \frac{A_{st} f_{yt} d_c}{s} tan\theta \frac{1+\mu tan\theta}{tan\theta-\mu} + n_{bars} P_s$$

The axial capacity of the column is taken as the maximum of the capacity from the longitudinal reinforcement and the capacity from the shear-friction model. For the maximum capacity model, the shear friction coefficient was derived as shown in Eq. 2.33.

$$[2.33]\quad \mu_m = tan\theta - \frac{100}{4}\left(\frac{\Delta}{L}\right)_{axial} \geq 0$$

Combining Eq.2.32 and 2.33, Elwood and Moehle (2006) derived Eq. 2.34 to account for the drift ratio at which axial failure occurs.

$$[2.34]\quad \left(\frac{\Delta}{L}\right)_{axial} = \frac{4}{100} \frac{1+(tan\theta)^2}{tan\,\theta + P\left(\frac{s}{A_{st} f_{yt} tan\theta}\right)}$$

This model has provided adequate correlation to the database assembled by Lynn (2001) and Sezen (2002). However, this model does not take into consideration the effect of the loading history. As concluded by Goodnight et al. (2003), the loading history on the column plays a crucial role in buckling. This is due to the residual tensile strain in the bar when it is subjected to compression stress after tension.

Ousalem et al. (2004) proposed a model to calculate the drift ratio at axial failure as shown in Eq. 2.35 based on the concrete strength, the transverse reinforcement ratio ρ_{sx}, the transverse reinforcement strength $f_{y,tr}$ and the axial load ratio ν.

$$[2.35]\quad \theta(\%) = \frac{1}{K}\left(\frac{0.97 - 1.33K}{\sqrt{0.03 + 1.33K}}\right)^{-\frac{1}{0.36}}$$

Where $K = \frac{\rho_{sx}\, f_{y,tr}}{n\, f_c}$

Matamoros and von Ramin (2005) have also proposed a model for the drift ratio as shown in Eq. 2.36. This model depends on the transverse reinforcement ratio and axial load.

$$[2.36]\quad \delta_a = \frac{1-x}{x}\frac{1}{1.5(6^{\lambda})}$$

Where $x = \frac{30(\beta f_c)}{f_{y,tr}} \sin^2 \emptyset\, , \lambda = 1 + 2\left(\frac{P}{f_c A_g}\right)^{0.35}\, ,\ \beta = 0.85 - 0.004 f_c \geq 0.5\ (MPa)$

Where $\emptyset$ is the angle of inclination of the compression field related to the vertical web reinforcement.

2.5.6 Shear Strength Models

From the experimental tests conducted by Priestley et al. (1994), a shear strength model was proposed by the same researcher in 2004. This shear strength model suggests that the shear strength of a member can be obtained as the sum of contributions of strength from concrete V_c, transverse reinforcement V_s and axial load V_p. Concrete shear strength is found according to Eq. 2.37. The shear strength contribution from the transverse reinforcement is based on a truss mechanism that develops in the member web, assuming a 30-degree angle between the compression diagonal and the column axis, whichever is larger and is given in Eq. 2.38. Equation 2.39 is the shear contribution from the axial load (all equations are in psi).

$$[2.37]\quad V_c = k\sqrt{f_c}0.8A_g$$

$$[2.38]\quad V_s = \frac{A_v f_{y,tr} d'}{s_h}\cot 30$$

$$[2.39]\quad V_p = P\tan\alpha = \frac{d-c}{2L_s}P$$

where d' is the distance between centers of the peripheral hoop (i.e., the size of the core), d is the overall depth, c is the depth of the compression zone, L_s is the shear span of the cantilever column and half the length for a column in reversed curvature, P is the axial load.

Lynn (2001) calibrated the following model for the shear strength of a column, based on a collection of 36 column tests from eight different experimental databases. The proposed expression, in psi, is shown in Eq. 2.40.

$$[2.40]\quad V_n = kV_c + \frac{1}{2}V_s = k\frac{A_g 6\sqrt{f_c}}{\frac{L_s}{d}}\sqrt{1+\frac{P}{6\sqrt{f_c}A_g}} + \frac{1}{2}\frac{A_{s,tr}f_{y,tr}d}{s_h}$$

Where $A_{s,tr}$ is the effective transverse reinformcent area. The same model was further developed by Sezen (2002) using an enlarged database of 51 shear critcal columns:

$$[2.41]\quad V_n = k(V_c + V_s) = k\left(\frac{6\sqrt{f_c}}{\frac{L_s}{d}}\sqrt{1+\frac{P}{6\sqrt{f_c}A_g}}\right)0.80A_g + k\frac{A_{s,tr}f_{y,tr}d}{s}$$

where V_c and V_s are the shear strength contributions of concrete and transverse reinforcement, respectively. The coefficient k varies from 1.0 to 0.7 depending on the displacement ductility as shown in Figure 2.13.

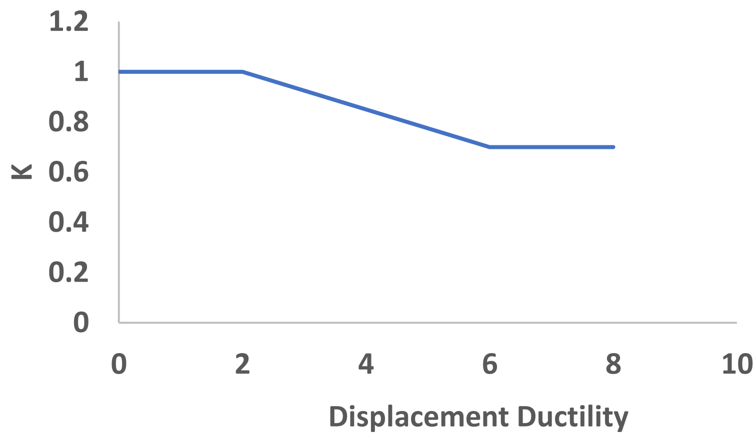

Figure 2.13: k as a function of the Ductility Demand (Modified from Pantazopoulou 2003)

Sasani (2004) developed a model for shear strength and its evolution as a function of ductility using a database of 89 columns, as depicted in Equation 2.42 (in psi).

$$[2.42]\; V_c = 0.22\left[a_{sp}(1-0.08\mu) + \frac{2.9P}{A_g f_c}\right]\sqrt{f_c f_{ss}}bd + \frac{2}{3}\frac{A_{s,tr}f_{y,tr}d}{s_h}$$

Where μ is the displacement ductility; f_{ss} is a scaling stress equal to 145 psi, and $a_{sp} = \left(3.7 - \frac{M}{V\cdot h}\right) \geq 1$, whereas $\frac{P}{A_g f_c} \leq 0.42$.

2.6 Summary and Conclusion

This chapter provides a summary of experimental studies of full-scale columns under reversed cyclic loading. The aim of these experimental studies was to provide an understanding of the behaviour of columns with certain characteristics. For example, Lynn (2001) and Sezen (2002) focused on studying the behaviour of columns with sparsely spaced transverse reinforcement. Matchulat (2009) reproduced the experimental study of Lynn (2001) and Sezen (2000). The experimental study of Lam, Wu, Wong, Wang, Liu and Li (2003) was similar to Lynn (2001) and Sezen (2002). These three studies had compatible conclusions in terms of the relation between the axial load and stirrup spacing and the deformation capacity of the columns.

In the available experimental data set, the uncertainty in the prediction of the deformation capacity and shear strength was still present. For example, Elwood et al. (2005) developed an analytical model for the deformation capacity at axial failure derived from the deformation capacities of the experimental columns of Lynn (2001) and Sezen (2002). The deformation capacity at axial failure in Matchulat (2009) experimental study was not compatible with the calculated deformation capacity at axial failure from Elwood et al. (2005), despite the similarities in the column types in the data set of Matchulat (2009), Lynn (2001) and Sezen (2002) (Shear critical columns). Additionally, as provided in Section 2.5.4 of this chapter, many analytical models were developed from several researchers for predicting the deformation capacity of the columns at shear and axial failure. Each analytical model showed well correlation to the deformation capacities of the data base used to develop the analytical model and may not correlate well to the deformation capacities of other columns in a different data set. As concluded in Ghannoum and Moehle (2012), most of the analytical models provided in Section 2.5.4 for deformation capacity at shear failure were over conservative relative to deformation capacities of their columns in the three-storey, there-bay frame.

Differences in material strength, testing procedures, the availability of another path for load redistribution (such as frame tests) in an experimental test create sources of uncertainties in the deformation capacities calculated analytically. Additionally, as concluded by Goodnight et al. (2013), the loading protocol plays a role in the extent of damage caused to the compression reinforcement due to buckling. Size also contributes to determining the failure type of the column. For example, Wu (2008) concluded that in short columns the available models in literature for shear strength estimation generally overestimates the actual shear strength of the columns. The uncertainties may not only arise from experimental aspects. The approaches the researchers undertake in calculating the sectional responses of a column may differ leading to additional errors in the estimation of deformation capacities.

As the experimental data of deformation and shear strength play a crucial role in developing international assessment codes, the errors discussed lead either to under or overestimate the reinforced concrete column’s deformation and shear capacity. For example, the ASCE SEI 41/13 showed significant under estimation of the deformation capacity at shear failure relative to the deformation capacity from Sokoli and Ghannoum (2016) specimens. Sokoli and Ghannoum (2016) columns were well detailed columns and their transverse detailing comply to the ACI 318M-14 standard for shear design. With the development of the ASCE SEI 41 code to the 2017 version the correlation of deformation capacities of reinforced concrete code-based estimates to experimental columns was not yet investigated.

Successful research efforts in developing simulations of a column’s response analytically was provided up to the point of shear failure. Flexure and slip rotations showed well correlation to experimental evidence, once shear failure occurred higher discrepancy between analytical and experimental findings were observed.

The efforts in this thesis were placed on investigating the behavioural trends of columns with different design parameters similar to old type construction. The design parameters were longitudinal reinforcement ratio, the transverse reinforcement detailing, the axial load, longitudinal reinforcement detailing (including lap splice) and the aspect ratio of the section. The column’s capacities (deformation and shear) were solved analytically using advanced non linear finite element analysis (ATENA 3D). The aim of this study was to enlarge the available data set with columns having constant material properties and loading protocols. This is to provide a rational investigation of the effect of each design parameter on the column behaviour and its correlation to international assessment codes. This will develop a better understating of the effect of design parameters which will cover the research gap associated with the discrepancies that arise between different databases and the correlation to developed analytical models.

3. A Comparative Study- Part 1: Model Preparation

For the aim of studying the reinforcement detailing effect on the deformation capacity of nonconforming components, a data base of columns with different longitudinal and transverse reinforcement detailing was modelled using advanced finite element modelling in ATENA 3D Engineering (https://www.cervenka.cz/). The first section will present the geometric properties of the columns and the investigated variables in the finite element models. The second section will introduce the model parameters and the software solution algorithms. Loading conditions and mesh discretization will also be presented in this chapter.

3.1 Model Geometric Properties

Assembling a database of tests conducted by different researchers has the value of enlarging the population of similar samples by crossing the boundaries of the limited scope of each individual experimental study. However, the differences in the fundamental properties (e.g. material strength, size, method of testing) between groups of experiments coming from different investigators inhibit, to some degree, the seamless illustration of parametric trends that could clearly illustrate the role of every variable in the mechanistic problem studied. So usually first level of calibration of analytical or empirical design equations for predicting performance indicators needs some form of independent benchmarking. Here benchmarking is pursued by examining idealized columns with identical material properties and different detailing parameters designed to highlight to what extent each affects the column behavior. Because it is of interest to observe how brittle reinforcing details may affect the response in various column conditions, the benchmark columns include samples representing nonconforming columns idealizing the typical detailing practices in pre-1980's structures.

A common modelling approach was used in the investigation of benchmark column behavior. All models were prepared in the ATENA 3D Engineering platform of ATENA software (ATENA V.5 3D Engineering) considering different structural geometries, as well as longitudinal and transverse detailing of the model columns. ATENA Engineering was chosen for this analysis because of the available advanced concrete models that is not available in any other finite element program. Using ATENA Studio (ATENA Studio x64 V.5.6.1) algorithms the resistance curves of the columns were calculated, and the deformation capacities and base shear strengths for the columns were defined using the same approach as what was used in commensurate experiments.

Figure 3.1 presents the five different types of column models considered in the study. The columns were detailed based on famous design practices prior to the 1980s. Each model case explores one important parameter that may dominate column behavior in terms of strength hierarchy and deformation capacity: (1) In the first case the longitudinal reinforcement bars are fully anchored into the foundation with a 90° hook, (2) In the second case, bars are lap-spliced over a short lap length of $15d_b$, (3) A third case has the bars extending into the foundation with a short anchorage length of $15d_b$, (4) The fourth column example has a deep cross section (700 mm depth), (5) In the fifth benchmark example a hinge of limited flexural strength is fabricated at the base of the column – where the longitudinal reinforcement crosses the center of the cross section and therefore produces a zero moment point after cracking. This was a detail that was used frequently in older construction. Each case of longitudinal detailing shown in Figure 3.1 is modeled with different combinations of axial loading (10%, 35%, 50% of crushing load), longitudinal reinforcement (shown in Figure 3.2) and stirrup spacing (100-mm and 200-mm stirrup spacing) using an 8 mm stirrup diameter.

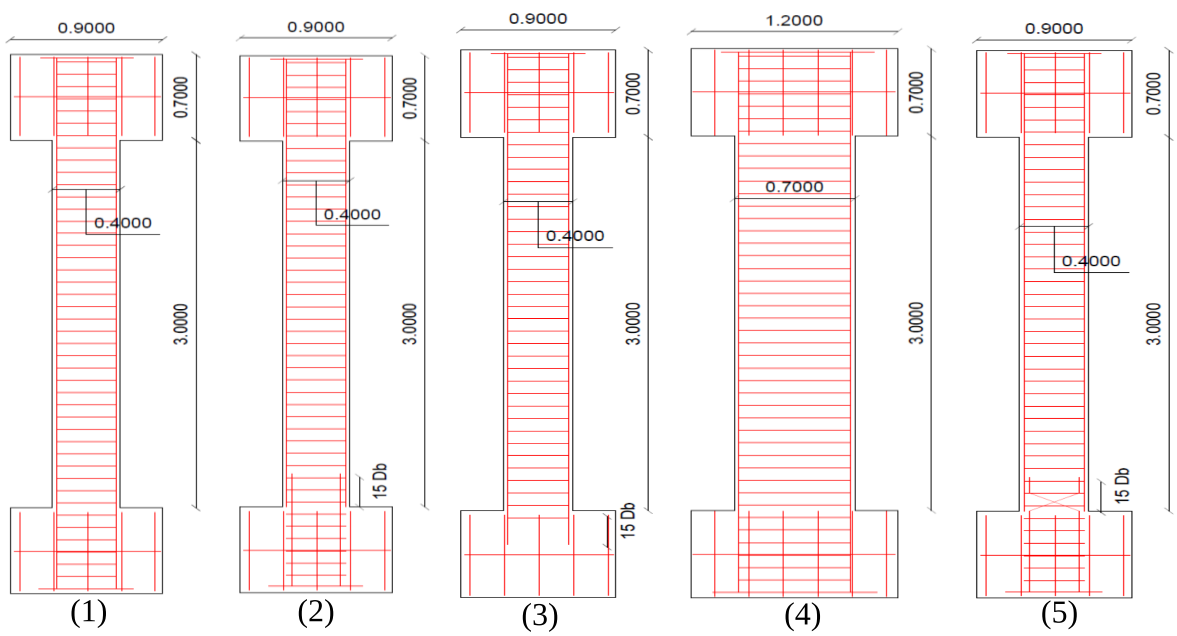

Figure 3.1: Column Longitudinal Reinforcement Detailing

For easy reference of the results in the forthcoming sections, a column identification code has been adopted, as described in the following: The first numeral following the letter C (for Column)-for example C35- corresponds to the normalized axial load ratio applied to the columns which in this case is 35 percent of the crushing load (calculated as $\frac{P}{A_g f_c}$), followed by the section ID number (each section contains a different amount of longitudinal reinforcement, so as to control the hierarchy between flexural and shear demands as shown in Figure 3.2) whereas the last digit in the numeral represents the stirrup spacing in cm along the length of the shear span of the column. The column's dimensions were typical dimensions of reinforced concrete column which were designed prior to the 1980's as shown in Figure 3.2. The longitudinal and transverse reinforcement bars were selected from European sizes.

The columns were modeled using 3D macro elements. The clear (deformable) length was 3 m. In lateral sway half the length of the columns would be acting as the column shear span. So, in modelling the columns as cantilevers to emulate the vast majority of column experiments which have been conducted as laterally driven cantilever elements fixed at the base, the clear length of the cantilevers was 1.5 m. The foundation was modelled as a block with dimensions (0.9 x 0.9 x 0.7) m. The dimensions of the foundation were increased for Case 4 to (1.2 x 1.2 x 0.7) m.

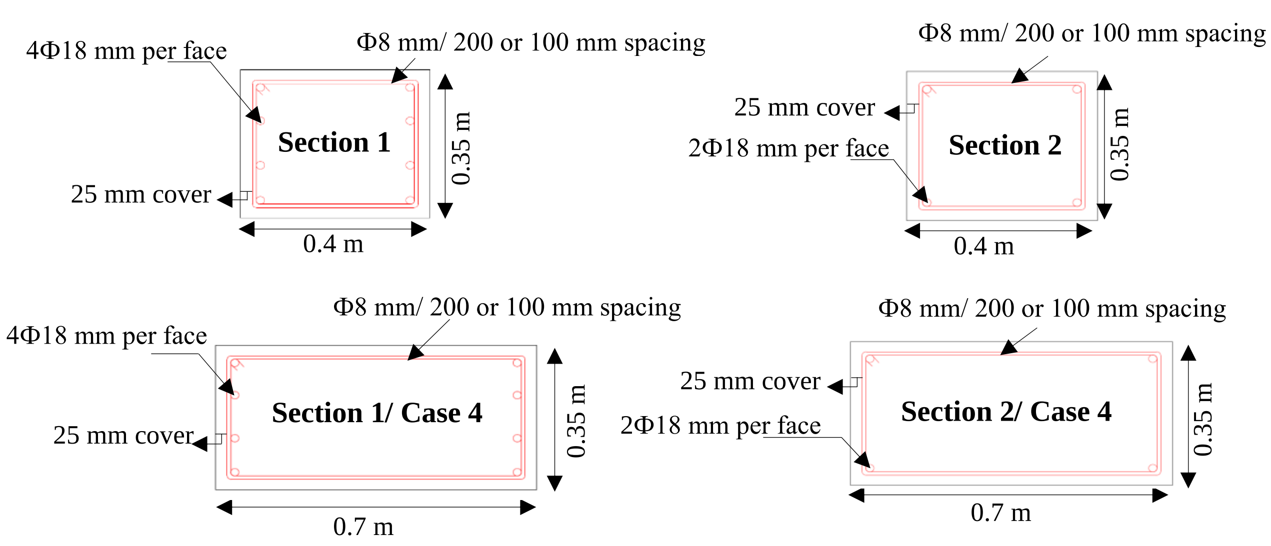

Figure 3.2: Column Sectional Geometry

3.2 Constitutive Material and Finite Element Parameters

Constitutive materials used for modeling reinforced concrete and steel are reviewed in this section. Moreover, investigation of proper bond stress-slip models is presented from current design provision for estimating the required development lengths (ACI 318M 19, ACI 408R-03).

3.2.1 Concrete

NonLinearCementitious2User (Cervenka et al. 2020) is used for modeling the constitutive behavior of concrete. This model uses a combination of fracture and plasticity relationships to simulate the full range of the inelastic stress – strain behavior of concrete (Cervenka et al. 2020). The user can define uniaxial material stress-strain laws for uniaxial tension and compression as well as the characteristics of fracture and non-associative plastic failure of the material.

The response of concrete in compression was modelled using Hognestad's Parabola for the ascending branch as shown in Eq. 3.1. Kent and Park (Kent et al. 1971) proposed slope presented in Eq. 3.2 for the softening stress strain relation for the concrete was used for the descending branch. Equation 3.3 represents the strain of unconfined concrete at 50% of the concrete strength on the softening curve and is taken from Kent and Park (1971) concrete stress strain model.

[3.1] $\sigma_c = f_c\left(\frac{2\varepsilon_c}{\varepsilon_o} - \left(\frac{\varepsilon_c}{\varepsilon_o}\right)^2\right)$

[3.2] $Z = \frac{0.5}{\varepsilon_{c,50} - \varepsilon_c}$

[3.3] $\varepsilon_{c,50} = \frac{3+0.29f_c}{145f_c-1000}$

where ε_c is the concrete strain, σ_c is the compressive stress, f_c is the compressive concrete strength and ε_o is the strain corresponding to the peak strength which is taken as 0.002.

To accommodate strength enhancement due to confinement, the Park, Priestley and Gill (Park et al. 1982) model for confined concrete was employed to represent the behavior of the concrete core. The confinement in the model is accounted for through the constant K defined by Eq. 3.4.

[3.4] $K = 1 + \rho_{s,tr}\frac{f_{y,tr}}{f_c}$

where $\rho_{s,tr} = \frac{A_{ws}(2b_c+2h_c)}{b_c h_c S_h}$ is the volumetric ratio of transverse reinforcement. A_{ws} is the area of the transverse reinforcement bar, b_c and h_c are the concrete core section width and depth from center to center of transverse reinforcement respectively. According to Park, Priestley and Gill (Park et al. 1982) model for confined concrete, the ascending and descending branches are modified to account for confinement as defined by Eq. 3.5 and 3.6.

[3.5] $\sigma_c = f_c K \left(\frac{\varepsilon_c}{0.002K} - \left(\frac{\varepsilon_c}{0.002K}\right)^2\right)$

[3.6] $\varepsilon_{c,50} = \frac{3+0.29f_c}{145f_c - 1000} + 0.75\, \rho_{s,tr}(\mathrm{b_c}/\mathrm{s}_h)^{0.5}$

Moreover, the transverse volumetric ratio $\rho_{s,tr}$ is multiplied by the effectiveness coefficient of the confinement pressure produced from the transverse reinforcement, denoted by K_e as per Eq. 3.7.

[3.7] $K_e = \left(1 - \frac{s_h}{2b_c}\right)\left(1 - \frac{s_h}{2h_c}\right)\left(1 - \frac{\sum b^2{}_i}{6b_c h_c}\right)$

Here s_h is the longitudinal spacing of transverse reinforcement.

For the finite element models the modulus of elasticity was 30000 MPa using the initial slope in Hognestad's stress strains curve with a concrete strength of 30 MPa.

The various components of the stress strain concrete material laws used for the models are illustrated in Figure 3.3. Detailed calculations can be found in Appendix A.

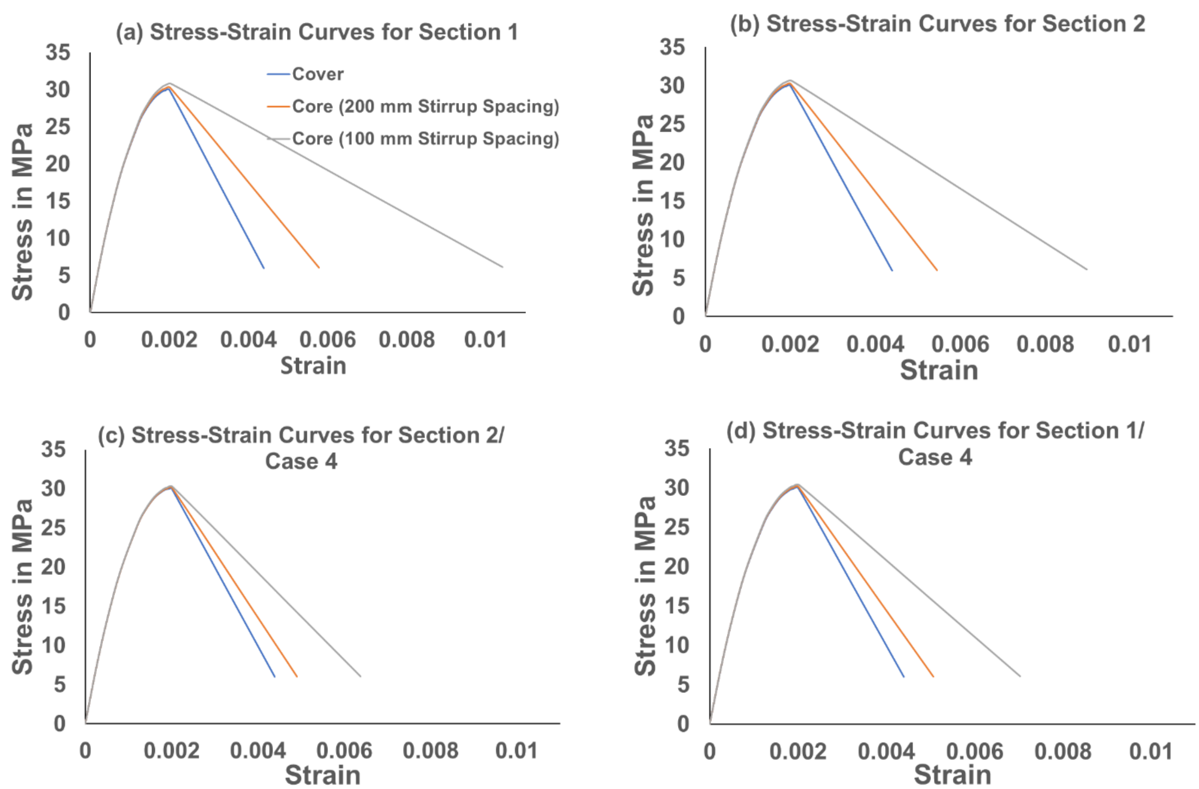

Figure 3.3: Stress-Strain Curves for Modelled Columns. (a): Concrete Stress Strain Relation for Section 1. (b): Concrete Stress Strain Relation for Section 2. (c): Concrete Stress Strain Relation for Section 1 in Case 4. (d): Concrete Stress Strain Relation for Section 2 Case 4.

Note that concrete ductility increases with the increase of confinement (higher ductility was found for columns with 100 mm stirrup spacing as opposed to columns with 200 mm stirrup spacing). For tension, the default program softening stress-strain branch was used as shown in Figure 3.4 for concrete with a maximum tensile strength of f_t= 2.71 MPa.

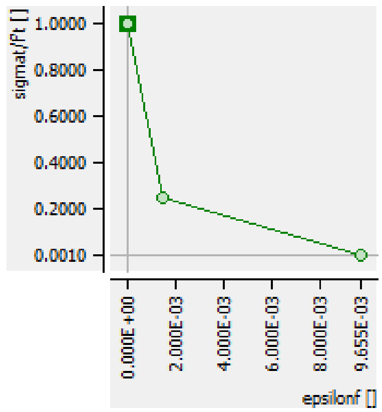

Figure 3.4: Stress-Strain Curve for All Columns in Tension

Concrete Constitutive Models (Fracture and Plastic)

Crack formation in simulation of concrete is shown in Figure 3.5. The cracks start to form in the process zone decreasing the tensile stresses in the concrete beyond the peak. Once the crack has been fully developed in the cracked stage, the crack opening releases all tensile stresses (Cervenka et al. 2020).

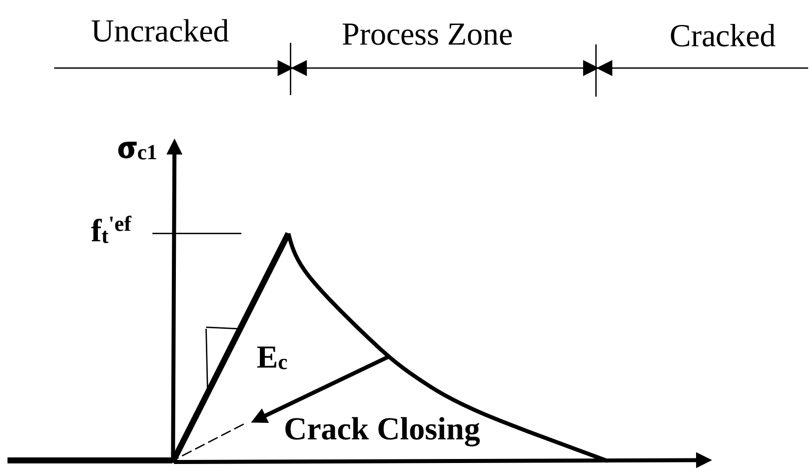

Figure 3.5: Crack Opening (Modified from Cervenka et al. 2020)

In ATENA 3D the cracking criterion for concrete is calculated using the Rankine formulation (fracture). The failure criterion used for the plasticity model is Menetrey (1997) and (Willam (1989)).

The cracked stiffness is calculated with relation to the retention shear factor r_g as shown in Eq. 3.8. (Cervenka et al. 2020). Equation 3.9 defines the shear modulus of a cracked section. Equation 3.10 defines the initial shear modulus. The tensile strains are calculated in accordance with Eq. 3.11.

[3.8] $E_{ijij}^{\prime cr} = \frac{r_g G}{1-r_g}$

[3.9] $G = r_g G_c$

[3.10] $G_c = \dfrac{E_c}{2(1+v)}$

[3.11] $if\ \varepsilon_1^f < \varepsilon_{loc}^f,\ \ \varepsilon_1{}'^f = \varepsilon_1^f\ else\ \varepsilon_1{}'^f = \varepsilon_{loc}^f + \left(\varepsilon_1^f - \varepsilon_{loc}^f\right)\frac{L_t}{L_{ch}{}^t}$

where, $E_{ijij}^{\prime cr}$ is the crack stifness, r_g is the shear retention factor and G is the elastic shear modulus after cracking (Cervenka et al. 2020). G_c is the uncracked elastic shear modulus. E_c is the uncracked Young's Modulus. The retention shear factor, r_g, is defined in Figure 3.6.

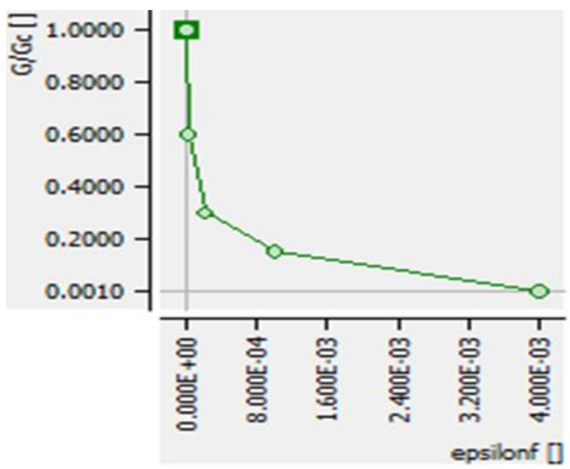

Figure 3.6: Shear Retention Factor, r_g, for the Column Models

Parameter ε_1^f is the tensile strain tensor at the finite element integration points (Cervenka et al. 2020). ε_{loc}^f is the localized tension strain and is equal to 0 for plain concrete (Cervenka et al. 2020). For fibre reinforced concrete ε_{loc}^f is larger than zero to represent the strain hardening after initiation of the first crack (Cervenka et al. 2020). After calculating the tensile strain according to Eq. 3.11, the corresponding tensile stress is found from Figure 3.4. Equation 3.11 is modified to calculate compression strains as shown in Eq. 3.12. After the strains are calculated in compression, the compression stress is found in accordance to Figure 3.3.

$$[3.12]\ \ if\ \varepsilon_2^P < \varepsilon_{loc}^P,\ \ \varepsilon_2{'}^P = \varepsilon_2^P\ else\ \varepsilon_2{'}^P = \varepsilon_{loc}^P + (\varepsilon_2^P - \varepsilon_{loc}^P)\frac{L_c}{L_{ch}{}^c}$$

where ε_{loc}^P is the localized compressive strain and corresponds to the strain corresponding to the maximum compressive strength after subtracting the linear portion. ε_2^P is the compressive strain tensor at the finite element integration point.

L_t and L_c represent the crack band size and crush band size respectively (Bazant and Oh 1983). The crack/crushing band size corresponds to the element size as shown in Figure 3.7 (Cervenka et al. 2020). Where L_c is the diagonal element length parallel to the crack direction and L_t is the diagonal element length perpendicular to the crack direction. $L_{ch}{}^c$ and $L_{ch}{}^t$ in Eq. 3.11 and 3.12 decrease the mesh dependency and represent the valid size for the process zone in compression and tension (Cervenka et al. 2020). For the column models 0.03 and 0.050 m are used for $L_{ch}{}^c$ and $L_{ch}{}^t$ respectively with trial and error so as to capture an appropriate response.

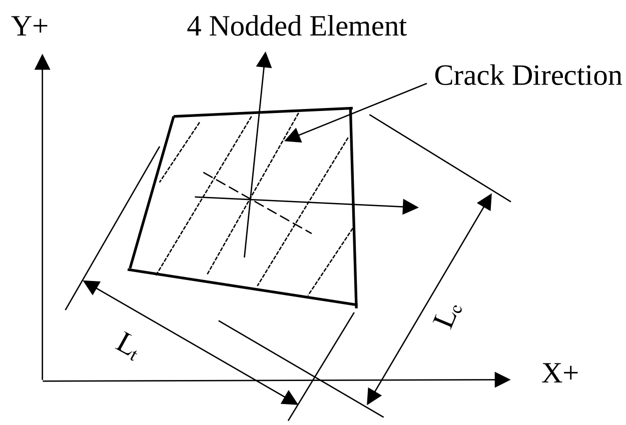

Figure 3.7: Definitions of L_t and L_c (Modified from Cervenka et al. 2020)

Equation 3.12 is used to calculate the crack width.

$$[3.12]\ w_t = \varepsilon_1{'}^f\ \ L_t$$

Where $\varepsilon_1{'}^f$ is calculated in accordance with Eq. 3.11. The crushing width is calculated in accordance to 3.13.

[3.13] $w_d = \left(\varepsilon_{eq}^{p} - \varepsilon_{loc}^{p}\right) L_c$

The parameter ε_{eq}^{p} is the equivalent plastic strain and is equal to the strain corresponding zero compressive stress (Cervenka et al. 2020). ε_{c}^{p} is the strain corresponding to the maximum compressive stress.

3.2.2 Reinforcement

A bilinear stress strain diagram was used for the steel reinforcement with strain hardening. Table 3.1 depicts the mechanical properties of the longitudinal and transverse reinforcement used in the models.

Table 3.1: Mechanical Properties for Longitudinal and Transverse Reinforcement

	Longitudinal Reinforcement: (ASTM A706 Grade 60 ksi)	Transverse Reinforcement: (ASTM A615 Grade 40 ksi)
Yield strength	414 MPa	276 MPa
Ultimate strength	552 MPa	483 MPa
Strain Rupture	120 mm/m	120 mm/m

3.2.3 Bond Stress-Slip Relationship

In order to be able to study the effect of slip of reinforcement relative to the concrete on the rotation capacity and the calculation of failure of columns, it was essential to explicitly account for the mechanics of bond. To this end, the longitudinal reinforcement is connected to the concrete through interface springs endowed with a proper bond stress- strain relationship in order to allow for the development of slip between the bar and concrete. In this manner, pullout or splitting behavior of the longitudinal reinforcement can be considered. Several bond models were studied and analyzed from several codes such as ACI-318M 2011, 2014, 2019, ACI-408R-03, CSA.A23.3-14. This section will provide a review for specifications for bond strength from the code and present the chosen model for the bond springs.

The bond slip model used in ATENA Engineering 3D is presented in Figure 3.8 (Cervenka et al. 2020). The bond stress-slip relation was assigned only to longitudinal reinforcement. Transverse reinforcement was assumed to have perfect bond connection with concrete.

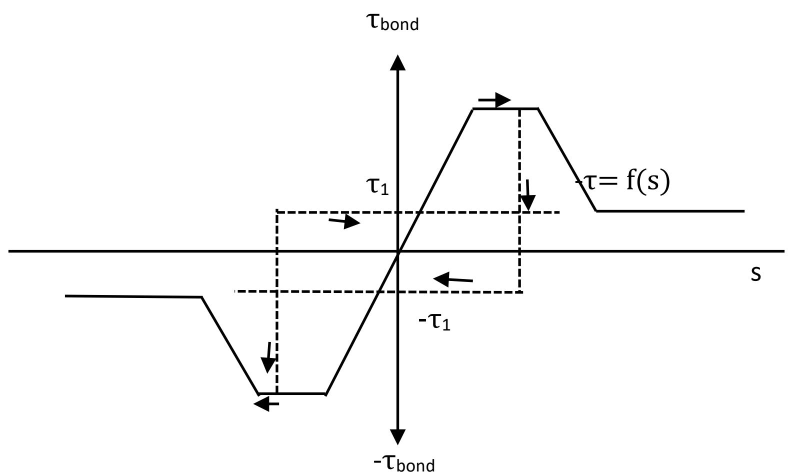

Figure 3.8: Bond Stress Slip Diagram Integrated in ATENA 3D Engineering (Modified from Cervenka et al. 2020)

The total bond slip (s) is found from $s = s_{i-1} + \Delta s_i$. The bond stress in a loading stage is found from the function ($\tau = f(s)$) which is defined by the user (Cervenka et al. 2020). In the case of unloading, when the slip changes signs, the bond stress will be equal to τ_1 or $-\tau_1$ depending on the change in slip Δs_i sign (Cervenka et al. 2020). For example, if $\Delta s_i > 0$, $\tau = \tau_1$, if $\Delta s_i < 0$, $\tau = -\tau_1$. The parameter τ_1 is a reduced bond stress that is given by the user and ranges between the maximum bond strength and the residual bond strength. The parameter τ_1 is not of concern for columns under monotonic loading, however, it is crucial to define this parameter in the case for columns under cyclic load.

Using design codes, the maximum bond strength is found to help in defining the bond stress relation for the spring connecting the longitudinal reinforcement to the concrete. The maximum bond strength from the codes is found through reverse engineering use of the calibrated relationship between bar stress, bond stress and the development length $\left(l_d = \frac{d_b}{4}\frac{f_y}{f_{bmax}}\right)$ where l_d is the required development length and f_{bmax} is the maximum bond strength. d_b is the longitudinal bar diameter and f_y is the yield strength of the longitudinal bars. Appendix B provides detailed calculation of the bond stress-slip relationship

ACI 318M-2019 CODE:

For Bars in Tension

The required bond length according to ACI 318M-11,14 and 19 versions for deformed reinforcement bars in tension is equal to the least of Eq. 3.14 and 300 mm.

$$[3.14]\quad l_{dt} = \frac{f_{yl}}{1.1\,\lambda f_c^{0.5}} \frac{\Psi_e \Psi_t \Psi_s}{\frac{c_b + K_{tr}}{d_b}} d_b$$

where, λ accounts for concrete weight, and is equal to 1 and 0.75 for normal and light weight concrete respectively. Ψ_t represents casting conditions and is equal to 1.3 when less then 300 mm of fresh concrete is cast below the development length, and 1 for other concrete casting conditions. Ψ_e accounts for epoxy coating of bar and is equal to 1 for the case of uncoated reinforcement. The Ψ_s factor accounts for bar diameter smaller and larger than 19 mm and equals 0.8 and 1 respectively. The 2019 version accounts as well for an additional factor Ψ_g which is the longitudinal reinforcement grade factor and is equal 1.0 for reinforcement grade 40 and 60. The confinement of a section provided from the transverse reinforcement K_{tr} is calculated using Eq. 3.15.

$$[3.15]\quad K_{tr} = \frac{40 A_{tr}}{s_h n}$$

where, A_{tr} is the total area of the stirrups crossing the potential splitting plane, n is the number of bars along the potential splitting plane and s_h is the longitudinal transverse spacing.

The term $\frac{c_b + K_{tr}}{d_b}$ is used to account for the confinement provided from the cover added to the transverse reinforcement. Here, c_b is the least of the half centre to centre of the longitudinal reinforcement spacing and the closest distance from the concrete edge to the centre of the longitudinal reinforcement. The maximum limit for this term is 2.5. If the term exceeds the upper limit value, then the failure predicted in this case is a pullout failure.

For Bars in Compression

According to ACI 318M-14,11 and 19 the longitudinal reinforcement in compression l_{dc} is computed according to the larger of Eq. 3.16 and 3.17 and 200 mm.

[3.16] $l_{dc} = \frac{0.24 f_{yl}}{\lambda f_c^{0.5}} d_b$

[3.17] $l_d = (0.043 f_{yl}) d_b$

Equation 3.17 is multiplied by the factor Ψ_r in ACI 318M -14 and 19, and is taken equal to 0.75 for special cases of hoop or spiral transverse reinforcement and 1.0 for other cases.

For Headed Bars in Tension

According to ACI 318M-14,11 the headed longitudinal reinforcement in tension l_{dh} computed according to the larger of Eq. 3.18 , $8d_b$ and 150 mm.

[3.18] $l_{dh} = \frac{0.19 f_{yl} \Psi_e}{\lambda f_c^{0.5}} d_b$

where, Ψ_e is defined in Eq. 3.26.

According to ACI 318M-19, the headed longitudinal reinforcement in tension l_d is computed according to the larger from among the result of Eq. 3.19, $8d_b$, and 6 in.

[3.19] $l_d = \frac{f_{yl} \Psi_e \Psi_p \Psi_o \Psi_c}{75 \lambda \sqrt{f_c}}$ *(SI units)*

where, Ψ_e is defined in Eq. 3.14. Ψ_p is 1.0 for longitudinal reinforcement bars No. 11 and smaller with $A_{tt} \geq 0.3A_{hs}$ or $s \geq 6d_b$, where s is the spacing of headed bars from center to center. A_{tt} is the total area of stirrups or tie parallel to the developed headed bar. A_{hs} is the total area of bars developed or headed. Ψ_p = 1.6 for other cases. Ψ_o is 1.0 for headed bars if the developed bars end inside the column core with a cover larger than 2.5 in. or a cover larger than $6d_b$. Ψ_o = 1.25 for other cases. Ψ_c accounts for concrete compressive strength and is 1.0 for concrete strength larger or equal to 6000 psi (48 MPa) and is taken equal to $(f_c/48)$ +1 for concrete strength less than 48 MPa. Parameter λ is defined in Eq.3.14.

For Bars in Tension with Standard Hooks

The development length of bars with standard hooks in tension According to AC1 318M-11,14 and 19 is the largest of $8d_b$, 150 mm and Eq. 3.20.

$$[3.20]\quad l_d = \frac{0.24 f_{yl} \Psi_e}{\lambda f_c^{0.5}} d_b$$

where, Ψ_e is defined in Eq. 3.19. Equation 3.20 is multiplied by the two factors $\Psi_c \Psi_r$ in version 14 and by the three factors $\Psi_c \Psi_r \Psi_o$ in version 19, where, Ψ_c= 0.7 for hook No. 36 and smaller with a clear cover equal or larger than 65 mm or 90-degree hook and the cover beyond the hook is 50 mm or larger and 1.0 for other cases. Parameter Ψ_r= 0.8 for the case of 90-degree hooks of No. 36 or smaller bars confined with stirrups or ties that with a spacing of $3d_b$ or less. Ψ_r is also taken 0.8 for 180-degree hooks of No. 36 or smaller bars if the confining transverse reinforcement is spaced not more than $3d_b$ along the developed bar. Ψ_r is 1.0 for other cases. Ψ_o is defined in Eq. 3.19.

ACI 408R-03 (US units):

The report of Committee ACI 408R-03 is a specialized guideline focussing on the topic of bond and development of strain tension reinforcement. The bond length specified by this code is calculated using Eq.3.21.

$$[3.21]\quad l_d = \frac{\left(\frac{f_{yl}}{f_c^{0.25}} - 2500\Phi \mathrm{w}\right)\lambda}{76.3\phi \frac{\left((c)(w)+k_{tr}\right)}{d_b}}$$

where, $w = (0.1C_{max}/C_{min}) + 0.9 \leq 1.25$ in *in* , $c= C_{min} + 0.5d_b$, C_{max} is the maximum of (c_b, C_s). The parameter c_b is defined in Eq. 3.15. Parameter C_s is the least of the clear cover and one-half of the clear spacing of the longitudinal reinforcement + *0.25in*, C_{min} is the minimum of (c_b, C_s). Parameter ϕ is the strength reduction factor which shall not be included in the calculations for assessment (nominal strength values are used throughout, so ϕ is taken equal to 1.0).

The code accounts for confinement from reinforcement -both transverse and longitudinal- through the K_{tr} value calculated using Eq.3.22.

$$[3.22]\quad K_{tr} = \frac{0.5 A_{tr} t_d f_c^{0.5}}{sn}$$

where, t_d is $0.78d_b + 0.22$. This term represents the effect of bar size on contribution of transverse reinforcement to bond strength.

A cap limit of confinement that affects the amount of transverse reinforcement is determined by this code to be $cw+K_{tr}/d_b \leq 4.0$.

CSA A23.3-14

For Bars in Tension

For bars in tension the code CSA A23.3-14 specifies the bond length l_d, according to Eq. 3.23.

$$[3.23]\quad l_d = 1.15\frac{K_1K_2K_3K_4}{d_{cs}+K_{tr}}\frac{f_{yl}}{f_c^{0.5}}A_b$$

where, K_1 is a factor representing the bar location and is equal to 1.3 for when 300 mm or more of fresh concrete is placed under the development length and 1.0 for other cases. K_2 is a coating factor that equals to 1.5 for epoxy-coated reinforcement if the clear cover is less than $3d_b$ or clear spacing between bars being developed is less than $6d_b$. This factor is equal to 1.2 for all other epoxy-coated reinforcement and it is equal to 1.0 for uncoated reinforcement. K_3 is the concrete density factor, and it is equal to 1.3 for structural low-density concrete and 1.2 for structural semi-low-density concrete and to 1.0 for normal-density concrete. K_4 is the bar size factor, and it is 0.8 for 20M and smaller bars and deformed wires and 1.0 for 25M and larger bars. The product K_1K_2 should not be taken greater than 1.7.

Specifications for confinement of a section are calculated according to Eq. 3.24.

$$[3.24]\quad K_{tr} = \frac{A_{tr}f_{y,tr}}{10.5ns_h}$$

The cap limit for confinement according to the CSA A23.3 is specified using the two confinement terms, d_{cs} and K_{tr} ; the sum of these terms cannot exceed $2.5d_b$. Term d_{cs} represents the confinement provided by the cover of the section. This term is similar to the c_b parameter defined by the ACI 318M and ACI 408R-03. K_{tr} represents the confinement provided by transverse reinforcement.

For Bars in Compression

For bars in compression the development length is calculated according to Eq. 3.25.

$$[3.25]\quad l_d = 0.24d_b\frac{f_{yl}}{f_c^{0.5}} \geq 0.044d_bf_{yl}$$

For Bars with Hooks in Tension

The basic required bond length for the hooked bars with a yield strength of 400 MPa is $100d_b/(f_c)^{0.5}$, which is multiplied by reduction factors as follows:

1) f_{yl} / 400, if the longitudinal bar yield strength is not 400 MPa.

2) 0.7, in the case of bars with hooks of 35M or smaller bars and the clear cover is 60 mm and more or for 90° hooks where the cover beyond the on hooked bars is 50 mm or more.

3) 0.8, in the case of bars with hooks of 35M or smaller bars and the hook is confined with at least three stirrups along a length equal to the bar diameter or greater and a maximum spacing of $3d_b$.

4) 1.3, for low-density concrete.

5) 1.2, for epoxy-coated reinforcement.

fib Model Code 2010 (Design Equation)

The design bond strength in the fib Model Code (2010) is defined by Eq. 3.26.

$$[3.26]\quad f_{bd} = \frac{\eta_1\eta_2\eta_3\eta_4\left(\frac{f_{ck}}{25}\right)^{0.5}}{\gamma_{cb}}(\propto_2+\propto_3)$$

Where, f_{ck} is the characteristic compressive strength of concrete. The coefficient η_1 is 1.75 and 0.9 for ribbed and smooth bars respectively. η_2 equals 1 when good bonding conditions are present. η_3 represents the bar diameter reduction factor for bar diameters more then 25 mm. If the bar diameter is larger than 25 mm, $\eta_3 = (25/d_b)^{0.3}$ and is taken 1.0 for $d_b \leq 25$ mm. The η_4 factor is used to adjust the yield strength of longitudinal reinforcement and is calculated from $(500/f_{yk})^{0.82}$, where, γ_{cb} is a material safety factor for concrete, which in this case will not be included in the calculations (it will be taken equal to 1 since nominal material properties are used for assessment). The product of $\frac{\eta_1\eta_2\eta_3\eta_4\left(\frac{f_{ck}}{25}\right)^{0.5}}{\gamma_{cb}}$ in Eq. 3.26 represents the basic bond strength $f_{bd,0}$. The basic bond strength is defined as an average stress on the nominal contact surface of a straight length of bar over the bonded length, l_b. The factor $(\propto_2+\propto_3)$ represents the confining effect provided from the cross-section's cover (contributed by coefficient $\propto_2$) and the transverse reinforcement (contributed by coefficient $\propto_3$). A cap limit for the sum of the two confinement factors $\propto_2$ and $\propto_3$ is the value of 2. The two factors $\propto_2$ and $\propto_3$ are calculated in accordance with Eq.3.27 and 3.28. The confinement effect is defined in Eq. 3.29.

$$[3.27]\quad \propto_3 = K_d\left(K_{tr} - \frac{\propto_t}{50}\right) \geq 0$$

[3.28] $\propto_2 = \left(\frac{c_{min}}{d_b}\right)^{0.5} \left(\frac{c_s}{2C_{min}}\right)^{0.15}$

[3.29] $K_{tr} = \frac{n_t A_{st}}{n_b d_b s_h} \leq 0.05$

where n_t is the number of legs of confining reinforcement crossing a potential splitting failure surface at a section. A_{st} is the cross-sectional area of one leg of a confining bar. s_h is the longitudinal spacing of confining reinforcement. n_b is the number of anchored bars on a potential splitting plane. Parameter α_t is the bar size adjustment factor, which equals 0.5 for bars up to and including size 25 mm. K_d for Sections 1 and 2 is equal to 20 where the legs of a link are perpendicular to the splitting plane provided, whereas no anchored bar or pair of lapped bars are further than either $5d_b$ or 125 mm from where the leg crosses the splitting plane as per fib 2010 Model Code. c_s is defined in Figure 3.9.

fib Code -Calibrated Equation (Model Code 2010)

The fib Model Code 2010 provides an analytical equation calibrated with a database of lap splice and beam end tests to calculate the maximum bond strength as shown in Eq. 3.30.

[3.30] $f_{stm} = 54\left(\frac{f_{cm}}{25}\right)^{0.25} \left(\frac{l_b}{d_b}\right)^{0.55} \left(\frac{25}{d_b}\right)^{0.2} \left[\left(\frac{c_{min}}{d_b}\right)^{0.25} \left(\frac{c_{max}}{c_{min}}\right)^{0.1} + k_m K_{tr}\right]$

where, f_{stm} is the maximum estimated bar stress (mean value) MPa. f_{cm} is the mean concrete cylinder compressive strength MPa. l_b and d_b are the bonded length and diameter of the lapped or anchored bar respectively (mm). c_{max} and c_{min} are defined in Figure 3.9. Note that the definition of c_{min} and c_{max} are different than C_{max} and C_{min} in the ACI 408R-03. K_m is a constant that represents the efficiency of the confinement and is equal to 12, where bars are confined with a bent of link around the bar with at least a 90-degree hook.

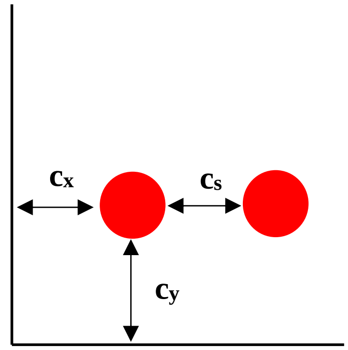

c_{min}= min (c_s/2, c_x and c_y).

c_{max}= max (c_s/2, c_x).

Figure 3.9: c_{min} and c_{max} Values Modified from fib 2010 Model Code

The calculation of the bar stress is simplified from Eq. 3.30 assuming l_b/d_b =5 with a uniform bar bond stress over this length assuming splitting failure ($\tau_{u,split}$) for $d_b \leq 25\ mm$, c_{max}/c_{min} = 2.0, c_{max}= c_{min} and K_{tr}= 0.02 where the bars are confined by stirrups. This simplification of Eq. 3.30 is given in the Model Code 2010 and presented here in Table 3.2.

Table 3.2: Bond Stress-Slip (fib Model Code 2010)

	1	2	3	4	5	6
	Pull-Out (PO)		Splitting (SP)			
	$\varepsilon_s < \varepsilon_{s,y}$		$\varepsilon_s < \varepsilon_{s,y}$			
	Good Bond Cond.	All Other Bond Cond.	Good Bond Cond.		All Other Bond Cond.	
			Unconfined	Stirrups	Unconfined	Stirrups
τ_{bmax}	$2.5\sqrt{f_{cm}}$	$1.25\sqrt{f_{cm}}$	$7.0\left(\frac{f_{cm}}{25}\right)^{0.25}$	$8.0\left(\frac{f_{cm}}{25}\right)^{0.25}$	$5.0\left(\frac{f_{cm}}{25}\right)^{0.25}$	$5.5\left(\frac{f_{cm}}{25}\right)^{0.25}$
s_1	1.0 mm	1.8 mm	$s(\tau_{bmax})$	$s(\tau_{bmax})$	$s(\tau_{bmax})$	$s(\tau_{bmax})$
s_2	2.0 mm	3.6 mm	s_1	s_1	s_1	s_1
s_3	c_{clear} 1)	c_{clear} 1)	$1.2s_1$	$0.5c_{clear}$ 1)	$1.2s_1$	$0.5c_{clear}$ 1)
α	0.4	0.4	0.4	0.4	0.4	0.4
τ_{bf}	0.4 τ_{bmax}	0.4 τ_{bmax}	0	0.4 τ_{bmax}	0	0.4 τ_{bmax}

where, c_{clear} is the maximum spacing between the ribs on bar reinforecement. s_1 is the slip in the longitudinal bars at the maximum bond stress representig the beginning of the plateau region. s_2 is the slip at the maximum bond stress representing the end of the platue region. s_3 is the slip at the beginning of the residual strength region.

The maximum bond stress is divided into three types; in the first type, τ_{bmax} is the bond strength when pullout failure is assumed. This type of failure is present in reinforcement embeded into the foundation where significant confinement is present. The senond type, $\tau_{u,split}^{1}$, is the maximum bond stress when splitting failure is assumed with high transverse confinement. The third, $\tau_{u,split}^{2}$, is the maximum bond stress when splitting failure is assumed with low transverse confinement. τ_{bf} is the residual bond stress. Equations 3.31- 3.34 depict the bond stress-slip function where s is the slip at a bond stress of τ_o.

[3.31] $\tau_o(s) = \tau_{bmax}\left(\frac{s}{s_1}\right)^{0.4}$ $\quad for\ 0 \leq s \leq s_1$

[3.32] $\tau_o(s) = \tau_{bmax}$ $\quad for\ s_1 \leq s \leq s_2$

[3.33] $\tau_o(s) = \tau_{bmax}\left(\tau_{bmax} - \tau_f\right)\frac{s-s_2}{s_3-s_2}$ $\quad for\ s_2 \leq s \leq s_3$

[3.34] $\tau_o(s) = \tau_{bf}$ $\quad for\ s \geq s_3$

Table 3.3 summarizes the equations for development length taken from ACI-318M 2011, 2014, 2019, ACI-408R-03, CSA.A23.3-14 and the design bond strength from fib Model Code (2010).

Table 3.3: Code Requirements for Bond and Calculated Bond Strength

Code	Fib Design Equation	ACI-318M 2011, 2014, 2019	ACI-408R-03	CSA.A23.3-14
Equation	$f_{bd} = \eta_1\eta_2\eta_3\eta_4\left(\frac{f_{cm}}{25}\right)^{0.5}(\propto_2 + \propto_3)$	$l_d = \frac{f_y}{(1.1)\lambda(f_c)^{0.5}}\frac{\Psi_e\Psi_t\Psi_s}{\frac{c_b+K_{tr}}{d_b}}d_b$	$l_d = \left(\frac{\frac{f_y}{(f_c)^{0.25}} - 2500w\Phi}{\frac{76.3\Phi(cw+K_{tr})}{d_b}}\right)d_b$	$l_d = 1.15\left(\frac{k_1k_2k_3k_4}{d_{cs}+k_{tr}}\right)\left(\frac{f_y}{f_c^{0.5}}\right)A_b$
K_{tr}	$\frac{n_tA_{st}}{n_bd_bs}$	$\frac{40A_{tr}}{n.s}$	$\frac{n_tA_{st}}{n_bsd_b}$	$\frac{A_{tr}f_{ty}}{10.5ns}$
Confinement Cap limit	$\propto_3 = K_d\left(K_{tr} - \frac{\propto_t}{50}\right) \geq 0$ $\propto_2 = \left(\frac{c_{min}}{\Phi}\right)^{0.5}\left(\frac{c_s}{2c_{min}}\right)^{0.15}$ $\propto_2 + \propto_3 \leq 2$	$\frac{c_b+K_{tr}}{d_b} \leq 2.5$	$\frac{(cw+K_{tr})}{d_b} \leq 4$	$d_{cs} + K_{tr} \leq 2.5d_b$
Section Number	1 1 2 2	1 1 2 2	1 1 2 2	1 1 2 2
Stirrup Spacing cm	10 20 10 20	10 20 10 20	10 20 10 20	10 20 10 20
Maximum Bond Strength (MPa)	3.2 3 4.3 3.7	4.6 4.7 4.7 4.7	3.6 3.4 3.8 3.6	4.5 4.7 4.7 4.7

Using the discussed code provisions, the bond maximum strength is calculated for column Case 1 shown in Figure 3.1 and considering the two column Sections (1 or 2) shown in Figure 3.2, for two values of stirrup spacing 20 cm and 10 cm as shown in Table 3.3. Note that Section 1 represents column sections with 4 bars 18 mm in diameter, and Section 2 represents column sections with 2 bars of 18 mm diameter. Table 3.3 also summarizes the confinement factor K_{tr} for each code with its maximum limit. Table 3.3 depicts the values according with the ACI-318M-2019 and CSA.A23.3-14, equations for the bars in tension with no hooks which is the worst-case scenario. The section number in Table 3.3 refers to sections with dimensions of 400 x 350 mm from Figure 3.2.

The results of the maximum bond strength shown in Table 3.3 show close estimates for the two section types and the two stirrup spacing cases. The maximum bond strength ranged between 3.0 and 5.0 MPa. It is shown that ACI-318M 2011, 2014, 2019 and CSA.A23.3-14 give approximately the same estimates. This is because the similarities in the l_d specification and confinement limit. The confinement coefficient in the ACI-318M 2011, 2014, 2019 consists of a factor of 40 where as this factor in the CSA.A23.3-14 depends in the transverse reinforcement yield strength ($f_{y,tr}/10.5$). Using a transverse reinforcement of strength of 276 MPa the confinement factor in the CSA.A23.3-14 is 26.3 which contributed by a small margin or made no difference in the bond strength calculation relative to ACI-318M 2011, 2014, 2019.

From Table 3.3 it is concluded that codes show insensitivity in estimating the bond strength for different stirrup spacing. For example, the Fib Design Equation obtained from the Model Code (2010) and ACI-408R-03 provisions show a difference of 0.2 MPa in bond strength between the section with 100 mm and 200 mm stirrup spacing. Moreover, the bond strength values calculated according to ACI-318M 2011, 2014, 2019 and CSA.A23.3-14 show no differences. This lack of any apparent sensitivity was due to the upper cap limit for consideration of confinement effects, applied in both Codes. Exceeding the cap limit means that the sectional confinement from the transverse reinforcement and cover are sufficient to preserve the bond integrity between the longitudinal reinforcement and concrete along the length of the anchorage. This leads to a reduction in the required development length according to the bond code provisions. The slitting failure is eliminated, and the predicted mode of failure is pullout of the developed length from the concrete foundation or joint. According to the development length equations form the codes, allowing the cap limit to exceed 2.5 will decrease the required development length which is not favorable for practical design applications. This is why the limit cap of 2.5 is enforced. The 2.5 maximum confinement limit also means that decreasing the transverse spacing to less than 168 and 366 mm for Section 1 and 2 respectively or increasing the concrete cover will not affect the pull-out failure. The confinement limits in the ACI-408R-03 and the Fib Design Equation were not reached, therefore mixed pull out – splitting failure would be estimated from both codes.

In the experimental analysis of Sokoli and Ghannoum 2016, it was found that the development lengths calculated from the ACI 318M-2014 code is overestimated compared to the degraded bond length provided from experimental columns with the confinement factors limited to 2.5. Overestimating the development length underestimates the bond strength. Moreover, all sections had a confinement factor that was more than 2.5,which indicates that the columns will fail due to bond pullout, however, only one column sustianed bond failure and the type of failure was splitting. Better estimation of developed length and bond failure type when the cap limit was increased to 3.0.

Using the fib model code, a pull-out failure will occur in an anchorage if the clear cover is greater than $5d_b$ and the clear spacing between the bars is greater than $10d_b$. These conditions are not satisfied in the columns of the present study simultaneously. Therefore, splitting failure is expected along the shear span of the column. Good bond conditions were assumed; for the case of 100 mm stirrup spacing the maximum bond strength was used as shown in Column 4 of Table 3.2. However, in the case of 200 mm stirrup spacing, the unconfined maximum bond stress was used as shown in Column 3 of Table 3.2 as the effective confining pressure in this case is, K_e <0.3. When modelling the lapped splice at the base of the column, a pullout failure is assumed for the bar in the foundation where significant amount of confinement is found due to the vast amount of concrete an transverse reinforcement surrounding the bar and therefore resisting its vertical slippage. The bond stress-slip relation calcutions for the longitudinal bars in the column shear span are done as follows:

$\tau_{bmax}= 2.5(f_{cm})^{0.5}$

s_1 for columns with 20 cm stirrup spacing

$\tau_o/\tau_{bmax} = (s/s_1)^{\alpha}$,

$7.32/13.69= (s/1)^{0.4}$

$s_1= 0.20$ mm

s_1 for columns with 10 cm stirrup spacing

$\tau / \tau_{bmax} = (s/s_1)^{\alpha}$,

$8.37/13.69 = (s/1)^{0.4}$

$s_1 = 0.3$ mm

For notation definition the reader is advised to check section on *fib Code-Calibrated Equation-Model Code 2010* earlier in this chapter.

For bars with 18mm diameter, c_{clear} is 13 mm according to the ASTM-A615. The slip value s_2 for both conditions of stirrup spacing is taken equal to 1 mm according to the fib Model Code 2010 as shown in Table 3.2. The value of s_3 for columns with 200 mm stirrup spacing is, 1.2x1 =1.2 mm and s_3 for columns with 100 mm stirrup spacing is calculated as, $0.5xc_{clear}$ =0.5x13= 6.5 mm.

It is concluded that the fib Model Code (2010) (Calibrated Model) shows greater sensitivity to the transverse reinforcement spacing and effectively confinement on bond strength, with a difference in the estimated bond strengths for the two cases of approximately 1 MPa. Moreover, the fib model code provides an easy and explicit procedure to calculate the reinforcement slips coordinates of the bond-slip law.

To summarize, the codes bond provisions have shown insensitivity in quantifying the bond strength of the two different transverse confined sections for mixed splitting-pullout mode of behavior. Additionally, experimental evidence has illustrated the conservative estimate of failure type when the limiting cap is used. The fib model column (2010) showed better sensitivity for the two confinement cases, a more realistic bond failure type predication and an explicit procedure for slip calculation. Therefore , the fib Model Code (2010) was chosen to be used for the model's bond stress slip relation. Bond strength, in particular, has been calculated for the two types of sections depicted in Fig. 3.10.

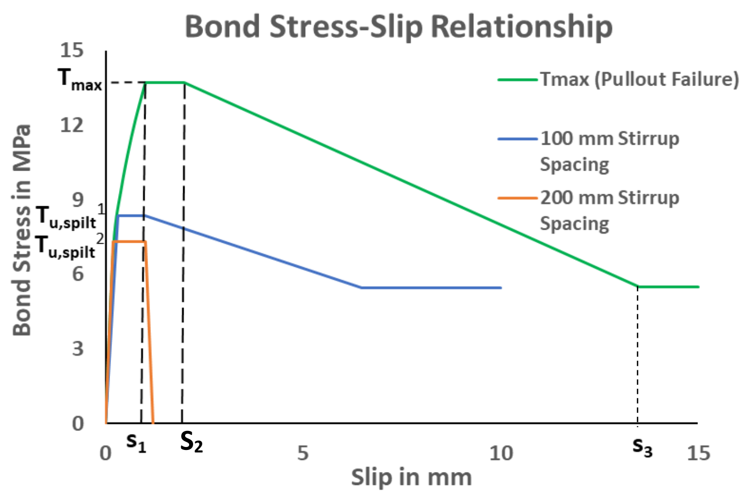

Figure 3.10: Bond stress-slip relation for column Models

3.3 Loading and Boundary Conditions of the Model

In all finite element models of the columns considered, the columns were supported by a foundation block with the bottom surface of the foundation being restrained from movement in all three directions (x, y, z). The dimensions for the foundation block are given in Section 3.1. For the cantilever column cases studied, an elastic steel plate is applied at the top and along the side (width) of the column at the position of the lateral action of the piston, to prevent localized damage to the concrete due to application of axial and lateral load. The column configuration is shown in Figure 3.11a. Axial loads corresponding to crushing ratios of 0.1, 0.35 and 0.5 were applied. Two monitoring points were placed at the point of load application; one was to record the reactions and the other to record displacements. In all cases, only half of the column width is modeled due to symmetry, to reduce the amount of required computational effort. Therefore, the nodes on the plane of symmetry were restrained from movement in the out of plane direction allowing the column to roll vertically as shown in Figure 3.11b. Therefore, in order to find the column shear strength so as to compare with experimental evidence, the load recorded from the load monitor should be multiplied by 2. The tributary axial load (i.e., the load corresponding to half of the column cross section) was applied in the first step of loading followed by a history of lateral displacement at the top. Lateral loading was controlled by the magnitude of applied displacement which was applied in monotonic increments of 0.4 mm in all following lateral steps as shown in Figure 3.11c.

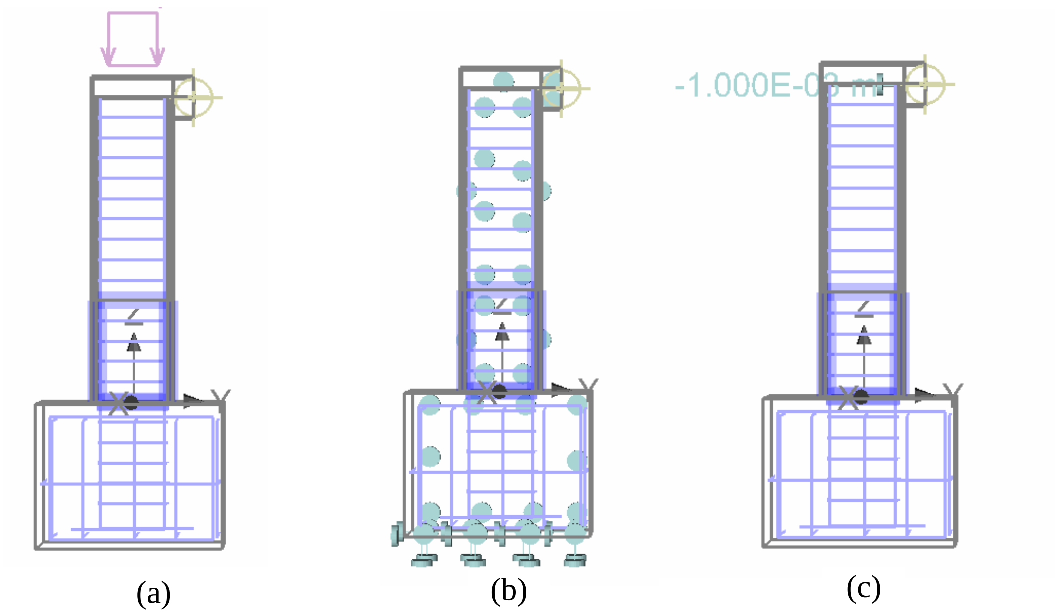

Figure 3.11: Loading and Boundary Conditions (a) Axial Loading (b) Boundary Conditions and Restraints (c) Lateral Loading

3.4 Mesh

The column span length, foundation and plate were modelled using 3D macro elements available in ATENA 3D Engineering. Concrete material models described in Section 3.2.1 were assigned to the macro element simulating the shear span and the foundation. The longitudinal and transverse reinforcement were modelled with 3D trusses elements. When assigning the reinforcement material model to the truss elements, the bar diameters were specified, and the longitudinal reinforcement was connected to the concrete with an imperfect connection through springs having the appropriate bond stress-slip relation as shown in Figure 3.10. The transverse reinforcement was connected to the concrete with a perfect connection. To ensure no separation occurs between the plate and the column, a small portion of the reinforcement is extended into the plate and the requirement that “no slip” of the bars at the top is applied. The embedded portion of the reinforcement was modelled based on the column cases shown in Figure 3.1 and slip was permitted at the bottom tip of the reinforcement.

The ATENA element library provides several options for elements and material constitutive models that may be used to formulate the mesh. Elements may be mainly divided into 3 groups: plane elements for 2D, 3D and axisymmetric analysis, solid 3D elements and special elements that may be used for modeling external cables and springs. Three types of 3D solid elements are available: tetrahedral elements, brick elements (hexahedral) and wedge elements. The elements used in these columns are 3D brick elements to discretize the macro elements.The 3D trusses were discretized within the macro elements. The column was discretized into two parts. The first 0.5 m from the foundation is discretized into elements with a size of 0.025 m where most of the plastic response will occur. For the rest of the column the size of the mesh was increased to 0.05 m. A total number of 5240 3D brick elements were used.

3.5 Solution Parameters

Full Newton Raphson method was the solution algorithm used in the nonlinear analyses and was solved according to Eq.3.35 (Cervenka et al. 2020).

[3.35] $K(p_{i-1})\Delta p_i = q - f(p_{i-1})$

Here q is a vector representing the total applied loads on joints. Δp_i is the deformation increments due to increasing load increments at the current loading point. $K(p_{i-1})$ is the stiffness matrix at a previous loading point. $f(p_{i-1})$ is the vector of total internal joint forces at a previous loading point.

To solve p_i at load level Q using Eq. 3.36 (Cervenka et al. 2020) the following is established:

[3.36] $p_i = p_{i-1} + \Delta p_i$

Equation 3.35 and 3.36 are nonlinear equations due to the nonlinear response of the internal forces and the stifness matrix, therefore, nessesary iterations are completed to achieve convergence. Equations 3.37- 3.40 represent convergance criteria that chould be achieved during the analysis. Here, superscript k specifies the kth component of a vector (Cervenka et al. 2020).

[3.37] $\sqrt{\frac{\Delta p_i^T \Delta p_i}{p_i^T \Delta p_i}} \leq \varepsilon_{rel.disp}$

[3.38] $$\sqrt{\frac{\left(q-f(p_{i-1})\right)^{T}(q-f(p_{i-1}))}{f(p_i)^{T}f(p_i)}} \leq \varepsilon_{rel.force}$$

[3.39] $$\sqrt{\frac{\Delta p_i^{T}(q-f(p_{i-1}))}{p_i^{T}f(p_i)}} \leq \varepsilon_{rel.energy}$$

[3.40] $$\sqrt{\frac{\max\left(\left(q^{k}-f^{k}(p_{i-1})\right)\right)\max\left(\left(q^{k}-f^{k}(p_{i-1})\right)\right)}{\max\left(f^{k}(p_i)\right)\max\left(f^{k}(p_i)\right)}} \leq \varepsilon_{abs.force}$$

Equation 3.37 checks the variation in the deformation by checking the last iteration, whereas Equation 3.38 checks the variation in the out of balance forces. Equation 3.39 checks the variation in the out of balance energy criterion. Equation 3.40 checks the out of balance forces. Figure 3.12 presents the Full Raphson Newton Method (Cervenka et al. 2020). The parameter, ε, (convergence limit) is set to 0.01 with a maximum number of 40 iterations. The tangent predictor was used during the iterations.

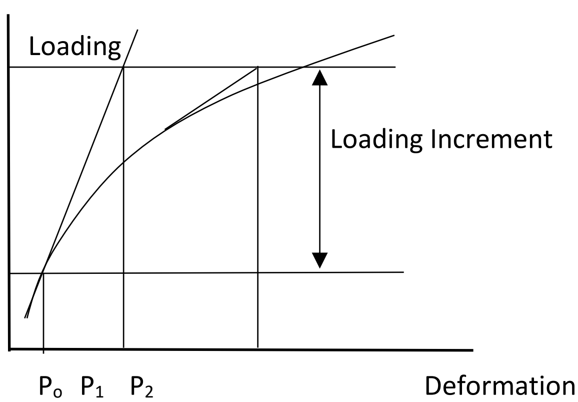

Figure 3.12: Full Raphson Newton Method. (Modified from Cervenka et al. 2020)

The line search method was activated. This method reduces the work done to calculate the out of balance internal forces on displacement increments (Cervenka et al. 2020). For example, assume that the two solved points are, p_o and $p_o + n\delta p$, while their out of balance forces are $g(p_o)$ and $g(p_o + n\delta p)$. The goal of this procedure is to set the parameter n to reduce the work done calculating the out of balance forces (Cervenka et al. 2020). All input parameters for the analysis are shown in Figure 3.13.

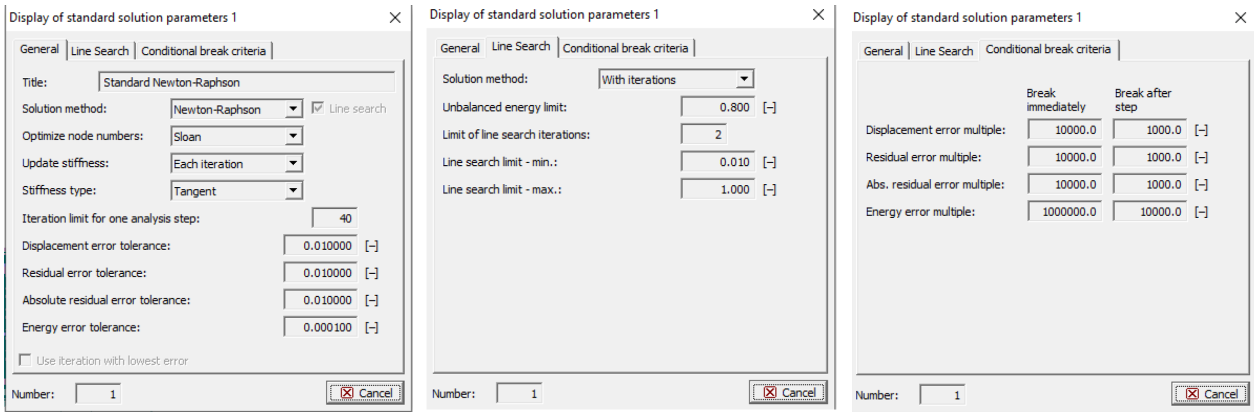

Figure 3.13: Solution Parameter used for the Analysis

4. A Comparative Study-Part 2: Results

This Chapter explores the deformation, lateral resistance and the mode of failure of each benchmark column presented in Part 1. This section will also present the effect of each parametric detailing on the seismic behavior of the columns. The deformation capacity at shear failure will be compared to available analytical models presented in Chapter 2 (literature review). The bond failure type of the benchmark columns will be presented and compared with the ACI 318M and ACI 403R code specifications.

4.1 Seismic Strength and Deformability

The column's resistance curve is a graph that plots the lateral load resistance on the y-axis, against the drift ratio on the x-axis, under monotonic or cyclic loading. The drift ratio here is defined as the lateral displacement divided by the length of the column's shear span. The moment at the fixed end of the cantilever column is the sum of the column shear resistance (V) multiplied by the length of the shear span and the effect of the eccentric axial load (the axial load multiplied by the displacement at the tip of the cantilever as shown in Figure 4.1). The additional moment caused by the eccentric axial load during lateral loading is called the P-Δ effect as shown in Eq. 4.1. The apparent degradation of the lateral load resistance in the column may be due to shear degradation or due to P-Δ effects or a combination of both mechanisms. The P-Δ effect was eliminated at each lateral displacement step by adding the drift ratio multiplied by the axial load as shown in Eq. 4.2. The aim of eliminating the P-Δ effect was to investigate the true source of lateral load degradation after reaching the maximum peak resisting load.

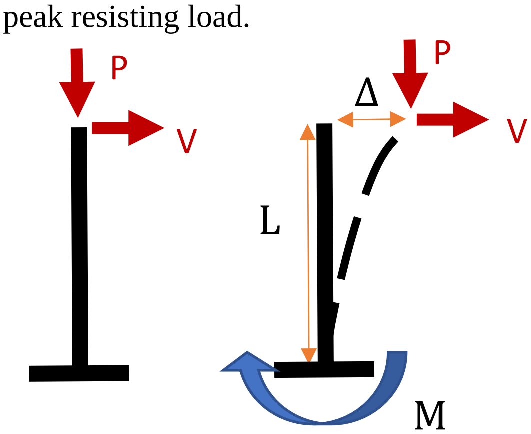

Figure 4.1: P-Δ Effect

[4.1] $M = P\Delta + VL$

[4.2] $M/L = P\theta + V$

In the above, *P* is the axial load, *M* is the moment at the fixed support of the cantilever column and *L* is the length of the shear span. The Term *M/L* presents the total lateral load resistance that may be supported by the members' flexural strength. Δ is the lateral displacement and θ is the drift ratio. Table 4.1 depicts the maximum lateral resistance load (base shear), the yield deformation and the ultimate deformation capacities for the five benchmark columns depicted in Figure 3.1.

Table 4.1 displays the base shear strength (the ultimate strength from the resistance curve). Δ_y is the effective yield displacement which is found using ASCE SEI/41-17 standards. To determine the effective yield displacement, a line is extended from the origin passing through the point of intersection of the resisting curve and a horizontal line passing through 80% of the maximum lateral load resistance. The extended line continues to intersect the horizontal line of the maximum resisting curve from which a vertical line is projected on the x-axis. The effective yielding is also recorded in Table 4.1. Figure 4.2 depicts an example of this procedure.

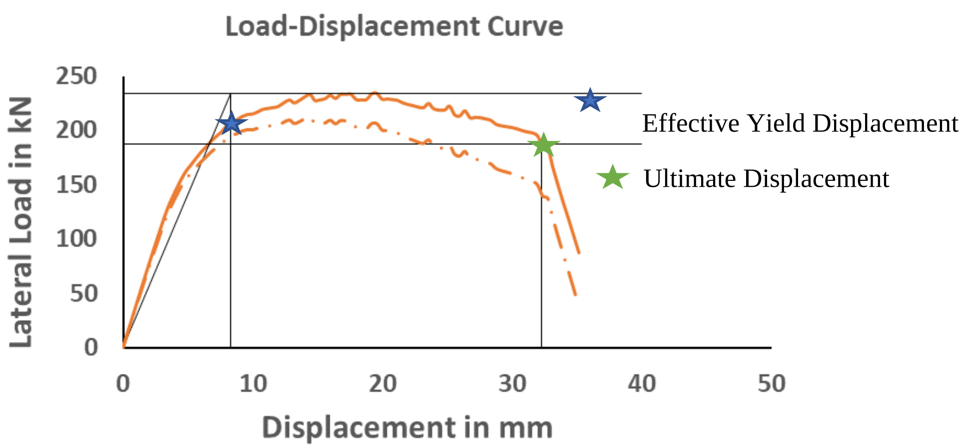

Figure 4.2 : ASCE SEI 41-17 Procedures for Determining the Effective Yield Displacement

The dotted curve is the lateral resistance curve before correcting for P-Δ effect and the continuous curve is after eliminating the secondary order effect. Δ_u is the displacement after a reduction of 20% of the lateral resistance on the post peak resistance curve as shown in Figure 4.2.

Table 4.1: Yield and Ultimate Deformation Capacities and Base Shear Strength for Benchmark Columns

	100 mm Stirrup Spacing						200 mm Stirrup Spacing					
	4Φ18 bars per face			2Φ18 bars per face			4Φ18 bars per face			2Φ18 bars per face		
Axial load Ratio	Base Shear (kN)	Δ_y (mm)	Δ_u (mm)	Base shear (kN)	Δ_y (mm)	Δ_u (mm)	Base Shear (kN)	Δ_y (mm)	Δ_u (mm)	Base Shear (kN)	Δ_y (mm)	Δ_u (mm)
Case 1 (Full Anchorage in Foundation with 90-Degree Hook)												
10	153.12[1]	9.0	43.6	107.01[1]	7.0	55.0	153.5	8.8	37.5	106.54[1]	6.8	38.7
35	242.96	10.2	45.0	194.47	7.8	32.5	237.5	9.5	24.0	192.14	7.5	22.2
50	261.17	9.5	32.5	212.65	7.5	27.5	246.49	8.0	19.5	205.60	6.8	17.3
Case 2 (Lapped Splice)												
10	127.6[2]	11.5	26	103.34[2]	9.2	36.2	126.29[2]	10.8	17.2	101.93[2]	8.2	41.1
35	211.0	10.0	43.6	178.90	7.0	35.1	201.90	8.0	22.8	171.82	6.1	21.5
50	228.9	9.0	31	190.20	6.5	27.8	218.63	7.4	16.0	183.90	5.9	15.2
Case 3 (Short Anchorage Length)												
10	142.86	8.3	32.8	106.7[1]	7.3	52.3	137.22	7.3	15.0	106	7.0	21.0
35	238.53	10.0	35.1	194.08	8.0	32.0	231.72	9.1	20.8	192.9	7.8	22.0
50	259.46	9.2	33.4	211.48	7.7	27.5	246.35	8.0	20.0	205.31	6.8	18.0
Case 4 (Deep Cross Section)												
10	361.08[1]	5.0	35.0	265.9[1]	3.5	35.9	356.80	4.7	29.0	266.26[1]	3.3	28.5
35	638.14	5.8	24.0	549.71	4.8	20.4	625.37	5.3	18.0	544.51	4.7	15.5
50	704.50	5.7	15.7	608.94	4.7	14.4	673.80	5.0	11.5	588.46	4.4	11.5
Case 5 (Hinge Connection to the Foundation Base)												
10	82.28	6.2	54.8	70.71[2]	4.8	47.2	77.75	3.2	41.6	68.35[2]	3.2	47.5
35	161.36	5.3	43.0	153.34	5.1	34.0	159.39	5.1	22.7	152.05	4.9	21.1
50	190.51	5.9	27.8	179.48	5.8	21.4	185.99	5.6	15.1	175.99	5.7	13.5

The superscript (1) in Table 4.1, indicates that the column has failed due to splitting and the analysis has stopped due to extreme concrete nonlinearity on the tension side of the critical section. If nonlinearity of concrete was eliminated throughout the analysis, the column's resistance curve would continue (with no degradation) until longitudinal reinforcement rapture. Δ_u for these columns, in Table 4.1 marks the displacement at which the analysis diverges due to concrete nonlinearity and splitting. The superscript (2) in Table 4.1, indicates that the analysis has stopped due to nonlinearity of concrete because of bond splitting after extreme pullout slip in the longitudinal reinforcement. Parameter Δ_u for these columns, in Table 4.1 marks the displacement at which the analysis diverges due to concrete nonlinearity and splitting after extreme pullout. The degradation in the columns with these two superscripts after P-Δ effect corrections is negligible.

Table 4.2 presents the estimated displacement where axial failure occurs. This is defined according to the work of Yaravi (2011) as "*the point at which the peak vertical elongation of the column is recorded immediately prior to a sudden shortening of the column*". This is determined at the point when the vertical displacement at the point of lateral displacement application starts recording negative values (negative values means downward displacements). This point is the final axial failure, and the collapse of the column is expected at this point.

In Table 4.2, Δ_a is the displacement at axial failure. The cells in Table 4.2 that contain (--) mean that the columns do not exhibit axial failure. This group consists of 22 columns out of a total of 60 columns. Failure in these columns is due to bond disintegration and their lateral strength degradation is due to P-Δ effects.

Table 4.2 : Displacement at Axial failure

	100 mm Stirrup Spacing		200 mm Stirrup Spacing	
	4Φ18 bars per face	2Φ18 bars per face	4Φ18 bars per face	2Φ18 bars per face
Axial load Ratio	Δ_a (mm)	Δ_a (mm)	Δ_a (mm)	Δ_a (mm)
Case 1 (Full Anchorage in Foundation with 90-Degree Hook)				
10	--	--	--	--
35	46.4	41.2	23.2	26
50	34.2	32.0	19.2	18.0
Case 2 (Lapped Splice)				
10	--	--	--	--
35	42.8	35.2	22.8	22.4
50	32.8	28.0	15.6	15.6
Case 3 (Short Anchorage Length)				
10	--	--	--	--
35	--	38.4	41.2	26.8
50	33.6	31.2	19.6	18.0
Case 4 (Deep Cross Section)				
10	--	--	28	--
35	24.8	27.2	17.2	15.6
50	15.2	14	10.8	11.2
Case 5 (Hinge Connection to the Foundation Base)				
10	--	--	--	--
35	--	--	36.4	26.8
50	28.4	21.1	14.8	13.2

Note that the values of Δ_a (at axial load failure) in Table 4.2 is close to the value of Δ_u (at shear failure) listed in Table 4.1, particularly at high axil loads (when shear degradation is present). At low axial loads, when the column is controlled by bond failure the column’s axial failure is delayed.

4.2 Failure Modes

From the deformation capacities shown in Table 4.1 it is confirmed that the analytical models reproduce accurately the known experimental trends, namely that columns with well confined cores (i.e., with 100 mm stirrup spacing) are capable of providing larger deformation capacities as compared to columns with 200 mm stirrup spacing. It was found that the effective yielding force increased with the increase in the axial load; however this trend reverses at an axial load of 50% where it was found that early concrete crushing failure limited the resistance. The effective yield displacement at low axial load for Case 5, fabricated hinge, and Case 2, short lap splice length, was delayed due to high slip rotation at column yielding. The shear strengths of the column in both confining cases diverge at higher axial loads where the shear failure and concrete crushing occur. Generally, the ultimate deformation capacity degrades with the increase of the axial load ratio. The deformation capacities degrade significantly in the presence of short anchorage length or lap length, particularly when the flexural reinforcement ratio is high.

4.2.1 Column Set 1: Continuous Reinforcement

The resistance curves for this case are presented in Figure 4.3. At low axial load, the columns do not show any lateral load degradation after P-Δ corrections. These columns fail due to bond splitting. The shear degradation is present at the axial load of 35% and 50% of crushing load. When shear failure also occurs at 35% and 50% of crushing axial load, the difference between the maximum lateral load resistance is insignificant.

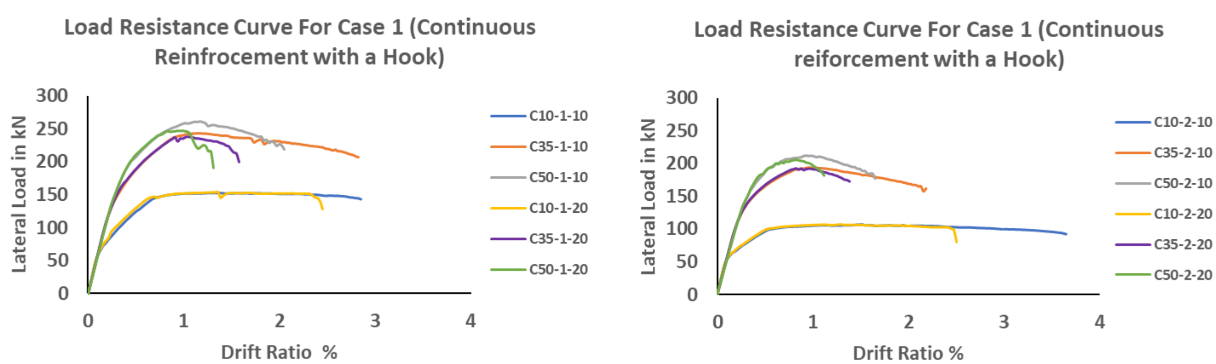

Figure 4.3: Load Resistance Curve for Case 1

4.2.1.1 Section 1: 4 ϕ 18 per face – ρ_l= 1.62%,

The longitudinal reinforcement yielded at a drift ratio of 0.67% for both cases of poor and well confined columns at an axial load of 10% of concrete crushing. In the case of poor confinement, transverse reinforcement yielded at a drift ratio of 0.8% with diagonal cracking in the web leading to shear failure. Shear failure is accompanied with bond splitting failure as shown in Figure 4.4a. With increasing lateral displacement, well confined columns failed due to extreme post yielding strains in the longitudinal reinforcement accompanied with splitting between cover and reinforcement. (No shear failure was observed in the well confined column). Yielding in the transverse reinforcement occurred only in one stirrup at 0.93% mm lateral drift ratio.

At moderate axial loads (35% of crushing load) the longitudinal reinforcement yielded at a drift ratio of 0.88% mm for both confinement cases. Two stirrups yielded at a displacement of 1.0% for the poorly confined column with diagonal cracking leading to initiation of shear failure with gradual loss of lateral load resistance. In the case of poor confinement, the longitudinal reinforcement in compression also yielded at 0.91%. With the increase of lateral displacement, the compression strains increased, leading to buckling of compression reinforcement. For the well confined column one stirrup yielded at a drift ratio of 1.0% mm. The following stirrup yielding initiated at a drift ratio of 1.4% mm with diagonal cracking leading to shear failure. The longitudinal reinforcement in compression yielded at 1.1% drift ratio. Shear failure in both cases was accompanied with concrete crushing. Figure 4.4b presents strains in the reinforcement ultimate drift and 4.4c for cracking pattern and concrete strains after axial failure at an axial load of 35% of crushing load.

In the case of axial loading of 50% of concrete crushing load, the longitudinal reinforcement yielded at a drift ratio of 0.67% for both confinement cases. For the poor confinement case, the compressive longitudinal reinforcement strains dramatically accelerated with increasing magnitude of the applied lateral displacement. This was accompanied with yielding in stirrups wrapping the compression reinforcement and concrete crushing limiting the strains in tension reinforcement to just yielding. The stirrups in the poor confining case occurred at a drift ratio of 1.1% due to diagonal cracking leading to shear failure. The same mode of failure was present in the column with good confinement, however, the shear failure occurred before compressive reinforcement buckling. The strains in the concrete with the cracking pattern at 50% of crushing is shown in Figure 4.4d for both confining conditions. Figure 4.4e represents the strains in the reinforcement for both cases of confinement after axial failure.

4.2.1.2 Section 2: 2Φ18 per face - ρ_l= 0.81%

At an axial load of 10% of concrete crushing load, the yielding of longitudinal reinforcement occurred at an earlier loading stage (approximately at a displacement of 8 mm) for both cases of confinement compared to column with higher longitudinal reinforcement ratios. Both cases of confinement failed due to splitting of the cover from tension reinforcement as shown in Figure 4.4f. No stirrup yielding was observed in both confinement cases.

At an axial load of 35%, yielding of longitudinal reinforcement occurred at a drift ratio of 0.8% for both confinement cases. The compression reinforcement in poor confinement yielded at a drift ratio of 0.83% mm. The strains in compression increased with the increase of lateral displacement allowing buckling of reinforcement. In the well confined case, the buckling initiated when the stirrups on the compression reinforcement yielded at a drift ratio of 1.25%. No web stirrup yielding was observed in this case indicating shear failure. The only yield strains in stirrups were observed on the compression side at the point of bearing of compression reinforcement due its high compressive strains, which led to buckling in the well confined column. Concrete splitting was also observed in both confining cases. The failure was controlled by flexure as shown from the crack pattern in Figure 4.4g. The reinforcement strains at 35% axial load are shown in Figure 4.4h.

At an axial load of 50% crushing load, the columns failed by crushing of concrete and reinforcement buckling. Any stirrups yielding was present only due to buckling mechanisms. The mode of failure is presented in Figure 4.4i at 50% concrete crushing axial failure. Note that the cracks presented are limited to 0.1 mm minimum. For each Figure reference, for example 4.4a, the column to the left is the well confined case and the column to the right is the poorly confined case.

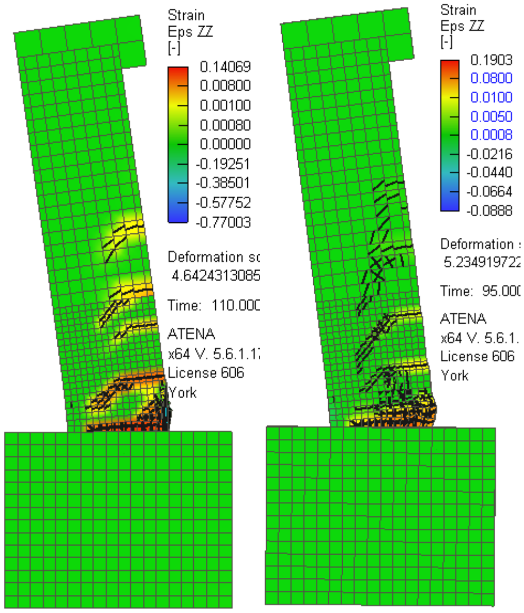

4.4a: ρ_l= 1.62%, *v*=10%

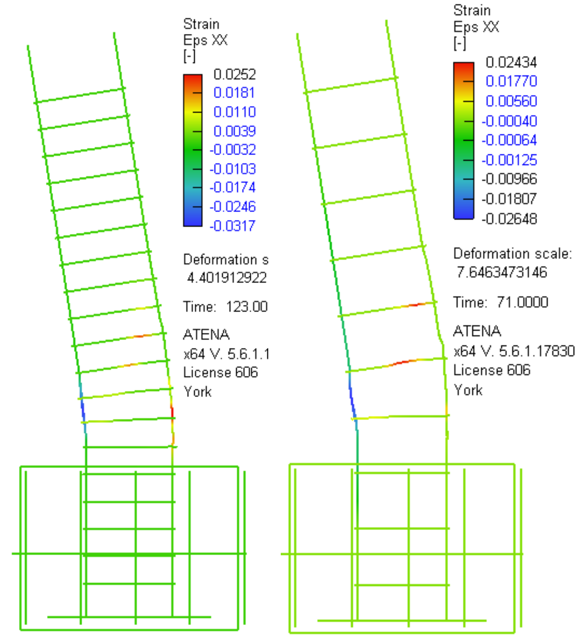

4.4b: ρ_l= 1.62%, *v*=35%

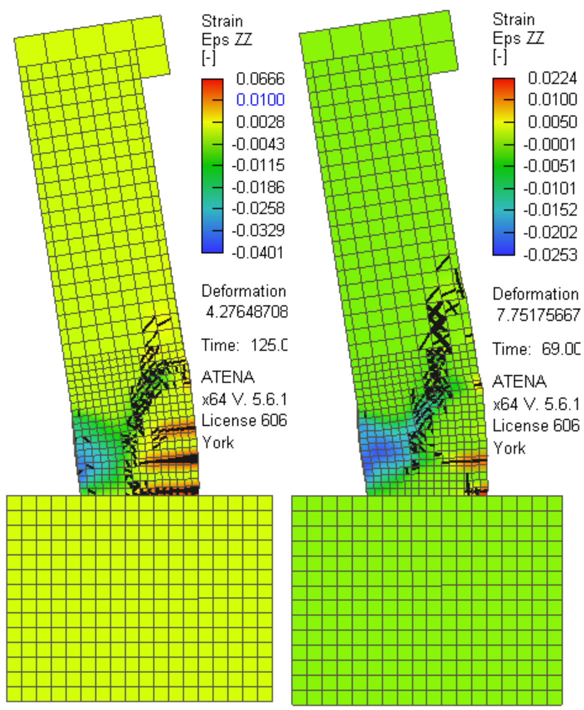

4.4c: ρ_l= 1.62%, *v* =35%

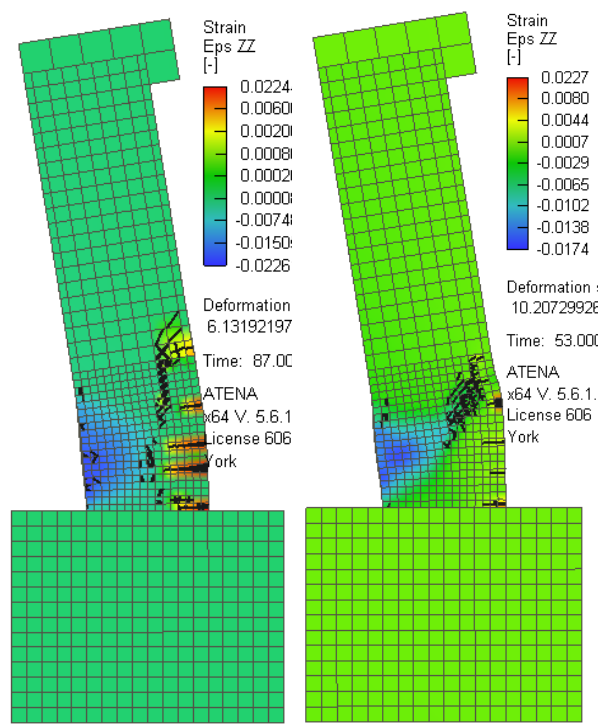

4.4d: ρ_l= 1.62%, *v* =50%

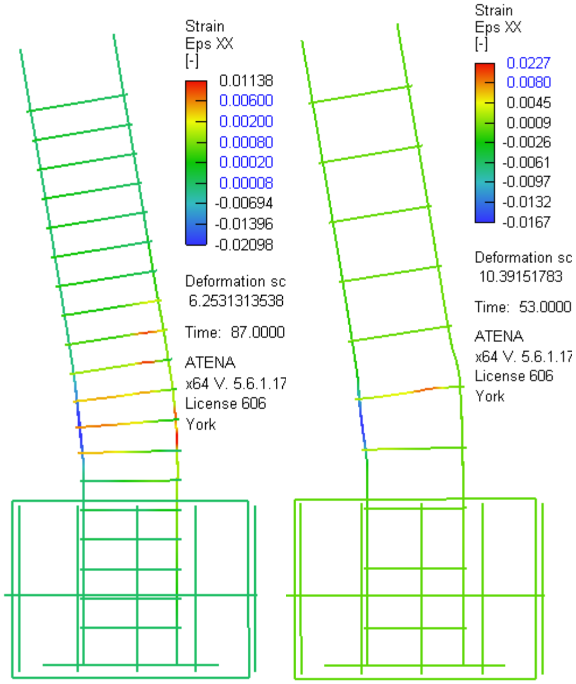

4.4e : ρ_l= 1.62%, *v*=50%

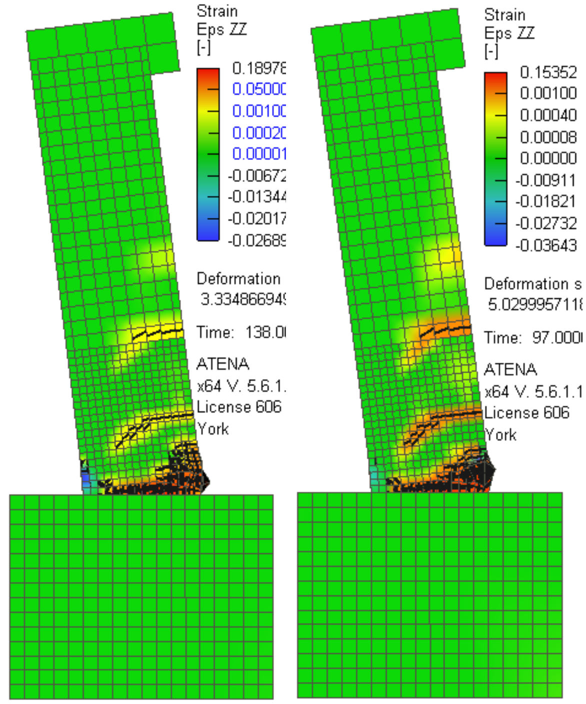

4.4f : ρ_l= 0.81%, *v*=10%

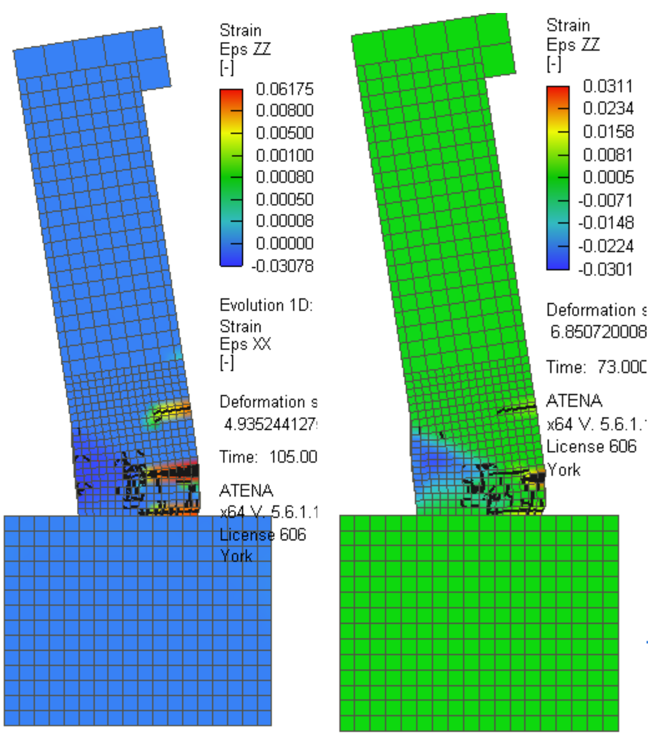

4.4g : ρ_l= 0.81%, *v* =35%

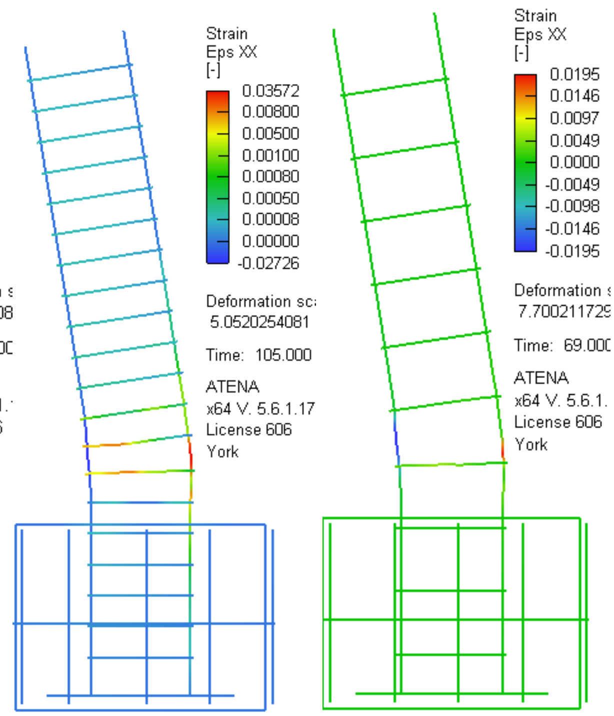

4.4h: ρ_l= 0.81%, *v* =35%

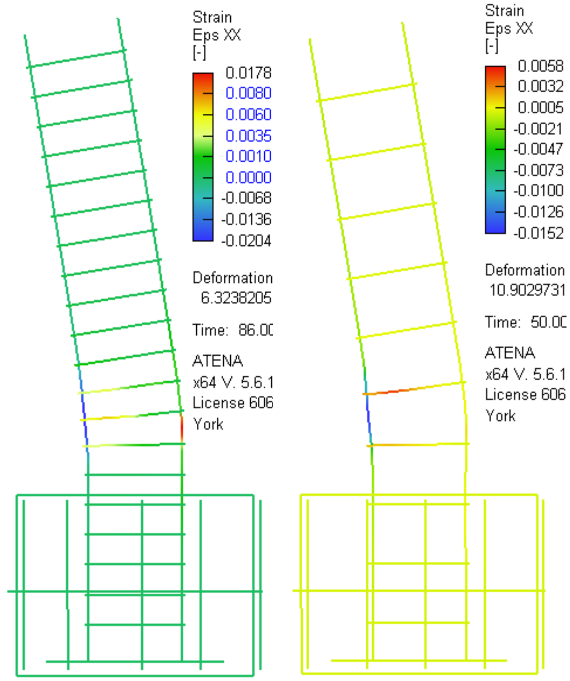

4.4i: ρ_l= 0.81%, v=50%

Figure 4.4: Mode of Failures for Column Case 1. Where v is the Axial Load Ratio of the Crushing Load and ρ_l is the Longitudinal Reinforcement Ratio.

4.2.2 Column Set 2: Lapped Reinforcement.

Figure 4.5 depicts the resistance curves calculated for the cases with a lap splice above the base. Pullout bond failure occurred at low axial loads and therefore the lateral resistance degradation was insignificant. However, the lateral resistance was deprecated in columns with high reinforcement ratio. With the increase of the axial load, the columns provided larger deformation capacities. The deformation capacity and base shear are reduced compared to the first case. Refer to Figure 4.3 for benchmark column case studies considered.

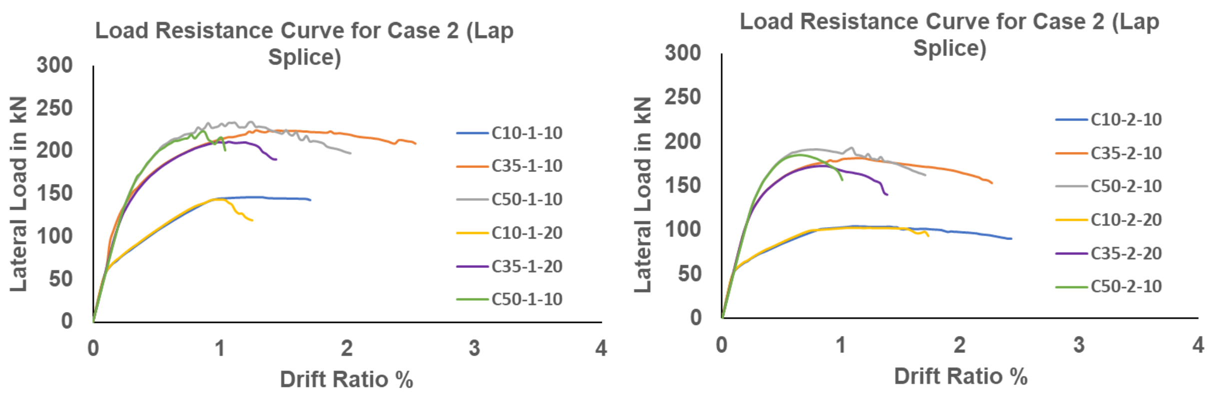

Figure 4.5: Resistance Curve for the Case 2 – short lap splice above the base

4.2.2.1 Section 1: 4 ф 18 per face – ρ_l= 1.62%

At an axial load ratio of 10% of concrete crushing load, the longitudinal reinforcement yielded at a drift ratio of 0.93% for both confining cases with approximately 1 mm slip in the longitudinal bar in tension. The deformation capacity decreased significantly in the presence of lap splice and low axial load. This was due to reinforcement slip which led to bond pullout failure at the critical section of the shear span, appearing at the early stages of lateral displacements. A drop in the lateral resistance occurred due to this pullout. Only one stirrup yielded along the lap length in the case of well confined column and no transverse yielding was observed in the column with poor confinement. High tension strain in the concrete cover was also observed, which indicated that the cover in tension spalled as shown in Figure 4.6a.

Bond pullout failure was also observed when the axial load was increased to 35% of the crushing load in both cases of confinement. The longitudinal reinforcement yielding in this case occurred at a drift ratio of 1.28 % and 1.36 % mm for both good and poor confinement respectively, with an average slip of 1 mm in the reinforcement bars. For the column with poor confinement, bar slip was accompanied with shear failure. Stirrup yielding and shear failure also occurred with the pullout failure in the well confined column. The pullout failure in both cases was accompanied by concrete crushing for both confinement cases. No drop in lateral load resistance occurred with an axial load of 35% of crushing load. The failure modes for this case is shown in Figure 4.6b.

With an axial load of 50%, no tension bar pullout occurred. The failure mode for the two confining cases was concrete crushing. Concrete crushing strains are shown in Figure 4.6c at high axial loads. The compression reinforcement yielded at a displacement of 1.04 % for both confinement cases. Stirrup yielding in the lap region occurred adjacent to longitudinal reinforcement buckling. Bar strains in the reinforcement at 50% axial load are shown in Figure 4.6d.

4.2.2.2 Section 2: 2Φ18 per face - ρ_l= 0.81%

The longitudinal reinforcement (for both confinement cases) yielded at a drift ratio of 0.8 % in tension with an average bond slip of 1 mm. Pullout bond failure was present in this case as well. The bond pullout in this case was accompanied with post flexural yielding strains. The flexural yielding in the anchored reinforcement was capable of providing large deformation capacity, preventing a drop in the lateral load resistance. No stirrup yielding was present in the lap region. The mode of failure for columns with axial load 10% of axial load percentage of concrete crushing load is presented in 4.6e.

When the axial load ratio was increased to 35% of concrete crushing, the yielding of longitudinal reinforcement was delayed up to a displacement of 1.25 %. This was followed by bond pullout for both confinement cases accompanied with post flexural yielding strains. The transverse reinforcement in the compression side yielded for the case of poor as well as good confinement in the lap region. One stirrup yielded at the critical section for the column with poor confinement. The longitudinal strains for both confining cases are found in Figure 4.6f. The flexural yielding in this case enabled the column to provide large deformation capacities with no sudden drop.

When the axial load was increased to 50% of concrete crushing, no yielding occurred in the longitudinal reinforcement in the case of low confinement due to concrete crushing. For good confinement, yielding of reinforcement with concrete crushing was the controlling mode of failure. See Figure 4.6g for strains in bars at high axial load.

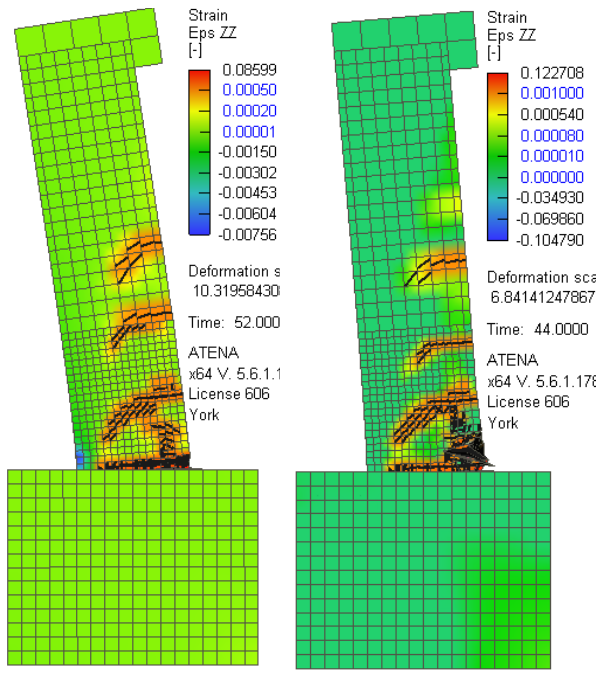

4.6a: ρl= 1.62%, *v*=10%

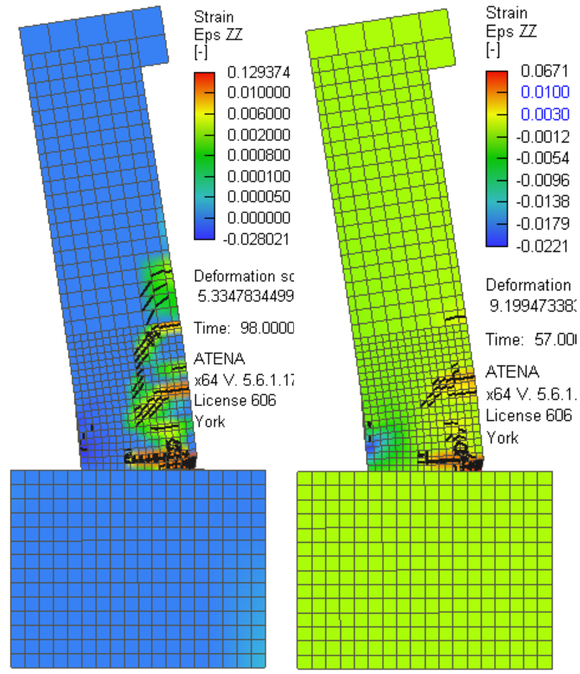

4.6b: ρl= 1.62%, *v*=35%

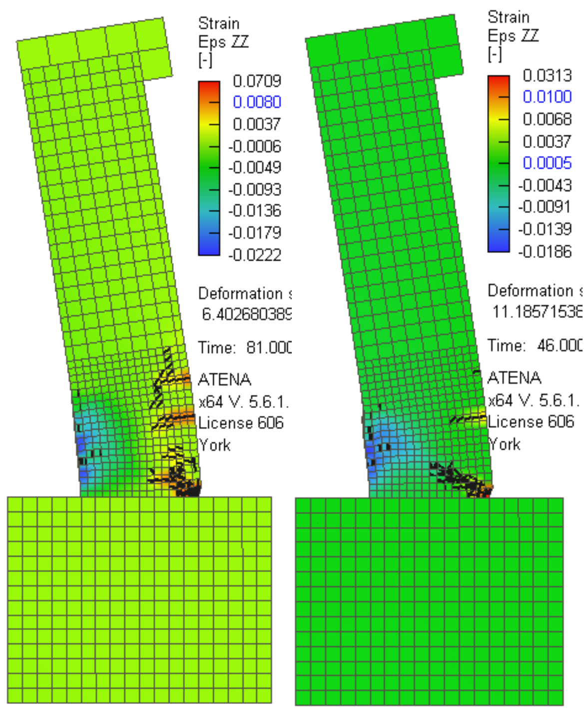

4.6c: ρl= 1.62%, *v*=50%

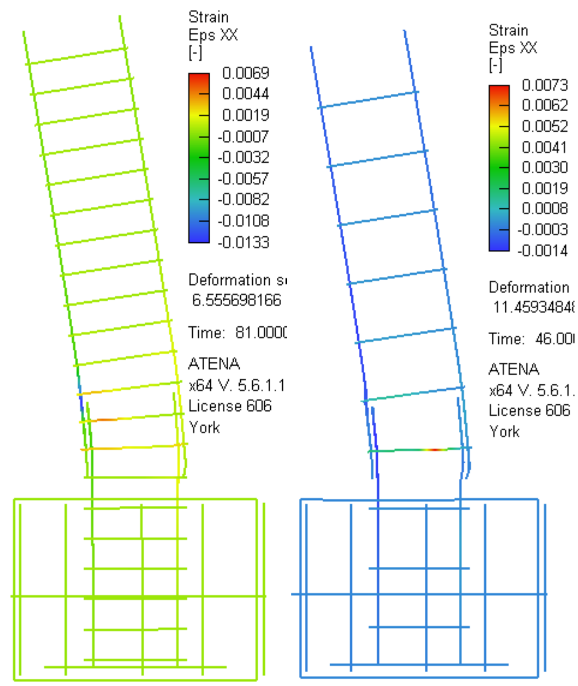

4.6d: ρl= 1.62%, *v*=50%

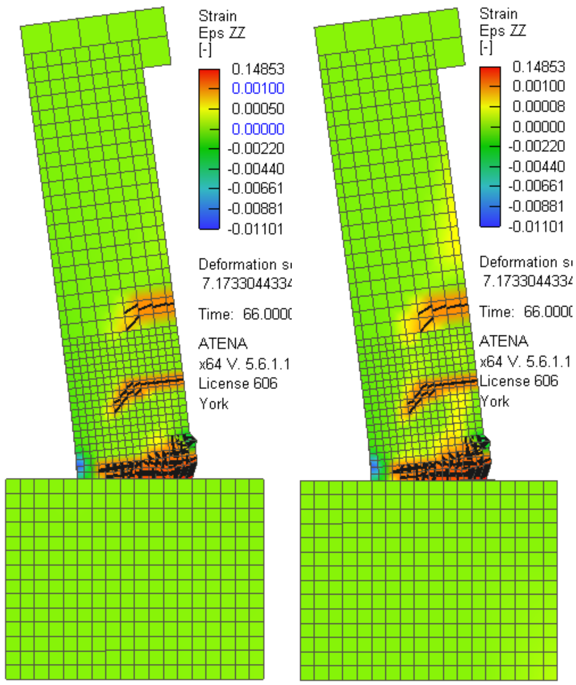

4.6e: ρ_l= 0.81%, *v*=10%

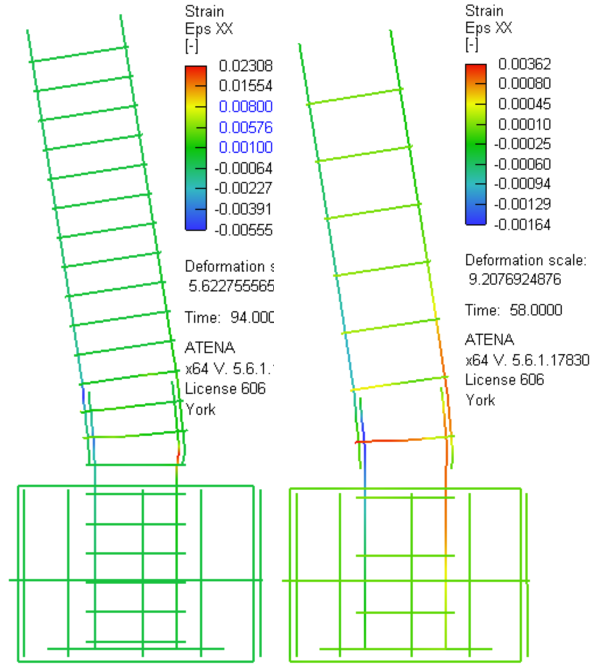

4.6f: ρ_l= 0.81%, *v*=35%

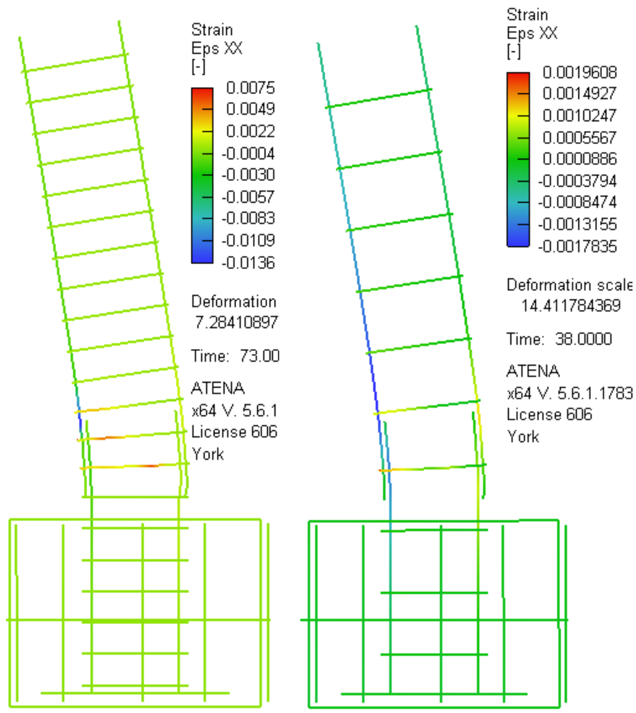

4.6g: ρ_l= 0.81%, *v*=50%

Figure 4.6: Mode of Failures for Column Set 2. Variable *v* is the Axial Load Ratio of the Crushing Load and ρ_l is the Total Longitudinal Reinforcement Ratio.

It was observed that the intensity of the pullout failure decreased with the increase of the axial load. This was because the high compression force mitigated the reinforcement slip. Therefore, the presence of a lap splice in the critical region of the column affected the ultimate displacement capacity of the column significantly under the action of a low axial load as compared to the same type of column but with higher axial load ratio. It was also found that the occurrence of a slip rotation increases the effective yield rotations, a result that causes delay in longitudinal reinforcement yielding. For example, in Case 1, when the reinforcement was fully anchored in the foundation, the longitudinal reinforcement yielded at a drift ratio of 0.67% and 0.53% for the section with longitudinal reinforcement ratio, ρ = 1.62% and 0.81% respectively. At the same analytical step, the slip was 0.14 and 0.17 mm respectively. In the presence of a lap splice, as in Case 2, the longitudinal reinforcement yielded at a delayed drift ratio of 0.93% and 0.8% for the two sections respectively. The slip was increased in an average of 1 mm with both sectional reinforcement ratios.

The maximum lateral load resistance was reduced in the presence of the lap splice. This occurred because of the slip in the extension bars lapped next to the anchored bars as shown in Figure 4.6f. This prevented the transfer of forces between the lapped bars and therefore decreased the maximum lateral load resistance.

4.2.3 Column Set 3: Short Anchorage Length

The case considered in this section has a short embedment length in the footing. Figure 4.7 depicts the load resistance curves for this group of benchmark examples.

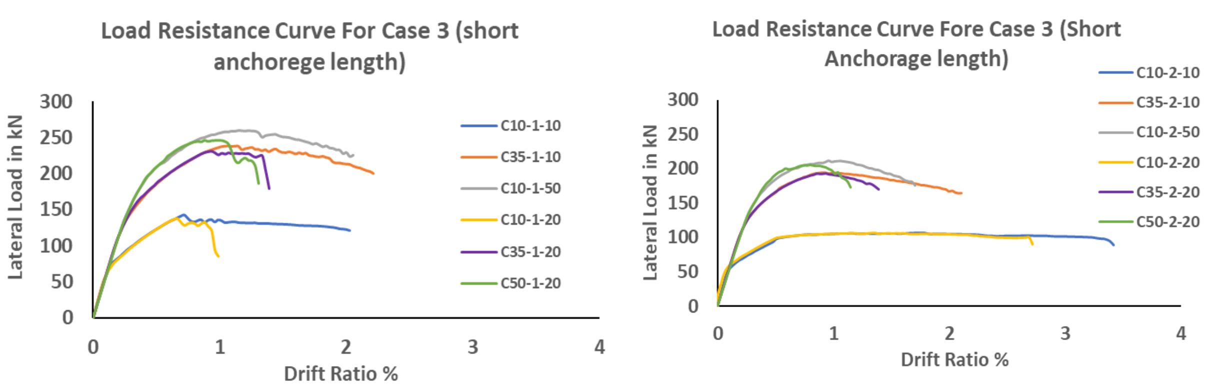

Figure 4.7 : Resistance Curve for Case 3

With reference to the resistance curves of Figure 4.7, it is concluded that the lateral load resistance dropped in the case of high reinforcement ratio, and low reinforcement ratio if the stirrup spacing was sparse.

4.2.3.1 Section 1: 4Φ18 per face – ρ_l= 1.62%

In the case of good confinement at an axial load of 10% of concrete crushing, the longitudinal reinforcement yielded at a drift ratio of 0.67% with an average slip drift of 0.12% mm in the reinforcement for the well confined column. An average of 0.4% slip drift occurred at a top drift ratio of 1.23%. Of this amount the top drift ratio resulting from slip is equal to, θ_{slip} = (1mm/0.7d), with d=358mm, i.e., θ_{slip}=0.4%, one third of the total drift ratio. This is followed by a gradual pullout failure with a decrease in the longitudinal reinforcement strains. The lateral load resistance is reduced significantly at a drift ratio of 2.3% with an approximate slip drift ratio of 2% at the reinforcement tip. In the case of low confinement (sparse stirrup spacing) at the same axial load, no longitudinal reinforcement yielding occurred. Pullout of the reinforcement occurred at top drift ratio of 1.0% with an approximate slip drift ratio of 0.8%, therefore 2/3 of the total displacement accounted for the slip contribution. No transverse reinforcement yielding strains were observed in both confinement cases. The slip in the reinforcement before complete pullout failure is depicted in Figure 4.8a.

When increasing the axial load to 35% of the crushing load, columns with poor confinement exhibited pullout failure at a top drift ratio of 1.35% with sudden reduction in the lateral load resistance at bar slip drift ratio of 0.8%. No longitudinal reinforcement yielding was observed. For poor confinement transverse reinforcement yielded at top drift ratio 1.25% (two stirrups yielded) with diagonal tension cracking, which indicated shear failure. For well confined columns for the same axial load, the longitudinal reinforcement yields at a top drift ratio of 0.93% with an average bar slip drift ratio of 0.12% at the lower reinforcement end. The longitudinal reinforcement pulls out gradually with a 1.0% average slip drift ratio at a top drift ratio of 2.2%. First transverse reinforcement yielded at a drift ratio of 1.25%. Shear failure also occurred in the columns with good confinement, developing a diagonal cracking pattern. Concrete crushing was observed in both confining conditions. The reinforcement slip is depicted in Figure 4.8b before complete pullout failure.

At an axial load of 50% of concrete crushing, similar behavior as the first case was observed for the two confinement cases. The concrete crushing controls the behavior in this case and the column behaves as a column with full anchorage as shown in Figure 4.8c (which depicts the strain in the reinforcement which is comparable to Figure 4.8e).

4.2.3.2 Section 2: 2Φ18 per face - ρ_l= 0.81%

In the presence of well confinement and a low axial load (10% of concrete crushing), the column was capable of developing the same behavior with that of an otherwise identical column with full anchorage. This was due to the development of post yield strains in the tension reinforcement prior to pullout of the reinforcement. The longitudinal reinforcement yielded at a drift ratio of 0.53% for both confinement cases. No yielding occurred in the transverse reinforcement, both confinement cases failed due to concrete splitting.

With the increase of the axial load to 35% of concrete crushing, the longitudinal reinforcement yielded at a top drift ratio of 0.83% for both confining cases. One transverse reinforcement yielded at a drift ratio of 2.3% with the transverse reinforcement on the compression side yielding at a lateral drift ratio of 1.22% which allowed compression reinforcement buckling for the column with good confinement. Reinforcement strains at failure are shown in Figure 4.8e.

The concrete crushing was present in the case of 50% crushing load. Figure 4.8f depicts the reinforcement strains at failure at 50% axial load crushing load.

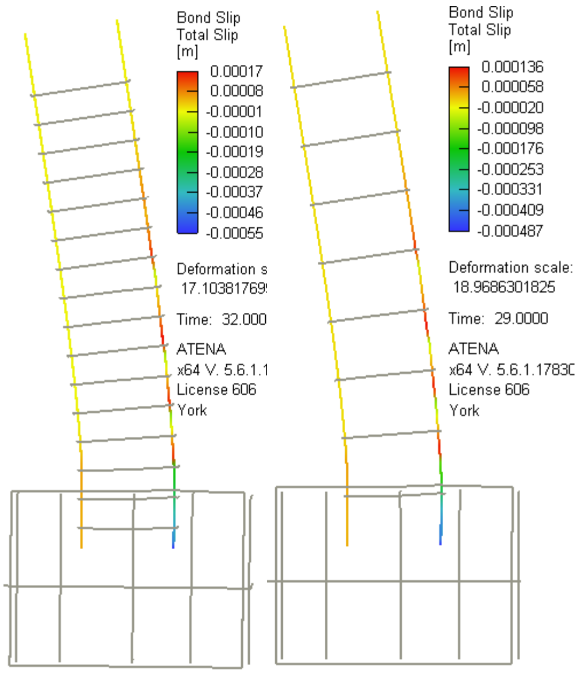

4.8a: ρ_l= 1.62%, v=10%

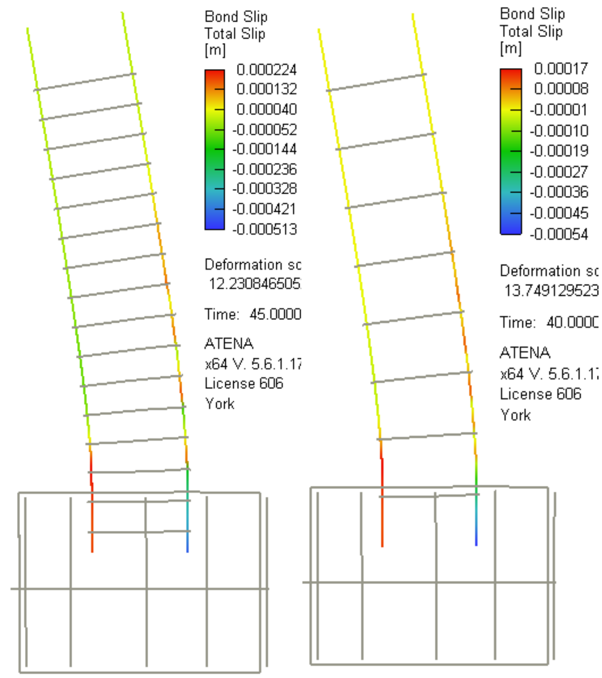

4.8b: ρ_l= 1.62%, v=35%

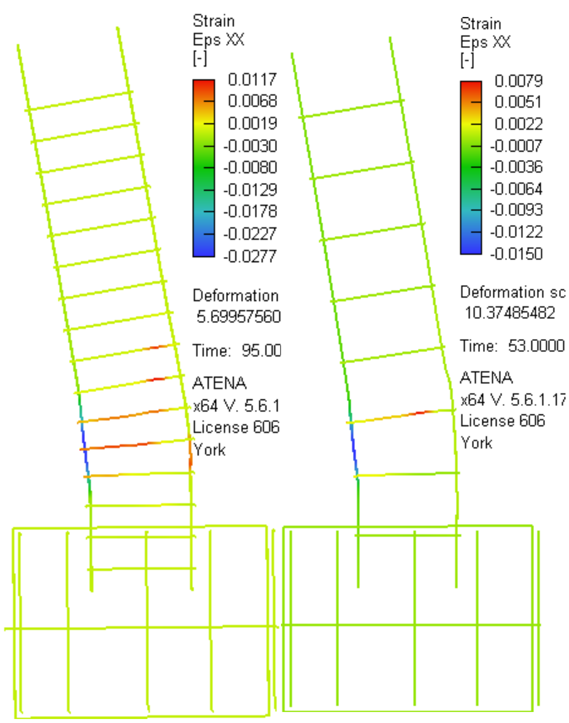

4.8c: ρ_l= 1.62%, v=50%

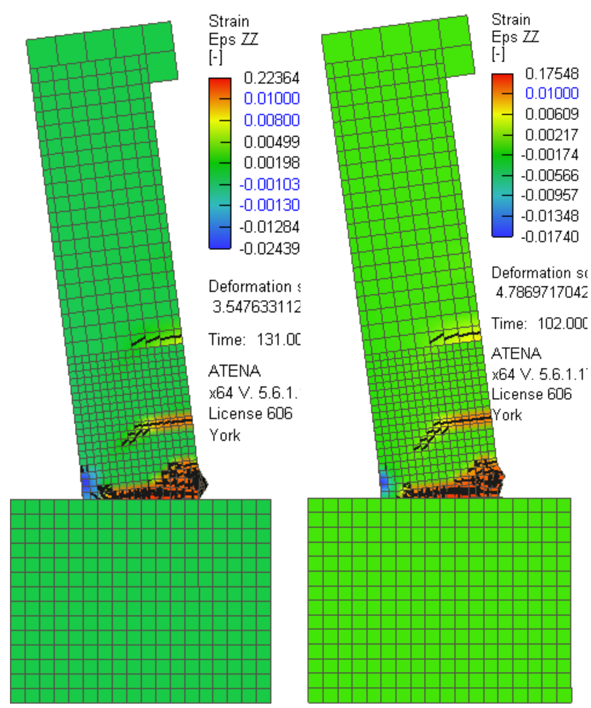

4.8d: ρ_l= 0.81 , %, v=10%

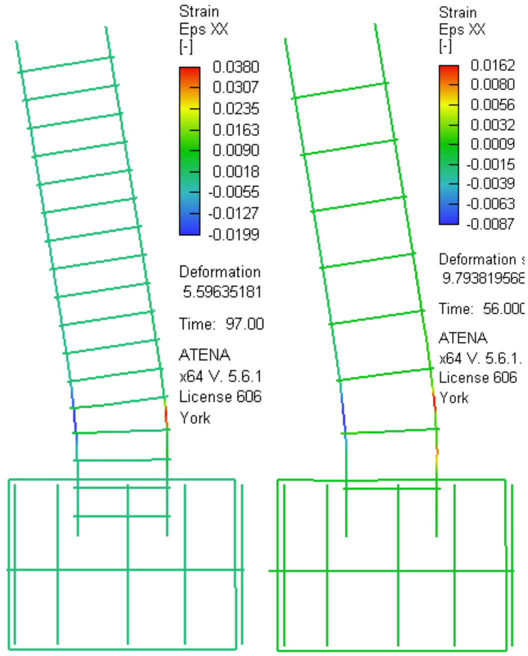

4.8e: ρ_l= 0.81 %, v=35%

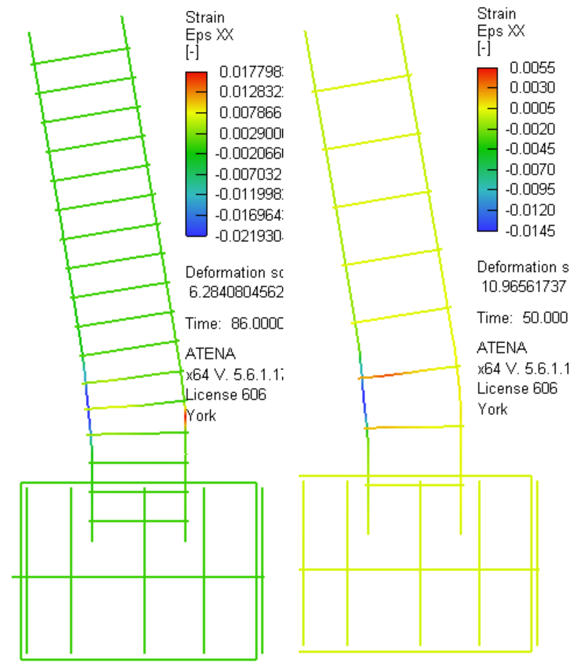

4.8f: ρ_l= 0.81 %, v=35%

Figure 4.8: Mode of failure for column Set 3. Where v is the axial load ratio of the crushing load

As concluded from Case 2 (lapped splice column case), the higher the axial load the less evident the pullout slip magnitude. Pullout occurred in the column around the ultimate resisting load as opposed to the splitting failure in the case of lap splice which was observed at, or just before yielding. Pullout failure in the case of the lap splice occurred earlier because the bond demand occurs within the shear span where resistance depends on the tensile strength of the cover, whereas in the case of the short anchorage length, the reinforcement was pulled-out from the foundation where higher bond resistance is possible due to triaxial confinement, and therefore the short reinforcement anchorage could support a higher pullout force. Thus, flexural yielding in low reinforcement ratios in the case of the short anchorage length overcomes the pullout failure in well confined sections.

4.2.4 Columns Set 4: Deep Cross Section

The benchmark case of the column with a deep cross section presented generally reduced deformation capacity as compared to the more slender columns examined in the preceding. Figure 4.9 depicts the resistance curve calculated for this group of elements.

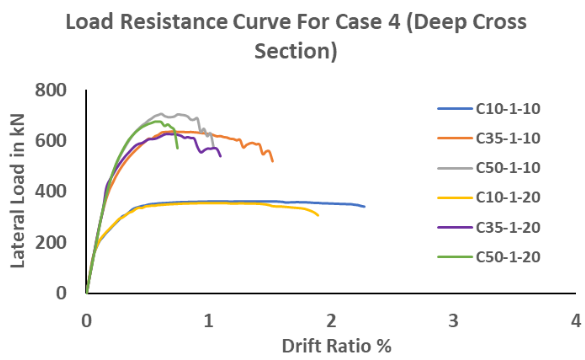

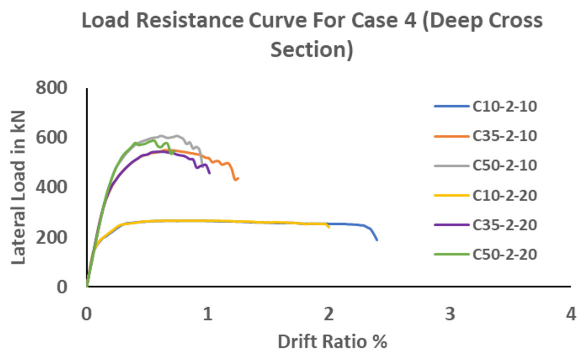

Figure 4.9: Load Resistance Curve for Deep Cross Section

Overall, the reported types of failure in this case are similar to those obtained for Case 1, but with less deformation capacities and larger lateral load resistance. Note that the deep cross section provides a higher lever arm which increases the maximum lateral load resistance. Therefore, shear failure was expected to occur at lower axial loads as well.

4.2.4.1 Section 1: 4Φ18 per face – ρ_l= 1.62%

At an axial load of 10% of crushing load, stirrup yielding occurred for both cases of confinement at 0.4% lateral drift ratio. The longitudinal reinforcement yielded at the next lateral step (0.43%). Both confining cases failed due to shear and by splitting bond failure shown in Figure 4.8a. When increasing the axial load to 35% of concrete crushing, the first transverse reinforcement yielded at a drift ratio of 0.4% and 0.48% for poor and well confined columns respectively. The yielding in the longitudinal reinforcement occurred at a drift ratio of 1.0% mm for both confining cases with diagonal cracking indicating shear failure. Buckling of reinforcement and concrete crushing occurred at the following lateral displacements. The concrete strains at failure and the crack pattern are shown in Figure 4.8b. When increasing the axial load to 50% of crushing load, one transverse reinforcement layer yielded for both confining cases around a lateral drift ratio of 1.0%. The failure of this column in both confining cases is controlled by concrete crushing and compression buckling. The strains in the column at 50% crushing load are shown in Figure 4.10c.

4.2.4.2 Section 2: 2Φ18 per face - ρ_l= 0.81%

Longitudinal reinforcement for both confinement cases yielded at a displacement of 4 mm. This leads to splitting failure for columns with low axial load (10%). With the increase of the axial load to 35% and 50 % of concrete crushing, concrete crushing and buckling occurred. Figure 4.8d, 4.10e and 4.10f depict column mode of failures for 10%, 35% and 50% of crushing load, respectively.

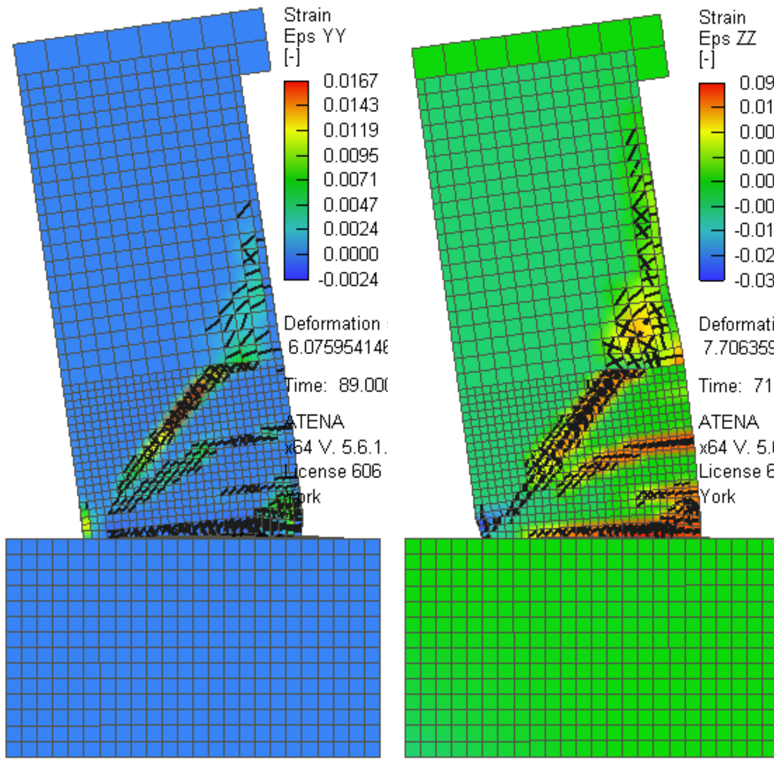

(a): ρ_l= 0.88%, v=10%

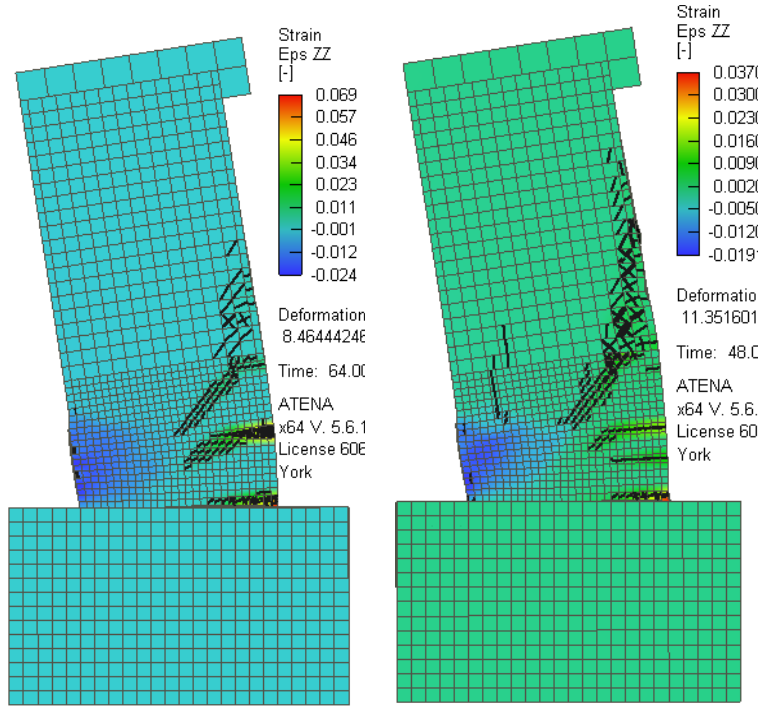

(b): ρ_l= 0.88%, *v*=35%

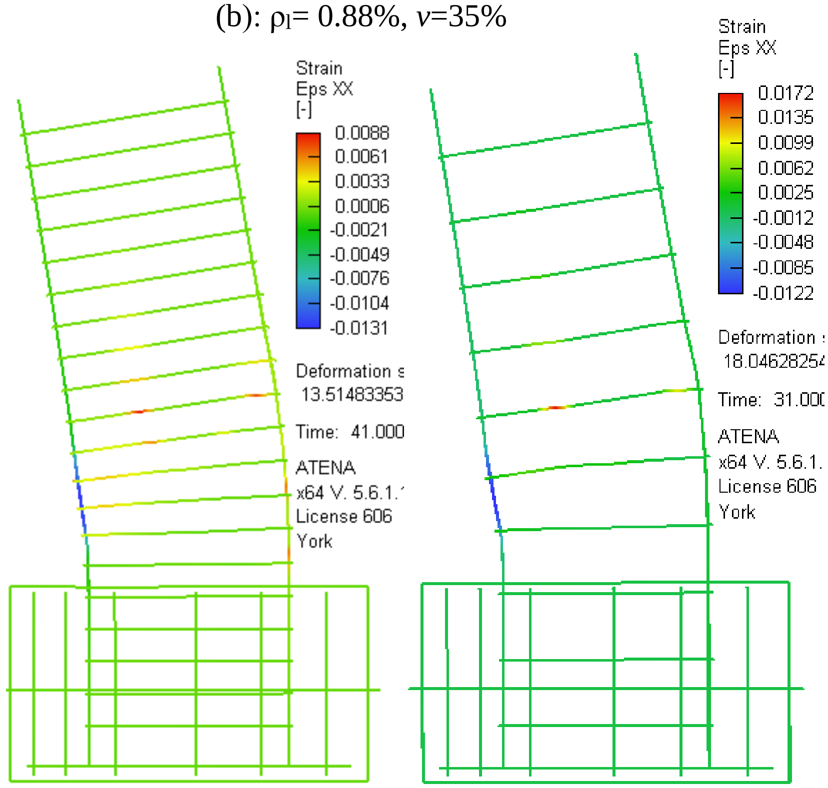

(c): ρ_l= 0.88%, *v*=50%

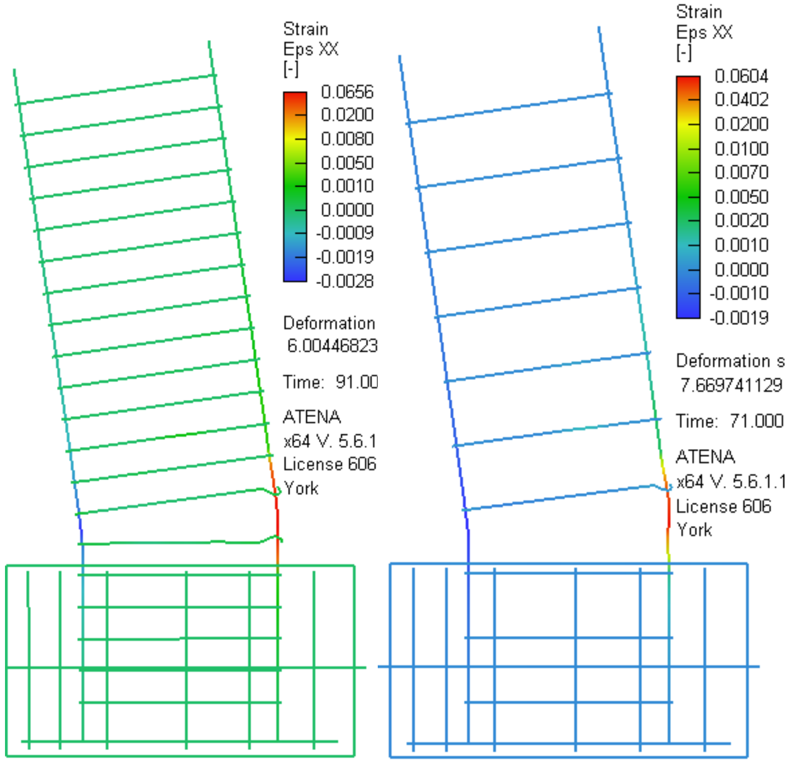

(d): ρ_l= 0.44%, *v*=10%

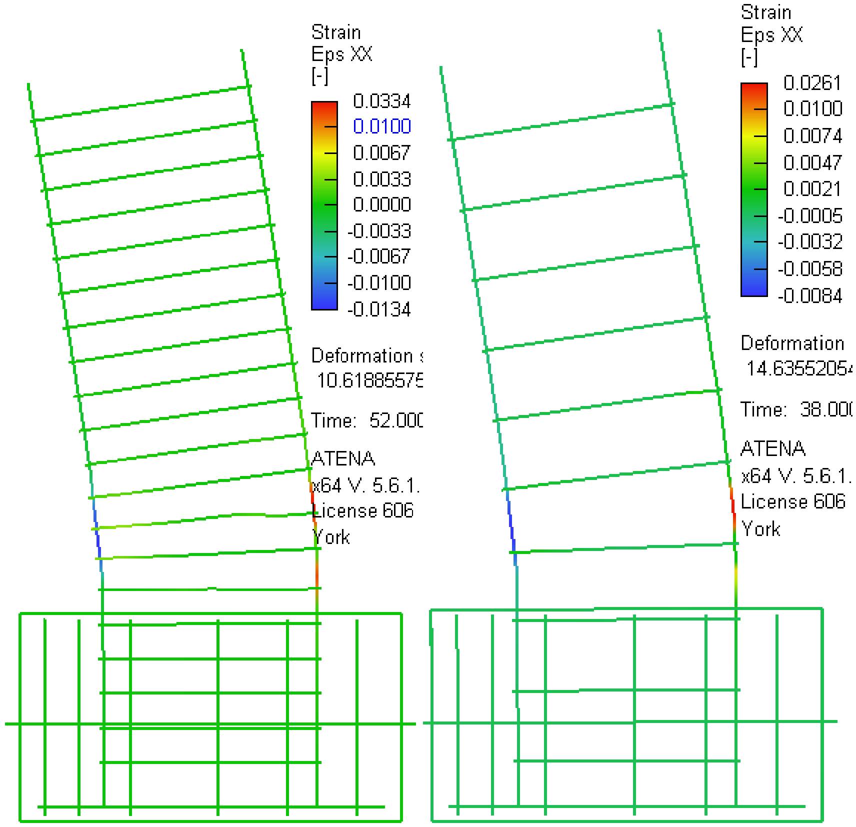

(e): ρ_l= 0.44%, *v*=35%

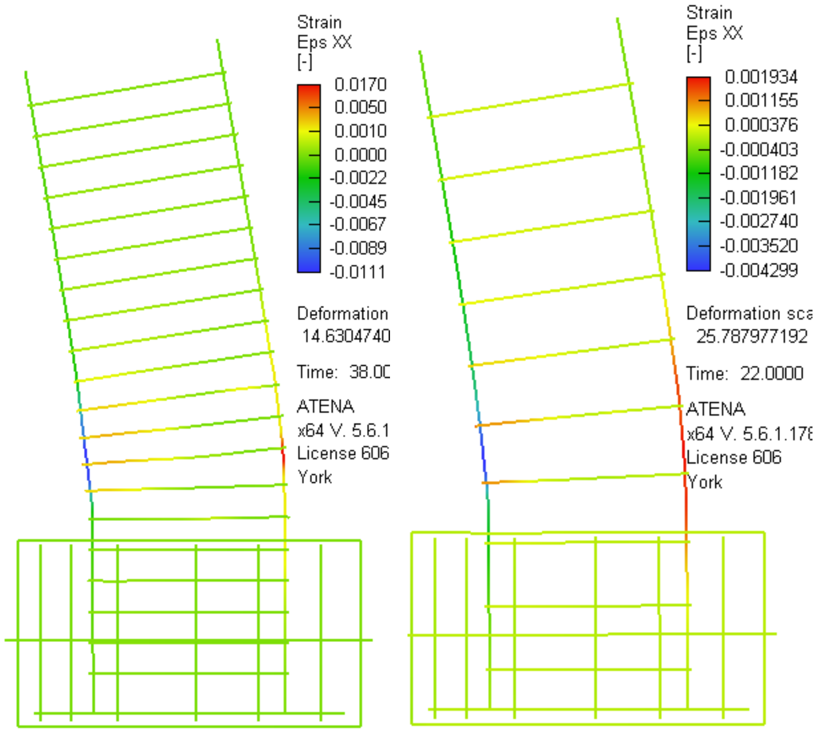

(f): ρ_l= 0.44%, v=50%

Figure 4.10: Mode of Failures for Column Set 4. Parameter v is the Axial Load Ratio and ρ_l is the Longitudinal Reinforcement Ratio

4.2.5 Columns Set 5: Fabricated Structural Hinge

This case is an unusual example for modern standards but one that is encountered in construction from the 1960's. The idea here was to limit the flexural strength of the critical section to a small value, by crossing some of the longitudinal bars through the web's centroid, in order to ensure that only limited amount of resisting reinforcement would be mobilized in flexural action. The estimated load resistance curves for this case are shown in Figure 4.11.

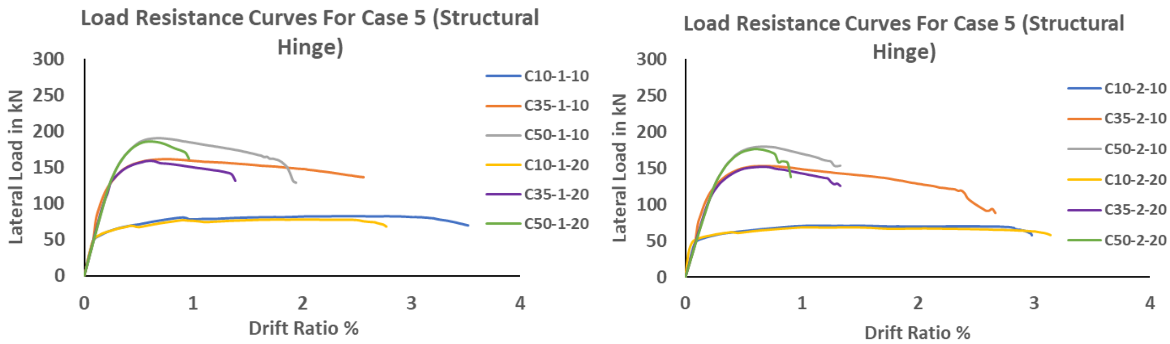

Figure 4.11: Load Resistance Curve for Case 5

Due to the geometrical arrangement of the longitudinal reinforcement at the critical section, where the longitudinal reinforcement forms a cross-X the member develops insignificant moment due to the very small lever arm. Therefore, all strains in the reinforcement are significantly below yielding. The column mainly failed by bond pullout failure at low axial loads (10%) and concrete crushing with bond splitting at higher axial load (50% and 35%) regardless of the reinforcement longitudinal ratio and the stirrup spacing. With low longitudinal reinforcement ratio (ρ_l= 0.81 %), the longitudinal reinforcement started to yield near column failure.

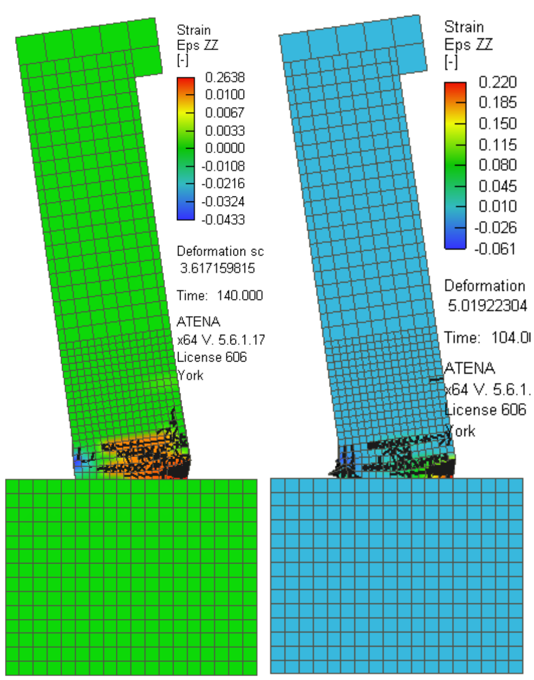

4.12a: ρ_l= 1.62%, *v*=10%

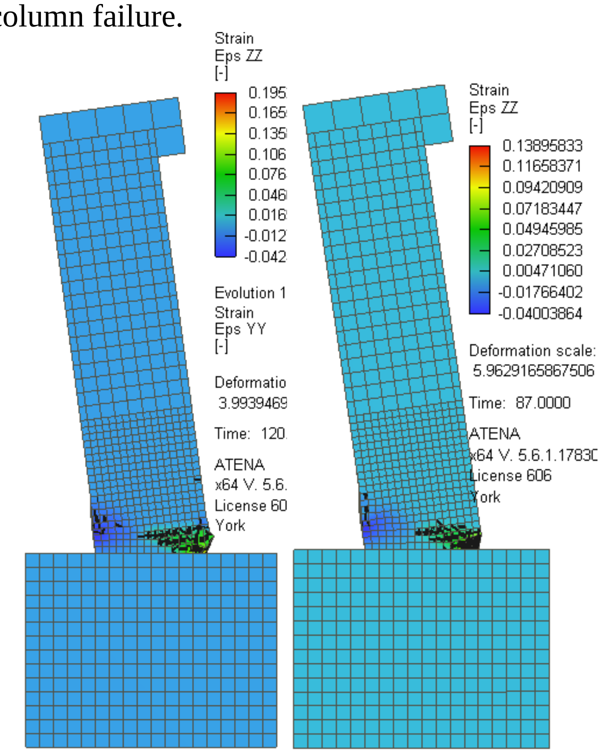

4.12b: ρ_l= 1.62%, *v*=35%

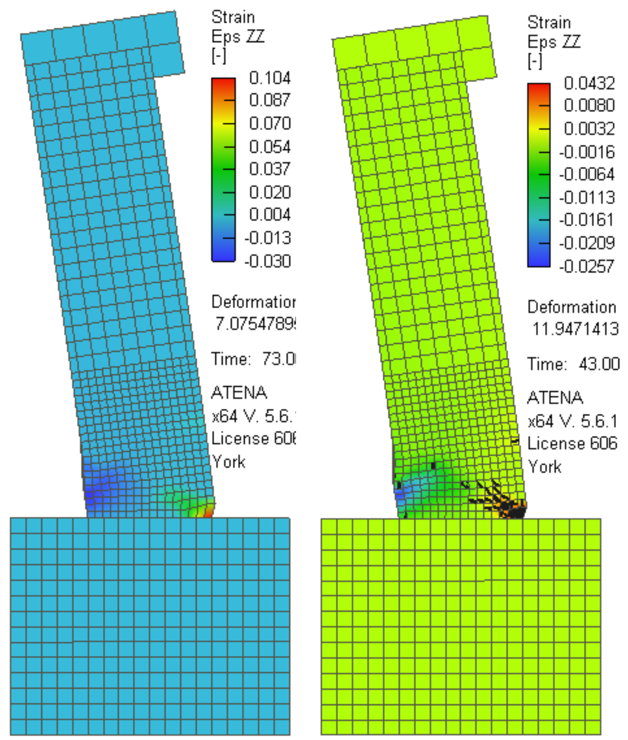

4.12c: ρ_l= 1.62%, *v*=50%

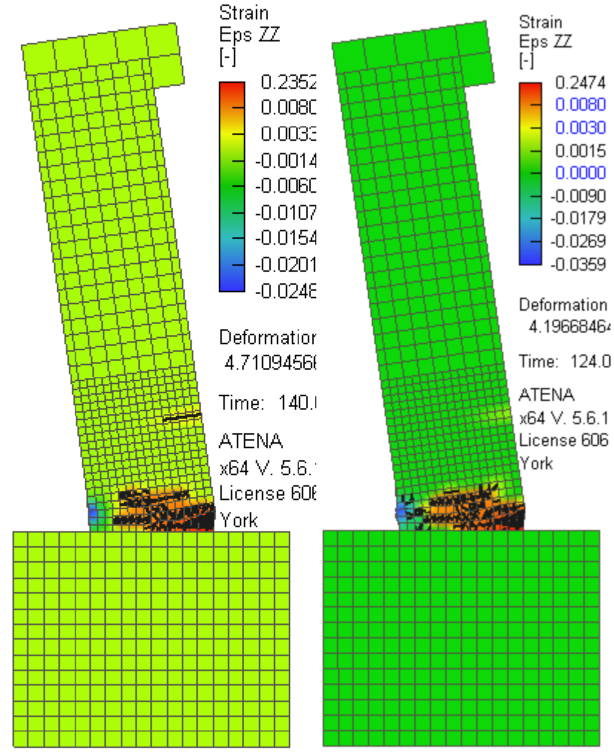

4.12d: ρ_l= 0.81%, *v*=10%

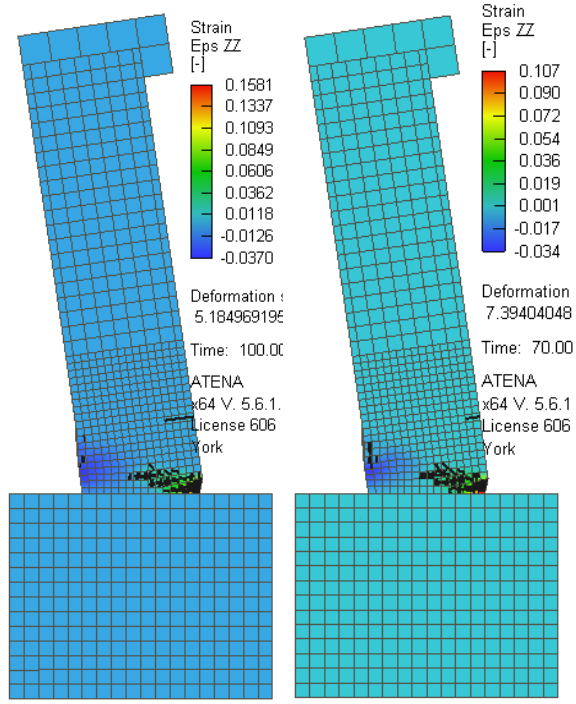

4.12e: ρ_l= 0.81%, *v*=35%

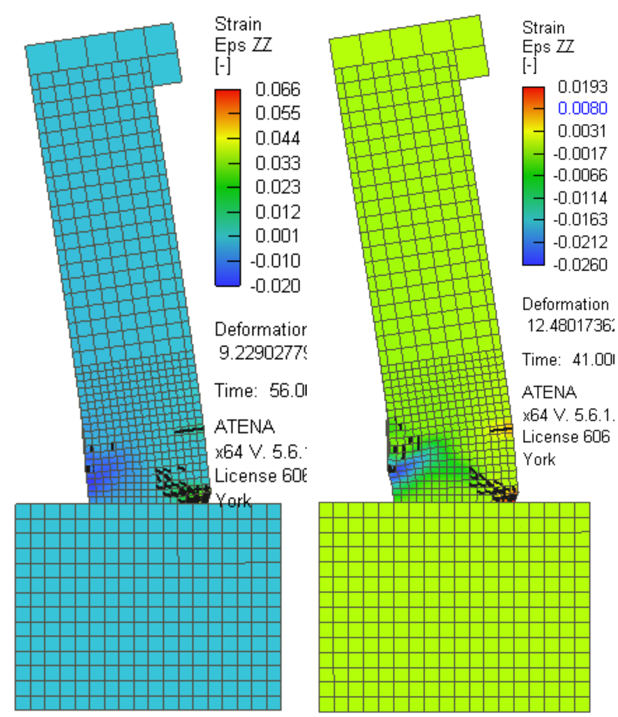

4.12f: ρ_l= 0.81%, *v*=50%

Figure 4.12: Mode of failures for column Set 5. Where *v* is the Axial Load Ratio of the Crushing Load and ρ_l is the Longitudinal Reinforcement Ratio

The results from the various benchmark cases described in the preceding sections are summarized in Table 4.3. Apart from the informative content, this table is meant to illustrate the complexity of the problem which explains the great range of responses that may be obtained from a simple structural component (a column cantilever) by altering the characteristic values of the important design variables. It also explains why the vast database of experimental results is not sufficient to lead to universally defined conclusions regarding the parametric relationship between drift capacity and strength.

Table 4.3: Summary of the Column's Mode of Failure

	100 mm Stirrup Spacing		200 mm Stirrup Spacing	
	4Φ18 bars per face	2Φ18 bars per face	4Φ18 bars per face	2Φ18 bars per face
Axial load Ratio	Failure Mode	Failure Mode	Failure Mode	Failure mode
Case 1 (Full Anchorage in Foundation with 90-Degree Hook)				
10	Flexure, Bond Splitting	Bond Splitting, Flexure	Bond Splitting, Shear	Bond Splitting, Flexure
35	Shear, Concrete Crushing, Buckling	Flexure, Concrete Crushing, Buckling	Shear, Concrete Crushing, Buckling	Flexure, Buckling, Concrete crushing
50	Concrete Crushing, Shear, Buckling	Concrete Crushing, Flexure, Buckling	Concrete Crushing, Buckling, Shear	Concrete Crushing, Buckling
Case 2 (Lapped Splice)				
10	Bond Pullout, Bond Splitting	Flexure, Bond Pullout, Bond Splitting	Bond Pullout, Bond Splitting	Flexure, Bond Pullout, Bond Splitting
35	Shear, Bond Pullout, Concrete Crushing	Bond Pullout, Concrete Crushing	Shear, Bond Pullout, Concrete Crushing	Bond Pullout, Concrete Crushing
50	Buckling, Concrete Crushing	Flexure, Concrete Crushing	Concrete Crushing	Concrete Crushing
Case 3 (Short Anchorage Length)				
10	Bond Pullout	Bond Splitting	Bond Pullout	Bond Pullout
35	Bond Pullout, Shear, Concrete Crushing	Flexure, Concrete Crushing, Buckling	Bond Pullout, Shear, Concrete Crushing	Flexure, Buckling, Concrete crushing
50	Shear, Concrete Crushing, Buckling	Concrete Crushing, Flexure, Buckling	Shear, Concrete Crushing, Buckling	Concrete Crushing, Buckling
Case 4 (Deep Cross Section)				
10	Shear, Bond Splitting	Flexure, Bond Splitting	Bond Splitting, Shear	Flexure, Bond Splitting
35	Shear Failure, Buckling, Concrete Crushing	Flexure, Concrete Crushing, Buckling	Shear Failure, Buckling, Concrete Crushing	Flexure Concrete Crushing, Buckling
50	Concrete Crushing, Shear, Buckling	Buckling, Concrete Crushing	Concrete Crushing, Shear, Buckling	Buckling, Concrete Crushing
Case 5 (Hinge Connection to the Foundation Base)				
10	Bond Pullout	Bond Pullout	Bond Pull out	Bond Pullout
35	Concrete Crushing, Bond Splitting	Concrete Crushing, Bond Splitting	Concrete Crushing, Bond Splitting	Concrete Crushing, Bond Splitting
50	Concrete Crushing, Bond Splitting	Concrete Crushing, Bond Splitting	Concrete Crushing, Bond Splitting	Concrete Crushing, Bond Splitting

4.3 Bond Failure

Table 4.4 displays the type of bond failure for columns subjected to low axial load, the code based predicted failure, the required and available developed length of the columns.

The type of bond failure can be determined by the value of the confinement term $(c_b+K_{tr})/d_b$ according to the ACI 318M. If this confinement term is more than 2.5, the failure is bond pullout. For Benchmark Cases 1 and 4 the effective calculated development length is l_d = 1500+700+300= 2500 mm (l_d= Shear span length + embedment length+ hook length) and the type of failure was by bond splitting. For Case 3, failure occurred by bond pullout, and the effective length was l_d = 1500+270= 1770 (l_d= Shear span length + embedment length). According to the ACI 318M, the confinement term is in the range of 2.5-3.45 for all sections. Using the confinement term individually, disregarding the difference between the required and effective development length, it is anticipated that the columns should all fail due to pullout failure, which was not the reported failure type in Case 1 and 4. When calculating the required bond length according to Eq.4.3, it is found that the code requires a length of 395.5 mm for reinforcement in tension for all cases when the confinement factors are limited to 2.5. As shown in Table 4.4, the available bond length is significantly smaller than the required for all cases. The code significantly underestimates the required bond length as shown in Table 4.4 when the confinement term is less than 3 with high longitudinal reinforcement ratio, which leads to eliminating the pullout failure in Column Case 3. To provide more accurate estimates for the required development length, the confinement factor should be 1, and the development length should be multiplied by a factor between 1-1.5.

$$[4.3] \quad l_{dt} = \frac{f_y}{1.1\,\lambda f_c^{0.5}} \frac{\Psi_e \Psi_t \Psi_s}{\frac{c_b + K_{tr}}{d_b}} d_b$$

According to the ACI 408R-03, the confinement term $\frac{cw+K_{tr}}{d_b}$ should be limited to 4. For all sections the confinement term was less than 4 and the required development length should range around 550 mm for all sectional cases. This code was expected to provide more dependable values, however the underestimation of the development length is still present.

Based on the experimental study of Sokoli and Ghannoum (2016), only one column sustained bond failure. In the author’s experimental analysis, the effective development length was equal to 805 mm and the required bond length was 934 mm according to ACI 318M with the confinement factor $(c_b+K_{tr})/d_b$ limited to 2.5. The confinement term of the column's section was 3. The authors conclude that the code was successful in predicting that the column will sustain bond failure, as the available developed length was less than the required. Additionally, the authors suggested that the cap limit should be increased to a maximum of 3 to have a more accurate estimation of bond length required to sustain bond failure. Moreover, when applying the cap limit of 3 instead of 2.5, the code prediction of the type of bond failure was correct.

Table 4.4: Summary of Bond Predicted Failures

Column	$\frac{(c_b + K_{tr})}{d_b}$	$l_{d,required}$/ According to ACI 318M (mm)	$\frac{(cw + K_{tr})}{d_b}$	$l_{d,required}$/ According to ACI 408R-03 (mm)	$l_{d,available}$ (mm)	Code Predicted Bond failure Type	Actual Bond Failure Type
Column Case 1 and 4							
C10-1-10	2.89	395.8	2.30	486.2	2500	Splitting	Splitting
C10-2-10	3.45		2.69	416.3		Splitting	Splitting
C10-1-20	2.61		2.17	515.6		Splitting	Splitting
C10-2-20	2.89		2.30	486.2		Splitting	Splitting
Column Case 3							
C10-1-10	2.89	395.8	2.30	486.2	1770	Splitting	Pull out
C10-2-10	3.45		2.69	416.3		Splitting	Splitting
C10-1-20	2.61		2.17	515.6		Splitting	Pull out
C10-2-20	2.89		2.30	486.2		Splitting	Splitting

Moreover, the required available length from the two codes do not include the effect of axial load. As concluded from section 4.2 the axial load plays a crucial role in determining whether bond failure (Splitting or Pullout) will occur or not. For Example, as shown in column C10-1-10, for case 2, the column failed due to pullout at low axial load. For the same column section geometry, when increasing the axial load, the pullout failure is not present anymore. Thus, in those cases the required developed length may be decreased with consideration of the confining term in the development length calculations.

4.4 Column's Correlation to Analytical Deformation Capacity at Shear Failure

This section will present a comparisons between the deformation capacities from Table 4.1 and the two analytical models for Elwood (2004) and Pujol (1996) for deformation capacities at shear failure.

4.4.1 Elwood 2004 Model

The rotations calculated from Elwood 2004 is plotted against the rotations at ultimate displacements from Table 4.1 as shown in Figure 4.13. It is found that Elwood (2004) model is insensitive to the reinforcement ratios. Columns with low and high reinforcement ratio showed similar results, whereas the database showed minor difference in the value of the deformation capacity due to the difference in confinement models applied to the columns. The effect of the axial load was negligible according with Elwood's Model. Increasing the axial from 0.1 to 0.35 decreases the rotations from 0.0359 to 0.0357, however, the rotations from the benchmark models changed from 0.025 to 0.016 for column C10-1-20 For case 1. The correlations were closer to columns with low axial load. The equation shows best sensitivty when changing the transverse reinforcement ratio.

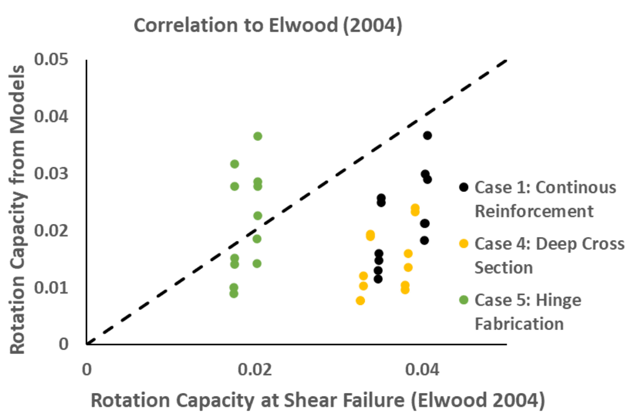

Figure 4.13: Elwood (2004) Correlations

4.4.2 Pujol 1996

Figure 4.14 presents the correlation between the column deformation capacity from the column database and Pujol 1996 model.

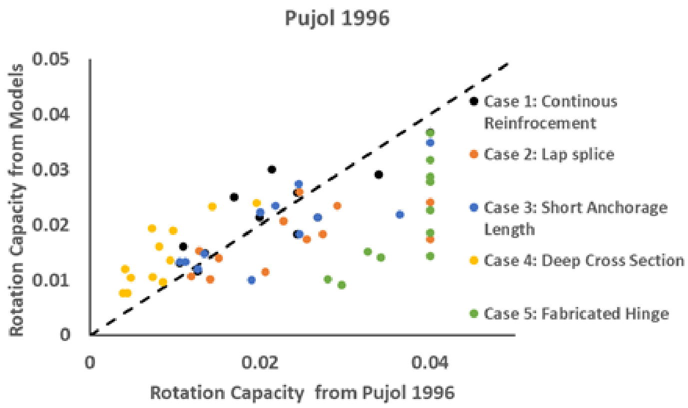

Figure 4.14: Pujol (1996) Correlation

Better correlation to this model was found. The axial load effect was reflected in the calculation of v_{max} (the stress at shear failure) in Pujol (1996) model, which was was taken at 0.8% of the maximum lateral load resistance from the benchmark columns. The model underestimates the deformation capacities of columns with sparse stirrup spacing compared to the deformation capacities from the benchmark columns. Also overestimated are the deformation capacities for the cases of lap splice and short anchorage length at low axial load for continuous reinforcement. The high slip effect at low axial load which leads to a reduction in the deformation capacities as concluded from the models was not reflected correctly. The difference deceased with the increase in the aspect ratio. For example, the deep cross section showed less correlation to the model. The model shows constant values with high shear spans, because it limits the deformation capacities to a maximum limit of 4.

5. Full Scale Columns

Columns in Chapter 4 were modelled as cantilever columns, simulating the majority of the column tests in the experimental literature, which have been tested as cantilevers having a length equal to half the length of a full swaying column, and subjected to combined axial and lateral forces. Only recently has the experimental literature been enhanced with full column tests under swaying loads. Note that the cantilever test has been used extensively in the literature on account of its relative versatility as compared with the full-length column tests. On the question of how relevant is the cantilever column test in understanding the lateral load behavior of laterally swaying columns the answer is that they are statically equivalent, and therefore they must be identical. Static equivalence refers to the fact that constant shear force occurs over the shear span in both cases, leading to a linear variation of moment, with zero value at the midheight of the storey for the full-length column, or the tip of the cantilever for the half model, and a maximum moment occurring at the base, as illustrated in Figure 5.1. There is similarity also in terms of drift ratios: for a storey relative displacement of Δ, the midheight experiences a lateral displacement of Δ/2, and the drift ratio for full column and cantilever is actually the same: $\theta = \frac{\Delta}{2L_s} = \frac{\Delta/2}{L_s}$

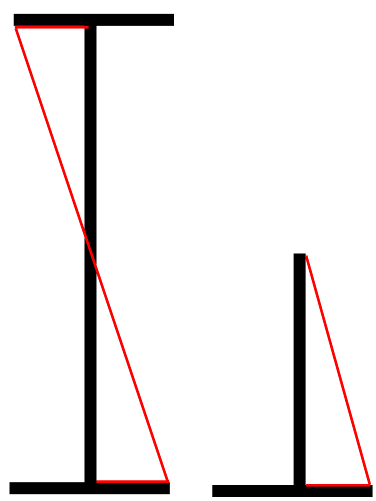

Figure 5.1: Moment Diagram for Full and Half Column

Despite the similarity from a global perspective, the detailing of reinforcement, which makes a notable difference on rotation capacity and contribution from bond slip in the lateral load resistance curve of a column is really not identical in the two cases: In general, in cantilever column specimens longitudinal is anchored either with significant amount of confinement and hooks, or directly welded on auxiliary steel plates that are used for load application during the tests, whereas in the case of the full column, reinforcement is usually straight and continuous at the column midheight. This Chapter will investigate the effect of these detailing differences on the response and resistance curve of columns. For this reason, the benchmark examples of the preceding chapters are modelled and analyzed here, as full-length swaying columns. To this end, two Cases are explored. In Case 1 continuous reinforcement throughout the bottom foundation and top beam have been used, whereas in Case 2 reinforcement is continuously anchored in the cap beam, but lap-splices at the bottom critical section of the column. Results obtained are compared with those from the cantilever model analyses in Chapter 4.

5.1 Boundary Conditions, Loading and Mesh

In the Finite Element model, boundary conditions are a point of major difference between the cantilever and the full-length column. The cantilever column is connected to a foundation with its bottom surface fixed from translation and rotation in all directions whereas the tip of the cantilever is free to grow longitudinally accumulating nonlinear length change due to cracking. On the other hand, a full-length column in a portal frame is partially restrained at the top – due to diaphragm action the top translation is slaved to the displacement of the diaphragm, whereas rotation is controlled by the relative stiffness of beams and columns converging to the beam column connection. Pantazopoulou (2003) suggested that the applied lateral load at the free end of the cantilever may result in a larger pullout failure relative to real columns. Second order effects that are related to the manner of load application in the cantilever examples further complicate the modelled boundary conditions, as this effect need to be modeled accurately for the sake of comparison of the results between identical examples in full-length and cantilever column models.

To study the differences in the two column cases resulting from the different reinforcing detailing as well as different boundary conditions, models for full-length columns were assembled having similar geometry and material models for reinforcement and concrete (concrete core and cover) to otherwise identical cantilever columns considered in Chapter 4. Modelling and Analysis was done using the ATENA 3D Engineering interface. The deformable length of the full-length column models was taken equal to 3.0m (i.e., double the length of the cantilever model). The boundary conditions of the full-length column at the base were identical to those of the cantilever model. At the top of the full-length column, at a height of 3.0 m, a cap beam was modelled with the same dimension and reinforcement in the foundation. The longitudinal reinforcement was extended into the beam using a 90 degree hook anchorage similar to that occurring at the base for the first column set. The same reinforcement connection was used at the top for the second column case, however using a lap splice at the critical section at the lower end of the column, similar to that used in second benchmark case in Chapter 4; the intention here was to evaluate how this rather frequent detail in older construction, which cancels the symmetry of the full-length column, affected the relevance of the cantilever column tests in interpreting the response of actual swaying columns.

For both cases of different longitudinal reinforcement detailing at the top and bottom, i.e., continuous and lap spliced, two different sections were modelled with different longitudinal reinforcement ratios. One section had longitudinal reinforcement of 4Φ18mm per face, whereas the second section had longitudinal reinforcement of 2Φ18mm as shown in Figure 3.2 in Chapter 3. Two different axial load ratios were applied to the full column model: 10% and 35% of the crushing load $\left(\frac{P}{A_g f_c}\right)$. Cantilever columns with 50% axial load were excluded from the full scale column analysis due to the limited response founded in columns with high axial loads (Concrete crushing). A total of 16 full-length benchmark columns were considered.

Difficulties were encountered in replicating the restraints of the bottom surface of the foundation at the top surface of the cap beam. In order to maintain symmetrical boundary conditions at the top and bottom, rotations of the cap beam should be restrained, so as to model the swaying column of a shear-type building. To achieve such condition, the nodes on the top surface of the beam should displace laterally while at the same time restraining them to displace as a rigid diaphragm vertically. The ATENA 3D Engineering interface does not permit this type of condition through the node master-slave option. This condition was enforced manually by typing the following syntax at each analytical step. This was recommended by the software providers (Cervenka Consultancy):

```
SUPPORT COMPLEX MASTER node  1 dof 3 * 1.0 SLAVE node 2 dof 3 VALUE 0.0
SUPPORT COMPLEX MASTER node  1 dof 3 * 1.0 SLAVE node 3 dof 3 VALUE 0.0
SUPPORT COMPLEX MASTER node  1 dof 3 * 1.0 SLAVE node 4 dof 3 VALUE 0.0
…..
```

SUPPORT COMPLEX MASTER node 1 dof 3 * 1.0 SLAVE node XX dof 3 VALUE 0.0

This syntax forces all displacements in the z direction in nodes 2, 3, 4 … XX to be same as in node 1.

The axial load was applied in the first analytical step on the top surface of the cap beam. The axial load was followed by steps of 0.4 mm lateral displacement applied manually on each node on the top surface of the cap beam.

The mesh size for the top part of the full column was the same as that of the cantilever column. The first 0.5 m of the column (measuring from the critical section at the base) was discretized to a 0.025 m hexahedral mesh size. The column height from 0.5 to 2.5 m was discretized to 0.05 m hexahedral elements and the last half meter of the column length (measuring from the critical section at the top) was also discretized to 0.025 m mesh elements.

5.2 Deformation and Strength Capacities

The deformation capacities and the shear base of the 16 full columns are depicted in Table 5.1. Benchmark example identification has been defined in Section 3.1 of Chapter 3. The calculated lateral load resistance curves for the full-length columns were plotted together with the load resistance curves of their cantilever counterparts in Figures 5.2 and 5.3(a) and (b). The full-length columns are represented by a dashed curve while the cantilever case is represented in the continuous curve of the same color – the color code identifies different pairs of cases (differentiated from each other based on the section type used and the axial load ratio). Second order P-Δ effects were eliminated from the curves to provide an objective comparison of resistances.

Table 5.1: Displacement at Yield and Ultimate and Base Shear Strength of the Full-length Column Models

Column ID	Base Shear Strength (kN)	Yield Displacement (mm)	Ultimate Displacement (mm)
Column Case 1: Columns with Full Anchored Reinforcement			
C10-1-10	154.03	17.5	66.0
C35-1-10	241.12	19.1	77.0
C10-2-10	106.90	13.5	48.5
C35-2-10	195.01	15.2	64.0
C10-1-20	153.60	17.5	53.0
C35-1-20	238.80	19.0	43.1
C10-2-20	106.64	13.2	48.2
C35-2-20	193.71	14.8	40.8
Column Case 2: Columns with Lap Splice at the Lower Critical Section of the Column			
C10-1-10	149.88	17.7	41.2
C35-1-10	233.98	17.8	60.0
C10-2-10	104.64	13.4	48.0
C35-2-10	190.76	14.5	60.0
C10-1-20	148.30	16.8	46.5
C35-1-20	229.71	17.4	40.0
C10-2-20	101.56	14.0	32.0
C35-2-20	188.50	14.1	38.0

The yield displacement is defined using the ASCE SEI 41/17 procedures described in Chapter 4. The ultimate displacement was identified at the post-peak response curve at 20% strength loss (with reference to peak value).

It was found that the lateral resisting load for the full-length column provides the exact lateral resisting load of the cantilever with identical properties, for the group of columns in Case 1 (continuous reinforcement at top and bottom). Negligible difference in the lateral load resistance was found in the cantilever case. However, the deformation capacities of the full-length and cantilever pairs show differences especially in the case of low axial load. Significant differences in all the characteristics of the response curves obtained for full-length and cantilever columns with lapped reinforcement at the base were found (strength and deformation capacity). These differences are discussed in Sections 5.3 and 5.4.

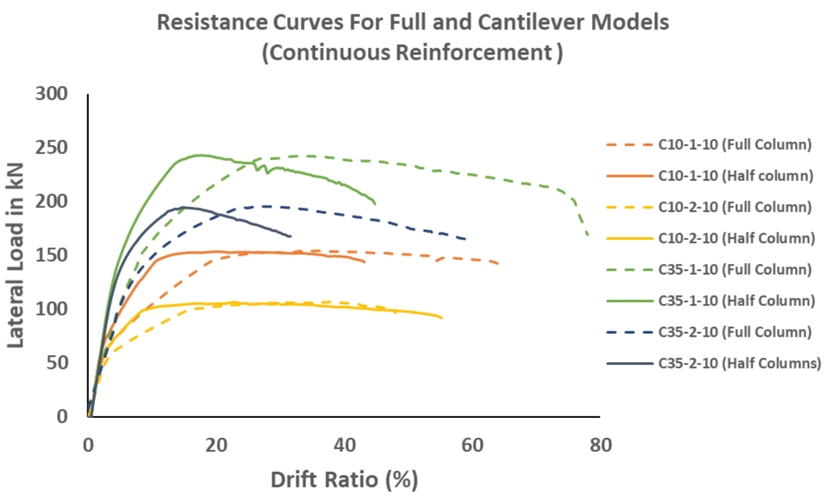

5.2(a)

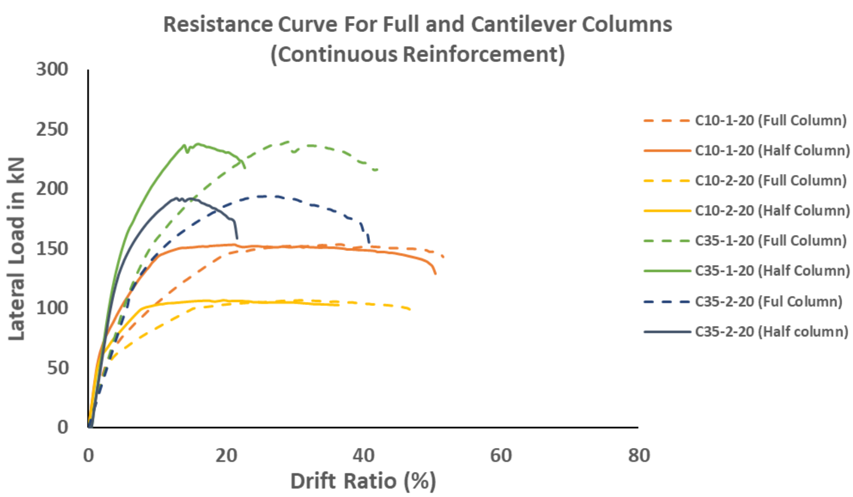

5.2(b)

Figure 5.2: Resistance Curves for Full-length and Cantilever Columns for the Continuous Reinforcement Case. (a) Columns with 100 mm Stirrup Spacing. (b) Columns with 200 mm Spacing

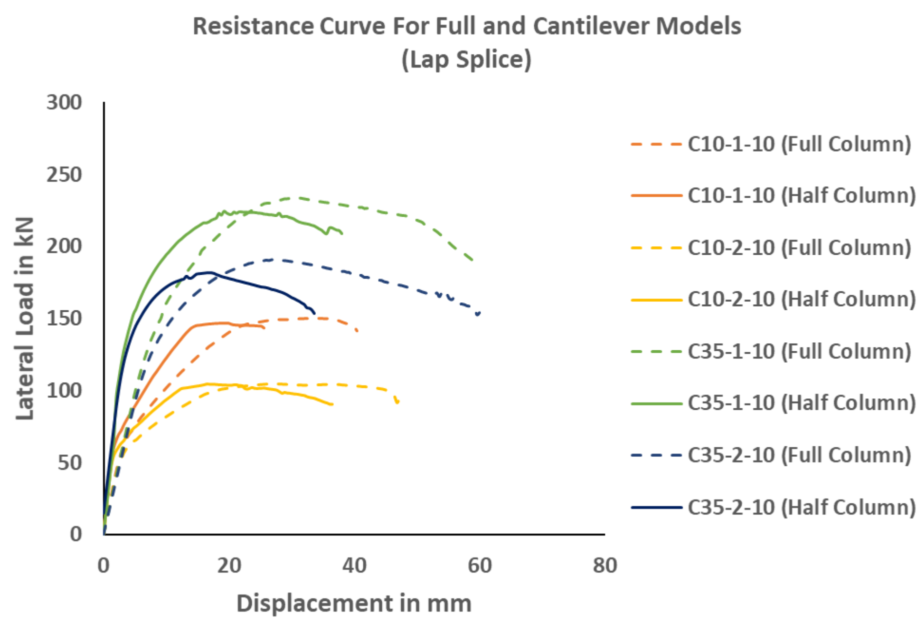

5.3(a)

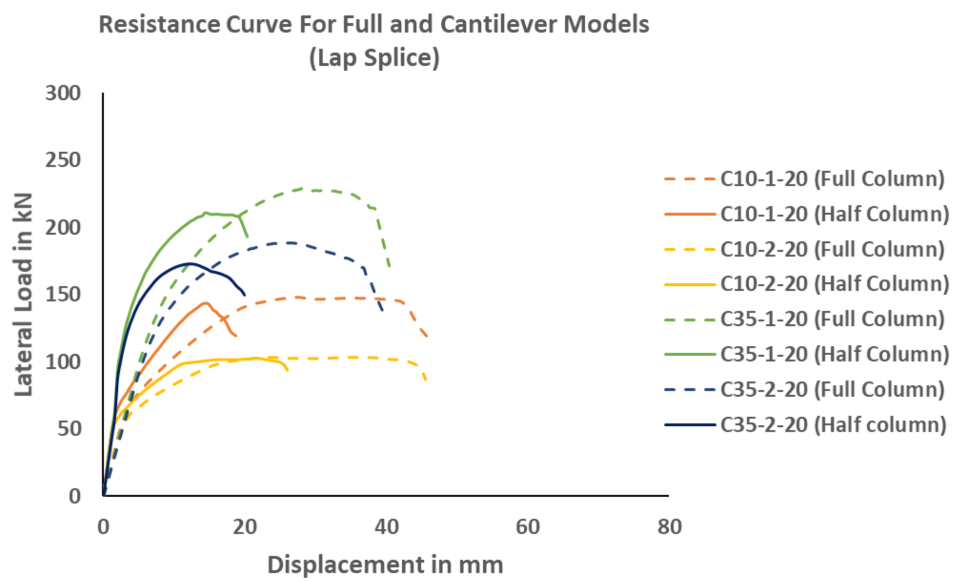

5.3(b)

Figure 5.3 : Resistance Curves for Full-length and Cantilever Columns for Lap Spliced Case. (a) Columns with 100 mm stirrup Spacing. (b) Columns with 200 mm Stirrup Spacing

5.3 Modes of failure

In this section the modes of failure for both column cases are investigated and comparisons are made for each benchmark pair (full-length and cantilever) with otherwise identical characteristics.

5.3.1 Case 1 : Continuous Reinforcement

From Figure 5.2 and 5.3 it was found that all columns have the same behavior up to the yielding point. The yield displacement of the full-length column was equal to double the displacement of the cantilever column. Therefore, the mechanistic assumption of the cantilever column representing the full-length column was valid up to yielding.

5.3.1.1 Section 1: 4Φ18 per face – ρ_l= 1.62%

With an axial load of 10% of crushing $\left(\frac{P}{f_c A_g}\right)$, with good confinement, the longitudinal reinforcement yields at a drift ratio of 0.63%. No yielding of the transverse reinforcement occurred at the bottom critical section, however, the 5th transverse reinforcement counting form the top critical section yields at a displacement of 1.21%. No other transverse yielding reinforcement is present in this case. However, the full scale column exhibits higher bond slip demand at the top beam column connection occurred, compared to the bottom connection. For example, in Figure 5.4a, at the ultimate displacement for column the reinforcement slip at the top column span-beam connection reaches 0.41 mm while the bottom total slip equals to 0.2 mm leading the full column to fail due to pullout at the top after the slip in the reinforcement increases precipitously. With the poor confinement, at 10% axial loads, the longitudinal reinforcement yield at lateral drift ratio of 0.63% similar to the column with cell confined stirrups. The first transverse reinforcement yielding occurred at the bottom column connection at the 3rd stirrup counting from the column base at a lateral drift ratio of 0.65%. With the increase of the lateral displacement , the 3rd stirrup counting from the top connection between the column and foundation yields at a drift ratio of 0.75%. With increasing the lateral displacement, the splitting of the concrete cover from the longitudinal reinforcement extends to almost half the column's length at the top half of the column as shown in Figure 5.4b.

With the increase of the axial load to 35% of crushing the longitudinal reinforcement yielding at the top and the bottom occurs at a lateral drift ratio of 0.88% for both confinement cases. At a drift ratio of 1% the first yielding of the transverse reinforcement occurred at 5th stirrup counting form the bottom and top critical section for both confinement cases. With sparse stirrup spacing the yield in longitudinal reinforcement occurred at a lateral drift ratio of 0.86%. The yielding of the transverse occurred at a lateral drift ratio of 1% . The shear failure occurring at 35% axial load, suppressed the splitting failure resulting in similar resistance curves (with similar failure modes at the top and bottom) with marginal differences (also see Section 5.4). The crack pattern and the concrete strains at shear failure for the case of good confinement and poor confinement is shown in Figure 5.4c and 5.4d respectively.

5.3.1.2 Section 2: 2Φ18 per face – ρ_l= 0.81%

For the case of lightly reinforced column, with 10% axial load , higher reinforcement slip and strains are observed in the full column case compared to the cantilever column case due to strain penetration (See Section 5.4). Therefore, the full scale column in this case fails due to splitting at the top and bottom at the same displacement of the cantilever column. The longitudinal reinforcement yields at a drift ratio of 0.53% and 0.50% for the case of good and poor confinement respectively. Figure 5.4c and 5.4d depict the failure mode for lightly reinforced columns with stirrup spacing of 100 mm and 200 mm respectively. The crack pattern and strains in the concrete for the poor and well confined column at failure is shown in Figure in the longitudinal and transverse reinforcement 5.4e and 5.4f respectively.

With the increase of the axial loading to 35%, the shear failure accompanied with concrete crushing suppressed the reinforcement slip failure at the top. Therefore, the full and cantilever columns exhibited similar lateral degradation in the resistance load same lateral drift ratio. The longitudinal reinforcement yields at a lateral drift ratio of 0.785%. The longitudinal reinforcement strains at ultimate displacement are depicted in figure 5.4g and 5.4h respectively.

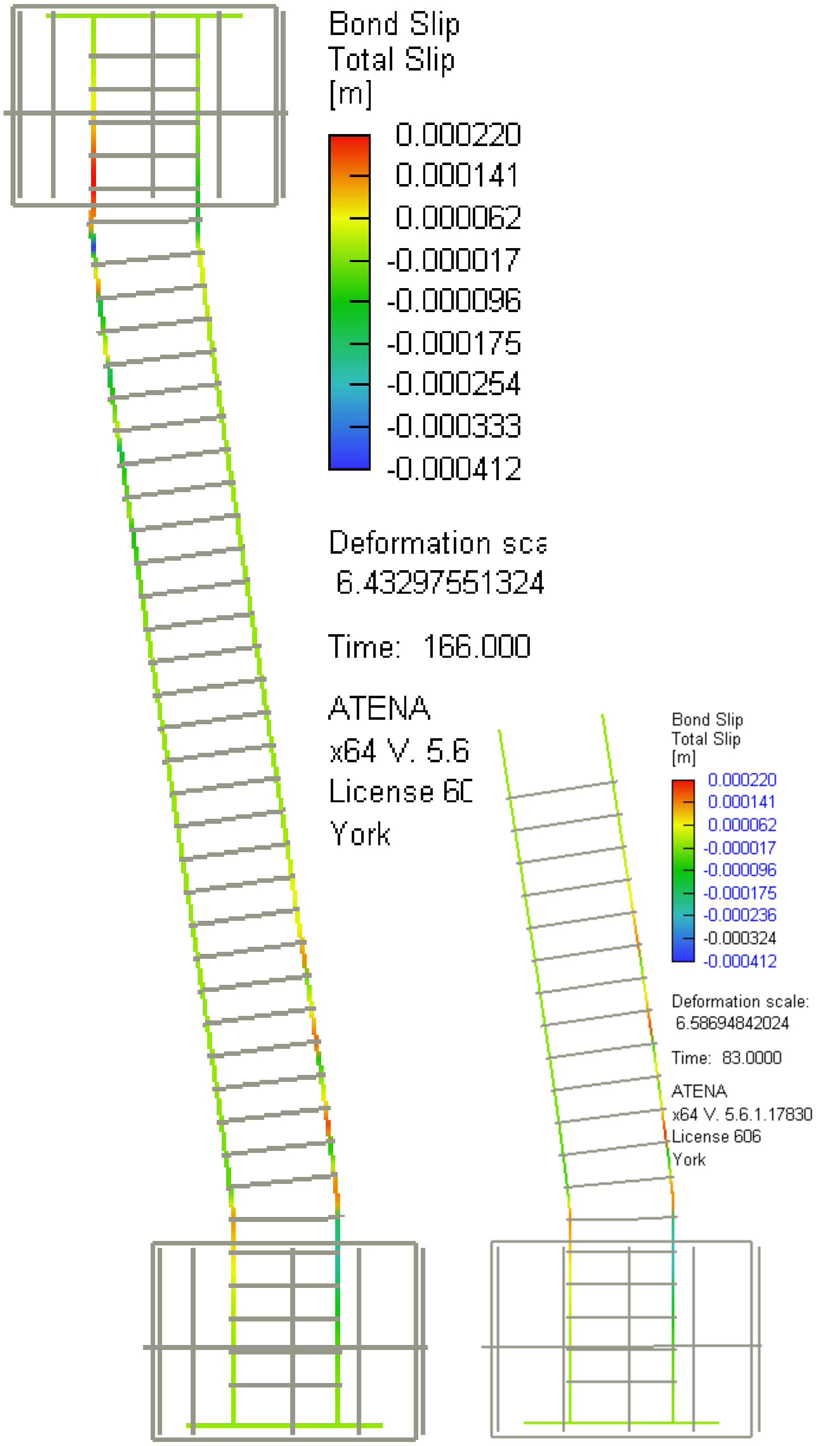

5.4a: C10-1-10. Total Bond Slip in the Reinforcement at Drift of 2.2%

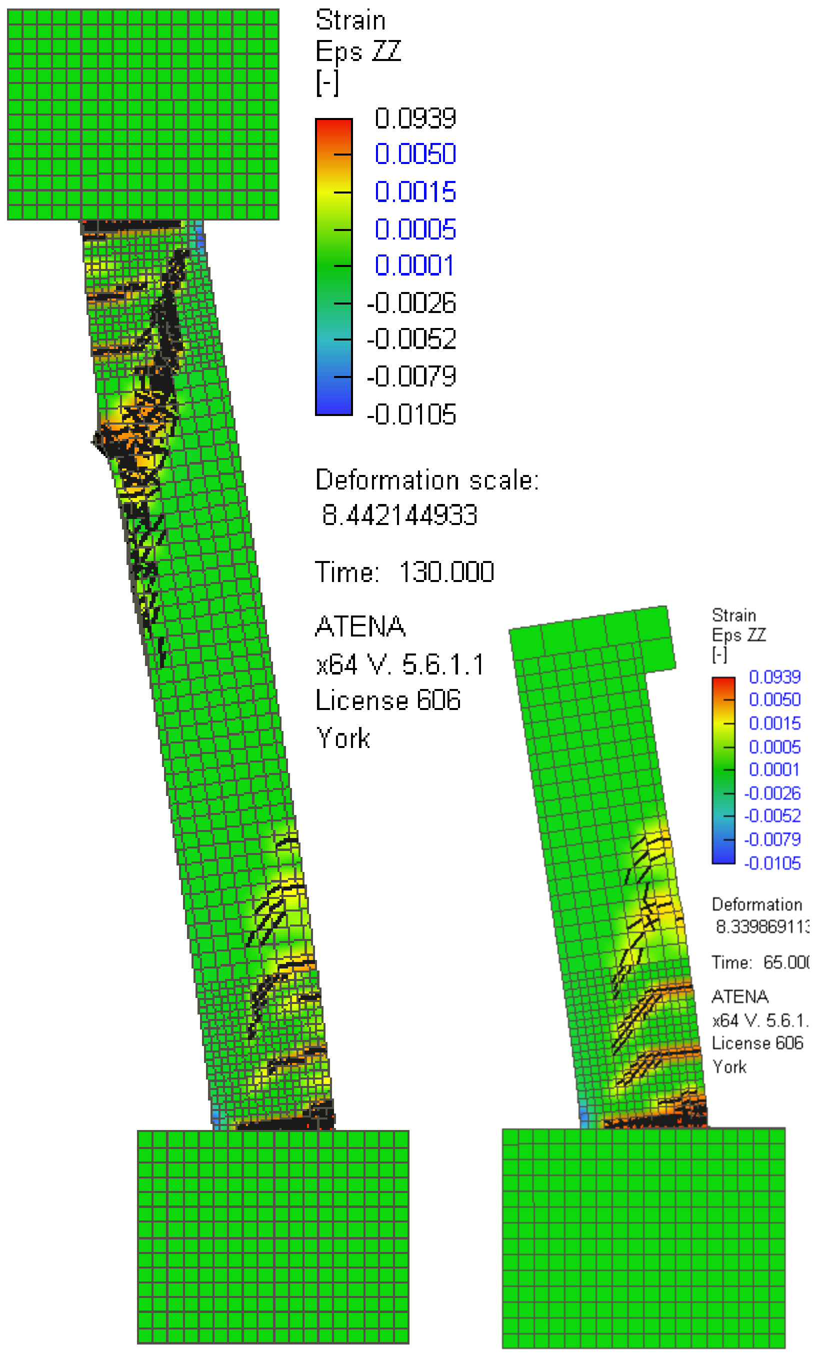

5.4b: C10-1-20: Crack Pattern and Concrete Strains
at Drift Ratio of 1.7%

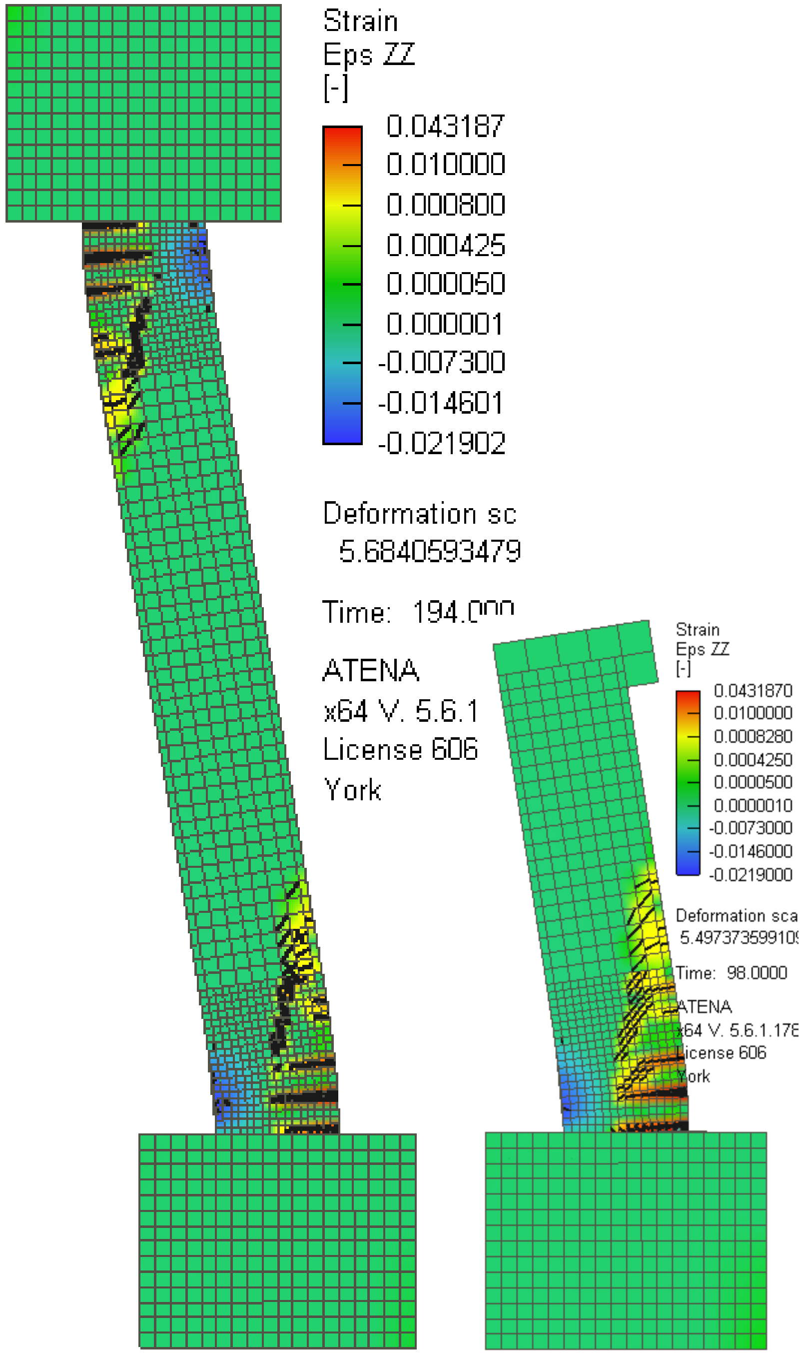

5.4c: C35-1-10: Concrete Strains and Crack Pattern at a Drift Ratio of 2.6 %

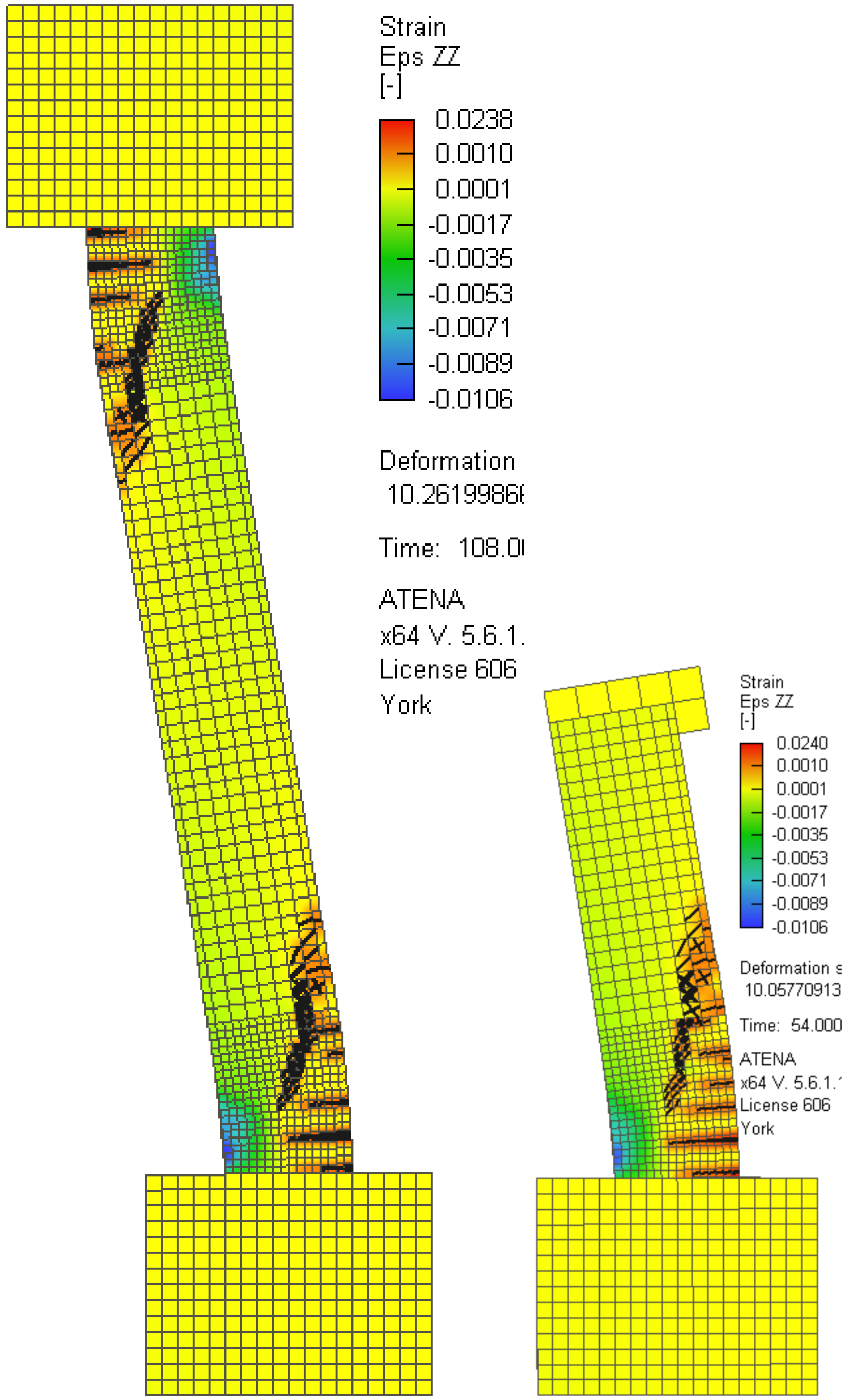

5.4d:C35-1-20: Concrete Strains and
Crack Pattern at a Drift Ratio of 1.43%

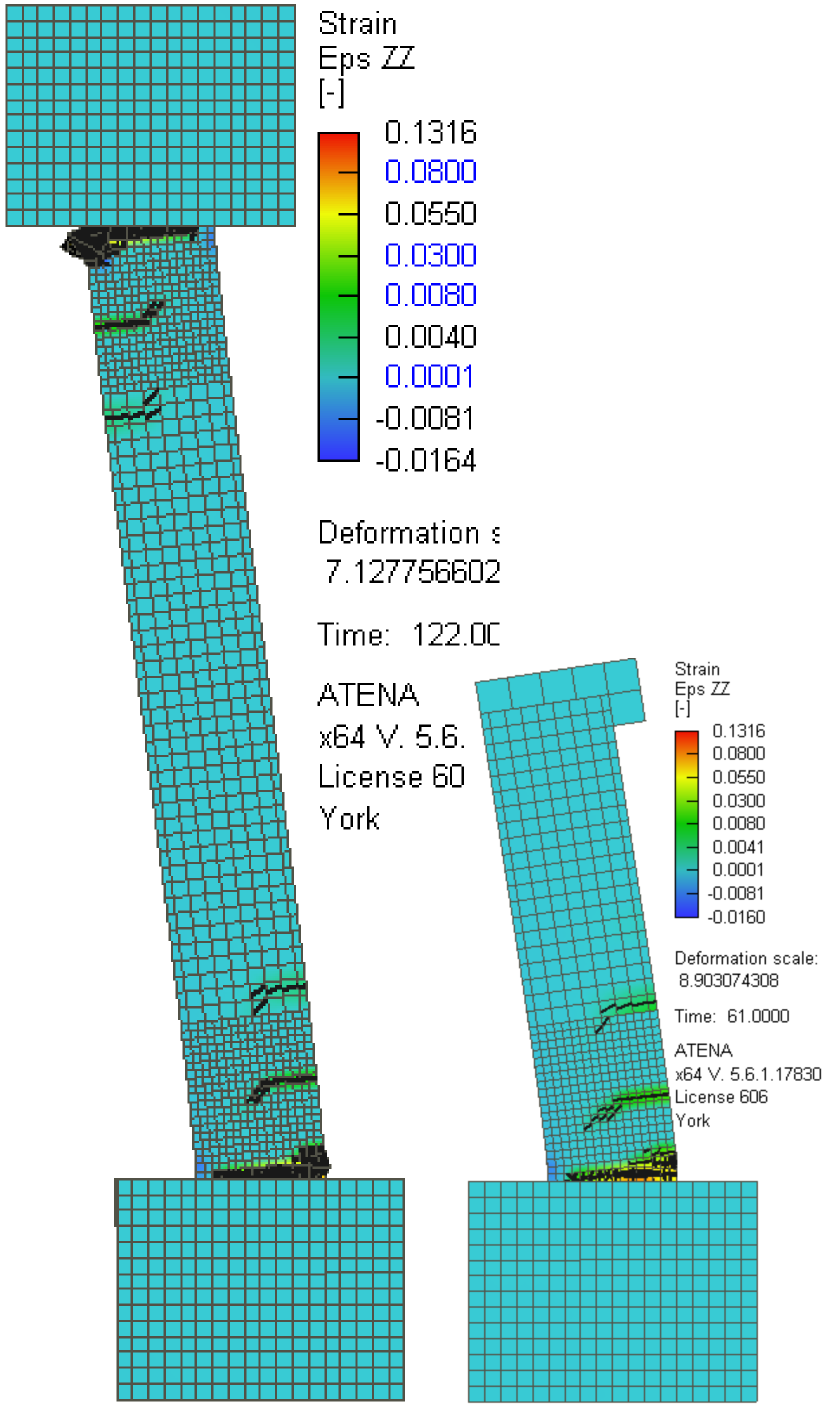

5.4e: C10-2-10: Concrete Strains and Crack Patterns at a Drift Ratio of 1.6%

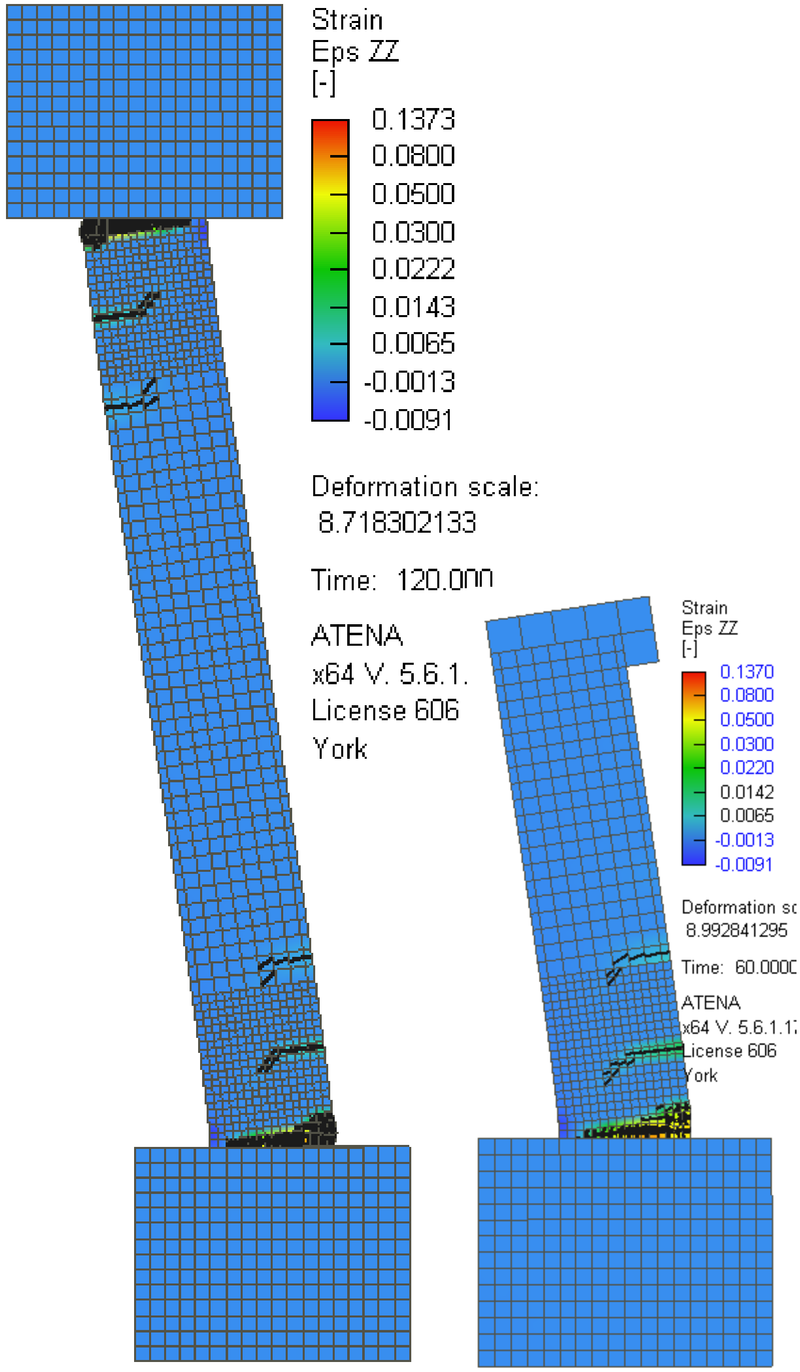

5.4f: C10-2-20: Concrete Strains and Crack Patterns at Drift Ratio of 1.58%

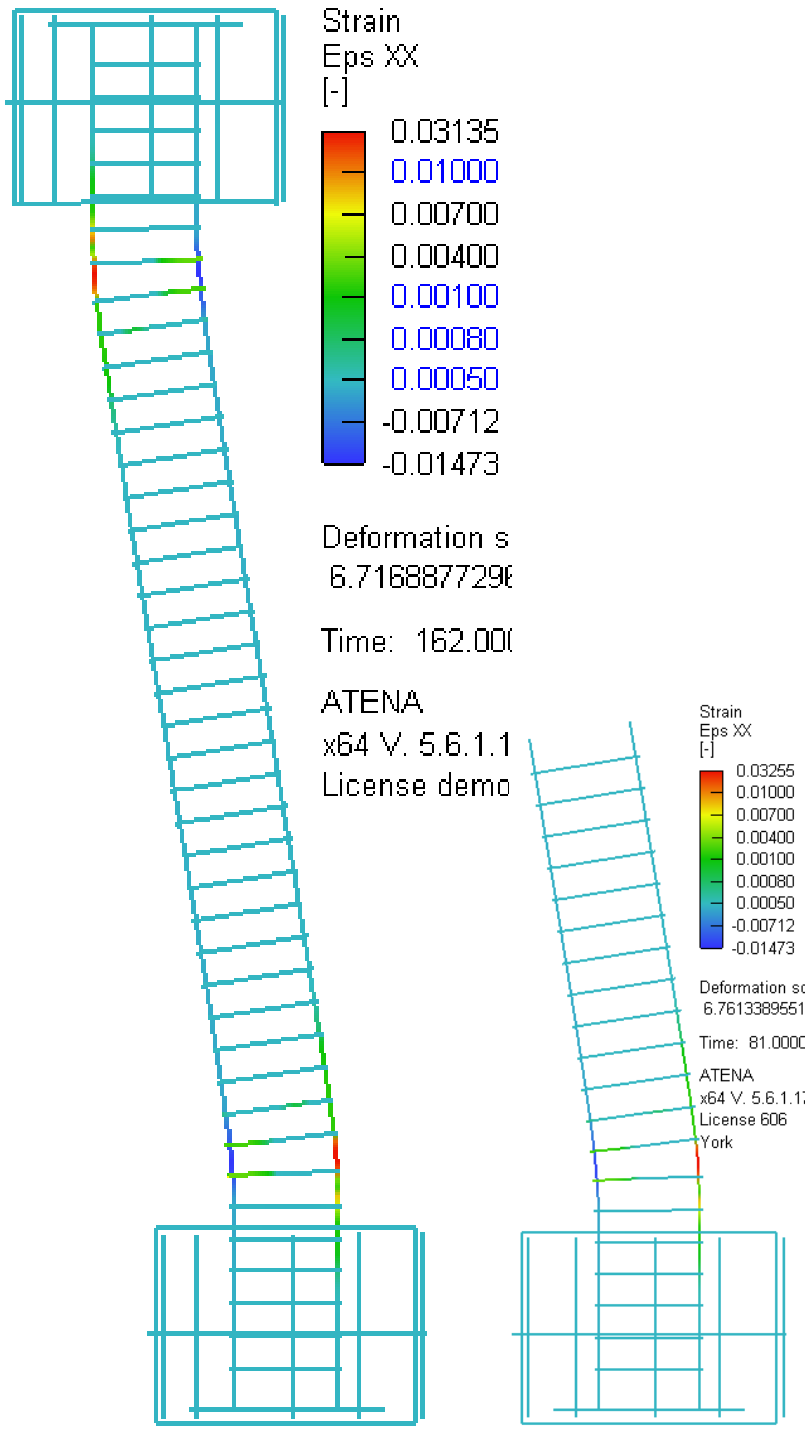

5.4g: C35-2-10: Strains in Longitudinal Reinforcement at Drift Ratio of 2.38%

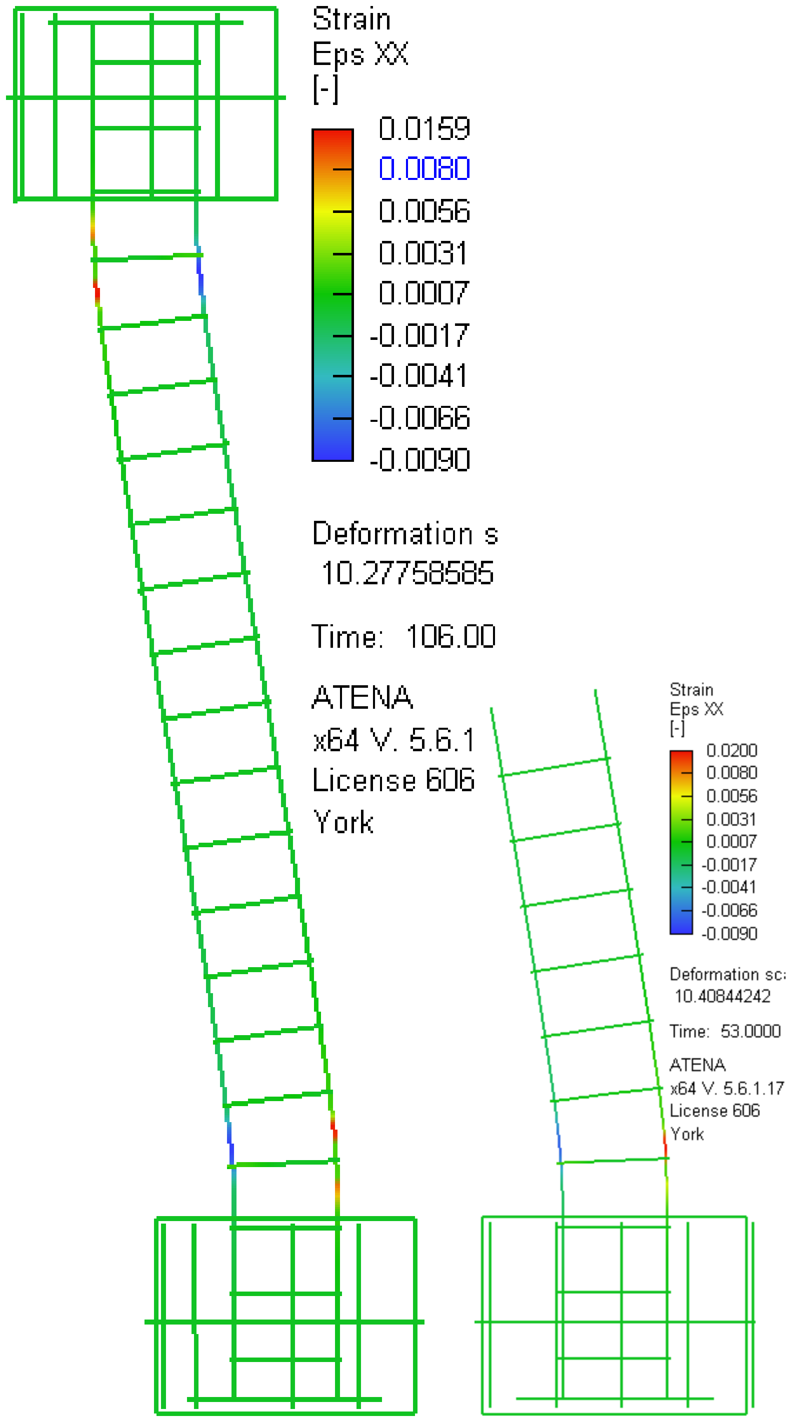

5.4h: C35-2-20: Strains in Longitudinal
Reinforcement at a Drift of 1.4%

Figure 5.4: Modes of failure in the Full Model with its Corresponding Cantilever Failure for column Case 1 (from a-h)

5.3.2 Case 2: Lap Splice

In the case of the lap splice, differences in the lateral drift ratio between the cantilever and the full column case were observed at yielding and ultimate.

5.3.2.1 Section 1: 4Φ18 per face – ρ_l= 1.62%

The yielding of the longitudinal reinforcement occurred at a lateral drift ratio of 0.718%. The lateral drift slip at longitudinal reinforcement yielding was 0.24%. The yielding of the longitudinal reinforcement at the top occurred approximately at the same lateral drift ratio. Transverse reinforcement yielding in the lapped region occurred at a lateral drift ratio of 1.23%, while no yielding was apparent in the transverse reinforcement at the top connection. With the increase of the lateral displacement, the column fails due to pull out failure. The differences in the drift ratio of reinforcement yielding in the case of the full and half column will be discussed in Section 5.4. With sparse stirrup spacing the pullout failure is occupied with shear failure at the top plastic hinge region. At the bottom, the stirrup yielding occurred in the lap region at a lateral drift ratio of 1.48%. The ability of the full column to develop higher strains in the longitudinal reinforcement relative to the cantilever column provides the full scale column with relatively higher ductility at ultimate. The crack pattern and concrete strains of column C10-1-10 and C10-1-20 are shown in Figure 5.5a and 5.5b respectively.

With increase of the axial load to 35% of crushing, the longitudinal reinforcement yields at a lateral drift ratio of 1% in both confinement cases. Shear failure initiates at the top at a lateral drift ratio of 0.904% in the case of good confinement and poor confinement. This limits the ultimate lateral drift ratio in the case of the full scale column to a value less than the drift ratio of the cantilever column. The first stirrup at the top column-beam connection yields at a lateral drift ratio of 1.6% in the case of good confinement and at a lateral drift ratio of 0.92% in the case of poor confinement. The crack pattern and the concrete strain for column C35-1-10 and C35-1-20 is shown in Figure 5.5c and 5.5d respectively.

5.3.2.2 Section 2: 2Φ18 per face – ρ_l= 0.81%

At an axial load of 10% of crushing, in the case of poor and good confinement the longitudinal reinforcement yields at a lateral drift ratio of 0.625% at the bottom plastic hinge region while the longitudinal reinforcement at the top yielded at a lateral drift ratio of 0.54%. The lateral drift ratio in the full column is limited to half the lateral drift ratio of the cantilever column due to splitting failure at the top plastic hinge region. Figure 5.5e and Figure 5.5f depict the crack pattern and the concrete strains in the columns C10-2-10 and C10-2-20 respectively.

With increasing the axial load to 35%, the longitudinal reinforcement yields at a lateral drift of 0.91% at the bottom plastic hinge region, while at the top, the longitudinal reinforcement yields at a lateral drift ratio of 0.81%. The transverse reinforcement yields in the lap splice region at a lateral drift ratio of 1.67%. The strains in the longitudinal reinforcement for columns C35-2-10 and C35-2-20 are shown in Figure 5.5g and 5.5h

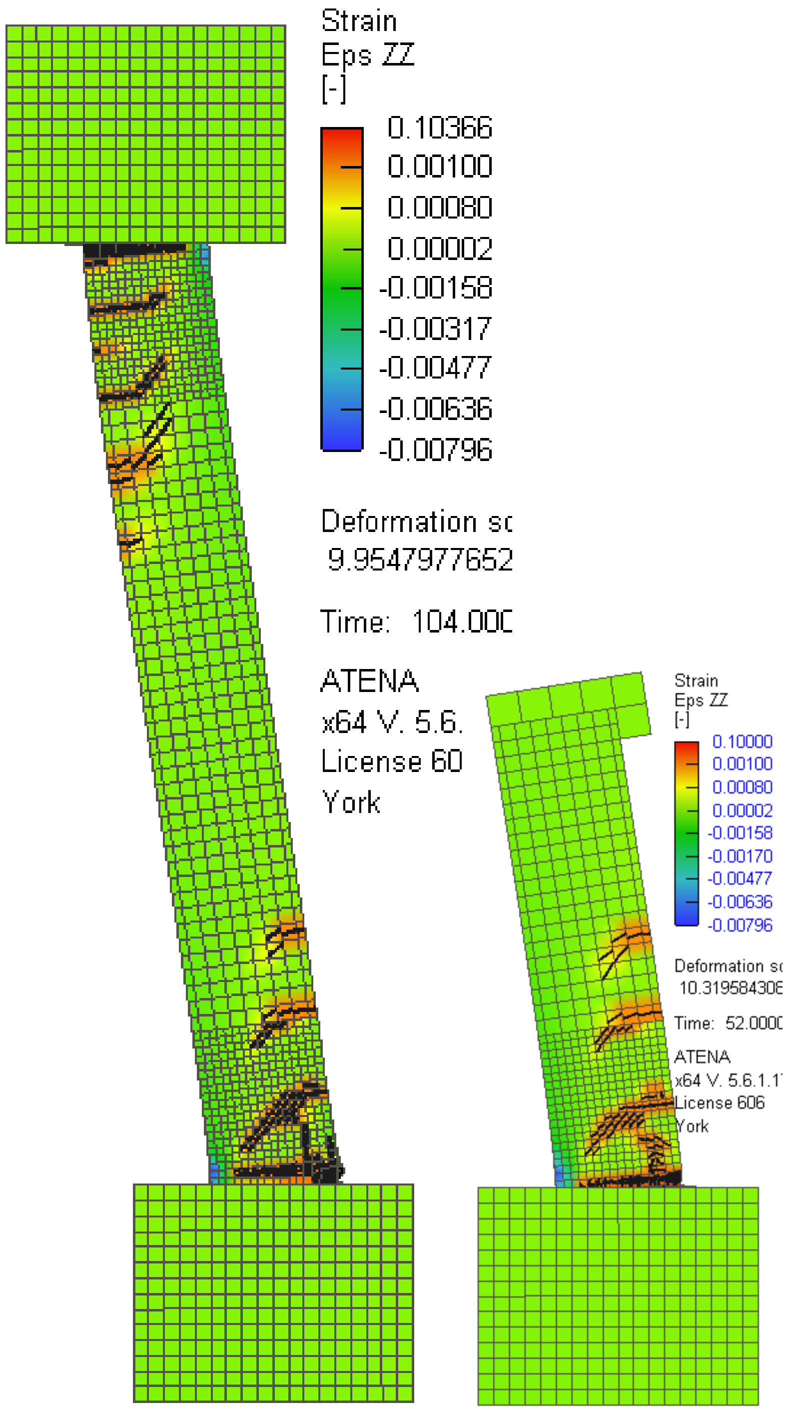

5.5a: C10-1-10: Concrete Strain and Crack Pattern at Drift Ratio of 1.3%

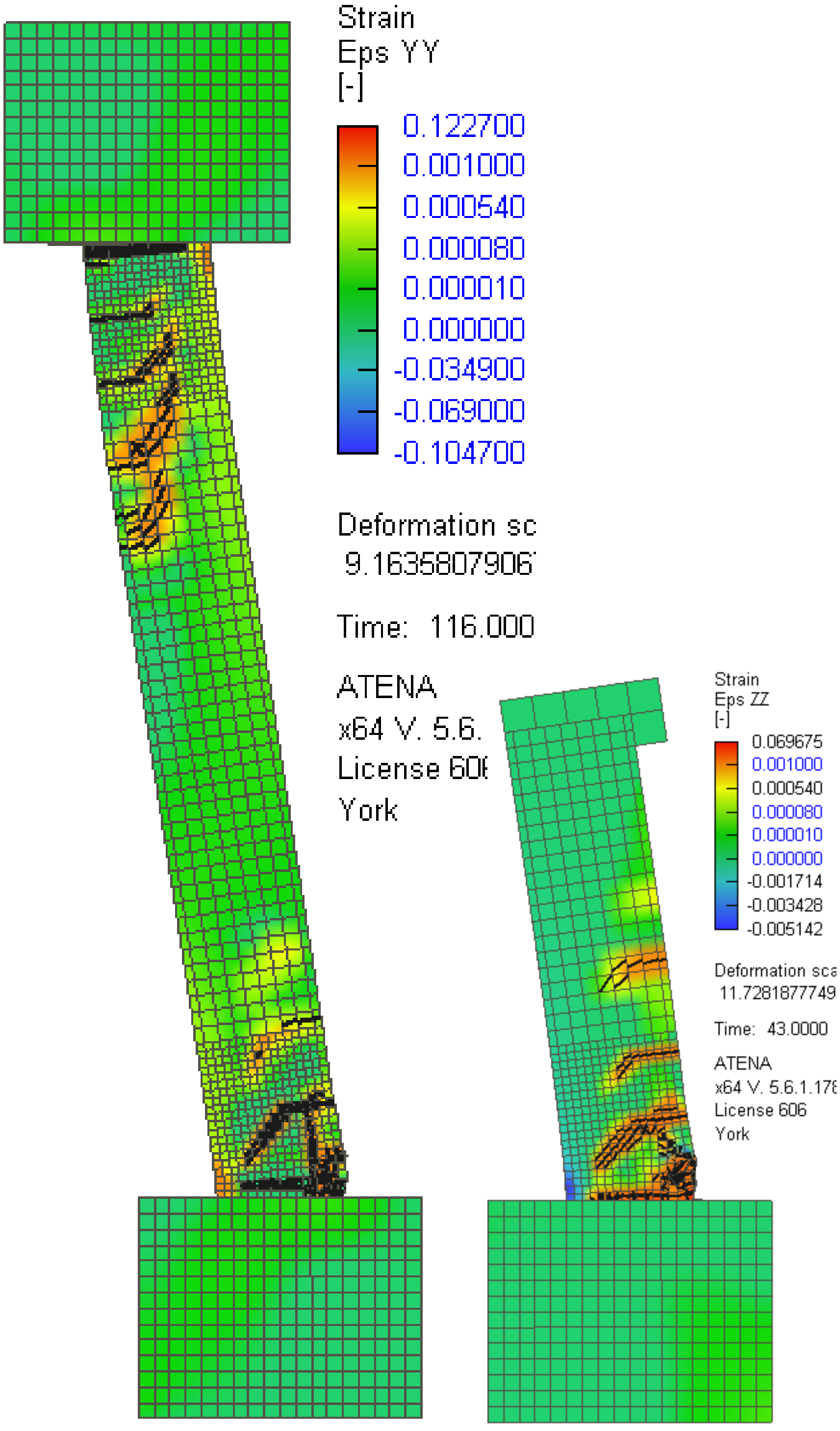

5.5b: C10-1-20: Concrete Strains and Crack Pattern at Drift Ratio of 1.43%

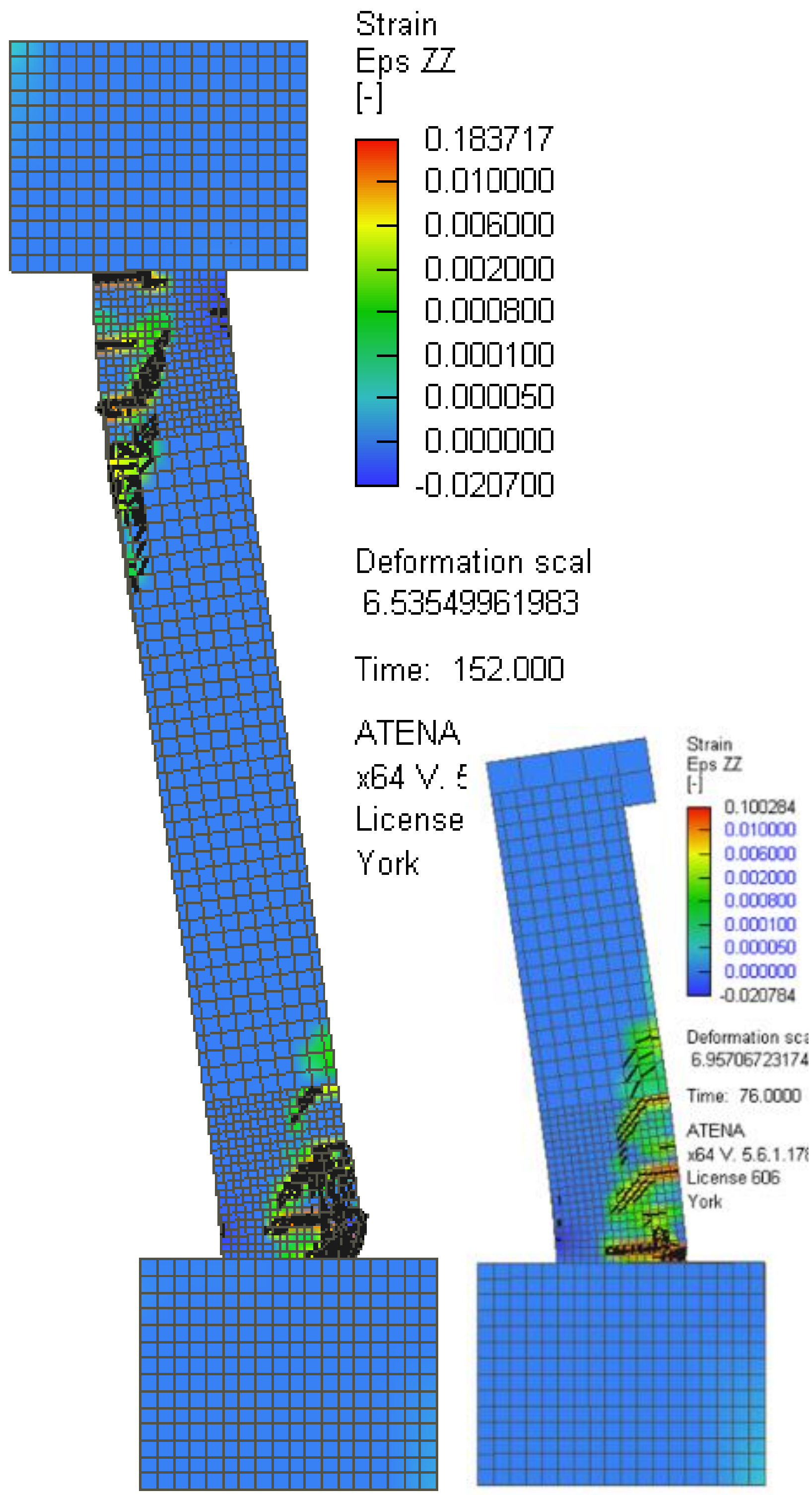

5.5c: C35-1-10: Crack Pattern and Concrete Strains at a Drift Ratio of 2.0%

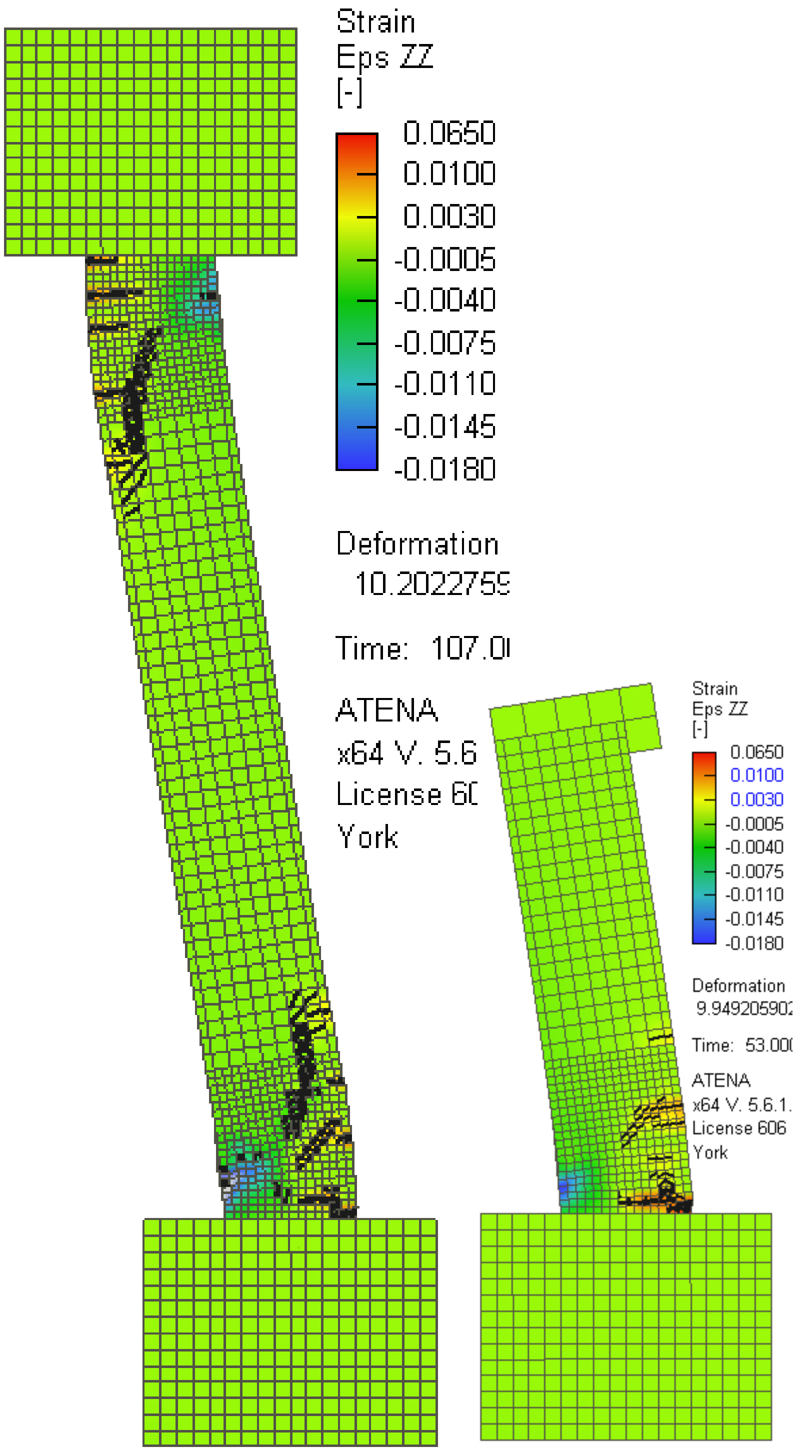

5.5d:C35-1-20: Concrete Strains and Crack
Pattern at Drift Ratio of 1.4%

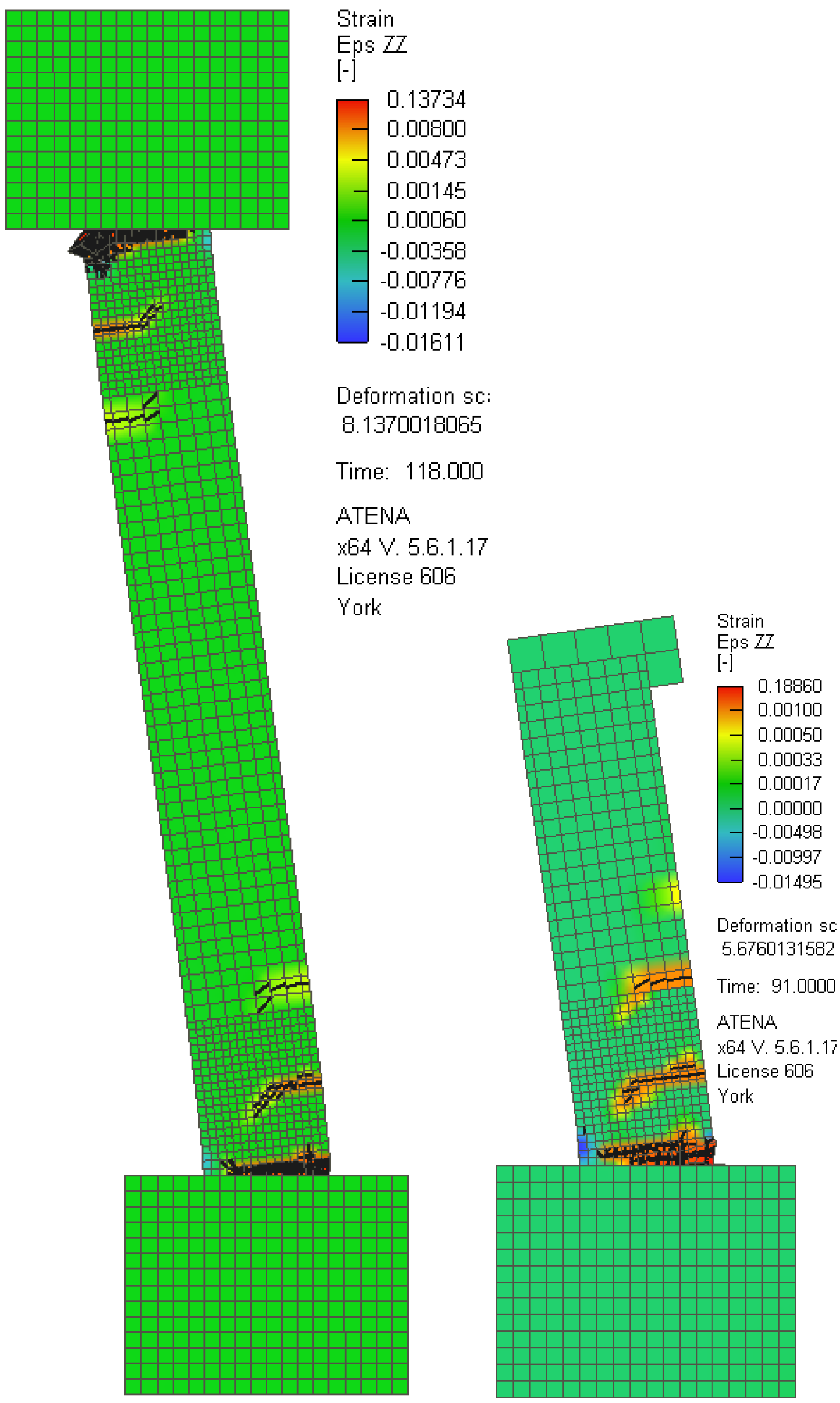

5.5e: C10-2-10: Concrete Strains
and Crack Pattern at Drift of 1.56%

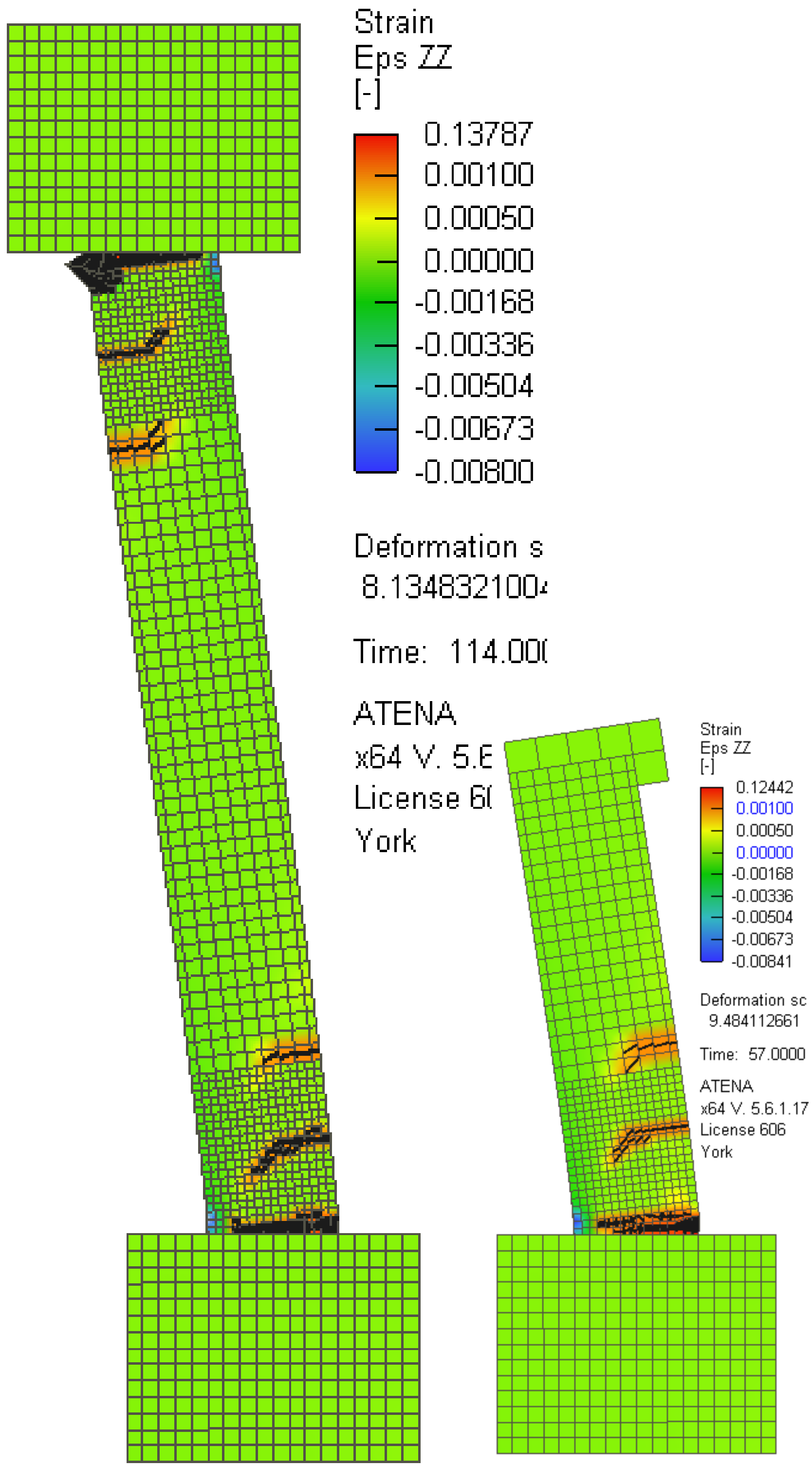

5.5f: C10-2-20: Crack Pattern and Concrete
Strains at a drift Ratio of 1.5%

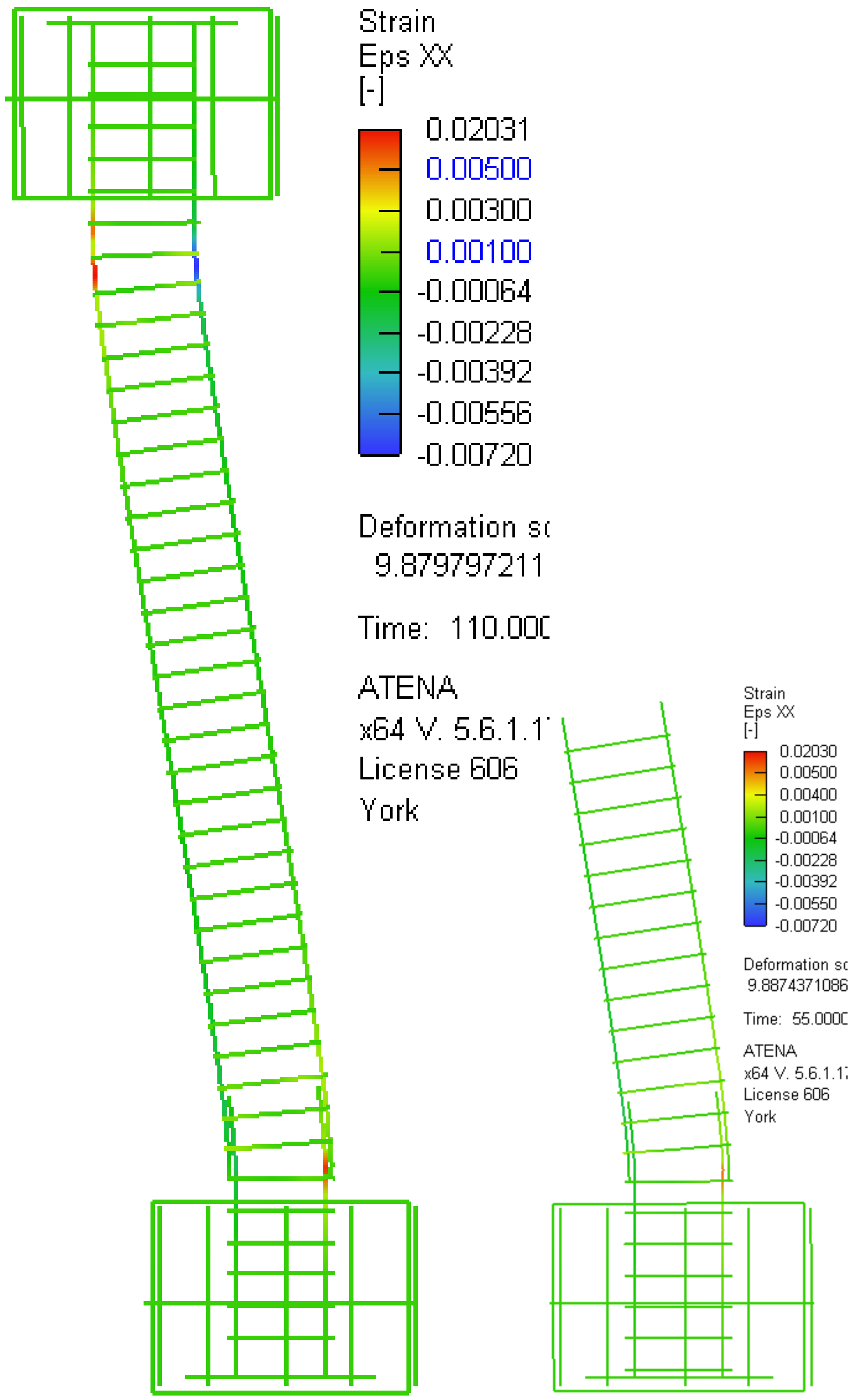

5.5g: C35-2-10: Strains in Longitudinal Reinforcement at Drift Ratio of 1.85%

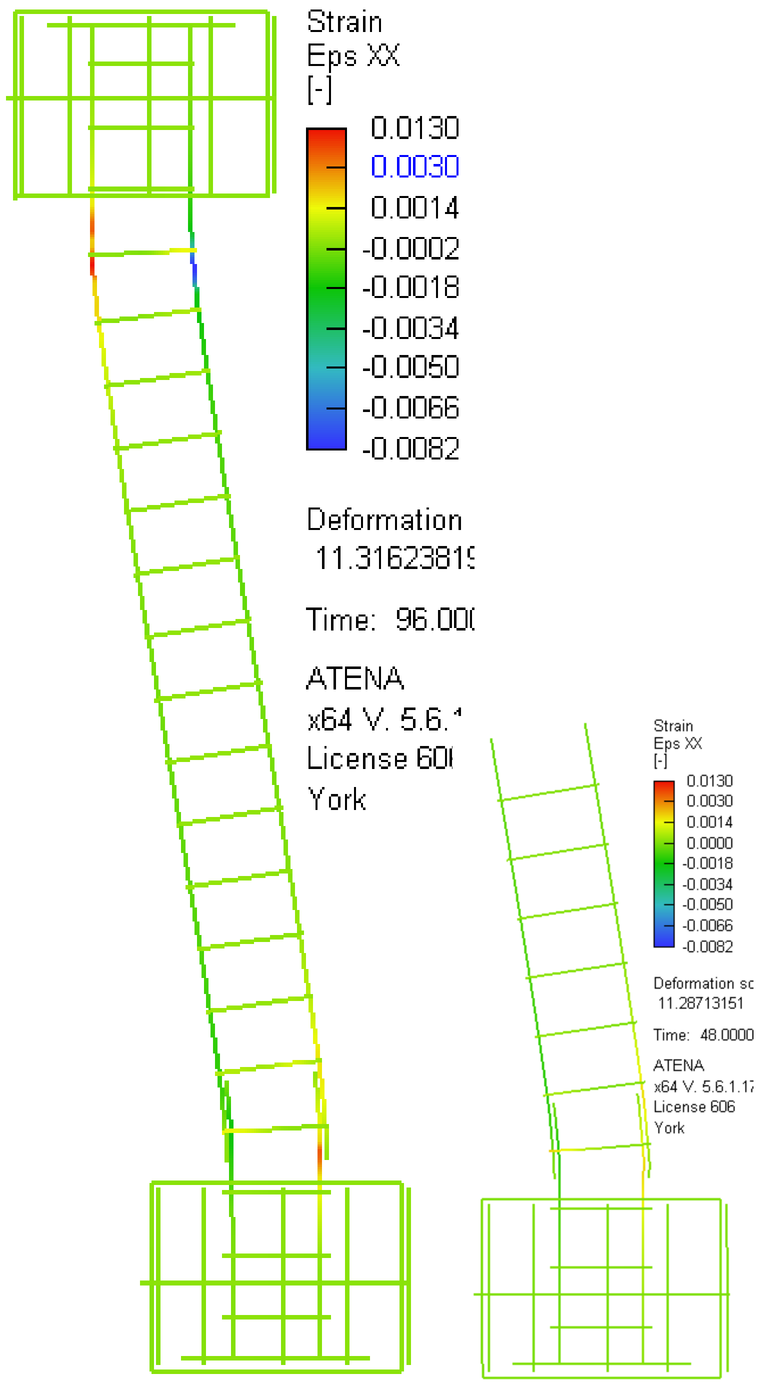

5.5h: C35-2-20: Longitudinal Strains at a
Drift Ratio of 1.2%

Figure 5.5: Modes of failure in the Full Model with its Corresponding Cantilever Failure for column Set 2 (from a-h)

5.4 Strain Penetration

It was stated earlier that the major differences between the cantilever and the full-length column models lie in their boundary conditions and the reinforcement detailing near the midheight. The boundary conditions at the swaying end of the cantilever column enforced strains in the longitudinal reinforcement to a zero value at a certain distance away from the steel plate. In the full-length column, this condition was not present, therefore the strains in the longitudinal reinforcement were permitted to penetrate towards the shear span of the upper half of the column. In the case of the lap splice, with the absence of the zero-strain condition for the longitudinal reinforcement at the midheight, the bar along the clear length of the column had a larger distance over which to develop (i.e., a milder strain gradient), which enabled enhanced stress transfer between the two lapped bars. This enabled the development of higher tension strains in the longitudinal reinforcement in the full-length column relative to the half column. Figure 5.6a plots the strains along the reinforcement bars for column C10-1-10 on the x-axis against the length of the shear span on the y-axis in the case of a lap splice for full-length and half column while 5.6b plots the strains along the reinforcement bars on the x-axis against the shear span length of the column on the y-axis for column C10-1-10 in the case of the continuous reinforcement connection for half and full-length column. The strains in Figure 5.6a were recorded when the tensile steel yields in the full-length column at a displacement of 21.4 mm and the corresponding displacement of the half column equal to 10.7 mm. The length of the full column (0-3.0 m) on the y-axis in Figure 5.6 extended from the bottom tip of the reinforcement embedded in the foundation (-0.7-0 m) up to the top tip reinforcement embedded into the beam (3-3.7 m).

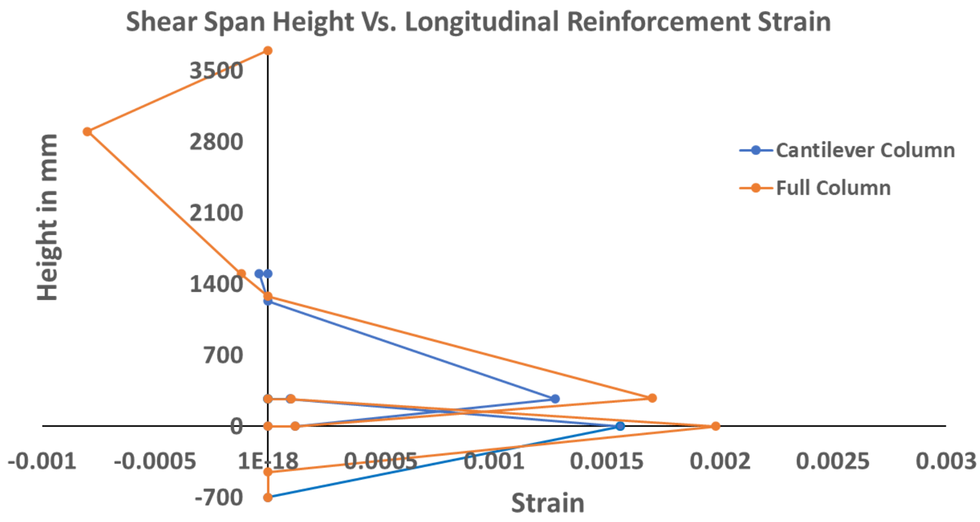

5.6a: Longitudinal Reinforcement Strains Along a Shear Span Length, for Column C10-1-10 Lap splice Case

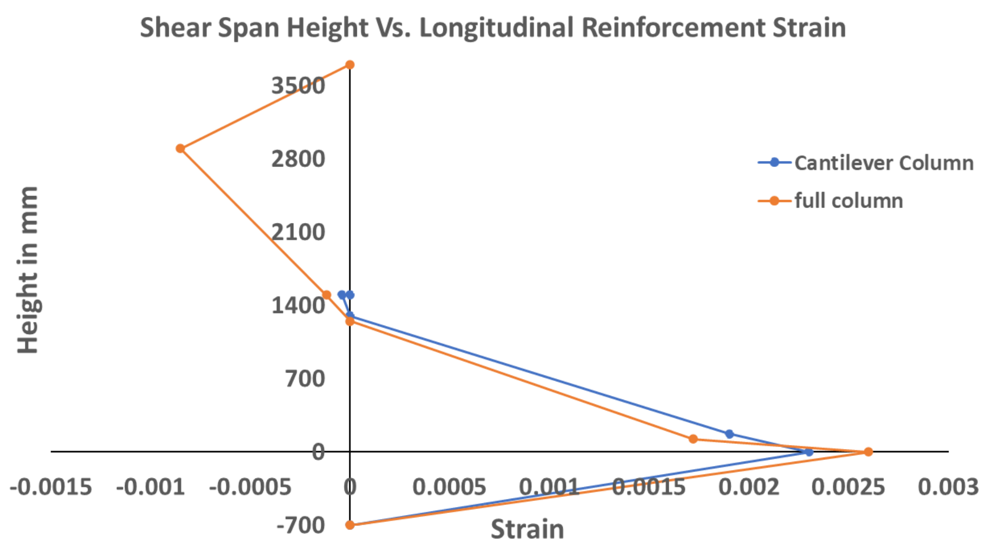

5.6b: Longitudinal Reinforcement Strains Along the Shear Span Length for Column C10-1-10 Continuous Reinforcement Case

Figure 5.6: Height Along the Shear Span Against Longitudinal Reinforcement Strains for Pairs of Full and Half Columns at Yielding in the Full Columns of C10-1-10 for Continuous and Lap Splice Case.

In the case of the lap splice as shown in Figure 5.6a, the longitudinal reinforcement of the full-length column developed yielding strains earlier than in the cantilever case. This results in developing effective yield drift ratios in the full-length column ($\theta_{y,full}$) lower than the yield drift ratios of the cantilever column ($\theta_{y,half}$). The effective yielding drifts for the full and cantilever column with a lap splice are shown in Table 5.2.

Table 5.2: Yield Drift Ratios for Cantilever and Full Column for the Case of Lap Splice .

Column	Effective Yield Rotation for Cantilever	Effective Yield for Full Column	
C10-1-10	0.74	0.59	$\theta_{y,full}$= 0.80($\theta_{y,half}$)
C10-1-20	0.60	0.45	$\theta_{y,full}$=0.75($\theta_{y,half}$)
C10-2-10	0.72	0.56	$\theta_{y,full}$=0.78($\theta_{y,half}$)
C10-2-20	0.55	0.47	$\theta_{y,full}$= 0.85($\theta_{y,half}$)
C35-1-10	0.66	0.59	$\theta_{y,full}$= 0.85($\theta_{y,half}$)
C35-1-20	0.46	0.48	$\theta_{y,full}$= 1.04($\theta_{y,half}$)
C35-2-10	0.53	0.48	$\theta_{y,full}$= 0.9($\theta_{y,half}$)
C35-2-20	0.41	0.45	$\theta_{y,full}$= 1.2($\theta_{y,half}$)

When comparing the effective yield displacement for the lap splice columns at low axial load in Table 5.2, it was concluded that: $\theta_{y,full} = 0.8\ \theta_{y,half}$. Given the theoretical yield rotations defined by Eq. 5.1, the stiffness of the full column ($EI_{eff,full}$) should be equal to approximately (0.8) times the effective stiffness of the cantilever column ($EI_{eff,half}$). The yield rotation for the full column in this case should be adjusted as shown in Eq. 5.2.

$$[5.1]\ \theta_y = \frac{M}{EI_{eff,half}}\frac{L_s}{3}$$

$$[5.2]\ \theta_y = \frac{M}{(0.8)EI_{eff,half}}\frac{H}{6}$$

where H is the length of the full column and L_s is the length of the shear span. When increasing the axial load and reducing the concrete confinement, yielding was controlled by the concrete nonlinearity prior to longitudinal reinforcement yielding. Therefore, in that case, the strain differences between the cantilever and full-length column in the lap splice case did not affect the yielding displacement value.

In the case of continuous reinforcement, yielding occurred simultaneously in the full-length and the cantilever column with less strain differences. Therefore, the effect of the strain differences in the yield rotation for the two scenarios were negligible.

The strain penetration also affects the ultimate displacement of the columns. For example, Figure 5.7 plots the height of the shear span of the pair full and half columns against the strains for column C35-1-10 and continuous reinforcement for cantilever and full column at a lateral displacement of 15.5 mm and 31 mm respectively. The length of the full column (0-3.0 m) on the y-axis in Figure 5.5 extended from the bottom tip of the reinforcement embedded in the foundation (-0.7-0 m) up to the top tip reinforcement embedded into the beam (3-3.7 m).

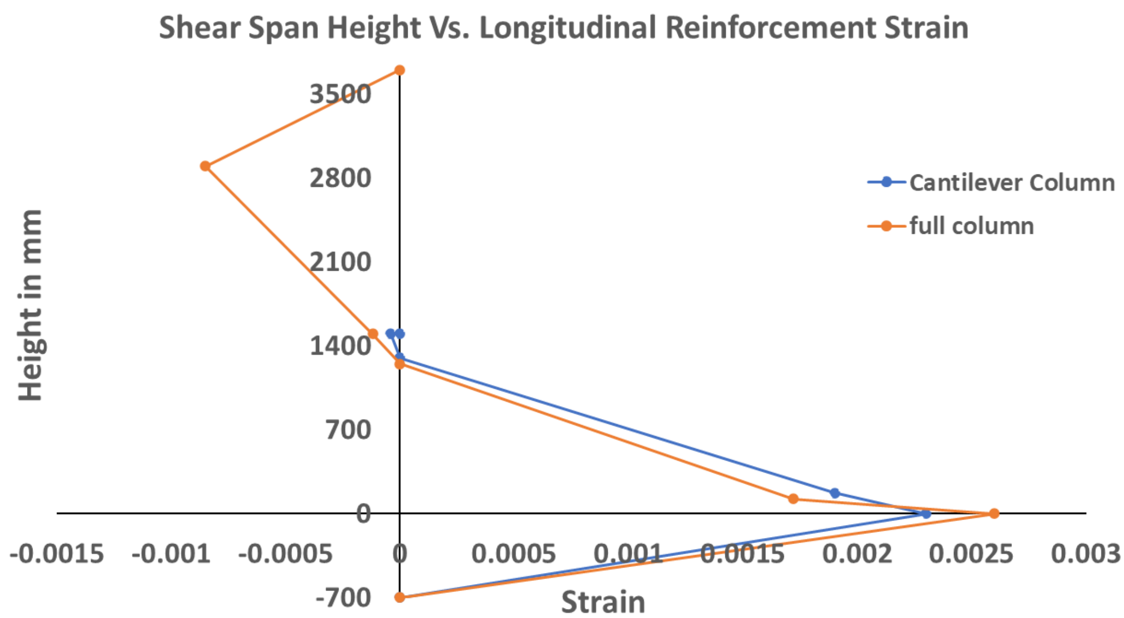

Figure 5.7: Longitudinal Reinforcement Strains Along the Shear Span Height at for Continuous Reinforcement (Column C35-1-10)

As shown in Figure 5.7, the strains in the full-length column penetrated beyond the midheight of the column. In the case of Column C35-1-10, which was a shear critical column, the strain penetrating upwards contributed in increasing the inclination angle of the critical shear crack in the full column. Figure 5.8a and b depicts the cracking pattern for the half and full-length column respectively. The maximum yield strain in the transverse reinforcement occurred in the fifth stirrup from the face of the critical section for the full column rather than the fourth in the cantilever column. This phenomenon decreased the ultimate rotation of the full-length column ($\theta_{u,full}$) to 0.86 of the ultimate rotation of the half column ($\theta_{u,half}$).

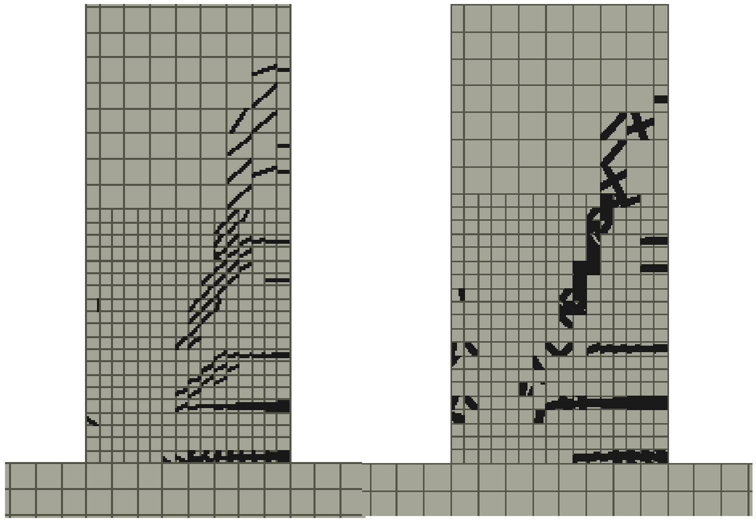

5.8(a): Half Column 5.8(b): Full Column

Figure 5.8: Crack Pattern for Column C35-1-10-Continuous Reinforcement Case.

For columns C35-1-20, C35-2-20 and C35-2-10, the differences between the drift ratios for the cantilever and the full-length column could be neglected. This was mainly because of the poor concrete confinement in those cases and therefore the ultimate displacement was controlled by concrete crushing. Table 5.3 depicts the relationship between the drift ratios for the full and half-length columns at high axial load for the first case.

Table 5.3: Ultimate Drift Ratios for Cantilever and Full-length Column at High Axial Load for the Case of Continuous Reinforcement.

Column	Effective Yield Rotation for Cantilever	Effective Yield for Full Column	
C35-1-10	3.00	2.56	$\theta_{y,full}= 0.86(\theta_{y,half})$
C35-1-20	1.6	1.43	$\theta_{y,full}=0.89(\theta_{y,half})$
C35-2-10	2.16	2.13	$\theta_{y,full}=0.99(\theta_{y,half})$
C35-2-20	1.48	1.36	$\theta_{y,full}= 0.92(\theta_{y,half})$

6. Seismic Assessment of Existing Structures

In this Chapter, a review of the two major international assessment codes of existing structures are presented (EUROCODE 8- Part III - 2005 and the ASCE/SEI 41-17) as a backdrop to the analytical results obtained in the preceding. Therefore, the deformation and strength capacities of the modelled columns were calculated using code-based equations and presented herein. The the analytical results calibrated against design expressions used in the assessment codes are illustrating the limits of the applicability and the discord between the different approaches used by current codes to define the so-called acceptance criteria in the seismic assessment practice.

6.1 Introduction

International seismic assessment codes of existing structures (EUROCODE 8- Part III - 2005 and the ASCE/SEI 41-17) provide estimates of deformation and shear strength in the form of Acceptance criteria/Limit States. Determining the limit state of a component plays a crucial role in the selection of suitable retrofit design of existing components.

The deformation capacity of the structural components may be calculated from the EUROCODE 8- Part III – 2005 based on the performance level of the column. The performance levels are divided into three categories in the EUROCODE 8- Part III – 2005, as follows: Damage limitation (θ_{DL} =θ_y), defined by the yield rotations, Significant damage (θ_{SD} =0.75θ_u), defined by 75% of the ultimate rotation capacity, and Near Collapse (θ_{NC} =θ_u), defined by the ultimate rotations. Detailed calculations of the performance levels are found the following sections.

The ASCE SEI 41-17 developed a backbone relationship between the lateral displacement and normalized lateral load as shown in Figure 6.1. In the figure, the modelling parameter b represents the plastic component of displacement or drift ratio at axial failure. Similarly, the modelling parameter a is the plastic component of the displacement or drift ratio at 20% of lateral resisting load on the post peak curve. Therefore, parameters a and b are plastic rotations. They were both determined from linear regression of experimental data of columns. Different equations were developed for circular section columns as they experienced different responses relative to rectangular section columns. From the experimental analysis it was found that, axial loading, the transverse reinforcement ratio and the parameter of V_p/V_n were the most influential factors on the deformation capacity of columns (Elwood et al. 2007), where V_p is the shear force of the column when flexural yielding is developed in the critical section and V_n is the shear strength of the column calculated from contributions of concrete and transverse reinforcement.

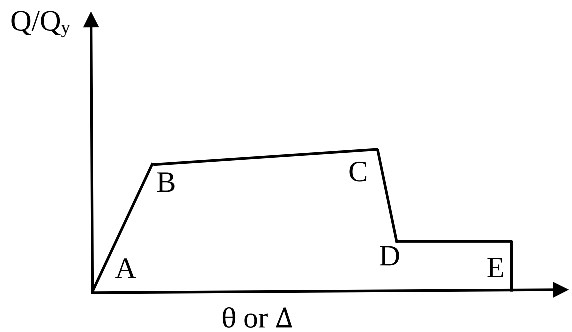

Figure 6.1: Backbone Response for Nonlinear Modeling of RC Components (Modified from ASCE SEI 41-17)

The Performance Levels of a component according to the ASCE SEI 41 17 are divided into three categories: Immediate Occupancy, Life Safety and Collapse Prevention. The equations developed for the parameter a and b and Performance levels will be presented in the following sections.

The calculations of the deformation capacities is not a straightforward procedure. Estimates of the curvatures at yielding and the depth of compression zone should be prepared before embarking on the actual assessment. Several approaches are available for the calculation of those two parameters (curvatures at yielding and ultimate and the depth of compression zone), however slight nuances in the methodology and simplifying assumptions built into uncertainties in the calculated deformation capacities. Available tools for the calculations of those parameters will be presented in detail in this chapter. The chapter will also explore whether this uncertainty will significantly affect the deformation capacity of the structure and therefore alter the possible retrofit strategy.

6.2 Depth of compression Zone at Yielding and Ultimate

The depth of the compression zone at yielding and ultimate can be calculated either using sectional analysis programs such as Response2000 (Bentz et al. 2001) or theoretical equations proposed by Priestley et al. (1996), Panagiotakos and Fardis (2001) and Pantazopoulou (1998) at yielding and ultimate respectively.

6.2.1 Response2000 Sectional Analysis (Bentz et al. 2001)

Using the sectional analysis from Response2000, the depth of the compression zone at yielding and ultimate were found. An example of the sectional analysis for one of the sections is shown in Figure 6.2.

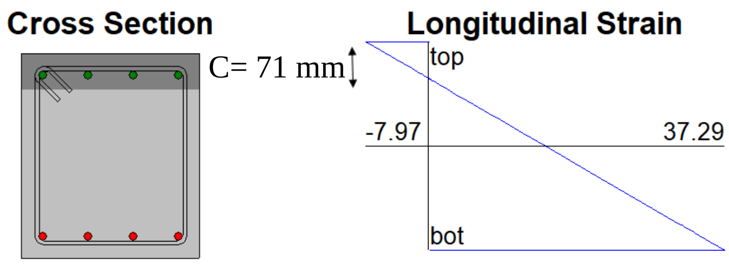

Figure 6.2: Sectional analysis From Response2000 used for the Calculations of the Depth of Compression Zone at Ultimate.

The depth of compression zone from Response2000 at yielding is recorded at the point of reinforcement yielding at low axial load. With the increase of the axial load to 35%, and 50% of crushing $\left(\frac{P}{A_g f_c}\right)$ the concrete nonlinearity controls the behavior of the section before longitudinal reinforcement yielding. Therefore, the yielding point is recorded at 75% of maximum moment. The depth of the compression zone at ultimate is recorded at the maximum moment resistance of the section.

6.2.2 Theoretical Calculations

Theorical expressions proposed by Panagiotakos and Fardis (2001) at yielding and by Pantazopoulou (1998) at ultimate are summarized in Eq. 6.1 -6.9 .

Depth of compression zone at yielding Proposed by Panagiotakos and Fardis 2001

The normalized depth of the compression zone at yielding, ξ_y, is calculated as shown in Eq. 6.1 (Panagiotakos and Fardis, 2001).

$$[6.1]\ \xi_y = (\alpha^2 A^2 + 2\alpha B)^{0.5} - \alpha A$$

where $A = \rho_1 + \rho_2 + \rho_v + \frac{N}{bdf_y}$, and $B = \rho_1 + \rho_2\delta_2 + 0.5\rho_v(1+\delta_2) + \frac{N}{bdf_y}$, when tension steel yielding controls. Whereas $A = \rho_1 + \rho_2 + \rho_v - \frac{N}{\varepsilon_c bdE_s}$ and $B = \rho_1 + \rho_2\,\delta_2 + 0.5\rho_v(1+\delta_2)$ values when nonlinearity in concrete controls and the moduli ratio $\alpha = E_s/E_c$. The other parameters are as follows: $\varepsilon_c = 1.8f_c/E_c$, ρ_1 is the tension reinforcement ratio, ρ_2 is the reinforcement ratio for compression reinforcement, ρ_v is the distributed longitudinal reinforcement along the web of the member. $\delta_2 = \left(\frac{d_2}{d}\right)$ where d_2 is the distance of the extreme compression fiber to the centroid of compression reinforcement.

Depth of compression Zone at Ultimate Proposed by Pantazopoulou 1998

The normalized depth of compression zone at ultimate, ξ_u, is estimated using interpolation, for a specified axial load ratio $N/A_c f_c$, as shown in Eq. 6.2 and 6.3 (Pantazopoulou 2003):

$$[6.2]\ \xi_u = 0.64 + \left((1-0.64)\frac{N-N_{balanced}}{N_{max}-N_{balanced}}\right),\ if\ N_{balanced} < N < N_{max}$$

$$[6.3]\ \xi_u = \delta_2 + \left((0.64-\delta_2)\frac{N-N_{min}}{N_{Balanced}-N_{min}}\right),\ if\ N_{min} < N < N_{balanced}$$

The values of N_{min}, N_{bal}, and N_{max} correspond to characteristic values of the depth of compression zone for $\varepsilon_{cu}=0.005$ (Pantazopoulou 2003), and are calculated as shown in Eq. 6.4, 6.5 and 6.6 respectively:

$$[6.4]\ \frac{N_{min}}{A_c f_c} = 0.72\delta_2 - \frac{f_y}{(1-\beta)f_c}[\rho_1 + \rho_v(1-\delta_2)],\ for\ x = d_2\ and\ \xi = d_2$$

$$[6.5]\ \frac{N_{balanced}}{A_c f_c} = (\rho_2 - \rho_1)\frac{f_y}{f_c} + 0.275\frac{f_y}{f_c}\rho_v + 0.462,\ for\ x = x_{balance}\ and\ \xi_{balanced} = 0.64$$

$$[6.6]\ \frac{N_{max}}{A_c f_c} = 0.85^2 + \frac{f_y}{f_c}[\rho_2 + 0.8\,\rho_v],\ for\ x = d, \xi = 1$$

Where β if the strain hardening ratio of the longitudinal reinforcement, defined by, $\beta = \frac{f_u - f_y}{f_u}$. All terms are defined in Eq. 6.1.

6.2.3 Differences in the Approaches for Estimating the Depth of Compression Zone

The sections of the benchmark columns were used to calculate the depth of the compression zone using the two approaches described in the previous sections (Sections 6.1.1 and 6.1.2). The depth of the compression zone at yielding and ultimate were calculated for three cases:

1- Case 1: dimensions (350 x 400) mm and continuous reinforcement connection,
2- Case 3: dimensions (350 x 400) mm and lap splice connection and
3- Case 4: dimensions (350 x 700) mm and continuous reinforcement connection.

The concrete stress-strain curves that were calculated in Chapter 3 and used in the advanced finite element models were used for material input in Response2000 (Bentz et al. 2001). The same reinforcement yield and ultimate strength used in the finite element model and presented in Table 3.2 in Chapter 3 were used for the depth of compression zone calculations. For sections of Case 3, the yield strength of the reinforcement was reduced to the maximum steel stress sustained by the lapped bars. The maximum steel stress in lapped reinforcement is calculated according to the two international assessment codes, ASCE ASE 41-17 and Eurocode 8 part III shown in Eq. 6.7 and 6.8 respectively.

[6.7] $f_s = 1.25\left(\frac{l_o}{l_d}\right)$

[6.8] $f_s = f_y\left(\frac{l_o}{l_{oy,min}}\right)$

where l_o is the avaible lapped length, l_d is calcuted with accordance to FEMA 356 as shown in Eq. 6.9. $l_{oy,min}$ is calculted as shown in Eq. 6.10.

[6.9] $l_d = \frac{1.25 f_y}{B\sqrt{f_c}}$

[6.10] $l_{oy,min} = \frac{0.3 d_b f_y}{\sqrt{f_c}}$

where B is equal to 2 for bars with diameters less than or equal to No.6, 1.66 for bar diamters more than or equal to No.7 and 5.4 for bars confined with stirrups of 90° hook arrangement. The bar yield stress is reduced to 241 and 273 MPa according to Eq. 6.7 and 6.8 respectively, for the lapped reinforcement benchmark columns. The two codes show close estimation, however, the ASCE SEI 41-17 was more conservative.

Figure 6.3 plots the compression zone depth at yielding calculated from Panagiotakos and Fardis (2001) against the values from Response2000.

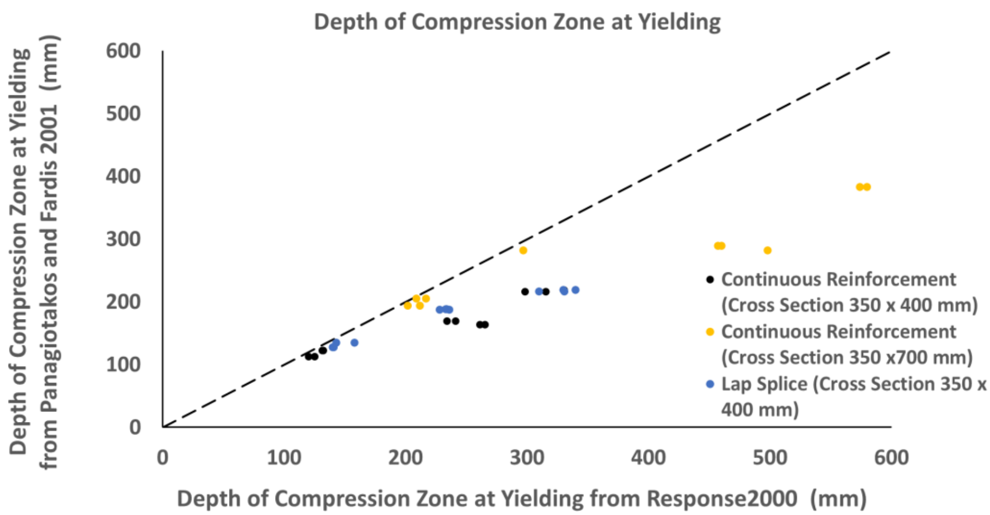

Figure 6.3: Depth of Compression Zone from Panagiotakos and Fardis (2001) vs. Response 2000 result

At yielding the differences between the depth of the compression zone from Response2000 and Panagiotakos and Fardis 2001 model increased with the increase of the axial load (35% and 50%). At high axial loads ($\frac{P}{A_g f_c}$ equal to 35% and 50%) when the concrete nonlinearity controls the section behaviour, Response2000 significantly overestimated the depth of the compression zone relative to Panagiotakos and Fardis (2001) model. This trend is found in all three sectional cases as shown in Figure 6.3. The effect of confinement on the depth of compression zone is not accounted for in Panagiotakos and Fardis (2001) model and is negligible in Response2000. It is also concluded that at 35% axial load the differences decreased with reducing the yield strength of steel in the case of lap splice as steel yielding controlled the yield curvature rather than concrete crushing. The highest difference was 38.5% at an axial load of 50% crushing load. The lowest difference is 6.01% at low axial loads.

An attempt to decrease the differences in the depth compression zone at yielding between Response2000 and Panagiotakos and Fardis (2001) models (especially at high axial loads) was achieved by recording the depth of the compression zone yielding at 80% of the maximum moment instead of 75%. The curvatures of the sections with an axial load of 35% and 50% ($\frac{P}{A_g f_c}$) are recorded at 80% of maximum moment and plotted against the depth of the compression zone from Panagiotakos and Fardis in Figure 6.4.

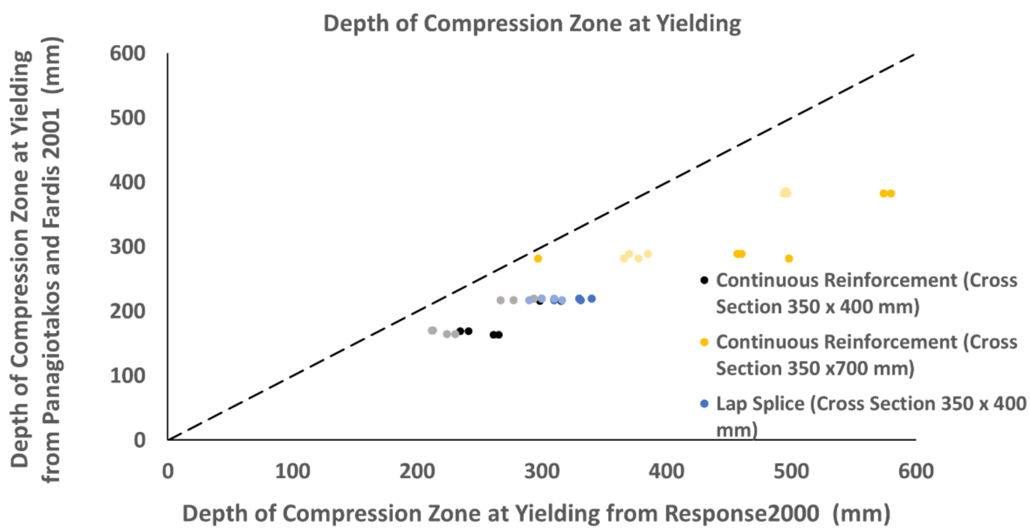

Figure 6.4: Depth of the compression Zone at 80% maximum Moment from Response2000

In Figure 6.4, the dark coloured points are the values for the depth of the compression zone from Response2000 at 75% of the maximum moment whereas the light-coloured points are the respective values for the depth of compression zone recorded at 80% of maximum moment. As shown in Figure 6.4 the differences in the compression zone calculations were attenuated when recording the depth of the compression zone at 80% of the maximum moment (the points become closer to the 45° line). The highest difference of 38.5% that appeared at high axial loads is reduced to 28.9%.

Figure 6.5 plots the differences of the compression zone depth at ultimate calculated from Pantazopoulou (1998) model against Response 2000 estimates. The depth of the compression zone at ultimate moment from Response2000 shows good correlation to Pantazopoulou (1998) proposed model. Differences are also present at high axial load but are negligible.

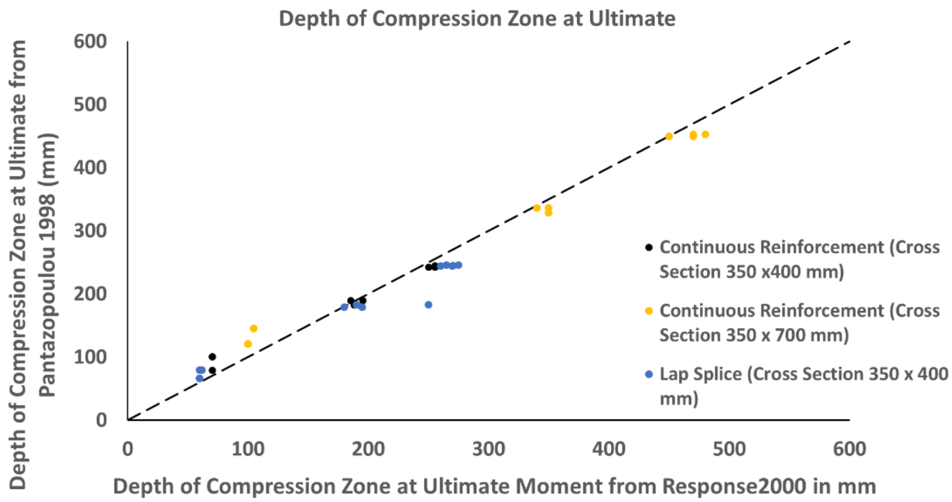

Figure 6.5: Depth of Compression Zone from Pantazopoulou (1998) vs. result from Response2000

6.3 Curvature Calculations

Many approaches are found in literature to compute the curvatures of a reinforced concrete section. The following section will provide the reader with three available tools for calculating the curvature at yield and ultimate. The three approaches include the computed result from Response2000 (Bentz et al. 2001), and the empirical equations proposed by Priestly et al. (1996) and by Panagiotakos and Fardis (2001).

6.3.1 Response2000 Curvatures (Bentz et al. 2001)

The curvatures of the cross sections were found using the nonlinear sectional analysis feature provided by Response2000 (version 1.05) with eliminating shear response. The material input in Response2000 (Concrete stress-strain curve and reinforcement strengths) was the same given for the finite element models to enable the comparison of deformation and strength with the theoretical calculated results.

The yield curvature from Response2000 was determined either at the point of nonlinearity of concrete or yielding of the longitudinal reinforcement at low and high axial loads respectively. The ultimate curvatures were recorded at two points: 1) At the maximum moment, 2) At 80% of the maximum moment on the post peak curve.

6.3.2 Panagiotakos and Fardis 2001 Empirical Equation

Using the empirical equations defined by Panagiotakos and Fardis (2001) the yield curvatures were calculated as shown in Eq. 6.11 and 6.12. The yield curvature is determined by the minimum between the two values of yielding of the longitudinal reinforcement and point of compressive cover delamination.

[6.11] $\varphi_y = \min\left\{\frac{f_{yl}}{E}\frac{1}{d-x_y}, \frac{\varepsilon_{c,y}}{x_y}\right\}$

[6.12] $\varphi_u = \frac{\varepsilon_{c,u}}{x_u}$

Here f_{yl} is the yield strength of the steel reinforcement in MPa. E is Young's Modulus of elasticity in MPa. $\varepsilon_{c,y}$ is 0.75 of $\varepsilon_{c,o}$,where $\varepsilon_{c,o}$ is the strain at peak strength. The parameter $\varepsilon_{c,u}$ is the strain of the concrete at 15 % reduction in maximum strength on the post peak concrete stress strain curve. x_y is the depth of the compression zone at yielding while x_u is the depth of the compression zone at ultimate. The depth of the compression zone at yielding and ultimate is determined according to Section 6.2.

6.3.3 Priestley et al. (1996) Curvature Estimates

Equation 6.13 has been proposed by Priestley et al. (1996) for yield curvature calculations.

[6.13] $\varphi_y = \frac{2.1\varepsilon_y}{h_c}$

where ε_y is the longitudinal reinforcement yielding strain = f_{yl}/E and h_c is the depth of the cross section.

To find the plastic curvature, Figure 6.6 was used. This figure represents the relation between the plastic curvature multiplied by the depth of the cross section vs. the total longitudinal reinforcement ratio. The plastic curvature was added to the yield curvatures calculated from Eq. 6.13. Each curve in Figure 6.6 represents a different axial load ratio.

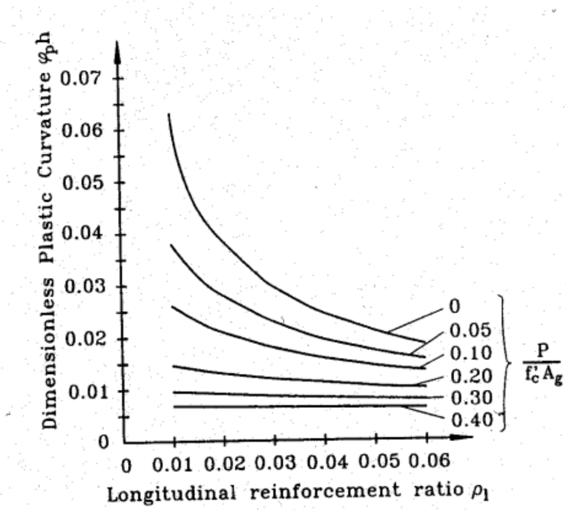

Figure 6.6: Plastic Curvature Calculation for Rectangular Cross Sections (Priestly et al. 1996)

6.3.4 Difference in Approaches of the Curvature Estimations

The curvature calculations at yielding and ultimate were calculated for the three sections described in Section 6.1.3 of this Chapter. The same material input presented in Section 6.1.3 for the three column sections was used for curvature calculations. The two approaches for the depth of compression zone calculations were considered. Figure 6.7 depicts the differences in the yield curvature calculations for all sections in the database using three approaches described previously. Figure 6.7a plots the curvatures calculated from the model by Priestley et al. (1996) against the computed curvatures from Response2000. Similarly, Figure 6.7b plots the curvatures calculated from the model by Panagiotakos and Fardis (2001) (using the depth of the compression zone from Response 2000) against the yield curvatures obtained from Response2000. Panagiotakos and Fardis approach (2001) calculations, using the depth of the compression zone from Panagiotakos and Fardis (2001) model rather than the depth of the compression zone at yielding from Response2000, are plotted against Response2000 curvatures in Figure 6.7c.

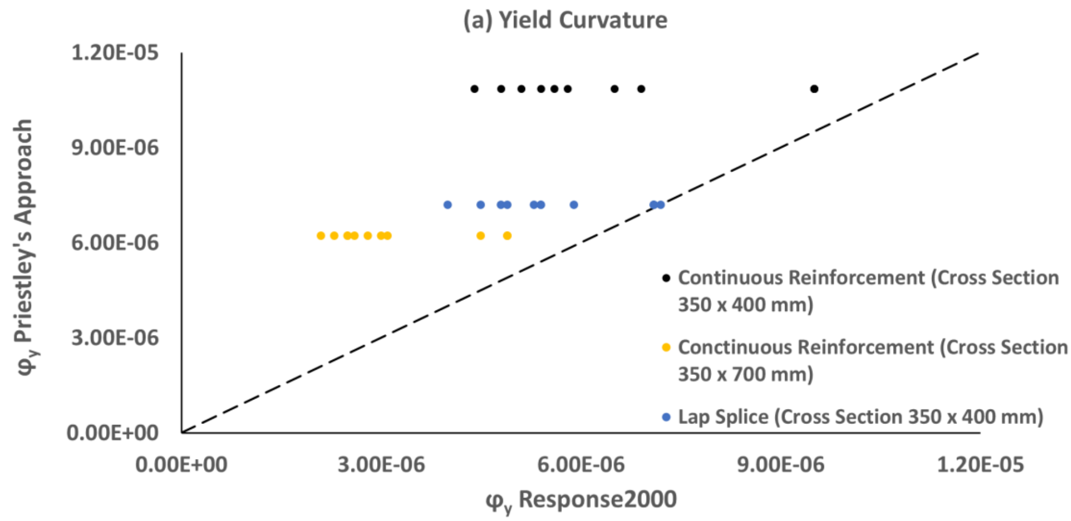

6.7a: Yield Curvatures from Priestley et al (1996) against Yield Curvatures obtained from Response2000

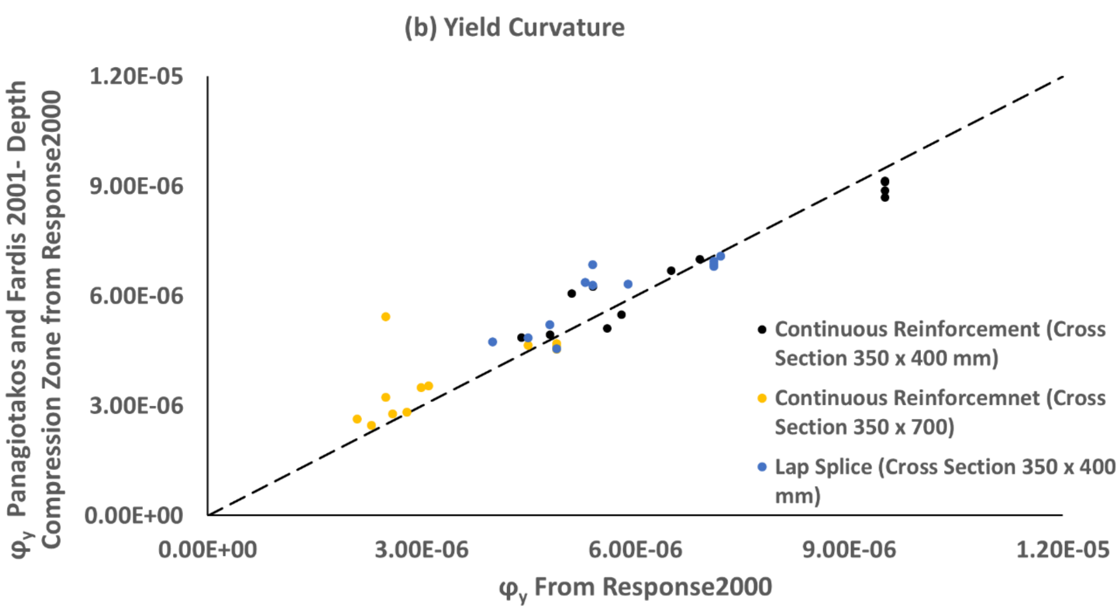

6.7b: Yield Curvatures from the model of Panagiotakos and Fardis (2001) against Response2000 Yield Curvatures

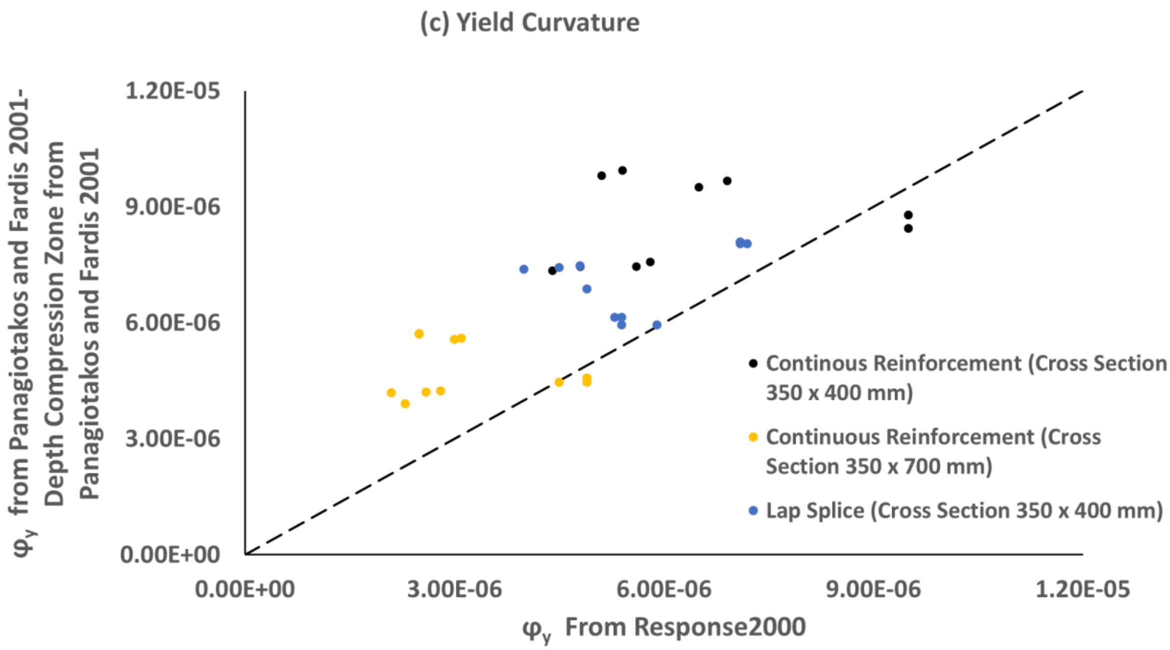

6.7c: Yield Curvatures from the model of Panagiotakos and Fardis (2001) against Yield Curvatures calculated from Response2000

Figure 6.7: Yield Curvature Calculations from Different Approaches

As shown in Figure 6.7a, the equation proposed by Priestley et al. (1996) overestimated the yielding curvatures as compared to Response2000. The curvatures calculated from Priestley et al. (1996) model showed insensitivity to axial load and longitudinal reinforcement ratio. The curvatures from Response2000 increased with the decrease of axial load ratio $\left(\frac{P}{A_g f_c}\right)$. As curvatures from Priestley et al. (1996) model were overestimated relative to Response2000 curvatures the smallest difference between the two approaches was observed when the yield curvatures in Response2000 were the highest. The systematic overestimation of one model vs. the Response 2000 estimates is owing to the fact that the former considers the contribution of strain penetration inside the anchorage, which is neglected in the computational approach. Therefore, in this database, Priestley et al. (1996) curvatures show better correlation to values obtained from sectional analysis at an axial load of 10% (when steel yielding controls the behavior of the section).

The yield curvature model of Priestley et al. (1996) was also insensitive to the longitudinal reinforcement ratio while Response2000 yield curvatures increased with the increase of the reinforcement ratio. Given that these curvatures overestimated the computed values for yield curvatures, the differences between the values from the two approaches decreased with the increase of the reinforcement ratio (higher reinforcement ratio provide higher yield curvatures in Response2000). It is also observed that the differences between the two approaches increased with the increase of a cross sectional depth as shown in Figure 6.7a. The differences also decreased when adjusting the strain ε_y in Priestley et al. (1996) by (l_o/l_d) in the presences of lap splice as required in the EUROCODE-8 III 2005 due to the control of steel yielding at axial load ratio $\left(\frac{P}{A_g f_c}\right)$ equal to 0.1 and 0.35.

Figure 6.7b plots the values of curvatures using the model proposed by Panagiotakos and Fardis (2001) against the calculated curvatures from Response2000. The depth of the compression zone was found from Response2000. Agreement in the two approaches was observed as shown in 6.7b. In Figure 6.7c, a significant scatter was found as the depth of the compression zone was calculated from Panagiotakos and Fardis (2001) model. The differences were significant in this case, especially at an axial load ratio of 0.35 and 0.50. The highest difference in the depth of the compression zone recorded from Response2000 and Panagiotakos approach of 38.8% reflected in a difference of 92.4% in the curvatures. To decrease the differences in the curvatures between the two approaches, Panagiotakos and Fardis (2001) curvatures using the depth of the compression zone from Panagiotakos and Fardis 92001) against Response2000 curvatures at 80% of the maximum moment is shown in Figure 6.8 in light colour. The dark coloured points in Figure 6.8 represent the curvature values at 75% of the maximum moment.

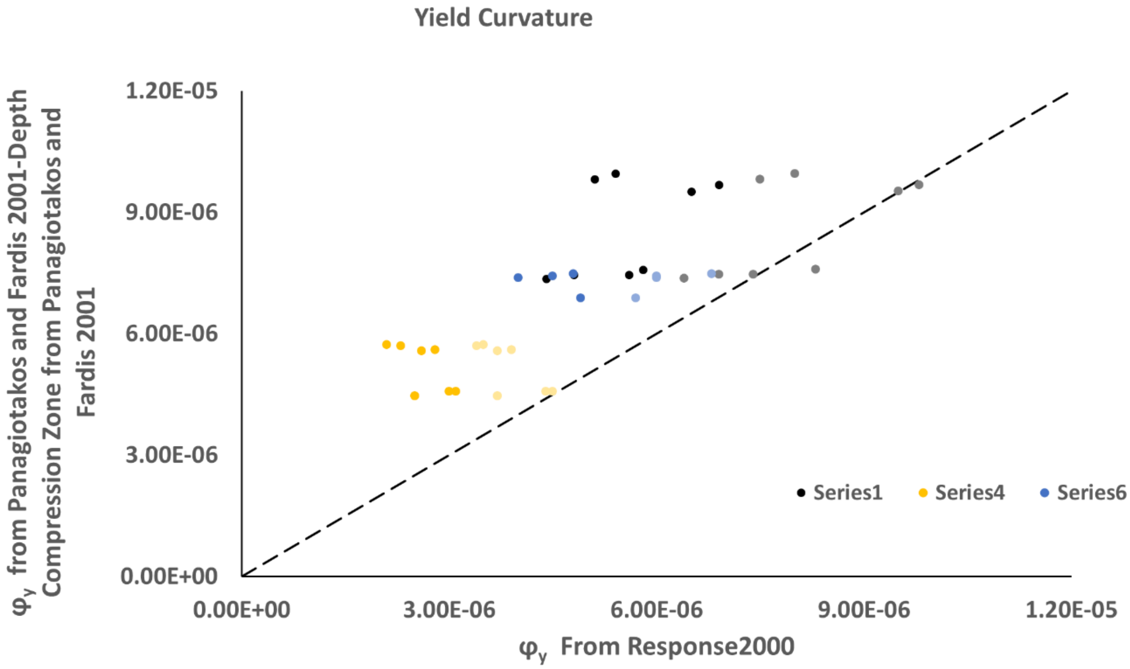

Figure 6.8: Yield Curvatures at 80% of the Maximum Moment from Response2000

The difference in the yield curvatures between the values calculated from Resposne2000 and from the model by Panagiotakos and Fardis (2001) using the depth of the compression zone from the same model is significantly attenuated when considering the point 80% of maximum moment from Response2000. In this case the largest difference recorded (92.6 %) decreases to (30.8 %).

The plots in Figure 6.9 depict the differences between the theoretical relation and Response2000 estimates for curvature at ultimate moment. Figure 6.9a plots the ultimate curvatures from the Priestley et al. (1996) model against Response2000 values. Figure 6.9b plots the ultimate curvatures from Priestley et a (1996) model against ultimate curvatures from Resposne2000 at 85% of maximum at the post peak curve. Figure 6.9c plots the ultimate curvatures from Panagiotakos and Fardis (2001) against Response2000 ultimate curvatures using the depth of the compression zone from the model of Pantazopoulou (1998).

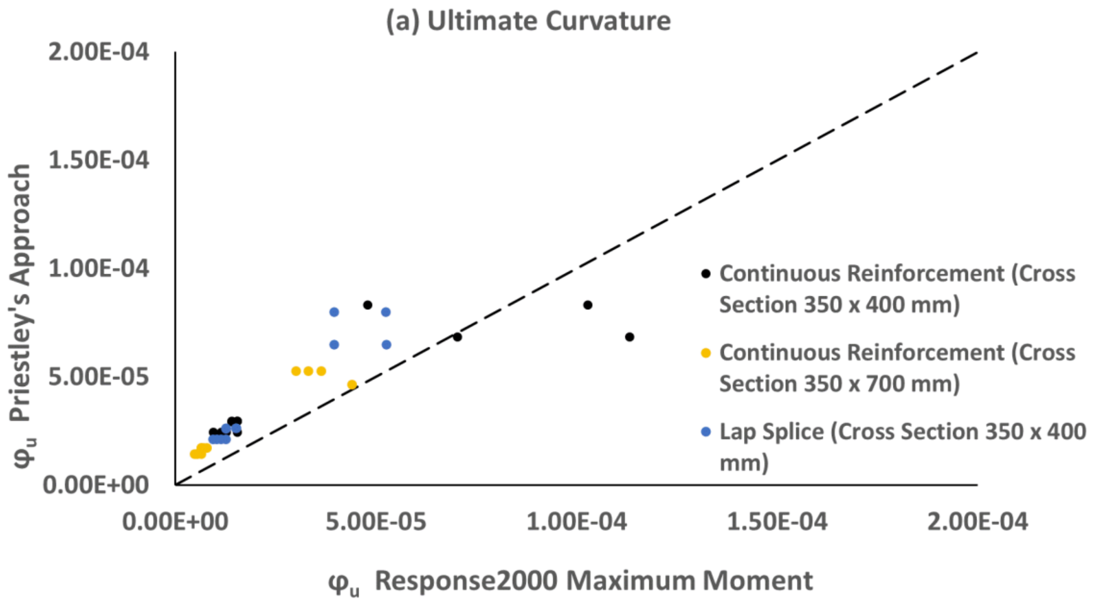

Figure 6.9a: Ultimate Curvatures from Priestley's et al. (1996) Model and Response2000 at Maximum Moment

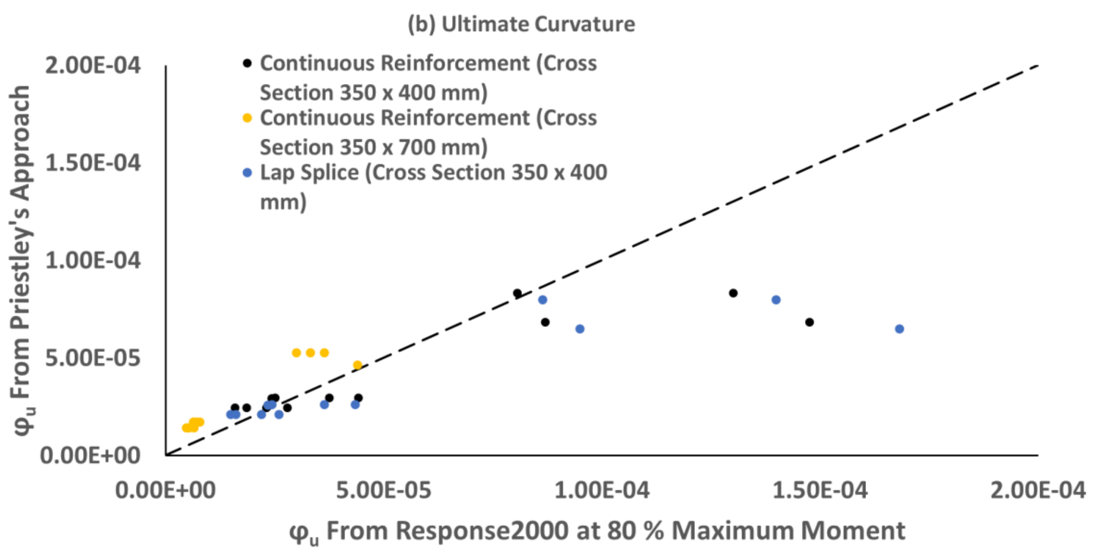

Figure 6.9b: Ultimate Curvatures from Priestley's et al. (1996) Model and Response2000 at 80% of the Maximum Moment on the post Peak Curve

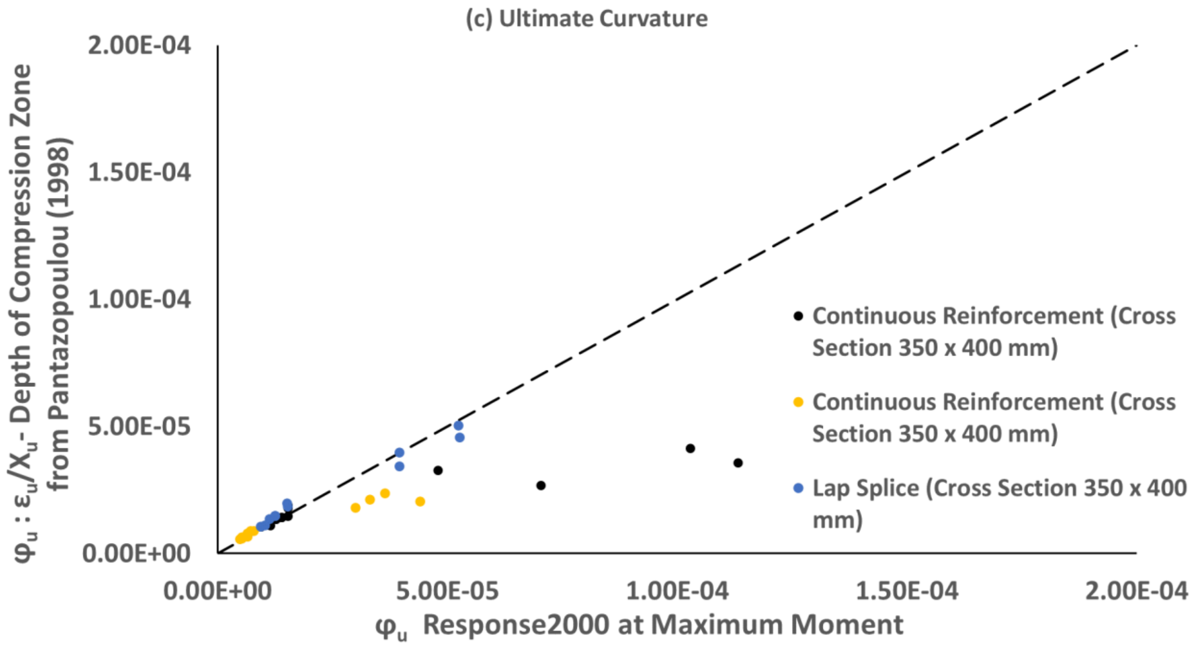

Figure 6.9c: Ultimate Curvatures from Priestley's et al. (1996) Model and Response2000 at 80% of the Maximum Moment on the post Peak Curve

Figure: 6.9 Ultimate Curvature Calculations

As shown in Figure 6.9a the differences in the ultimate curvatures between the two approaches (Priestley's Equation and Response2000 estimations) increased with the increase of the axial load and depth of the cross section. This difference with respect to Response2000 ultimate curvature values can reach 159.4%. However, as shown in Figure 6.9b, the differences between the curvatures found at 80% maximum moment on the post peak branch in Response 2000 and Priestley et al. (1996) showed a reduction in the differences to half that value. For example, the difference between the value of Priestley et al. (1996) curvatures and Response2000 curvature decreased from 159.4 to 47.5 % when comparing the values at 80% of the maximum moment on the post peak curve in Response2000 rather than recording the curvatures at maximum moment.

Figure 6.9c plots the depth of the ultimate curvatures found from empirical equations proposed by Panagiotakos and Fardis (using the depth of compression zone at ultimate from Pantazopoulou 1998) against Response2000. The difference between the two ultimate curvatures from the two approaches decreased with the increase in the axial load ratio.

6.4 Assessment Code Based for Deformation and Strength Capacities

The deformation and shear strength used in assessment codes in the form of Acceptance criteria/Performance levels are reviewed in this section. The deformation and strength capacity calculations for the benchmark column presented in Chapter 3 will be calibrated against code based deformation and strength values.

6.4.1 EUROCODE 8-Part III, 2005

The EUROCODE 8-Part III of 2005 provides analytical equations for the calculation of the deformation and strength capacities in the form of performance levels. The retrofit design of a reinforced concrete structural component depends on its level of performance found from the estimates of the deformation capacities. The performance levels are divided into three categories as follows:

1- Near collapse (NC) structures: Structural components in this level of performance retain low residual strength and stiffness while non-structural members have collapsed.
2- Significant Damage (SD) structures: Structural components in this level of performance may be economical to repair. Structures that have reached this limit state in a previous event are able to resist earthquake aftershocks.
3- Damage limitation (DL) components: Structural components in this level of performance retain the full strength and stiffness. Structural repairs in this level of performance are unnecessary.

Deformation Capacity Estimates

The rotation capacity at each limit state is reviewed in this case.

Near Collapse Limit State (Ultimate Rotations)

The ultimate rotation (θ_{um}) of a cantilever column swaying laterally under cyclic loading is calculated as shown in Eq. 6.13 for continuous deformed longitudinal reinforcement. The plastic rotation (θ_{um}^{pl}) is calculated as shown in Eq. 6.14 for continuous deformed longitudinal reinforcement.

$$[6.13]\quad \theta_{um} = \frac{1}{\gamma_{el}} 0.016(0.3^{v}) \left[\frac{\max(0.01;\omega')}{\max(0.01;\omega)} f_c\right]^{0.225} \left(\frac{L_v}{h}\right)^{0.35} 25^{\left(k\rho_{sx}\frac{f_{y,tr}}{f_c}\right)} (1.25^{100\rho_d})$$

[6.14] $\theta_{um}^{pl} = \theta_{um} - \theta_y$

$$= \frac{1}{\gamma_{el}} 0.0145(0.25^{v}) \left[\frac{\max(0.01;\omega')}{\max(0.01;\omega)} f_c\right]^{0.3} \left(\frac{L_v}{h}\right)^{0.35} \; 25^{\left(k\rho_{sx}\frac{f_{y,tr}}{f_c}\right)} (1.275^{100\rho_d}) f_c^{\,0.2}$$

where, γ_{el} is equal to 1.5 for primary seismic elements and to 1.0 for secondary seismic elements. h is the depth of the cross section. $L_v = M/V$ is the ratio of the moment/shear at the critical section. $v = N/(bhf_c)$ where b is the width of the section. N is the axial force and is positive for compression. ω, ω' are the mechanical longitudinal reinforcement ratios in tension and the compression, respectively. f_c and $f_{y,tr}$ are the concrete compressive strength (MPa) and the transverse reinforcement yield strength (MPa) respectively. $\rho_{sx} = A_{sx}/b_w s_h$ is the ratio of transverse steel parallel to the direction of the loading (x). s_h is stirrup spacing. ρ_d is the steel ratio of diagonal reinforcement. k is calculated by Eq. 6.15 and is defined as the confinement effectiveness factor. θ_y is the yield rotation and is calculated according to Damage Limitation state.

[6.15] $k = \left(1 - \frac{s_h}{2b_o}\right)\left(1 - \frac{s_h}{2h_o}\right)\left(1 - \frac{\sum {b_i}^2}{6h_o b_o}\right)$

where, b_o and h_o are the dimensions of the section's confined core to the center line of the loop. b_i is the center line spacing of longitudinal bars (indexed by i) laterally restrained by a stirrup corner or a cross tie along the perimeter of the cross section. Equation 6.13 and 6.14 are multiplied by 0.825 if the component was not detailed for earthquake resistance.

When a lap splice is present at the critical section of the column, ω' should be multiplied by 2 in Eq. 6.13 and 6.14. Moreover, Eq. 6.13 should be multiplied by $l_o/l_{ou,min}$ if $l_o < l_{ou,min}$, where l_o is the available lapped length and $l_{ou,min}$ is the minimum required length at ultimate and is calculated as per Eq. 6.16. The term θ_y should be calculated considering the effect of the lap length as specified in the damage limitation performance level presented in the following sections.

[6.16] $l_{ou,min} = d_b f_{yl}\left[1.05 + \frac{14.5 k_1 \rho_{sx} f_{y,tr}}{f_c}\right]$

where, d_b is the diameter of the lapped bar. f_{yl} is the yield strength of the lapped bars (MPa). f_c, $f_{y,tr}$, ρ_{sx} were defined from Eq. 6.14. The parameter k_1 was defined in Eq. 6.17.

[6.17] $k_1 = \left(1 - \frac{s_h}{2b_o}\right)\left(1 - \frac{s_h}{2h_o}\right)\left(\frac{n_{restr}}{n_{tot}}\right)$.

where, n_{restr} is the number of lapped bars restrained by a stirrup corner or a cross tie and n_{tot} is the total number of lapped bars along the cross-section perimeter.

Significant Damage State

At this limit state the chord rotation capacity is equal to 75% of θ_{um}. Where θ_{um} is calculated from the Significant Damage Limit State.

Damage Limitation State (Effective Yield Rotations)

The deformation capacity of a structural component at damage limitation limit state (at yielding) for continuous deformed longitudinal reinforcement is calculated as shown in Eq. 6.18 or 6.19.

[6.18] $\theta_y = \varphi_y \frac{L_v + a_v z}{3} + 0.00135\left(1 + 1.5\frac{h}{L_v}\right) + \frac{\varepsilon_y}{d - d\prime}\frac{d_b f_{yl}}{6\sqrt{f_c}}$

[6.19] $\theta_y = \varphi_y \frac{L_v + a_v z}{3} + 0.0013\left(1 + 1.5\frac{h}{L_v}\right) + 0.13\varphi_y\frac{d_b f_{yl}}{\sqrt{f_c}}$

where, φ_y is the yield curvature of the end section. z is the length of the internal lever arm which is equal to *d-d'* for components with rectangular sections. a_v is a factor equal to 1 or 0. a_v is 1 if the yield capacity of a section (M_y) is more than L_v times the shear resistance of the member considered without shear reinforcement (i.e., the concrete contribution term, where $V_{R,c}$ is calculated in accordance with EN 1992-1-1:2004, 6.2.2(1)). a_v equals to 0 if $M_y < L_v V_{R,c}$. ε_y is equal to f_y/E_s. Parameters d and d' are the distances of the tension and compression reinforcement from the extreme compressive fibre, respectively.

$V_{R,c}$ in accordance with EN 1992-1-1:2004, 6.2.2(1) is calculated using Eq. [6.20].

[6.20] $V_{Rd,c} = \left[C_{Rd,c} k_{sh} (100\rho_l f_{ck})^{\frac{1}{3}} + K_1 \sigma_{cp}\right] b_w d$

With a minimum of $V_{Rd,c} = (V_{min} + K_1 \sigma_{cp})\, b_w d$

where, f_{ck} is in MPa and is the characteristic compressive strength of concrete. $k_{sh} = 1 + \sqrt{\frac{200}{d}} \leq 2.0$ and the effective depth d is in mm. The term $100\rho_l$ accounts for dowel action effects; the magnitude of ρ_l considered in the above calculation is limited by, $\rho_1 = \frac{A_{s1}}{b_w d} \leq 0.02$ regardless of the actual amount of longitudinal reinforcement. A_{s1} is the area of the tensile reinforcement, which extends by a length $\geq (l_{bd} + d)$ beyond the critical section as shown in Figure 6.10. b_w is the width of the web cross section. $\sigma_{cp} = N_{Ed}/A_c \leq 0.2f_{cd}$ [MPa]. N_{Ed} is the axial force subjected to the cross section [in N] ($N_{Ed} \geq 0$ for compression). A_c is the area of the cross section. Recommended values of $C_{Rd,c} = 18/\gamma_c$ and $K_1 = 0.15$.

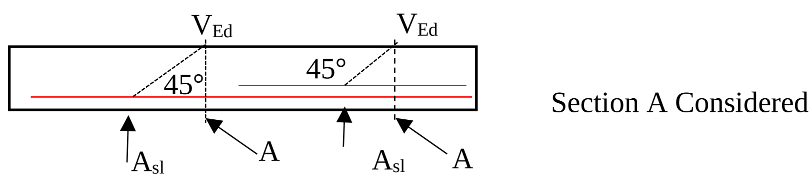

Figure 6.10: Concrete Contribution to Shear Strength Modified from EN 1992-1-1:2004, Section. 6.2.2(1)

With the presence of lap splice at the critical section of the member, the yield moment (M_y) and the yield curvature (φ_y) in Eq. 6.18 and 6.19 should be found considering the reduced steel reinforcement strength. The reduced steel strength is computed by multiplying the steel strength by a factor of $l_o/l_{oy,\,min}$ if $l_o<l_{oy,\,min}$. Here, l_o is the available lap length and $l_{oy,\,min}$ is the minimum required length to sustain flexural yielding. $l_{oy,\,min}$ is calculated according to Eq. 6.10 presented in Section 6.1.3. The yield strain in the last term in Eq. 6.18 should be multiplied by the factor $l_o/l_{oy,min}$. The second term in Eq. 6.18 and 6.19 should be multiplied by $M_{y,reduced}/M_y$, where $M_{y,\,reduced}$ is the flexural capacity of the section with reduced steel yield strength which is calculated as shown in Eq. 6.8 in Section 6.1.3. The reduced $M_{y,reduced}$ should be used to determine whether the term $a_v z$ contributes to the flexural rotation capacity in the first term in Eq. 6.18-6.1.

Shear Strength Estimates

The shear strength of a column according to the EUROCODE III 8 2005 is computed in accordance with Eq. 6.21.

$$[6.21] \quad V_r = \frac{1}{\gamma_{el}}\left[\frac{h-x}{2L_v} min(N; 0.55A_c f_c) + \left(1 - 0.05min(5; {\mu_\Delta}^{pl})\right) \cdot \right.$$
$$\left.\left[0.16max(0.5; 100\rho_{tot}) \cdot \left(1 - 0.16\,min\left(5; \frac{L_v}{h}\right)\right)\sqrt{f_c}A_c + V_w\right)\right]$$

γ_{el} is equal to 1.15 for primary seismic elements and 1.0 for secondary seismic elements. x is the compression zone depth. N is the compression axial force which is taken positive or 0 for compression and tension axial loads, respectively. A_c is the cross-section area, equal to $b_w d$. ρ_{tot} is the total longitudinal reinforcement ratio. Other parameters are defined in Eq. 6.13.

V_w in Eq.6.21 is the contribution of transverse reinforcement to shear resistance and is calculated in accordance with Eq.6.22 for rectangular cross-section columns:

$$[6.22] \quad V_w = \rho_{sx} b_w z f_{yw}$$

where, ρ_{sx} is the transverse reinforcement ratio. Other parameters are defined in Eq.6.13.

EUROCODE III 8 2005 Rotation Capacity at Yielding and Ultimate Using Different Approaches for Curvature Calculations.

Using the EURODCODE 8-III 2005, the yield rotations using different curvature approaches and depth of compression were calculated and shown in Figure 6.11. Figure 6.11a plots the yield rotations using Priestley et al. (1996) curvatures against the yield rotations from Response2000 curvatures. Figure 6.11b plots the yield rotations from Panagiotakos and Fardis (2001) (using the depth of the compression zone from Response2000) against the rotations from Response2000 yield curvature. Figure 6.11c plots the yield rotations from Panagiotakos and Fardis (2001) (using the depth of the compression zone from Panagiotakos and Fardis 2001) against the rotations from Resposne2000 yield curvature.

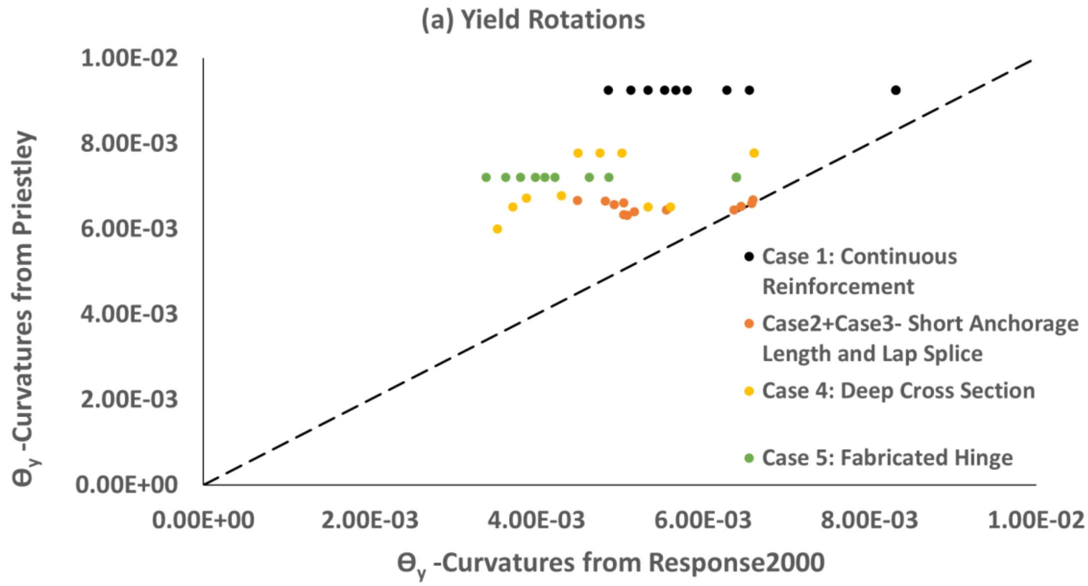

Figure 6.11a: Rotations from Priestly et al. (1996) Yield Curvatures and Response2000 yield Curvatures

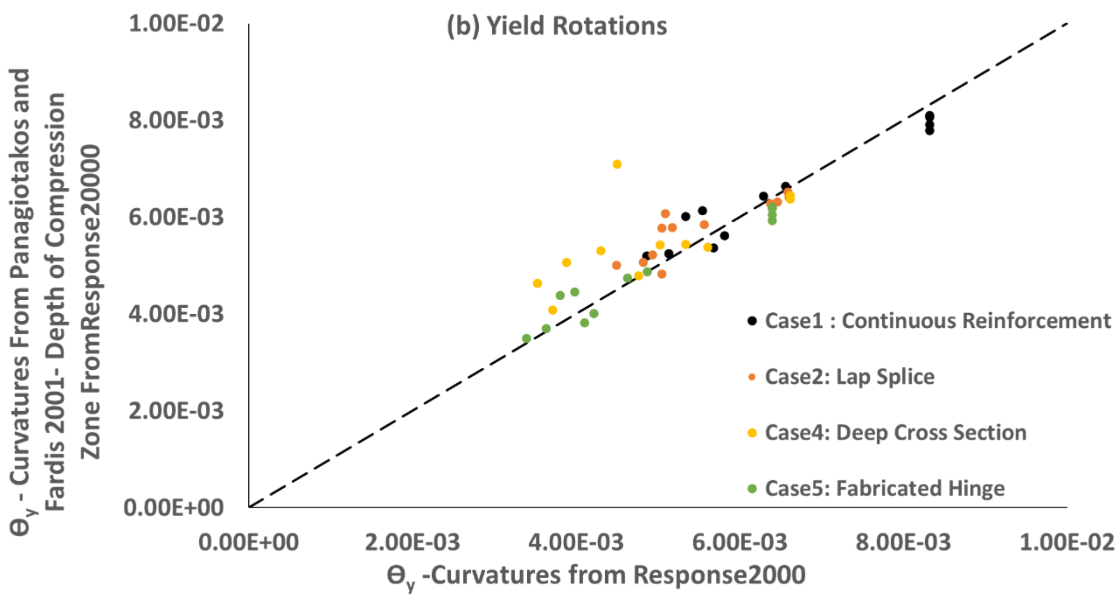

Figure 6.11b: Rotations from Panagiotakos and Fardis (2001) Curvatures Yield Curvatures and Response2000 Curvatures

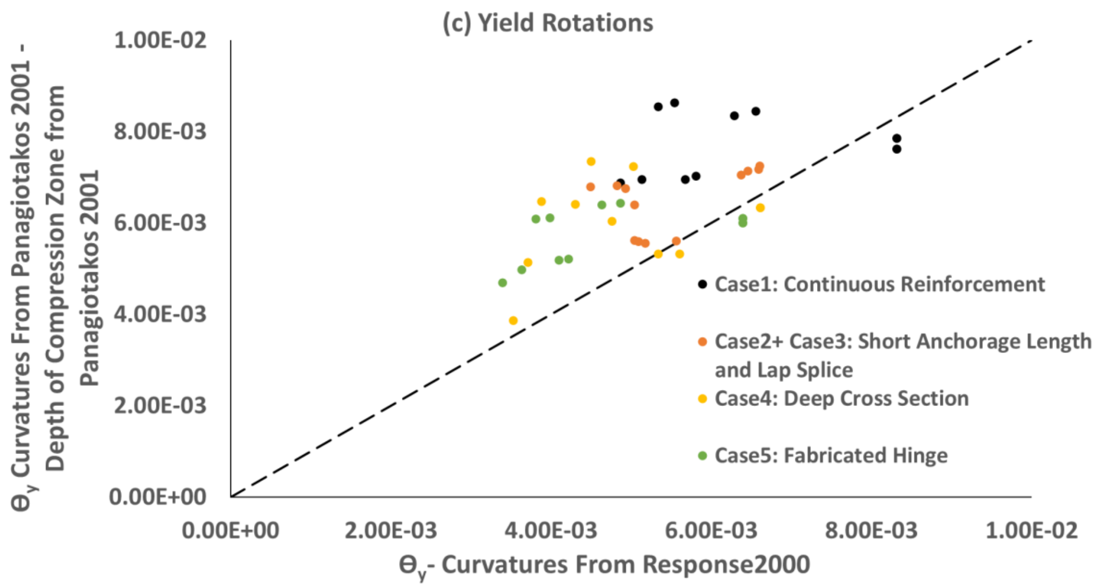

Figure 6.11c: Rotations from Panagiotakos and Fardis (2001) Curvatures Yield Curvatures and Response2000 Curvatures

Figure 6.11: Yielding Rotations Using Different Approaches for Curvature

The differences between the rotations calculated using curvatures from Response2000 and Priestley et al. (1998) are shown in Figure 6.11a. The highest difference recorded in the curvatures between Priestley et al. (1996) equation and Response2000 estimations was 82% (as mentioned in Section 6.2.4 of this Chapter which was in the case of low reinforcement ratio and deep cross section and an axial load 50% of crushing load) produces a difference of 39.1% in the case of yield rotations. In the case when the differences between the two curvature calculations were minimized to 2.6% at lower axial loads, the difference in rotations reached 1.93%.

When calibrating yield rotations obtained from Response2000 curvatures vs. rotations obtained from theoretical curvatures, the differences for most of the sections were less than 20% in all cases as shown in Figure 6.11b. When using the depth of the compression zone at yielding from Panagiotakos and Fardis (2001) model, as shown in Figure 6.11c, the scatter was increased. The highest difference recorded from these two cases was 59.1% at high axial load. When plotting the rotation from Panagiotakos and Fardis (2001) curvatures with the depth of the compression zone from Panagiotakos and Fardis (2001) model against rotations from Response2000 curvatures at

80% of maximum moment the highest difference decreased from 59.1% to 22.5% as shown in Figure 6.12. In this case most of the differences in the rotation in all the sections is less than 30%.

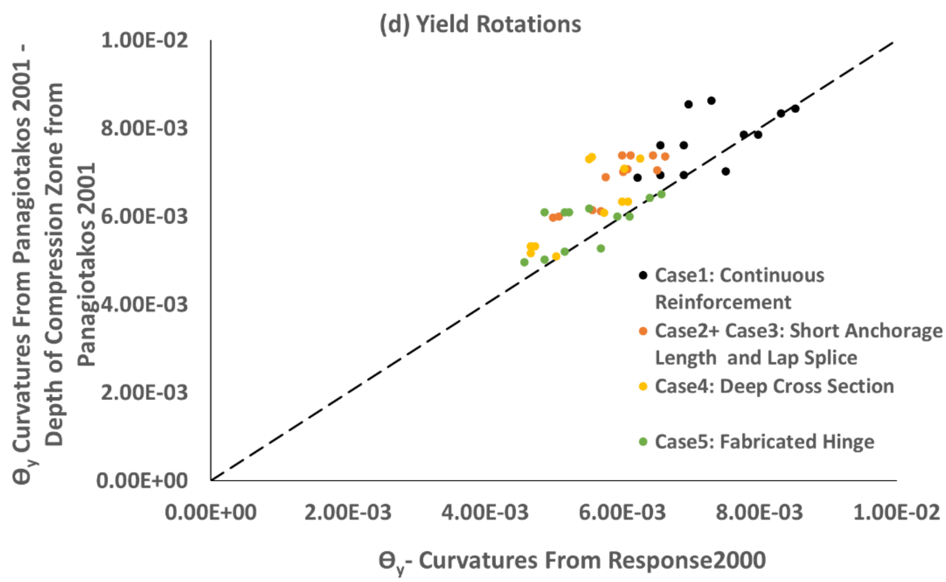

Figure 6.12: Yield Rotation from Panagiotakos and Fardis Curvatures against Resposne2000 Curvatures at 80% of Maximum Moment

Such differences in the yield rotations can over or underestimate the performance level of a component which may lead to an incorrect assessment of anticipated performance in a future design hazard, as well as mislead the selection of a retrofit design to increase the column's capacity. For example, using Priestley et al. (1996) equations for curvature to calculate the rotations for a column with high axial loads may overestimate the deformation strength of the component indicating that the structure is safe with no need for retrofit procedures. An overestimation in the deformation capacity of a component can also be found when using the empirical equation with the depth of the compression zone from Panagiotakos and Fardis (2001) to calculate the rotation capacities at high axial load.

The effect of the curvatures and depth of compression zone are negligible for all cases when calculating the ultimate rotations as shown in Figure 6.13a, b and c.

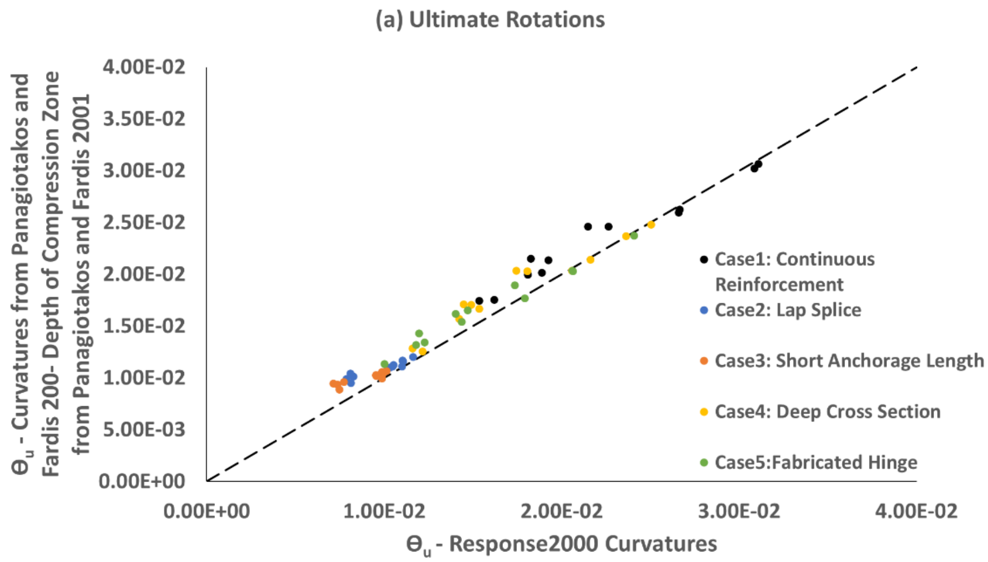

Figure 6.13a: Ultimate Rotation from Panagiotakos and Fardis (2001) Vs. Curvatures from Response2000

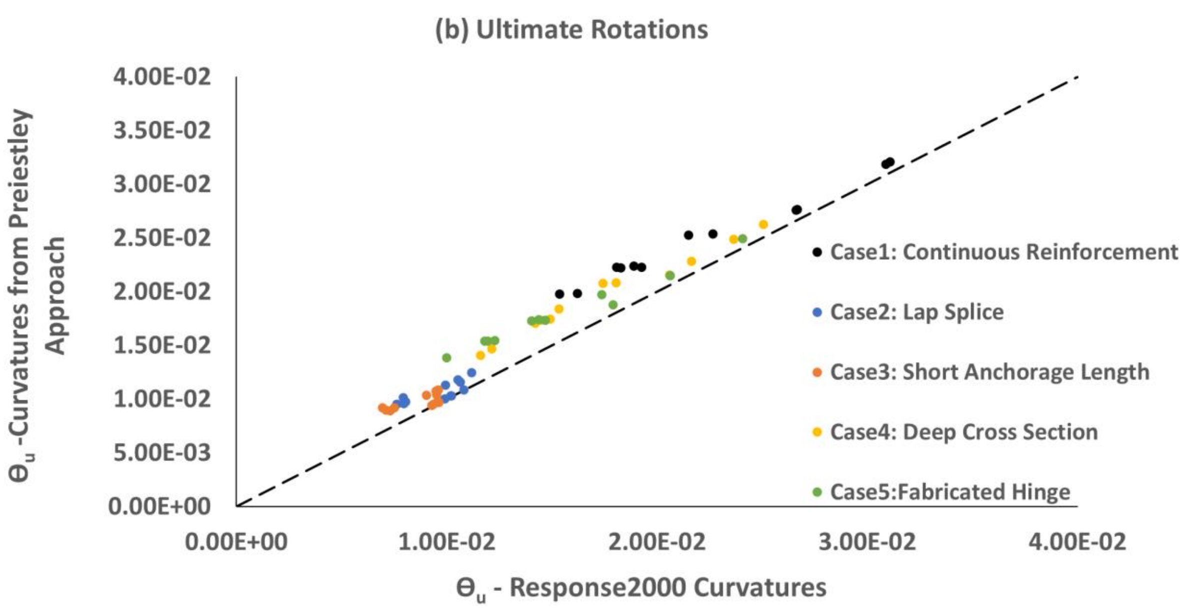

Figure 6.13b: Ultimate Rotation from Priestley's (2001) Model Vs. Curvatures from Response2000

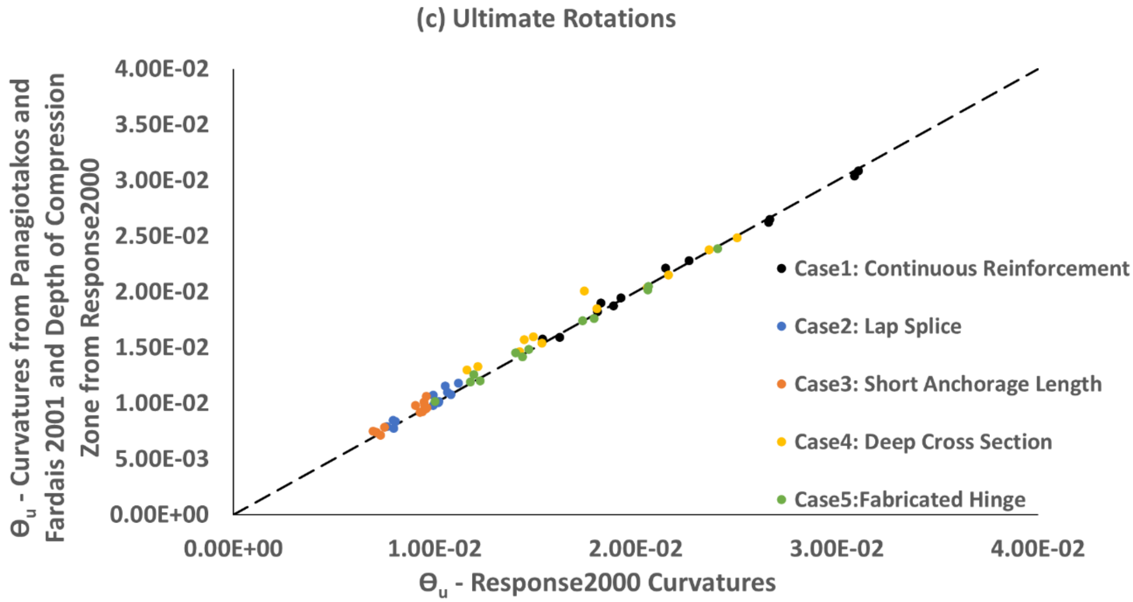

Figure 6.13c: Ultimate Rotation from Priestley's (2001) Model Vs. Curvatures from Response2000

Figure 6.13: Ultimate Rotations Using Eurocode III Part 3 2005 With different Yield Curvatures

The differences with respect to rotations from Response2000 curvatures does not exceed 13% for most cases and approaches. Therefore, regardless of the method used for curvature calculations, the ultimate rotation is not significantly affected. However, scatter was present in the yield rotations with the different curvature approaches used.

6.4.2 ASCE SEI 41-17

The performance level in this code is so called acceptance criteria and were used for retrofit design. The code classified component behavior based on the level of damage to three limit states:

1- In the Operational/Immediate Occupancy: the structural component in this acceptance criteria retains its strength and stiffness after being subjected to ground motion excitation.
2- Life Safety Performance: the component experiences partial or total collapse of the structure, however the vertical components still retain axial capacity.
3- Collapse Prevention: the structural component exhibits no margin against collapse.

The deformation capacity at each limit state is presented in this section.

Deformation Capacity Estimates

Table 6.1 presents the deformation capacities at different acceptance criteria for continuous and lapped reinforcement taken from the ASCE SEI 41/17. Yield rotations were calculated using Lehman's equation as shown in Eq 6.23, 6.24 and 6.25 for flexure, shear and slip respectively. This yield rotation is added to a plastic rotation component according to the calculated limit state.

[6.23] $\theta_{y,flexure} = \dfrac{\varphi L_s}{3}$

[6.24] $\theta_{y,shear} = \dfrac{V_p}{0.4E_c 0.8A_g}$

[2.25] $\theta_{y,slip} = \dfrac{\varphi f_{yl} d_b}{0.4E_c 0.8A_g}$

Table 6.1: Acceptance Criteria and Modeling Parameters form ASCE SEI 41/17 Assessment Codes of Existing Structures

Plastic Rotation	*IO*	*LS*	*CP*
Columns not Controlled by Inadequate Lap Splice Length			
$a = 0.042 - 0.043\dfrac{N_{UD}}{A_g f_c} + 0.063\rho_t - 0.023\dfrac{V_p}{V_{col}}$ $for\ \dfrac{N_{UD}}{A_g f_c} \leq 0.5, b = \dfrac{0.5}{5 + \frac{N_{UD}}{0.8A_g f_c}\frac{1}{\rho_t}\frac{f_c}{f_{y,tr}}} - 0.1 \geq a$	*0.15a ≤0.005*	*0.5b*	*0.7b*
Columns Controlled by Inadequate Lap Splice Length			
$0.025 \leq a = \left(\dfrac{1}{8}\right)\dfrac{\rho_t}{\rho_l}\dfrac{f_{y,tr}}{f_{yl}} \geq 0$ $b = 0.012 - 0.085\dfrac{N_{UD}}{A_g f_c} + 12\rho_t$	*0*	*0.5b*	*0.7b*

In the above expressions, V_p is the shear demand of the column resulting from the earthquake loads, whereas V_{col} is the shear strength of the column. f_c is the column concrete compressive strength. N_{uD} is the axial compressive load. $f_{y,tr}$ is the steel strength of the transverse reinforcement steel. A_g is the cross-sectional area of the column and ρ_t is the ratio of area of distributed transverse reinforcement to gross concrete area perpendicular to that reinforcement = *Av/(bd)*. L_s is the length of the shear span.

Shear strength Calculations

The shear strength for column assessment is calculated according to Eq. 6.26.

$$[2.26]\ V_{col} = \left[\left(\frac{A_V f_{y,tr} d}{s_h}\right) + \lambda\left(\frac{0.5\sqrt{f_c}}{\frac{M_{UD}}{V_{UD}}d}\sqrt{1 + \frac{N_{UG}}{0.5A_g\sqrt{f_c}}}\right)0.8A_g\right]$$

Where, A_V is the area of transverse reinforcement which for perimeter stirrups is $2A_{leg}$. Ratio $\frac{M_{UD}}{V_{UD}}$ is equal to the shear span length and s is the longitudinal transverse spacing.

6.5 ASCE/SEI 14/17 and Eurocode 8-part III 2005 Deformation and Strength Capacity Correlation

The deformation and shear strength of the columns calculated analytically from the finite element analysis is plotted against code based deformation and shear capacities to discover the efficiency of the codes in predicting the deformation capacities of columns.

6.5.1 Deformation Capacities

The numerical model's yield, maximum and ultimate rotations of cantilever columns are plotted against the three limit states as per ASCE SEI 41-17: Immediate Occupancy, life Safety and Collapse Prevention and per EUROCODE 8 III 2005 : Damage Limitation, Significant Damage and Near Collapse levels. The plots are shown in Figure 6.14 from a to f.

The yield rotations for the ASCE SEI 41-17 were calcuted from Lehman et al .(1998) model. The yield rotation in both codes were calculated using Panagiotoaks and Fardis (2001) depth of compression and plast hinge zone yielding curvature.

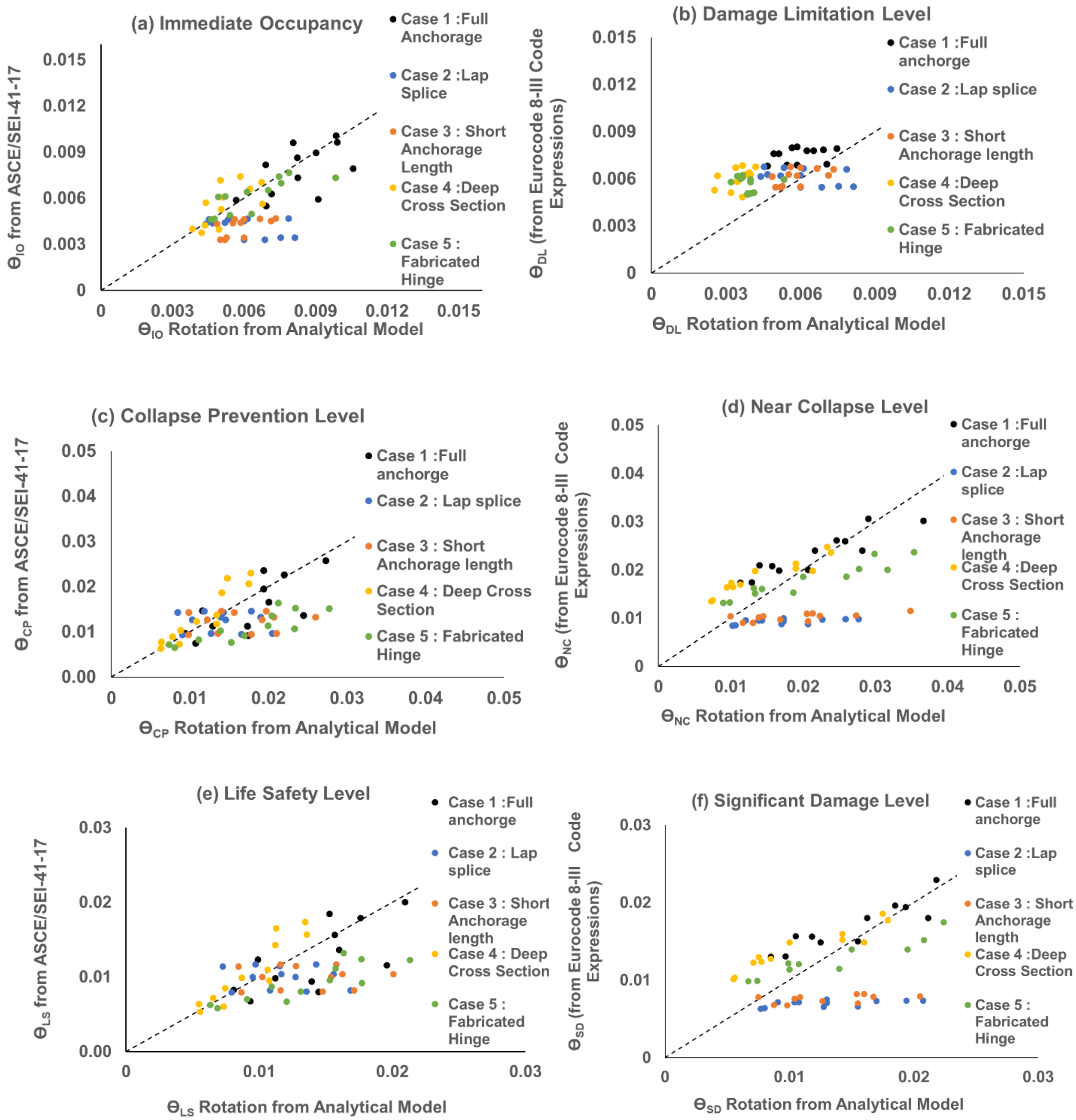

Figure 6.14: Code Estimated Rotation Capacities vs. Values from F.E. Models (a), (c), (e) Limit states from ASCE/SEI 41-17; (b),(d), (e) Limit states from Eurocode 8-III

At Immediate Occupancy the rotations decreased with the increase of the axial load as shown in Figure 6.14a. Most of the column cases, at this performance level, showed more scatter with the increase of the axial load. The code calculations do not correlate well with the column’s behavior at Immediate Occupancy in the lap spice case, as the delay in the yield rotation occurs due to the high slip demand, however the code rotation values depict a decrease in both flexural and slip rotations. The scatter in this case is most likely to decrease with the increase of the axial load with more conservative estimates in code values. Generally, the rotations at Immediate Occupancy showed good correlation in the deformation capacity estimates. This is the result of the flexural shear yielding strength (V_y) contribution in the calculations of yield rotations from Lehman et al. (1996) used to calculate Immediate Occupancy state.

At Damage Limitation the differences increased at low axial load as the EUROCODE 8 Part III-2005 showed less conservatism as shown in Figure 6.14b. However, conservative estimates for the lap splice were observed, similar to the Immediate Occupancy level especially at low axial load. The delay in the flexural yielding rotations due to increase in slip rotations was not reflected by the code properly. With the increase of the cross-section depth the differences increased with less conservative values in the code estimates. The shear rotations at yielding for the Damage Limitation do not capture the actual shear rotation demand of the column. This is because the shear rotation at Damage Limitation is insensitive to the shear demand. Therefore, due to the increase of the shear demand as a result of a larger internal lever arm in the cross section (where yielding of the stirrups at an earlier stage prior to or with flexural yielding at higher reinforcement), the scatter in deeper sections is more intense compared to the smaller cross section.

It is concluded from the Near Collapse/Collapse Prevention state, that the ASCE SEI 41 17 shows conservative estimates compared to the EUROCODE 8 Part III 2005 as shown in Figure 6.14 c and d respectively. At Near Collapse the differences increased with the increase in the axial load. For the lap splice and the short anchorage length, the increase of the ultimate deformation when increasing the axial load observed in the finite element analysis was not observed in the code estimates. For this case, the codes estimated a decrease in the rotation with the increase of the axial loads. Therefore, the differences between the codes and the finite element analysis values increased with the increase of the axial load. Both codes overestimated the rotation at this limit state for the lap splice and short anchorage length. The EUROCODE 8 Part III 2005 overestimated the deformation capacities of columns failing in shear and buckling and concrete crushing and better correlation to flexural columns compared to the ASCE SEI 41-17. ASCE SEI 41 17 shows good agreement when the column fails in shear or concrete crushing.

The Significant Damage/Damage Limitation shows the same scatter as Near Collapse/Collapse Prevention as shown in Figure 6.14 e and f respectively. The only differences between the two limit states/acceptance criteria, is that a factor multiplied the rotation values at Near Collapse/Collapse Prevention.

6.5.2 Shear Strength Estimates

The shear strength is plotted against the base shear found from the Finite element analysis assuming a displacement ductility demand factor of 1 for both codes. The plots are shown in Figure 6.15 for the ASCE SEI 41-17 and 6.16 for EUROCODE 8 Part III 2005.

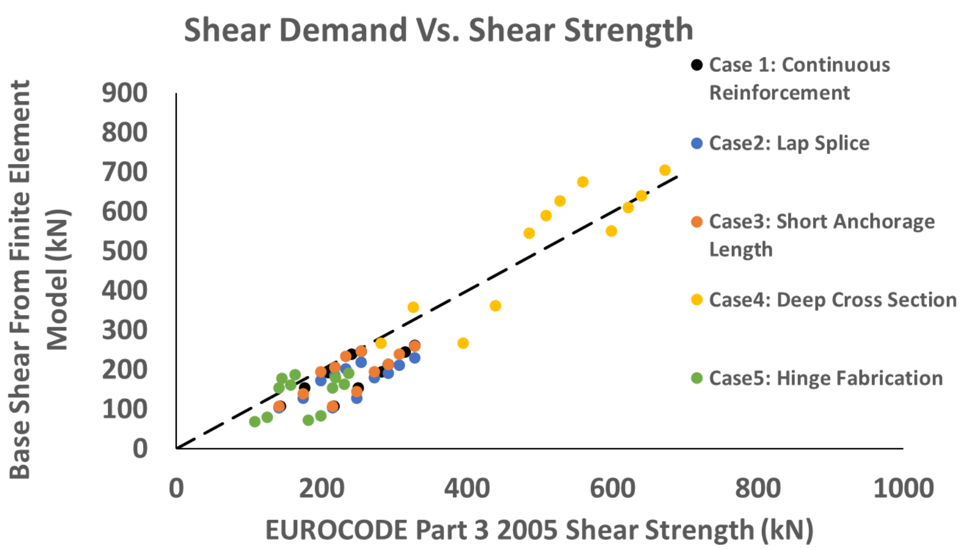

Figure 6.15: Base Shear demand at flexural yielding obtained from Finite Element Analysis vs. ASCE SEI 41-17 Shear Strength Calculations

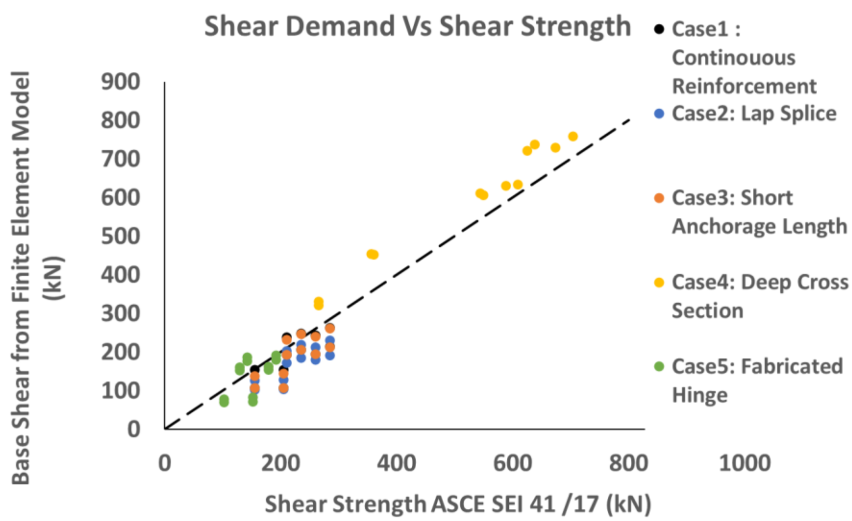

6.16: Base Shear demand at flexural yielding obtained from Finite Element Analysis vs. EUROCODE 8 Part III Shear Strength Calculations

The two codes show similar trends when comparing the base shear demand at flexural yielding (referred to also as flexural shear strength) to the shear strength from the two codes. From the two Figures 6.16 and 6.17, shear failure is estimated by the codes if the point is above the 45° line. The ASCE SEI 41-17 shows estimation of shear failure for all column cases for the deep cross section which is compatible with the finite element findings. The EUROCODE 8 Part III eliminates three columns with deep cross section from failing in shear. Therefore ASCE SEI 41-17 is more conservative for the case of deep cross section.

No shear failure was present in the case of fabricated hinge whereas the codes were conservative in the estimation of shear failure of four columns with sparse stirrup spacing. Columns with low axial load and sparse stirrup spacing are also close or on the 45° line in the ASCE SEI 41-17 which indicates good agreement between the finite element analysis findings and the code predictions. In the ASCE EI 41-17 the column shear strength is insensitive to the longitudinal reinforcement ratio and the steel yield strength. Shear failure occurred in the column with low axial load, sparse stirrup spacing and low reinforcement ratio for most of the column longitudinal detailing cases. However, these columns were located below the line in the ASCE SEI 41-17. The EUROCODE 8 Part III 2005 takes into consideration the longitudinal reinforcement ratio and therefore the columns that failed due to shear with low reinforcement ratio are located on the 45° line.

7. Behaviour of Columns Under Reversed Cyclic Loading

The efficiency of the finite element models in estimating deformation capacities and shear strength under cyclic load reversals will be explored in this Chapter. The experimental analysis for the full scale columns conducted by Sokoli and Ghannoum (2016) will be calibrated against the finite element analysis using ATENA Studio. The results and mode of failure of the finite element will be compared to the experimental results, in order to determine the advantages and the drawbacks of finite element modelling for developing column resistance curves.

7.1 Column's Geometry and Experimental Test Set up

The scope of Sokoli and Ghannoum (2006) experimental study aimed to investigate the role of high strength steel on the deformation capacity and shear transfer mechanisms of columns. The study of Sokoli and Ghannoum (2016) was the first to compare the performance of a column seismically detailed and reinforced with conventional steel strength of Grade 60 A706 (Column CS60) with the performance of columns seismically detailed and reinforced with newly developed high strength steel of Grade 80 (Column CS80) and Grade 100 (Column CS100).

Sokoli and Ghannoum (2016) subjected three columns to quasi-static reversed cyclic loading until shear and axial failure. The three columns were geometrically identical as shown in Figure 7.1. The three columns (CS60, CS80 and CS100) were designed to have the same flexural capacity and therefore identical shear demands. The hoop design was governed by shear requirements for all three columns. The specifications of hoop spacing according to ACI 318M-14 for confinement were meet in Column CS100. The hoop spacing in column CS60 and CS80 exceeded the maximum specified spacing for confinement according to ACI 318M-14 by 25 mm (1 in).

The longitudinal reinforcement for Column CS60 consisted of #10 bars with diameter of 32 mm. The transverse reinforcement for Column CS60 consisted of #5 bars with a diameter 16 mm and a spacing of 140 mm. For Column CS80, the longitudinal reinforcement consisted of #9 bars with diameter of 29 mm. The transverse reinforcement consisted of #bars with diameter of 13 mm and spacing of 140 mm. For Column CS100, the longitudinal reinforcement consisted of #8 bars with

25 mm diameter and the transverse reinforcement was spaced at a distance of 114 mm with #3 bars (10 mm diameter).

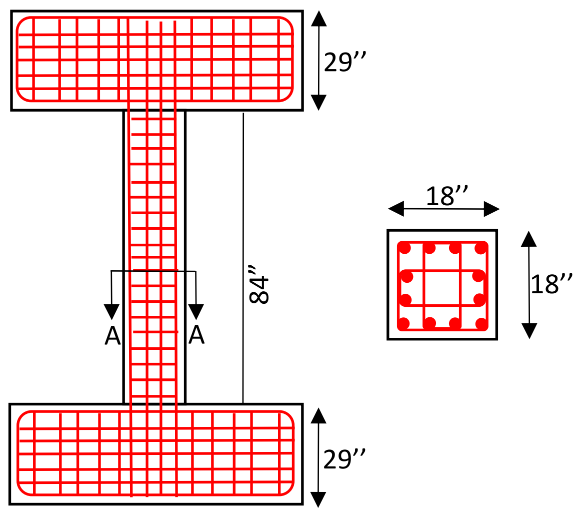

Figure 7.1: Vertical Section of Sokoli and Ghannoum (2016) and Geometry of Cross-Section

The three columns were tested under symmetric double curvature with fixed rotations at the top and bottom. The columns were prestressed to a strong ground floor. Two vertical actuators applied a constant compressive axial load during testing. The total resulting compressive load was 1646 kN. The applied lateral loading history was as per FEMA 461 recommendations, which consisted of two fully reversed cycles with increasing target drift ratio. The target drift ratios were 0.2, 0.3, 0.4, 0.6, 0.8, 1.0, 1.5, 2.0, 3.0, 4.0, 5.5, and 7.0%. The columns were instrumented to measure the applied loads, surface deformations and the strains in the bars.

7.2 Experimental Material Properties

The concrete strength was measured from the average of three-cylinder concrete compressive tests for each column. The average concrete compressive strength from the cylinder compressive strength tests were 26.4 MPa, 28.8 MPa and 32 MPa for Columns CS60, CS8 and CS100 respectively. The strength of the transverse and longitudinal reinforcement were measured from the averages of the tensile strength from three coupon tests per bar. Table 7.1 displays the yield and ultimate strength and the fracture elongation of each bar.

Table 7.1: Transverse and Longitudinal Reinforcement Strength (Sokoli and Ghannoum 2016)

Bar Size (mm)	Grade	Yield Strength ksi (MPa)	Ultimate Tensile Strength ksi (MPa)	Fracture Elongation %
No.10 (32)	60	67.3 (464)	94.9 (654)	18.3
No.9 (29)	80	79.1 (545)	106.5 (734)	15.5
No.8 (25)	100	101.5 (700)	128.5 (886)	11.6
No.5 (16)	60	68.5 (472)	95.8 (660)	14.4
No.4 (13)	80	83.7 (577)	11.4 (768)	12.1
No.3 (10)	120	118.9 (8200	141.0 (972)	10.1

7.3 Finite Element Modeling

ATENA GiD 15.0.1 interface was used to model the columns. ATENA GiD 15.0.1 has advantages over ATENA Engineering 3D interface that was used for the columns under monotonic loading described in Chapter 3. The first advantage is that ATENA GiD consumes less running time compared to ATENA Engineering 3D. When applying cyclic load to the finite element model, each analytical step should be approximately 0.1 mm to achieve convergence especially in the unloading phase of the cyclic reponse. This results in around 24000 analytical steps for the case of the described lateral loading history in the experimental analysis, so speeding up the solution was critical for the completion of the runs. Still, it took several days of running time to complete one column analysis. The second advantage, is the advanced concrete crack models (Fixed, Rotated and Hybrid) and solution parameters provided in the GiD 15.0.1 interface that allow the convergence of the problem to be achieved easily and fast. The variety in the concrete crack models allows the user additional options to achieve higher agreement in the results of the analytical and experimental problem.

7.3.1 Concrete Models

Due to difficulties in convergence of the NonlinearCementitious2 User Defined concrete model (used in monotonic loading), it was replaced with the concrete model NonlinearCementitious2 model. The concrete core and cover were assigned different concrete material properties. Concrete material parameters for concrete cover and core are given for the three columns are shown in Table 7.2.

Table 7.2: Input Parameters for Sokoli and Ghannoum Analytical Columns

Parameter	CS60 (Core)	CS80 (Core)	CS100 (Core)	Cover for all Columns
Young's Modulus (MPa)	23100	23100	23100	23100
Poisson's Ratio	0.2	0.2	0.2	0.2
Tension strength (MPa)	2.3	2.3	2.3	2.3
Compression Strength (MPa)	31.1	32	32.4	26.4, 28.8, 32
Energy Facture (MN/m)	133	133	133	133
Fixed Crack Model	0	0	0	0
Aggregate Size (m)	0.02	0.02	0.02	0.02
Unloading Factor	0.1	0.1	0.1	0.1
Plastic Strain ε_{cp}	0.00101	0.00101	0.00101	0.00085
Onset of Concrete Crushing (f_{co}) (MPa)	4.8	4.8	4.8	4.8
Critical Compression Displacement (w_d)	8.1	5.5	4.2	1.2
f_c reduction (MPa)	0.8	0.8	0.8	0.8
Crush Band Minimum (m)	0.3	0.3	0.3	0.3

The definition of each parameter will be described as following:

Compressive Strength, Critical Compression Displacement, and Crush Band Size

The concrete compressive strength used in the column cover was as specified in the experimental study. The concrete core strength is modelled to account for strength enhancement due to confinement of the transverse reinforcement and cover. The modified Kent and Park (Park et al. 1982) concrete stress and strain model was used to calculate the stress strain relationship for the core of the three columns. The Model is reviewed in Chapter 3, Section 3.2.1. The calculated stress-strain curves for all the columns are depicted in Figure 7.2 for the confined core and 7.3 for the stress strain curves of the unconfined cover for each column.

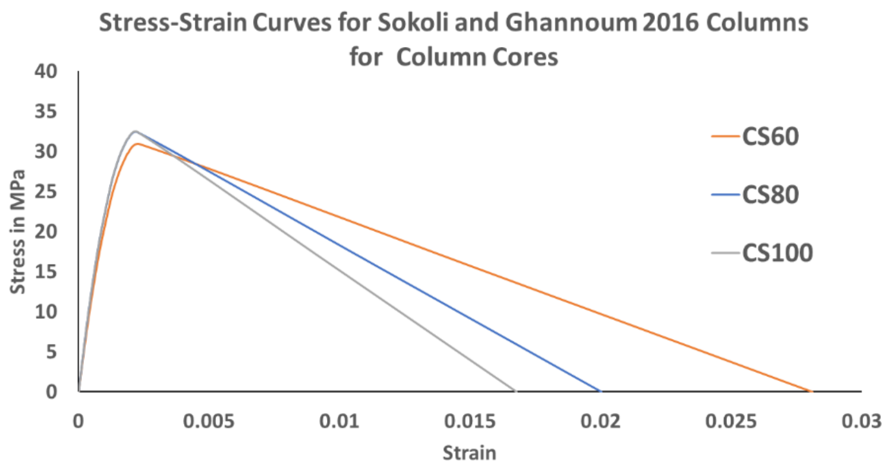

Figure 7.2: Stress-Strain Curve for Confined Core

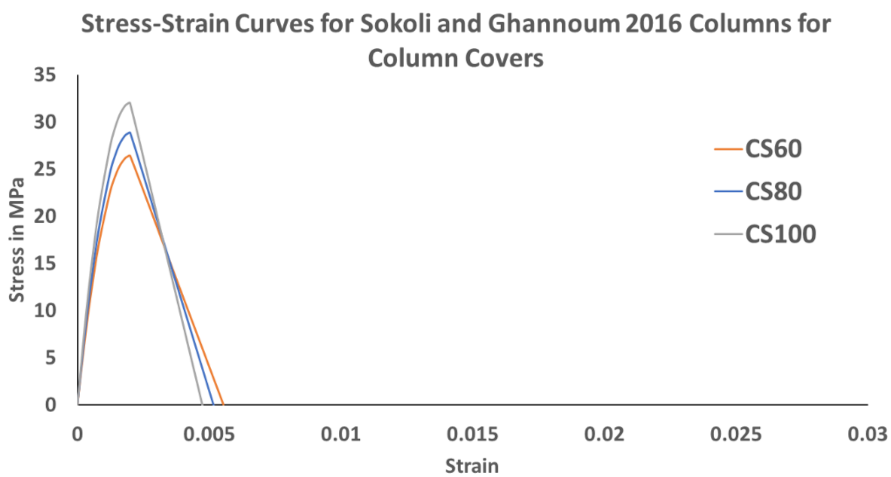

Figure 7.3: Stress-Strain Curves for Unconfined cover

The critical compression displacement (w_d) is defined in Figure 7.4. The critical compression displacement divided by the length of the process zone (e.g. the height of a cylinder tested in compression to measure the stress-strain response, length L_d in Figure 7.4) is the plastic compression strain. Parameter w_d represents the plastic shortening of the softening curve in the stress strain relation for each column.

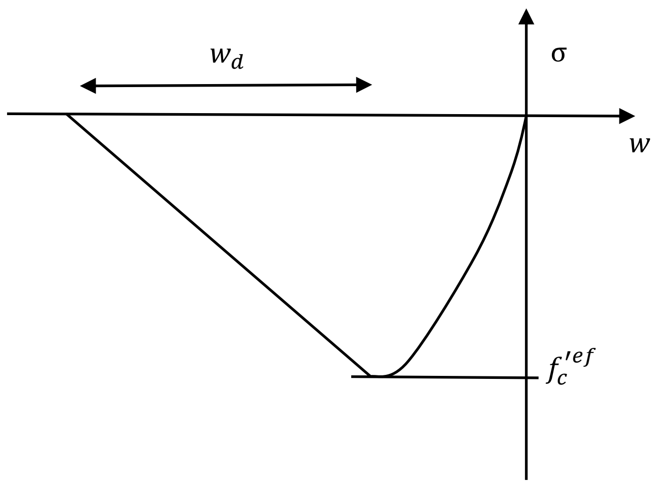

Figure 7.4: Critical Compressive Displacement Definition (Modified from Cervenka et al. 2020)

The critical compressive displacement was calculated in accordance to Eq. 7.1. (Cervenka et al. 2020)

[7.1] $w_d = (\varepsilon_d - \varepsilon_c)L_d$

where ε_d is the strain at a compressive strength of 0 (the last point on the softening branch of the concrete stress-strain curve that intersects with the x-axis) (Cervenka et al. 2020). ε_c is the strain corresponding to the maximum concrete strength. L_d is the crushing band size. If the crushing band size is not activated, L_d will be equal to the mesh size. In order to decrease mesh dependency, the crushing band size was activated and taken as 0.3 m (default value) (Cervenka et al. 2020). The parameter w_d was calculated based on the stress strain curves shown in Figure 7.2.

Young's Modulus:

The initial elastic modulus was calculated based on design code specifications (CSA. A23-14) as shown in Eq. 7.2

[7.2] $E_c = 4500\sqrt{f_c}$

Fracture Energy

The fracture energy is defined as shown in Figure 7.5. The fracture energy is crucial in the model used, for the calculations of the crack width (Cervenka et al. 2020) as shown in Figure 7.5.

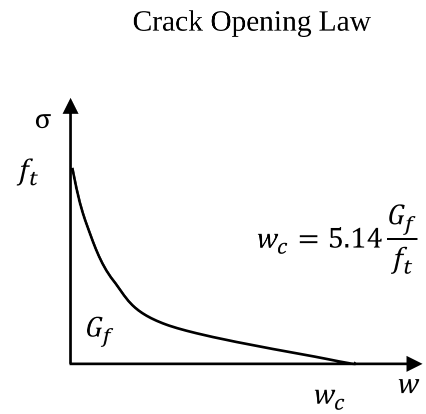

Figure 7.5: Fracture Energy Definition (Modified from Cervenka et al. 2020)

The energy fracture was calculated as shown in Eq. 7.3 from the fib Model Code 2010.

[7.3] $G_F = 73f_{cm}^{0.18}$ (in N/m)

Onset of Crushing

The onset of concrete crushing specified from ATENA 3D theory manual should range between 2 times the tensile strength of concrete and the maximum compressive strength (Cervenka et al. 2020). The input value in the program was taken as the minimum = $2f_t$.

Plastic Strain

The plastic strain of concrete is the strain corresponding the maximum compressive strength after subtracting the linear portion of the stress strain relation (f_c/E_c).

Unloading factor

The unloading factor is a factor that affects the unloading phase of the cyclic response. The factor ranges from 0-0.999. The value of 0 allows the unloading path of the hysteresis loop to go through the origin whereas the value of 0.999 allows the unloading stiffness to be parallel to the initial stiffness. Figure 7.6 depicts the concrete model under loading and unloading. An intermediate value allows for degradation of the unloading stiffness and softening of the unloading loops when tending to zero stress levels.

Stress-Strain Relation Ship Under Loading and Unloading

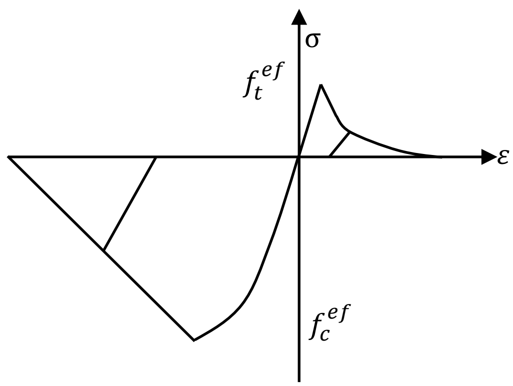

Figure 7.6: NonlinearCementitious2 Material Under Loading and Unloading. (Modified from Cervenka et al. 2020)

Fixed Crack Model Parameter

The NonlinearCementitious2 concrete model offers the user three different crack models; Fixed, Rotated and Hybrid.

Fixed Crack Model

In the fixed crack model, the crack direction is fixed after it has occurred in the finite element and is given by the orthotropy axis (Cervenka 1985, Darwin 1974). The fixed cracked model is depicted in Figure 7.7. (Cervenka et al. 2020)

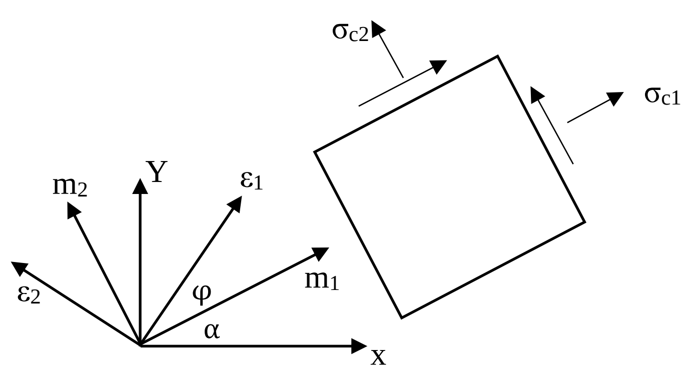

Figure 7.7: Fixed Crack Model (Modified from Cervenka et al. 2020)

In an uncracked section the principle stress and the strain axis coincide. After the section is cracked, the axes of orthotropy m_1 and m_2 form an angle with the principal strain axes ε_1 and ε_2. Here m_1 is the weak axis and is perpendicular to the crack direction while m_2 is parallel to cracking (strong axis) (Cervenka et al. 2020). Slip along the cracks due to shear stress are produced to achieve equilibrium. σ_{c2} and σ_{c1} are the shear stress normal and parallel to the crack. The shear modulus in an uncracked section derived from Kolmar 1986 in a fixed crack model is calculated by Eq. 7.4 (Cervenka et al. 2020). The reduced shear modulus after cracking is shown in Eq. 7.5 (Cervenka et al. 2020).

[7.4] $G_c = \dfrac{E_c}{2(1+v)}$

[7.5] $G = r_g G_c$

where G_c is the initial shear modulus, and G is the reduced shear modulus. E_c is the initial elastic modulus. v is Poisson's ratio. r_g is the shear tension factor and is calculated in accordance with Eq. 7.6 (Cervenka et al. 2020).

[7.6] $r_g = c_3 \dfrac{-\ln\left(\frac{\varepsilon_u}{c_1}\right)}{c_2}$

where ε_u is the crack opening strain, c_3 is the scaling user factor and is equal to 1 by default. Parameters c_1 and c_2 are calculated by Eq. 7.7 and 7.8 respectively (Cervenka et al. 2020).

[7.7] $c_1 = 7 + 333(p - 0.005)$

[7.8] $c_2 = 10 - 167(p - 0.005)$

where p is the transformed reinforcement ratio on the crack plane and ranges between 0 to 0.02. The shear stress on the crack plane is an additional constraint imposed on the shear modulus, it is calculated as $\tau_{uv} = G\gamma$ and is limited to f_t (Concrete tensile strength) (Cervenka et al. 2020).

Rotated Crack Model

The rotated crack model was developed by Vecchio 1986 and by Crisfield 1989. The axis of orthotropy rotates with the principal axis. The principal stress and strains coincide after cracking.

Therefore, no shear stresses are produced along the crack (Cervenka et al. 2020). Figure 7.8 depicts the concept of the rotated crack model.

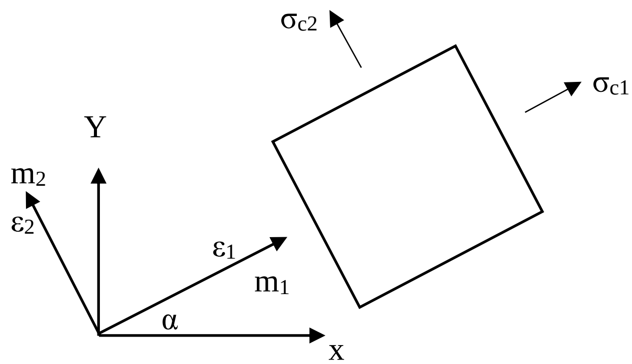

Figure 7.8: Rotated Crack Model (Modified from Cervenka et al. 2020)

In this case the principal axis rotates, therefore the crack direction rotates as well. The tangent shear modulus under rotated crack conditions to maintained the coincidence of the principal and the orthotropic axis is calculated in accordance to Eq. 7.9 (Crisfield 1989)

[7.9] $G_t = \dfrac{(\sigma_{c1} - \sigma_{c2})}{2(\varepsilon_1 - \varepsilon_2)}$

Equation 7.9 parameters are defined in Figure 7.2.

To activate the fixed crack a value of 1 is inputted to the parameter “fixed” in the concrete material definition window. A value of zero was given to that parameter to activate the rotated crack model. Applying a fraction between 0 and 1 enables a hybrid crack model which combines the fixed and the crack model.

Biaxial failure Criteria

The material failure criteria was biaxial failure. The biaxial failure law of the concrete is shown in Figure 7.9.

Biaxial Failure Law

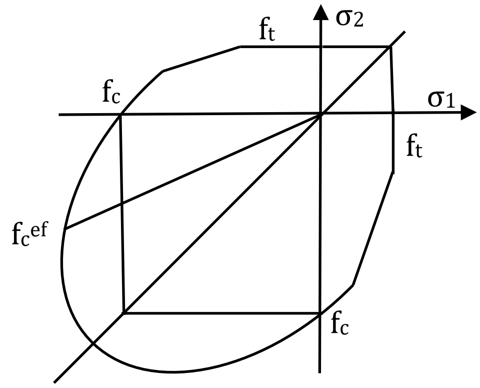

Figure 7.9: Biaxial Failure Law (Modified from Cervenka et al. 2020)

The biaxial failure criterion is developed by Kupfur et al. (1969). The compression-compression state function is shown in Eq.7.10 (Cervenka et al. 2020)

[7.10] $f_c'^{eff} = \frac{1+3.65a}{(1+a)^2} f_c$

Where a = $\frac{\sigma_{c1}}{\sigma_{c2}}$, f_c is the uniaxial cylinder strength and σ_{c1}, σ_{c2} are the principle stress in concrete.

For the tension-compression region, the strength decreases linearly according to Eq. 7.11 (Cervenka et al. 2020)

[7.11] $f_c'^{eff} = f_c r_{ec}$

where $r_{ec}$is the compressive strength reduction factor and is calculated in accordance to Eq. 7.12 and ranges from 1.0 - 0.9. This factor represents the reduction in the compressive strength in direction 2 due to the tensile stress in the principal direction 1. (Cervenka et al. 2020)

[7.12] $r_{ec} = \left(1 + 5.2378 \frac{\sigma_{c1}}{f_c}\right)$

7.3.2 Cyclic Reinforcement Models

The steel reinforcement stress strain relation under cyclic loading is described by the nonlinear Menegotto Pinto 1973 model, with consideration of the Bauschinger effect (R). The model is shown in Figure 7.10.

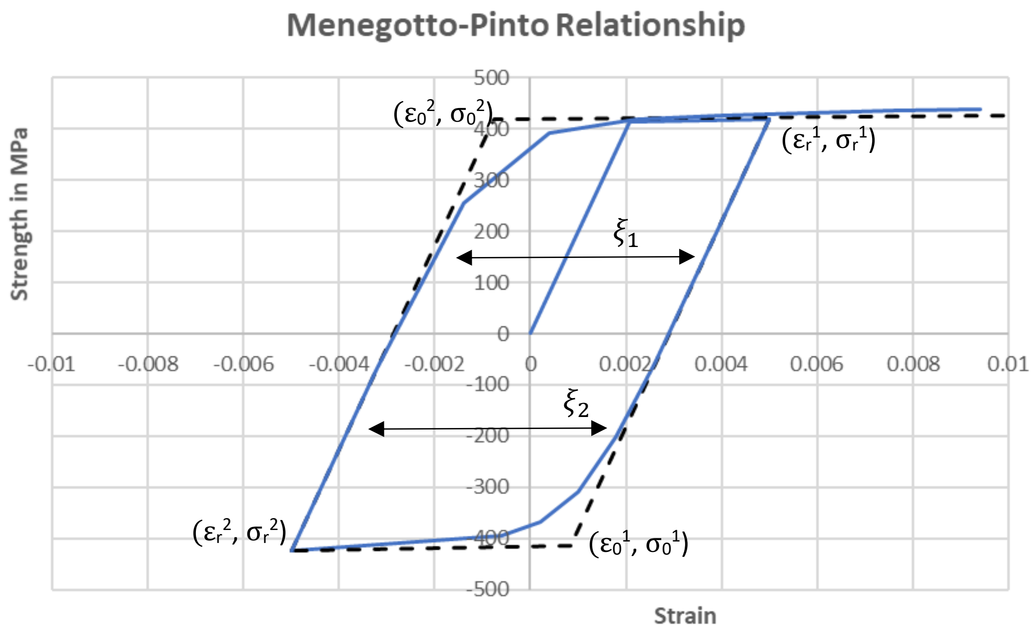

Figure 7.10: Menegotto Pinto Relation (Modified from Cervenka et al. 2020)

The steel stress in each branch of one complete cycle is calculated as shown in Eq. 7.13. (Menegotto et al. 1973).

[7.13] $\sigma = (\sigma_o - \sigma_r)\sigma^* + \sigma_r$

where the stress $\sigma^*$is defined in Eq. 7.14 (Menegotto et al. 1973).

[7.14] $\sigma^* = b\varepsilon^* + \dfrac{(1-b)\varepsilon^*}{\left(1+\varepsilon^{*R}\right)^{\frac{1}{R}}}$

and b is the hardening modulus of elasticity, the strain $\varepsilon^*$is defined in Eq. 7.15 and R is calculated in accordance to Eq.7.16 (Menegotto et al. 1973).

[7.15] $\sigma^* = b\varepsilon^* + \dfrac{(1-b)\varepsilon^*}{\left(1+\varepsilon^{*R}\right)^{\frac{1}{R}}}$

[7.16] $\varepsilon^* = \dfrac{\varepsilon - \varepsilon_r}{\varepsilon_o - \varepsilon_r}$

The strains ε_r and ε_o and the stresses σ_o and σ_r are described in Figure 7.11. The subscript ($_o$) presents the start point of the hysteretic branch while ($_r$) represents the end point of the branch. The strain and stress ${\varepsilon_o}^1$ and ${\sigma_0}^1$ respectively were calculated according to Eq. 7.17 and 7.18 (Hoehler 2002).

$$[7.17]\ \ {\varepsilon_o}^1 = \frac{E^2{\varepsilon_r}^1 - E{\sigma_r}^1 - f_yE - H\ |\varepsilon_r^1|E + H|\sigma_r^1| + Hf_y}{E(E-H)}$$

$$[7.18]\ \ {\sigma_o}^1 = \frac{-f_yE - H\ |\varepsilon_r^1|E + H|\sigma_r^1| + Hf_y + E{\varepsilon_r}^1H - {\sigma_r}^1H}{(E-H)}$$

where ${\varepsilon_r}^1$ is assumed 0.005 for calculation and presentation purposes (as shown in Figure 7.12) purposes and ${\sigma_r}^1$ is the corresponding stress. The strain and stress ${\varepsilon_o}^2$ and ${\sigma_o}^2$ respectively were calculated according to Eq. 7.19 and 7.20 (Hoehler 2002).

$$[7.19]\ \ {\varepsilon_o}^2 = \frac{E^2{\varepsilon_r}^2 - E{\sigma_r}^2 + f_yE + H\ |\varepsilon_r^2|E - H|\sigma_r^2| - Hf_y}{E(E-H)}$$

$$[7.20]\ \ {\sigma_o}^2 = \frac{f_yE + H\ |\varepsilon_r^2|E - H|\sigma_r^2| - Hf_y + E{\varepsilon_r}^2H - {\sigma_r}^2H}{(E-H)}$$

where ${\varepsilon_r}^1$ is assumed -0.005 for calculation and presentation purposes (as shown in Figure 7.12) and ${\sigma_r}^1$ is the corresponding stress. The parameter R that accounts for the Bauschinger effect and is calculated according to Eq. 7.21 (Menegotto et al. 1973).

$$[7.21]\ \ R = R_o - \frac{c_1\xi}{c_2 + \xi}$$

where $\xi_1$and ξ_2 are determined for loading and unloading branches as shown in Figure 7.11. The parameters R_o, c_1 and c_2 are constants that control the transition between loading and unloading.

The values given in the present simulations for parameters R_o, c_1 and c_2 are 7, 5000 and 20 and the longitudinal steel stress strain curve given for each column is shown in Figure 7.12. Where the continuous line is the steel stress strain relation and the discontinuous line is the tangent of the steel stress relation. The steel stress strain plot in Figure 7.11 assumes that the unloading and the reloading at a certain cycle occurs at a strain of 0.005 and -0.005 respectively for all columns.

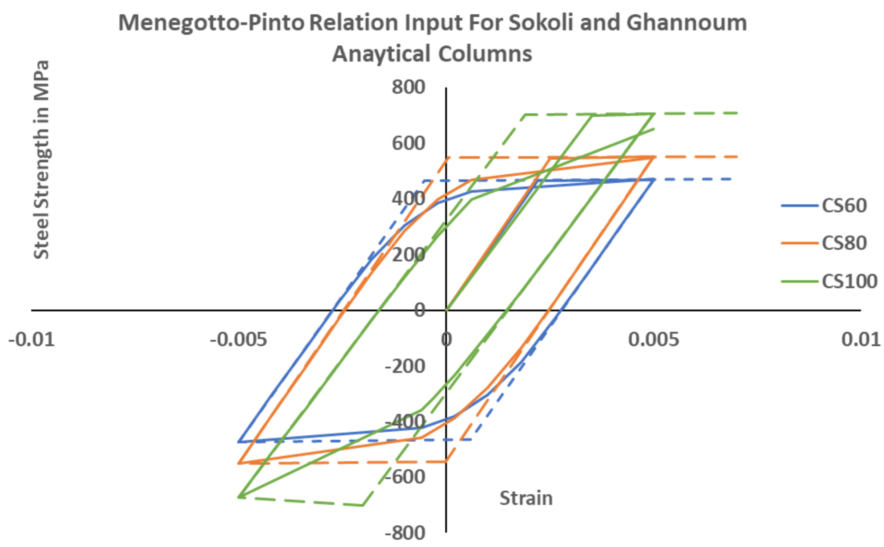

Figure 7.11: Stress Strain Relation for Steel of the Sokoli and Ghannoum Columns (2016)

7.3.3 Cyclic Bond Model

The constitutive model for bond described in Chapter 3 "Memory Bond Model" is used to simulate the properties of the springs that connect the reinforcement and concrete. Note for cyclic loading, it is crucial to define the parameter τ_1. When the bond changes directions (signs) during loading and unloading the bond strength is reduced to τ_1. The parameter τ_1 ranges between the maximum and the residual bond strength. The bond model under cyclic loading is shown in Figure 7.12.

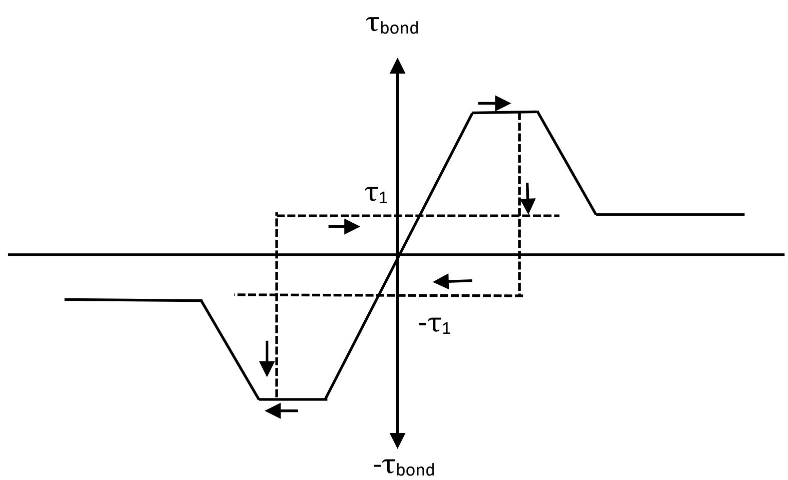

Figure 7.12: Bond Stress Relation for "Memory Bond Model" in ATENA 3D (Modified from Cervenka et al. 2020)

The fib 2010 Model code was used for the bond stress-slip relation for the springs reviewed in in Chapter 3. The sections of the three columns were well confined sections therefore the maximum bond strength assumed for a splitting case is $8(f_c/25)^{0.5}$.

The bond stress relation calculated for the three column cases are as following:

Maximum Bond Strength ($\tau_{u,split}$)

The unconfined concrete strength for all cases was used to calculate the maximum bond strength according to fib Model Code 2010, as $8\cdot(f_c/25)^{0.5}$

1) CS60: $\tau_{u,split}= 8(26.4/25)^{0.5}= 8.11$ MPa
2) CS80: $\tau_{u,split}= 8(28.8/25)^{0.5}= 8.23$ MPa
3) CS100: $\tau_{u,split}= 8(32/25)^{0.5}= 9.05$ MPa

The residual bond strength was equal to 0.4 $\tau_{u,split}$ and was used for the parameter $\tau_{1.}$

Slip Calculations

The slip at the maximum bond stress at the beginning of the plateau (s) is calculated from the fib Model Code 2010 shown in Eq. 7.22.

$$[7.22]\ \ s = \sqrt[0.4]{\frac{\tau_{u,split}}{\tau_{bmax}}}s_1$$

where s_1 for confined cases is equal to 1 mm (fib Model Code 2010). τ_{bmax} is the maximum bond stress when pullout failure is controlled and is calculated in accordance to Eq. 7.23 (fib Model Code 2010).

$$[7.23]\ \tau_{bmax} = 2.5(f_c)^{0.5}$$

1) CS60: $\tau_{bmax} = 2.5(26.4)^{0.5} = 12.8\ MPa$

$$s = \sqrt[0.4]{\frac{8.11}{12.8}}(1) = 0.32\ m$$

2) CS80: $\tau_{bmax} = 2.5(28.8)^{0.5} = 13.4\ MPa$

$$s = \sqrt[0.4]{\frac{8.23}{13.4}}(1) = 0.30\ m$$

3) CS100: $\tau_{bmax} = 2.5(32)^{0.5} = 14.1\ MPa$

$$s = \sqrt[0.4]{\frac{9.05}{14.1}}(1) = 0.33\ m$$

The parameter s_2 which is the slip at the end of the plateau is equal to the half the spacing of successive ribs on the longitudinal bars. The average maximum rib spacing for the reinforcement bars from ASTM A615 are 23 mm, 20 mm and 18 mm for column diameters of No.10, No.9 and No.8 respectively. The bond stress-slip relationship given to the columns are shown in Figure 7.13.

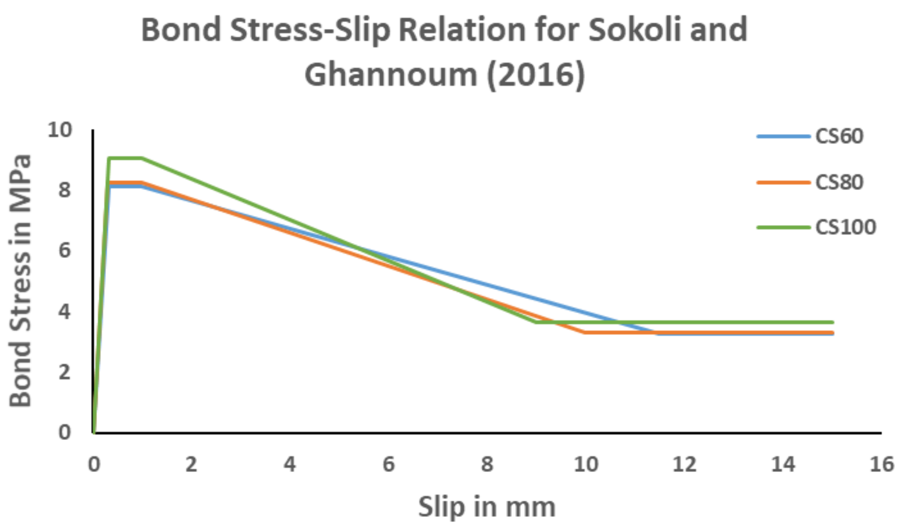

Figure 7.13: Bond Stress Slip Relationship

7.3.4 Mesh, Loading and Boundary Conditions

The column deformable length and the top and bottom blocks were modelled using 3D macro elements. The sectional geometry and the elevation are shown in Figure 7.1. The longitudinal and transverse reinforcement were modelled using 3D truss elements. Only half of the cross section was modelled due to cross-sectional symmetry. The nodes on the plane of symmetry throughout the height of the column were restrained from movement in the out of plane direction, however they were allowed to roll vertically. The bottom surface of the foundation was restrained from movement in all three directions x, y and z. To enforce all the nodes on the top surface of the beam block to displace vertically by an equal amount while undergoing the prescribe lateral displacement without rotation, a thick steel beam was considered acting above the top concrete beam. The deep stiff steel beam creates a diaphragm on the top surface of the beam block. The lateral displacement is applied on all the nodes along the depth of the deep steel beam. The axial load was applied in the first step followed by lateral displacements of approximately 0.1 mm. The lateral displacement load history is defined in Figure 7.14.

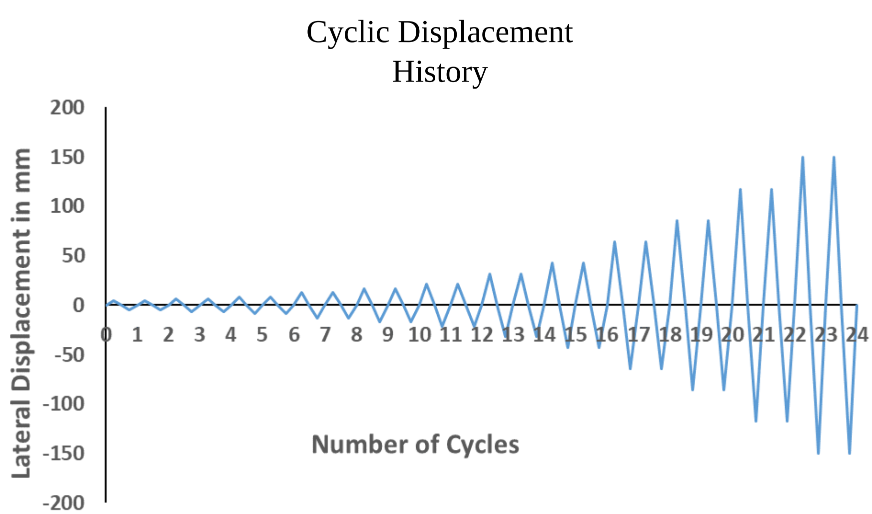

Figure 7.14: Lateral Displacement History

A hexahedral mesh was used for the model. The mesh size of 0.05 m was used for all macroelements.

7.4 Calibration of Analytical Columns with Different Concrete and Crack Models

Column CS60 was run under monotonic and cyclic loading for cracked and fixed models to explore the differences in each model. The behaviour of the concrete model used in the comparative study was also investigated under monotonic and cyclic loading. Figure 7.15 a and b depict column CS60 resistance curve under cyclic and monotonic loading for the rotated and fixed crack model respectively.

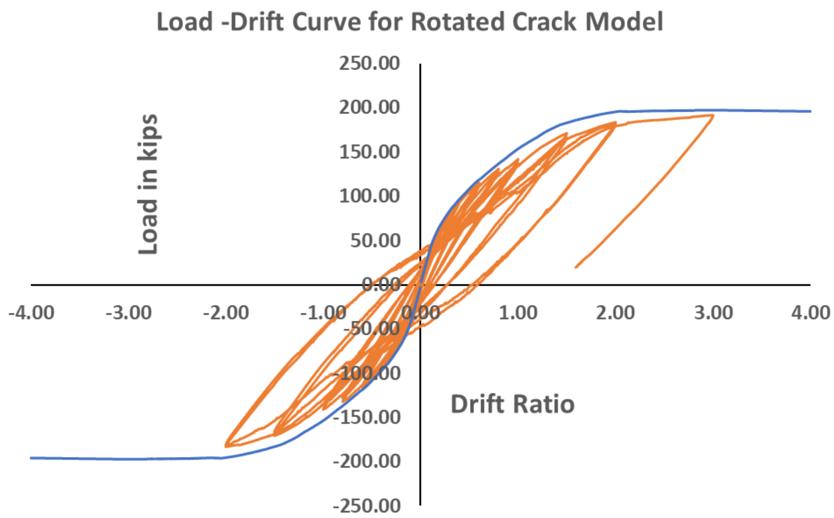

7.15a: Rotated crack model

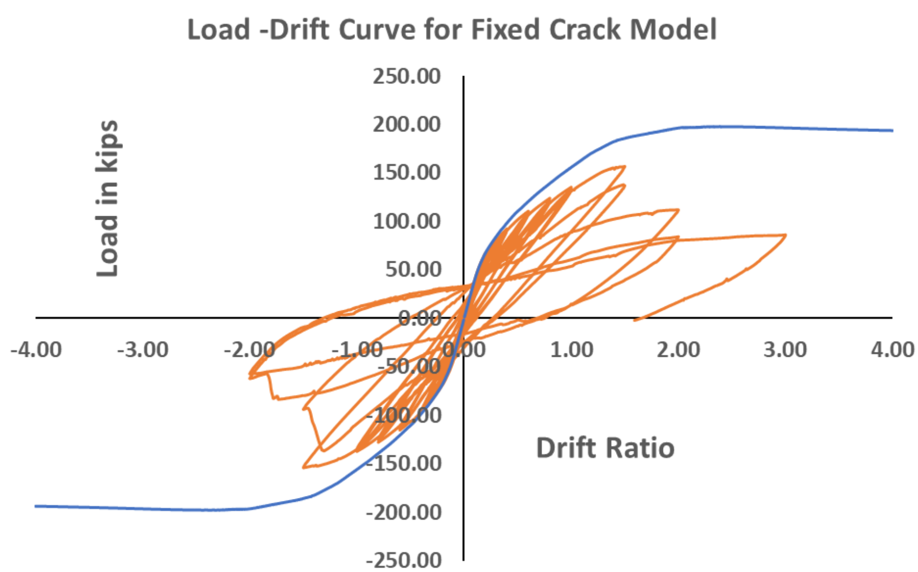

7.15b: Fixed Crack Model

Figure 7.15: Analytical Cyclic and Monotonic Response of Column CS60

It is concluded from the Figures 7.15 a and b that the crack models (rotated and fixed) show the same response under monotonic loading. The crack pattern for the column with the two crack models are shown in Figure 7.15a and b. Differences in the response of the two crack models were found in the cyclic response. Pinching was present in the column with a fixed crack model while no pinching was found in the case of rotated crack model. Figure 7.16 a and b depicts the crack pattern of the columns under cyclic loading. The minimum crack width for the columns in Figure 7.16 is 1 mm.

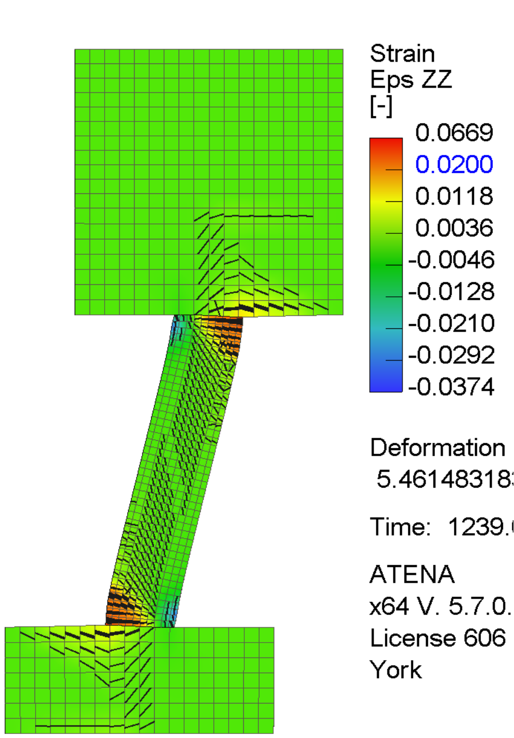

7.16a: Rotated Crack

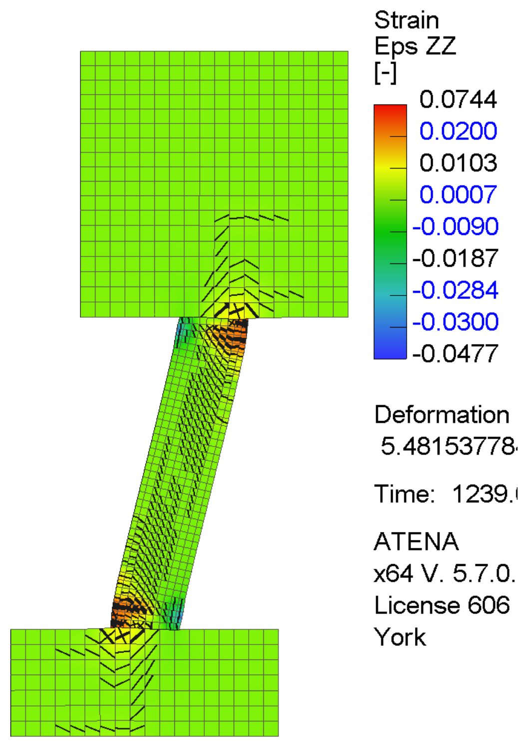

7.16b: Fixed Crack Model

Figure 7.16: Crack Pattern for Column CS60 for Rotated and Fixed Crack Models (Monotonic)

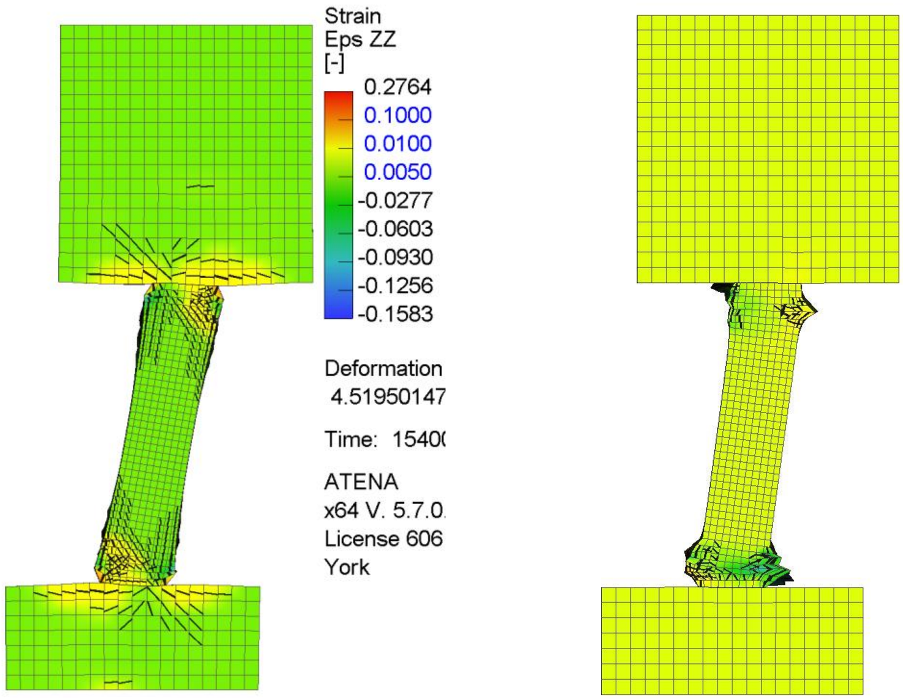

7.17a: Rotated Crack

7.17b: Fixed Crack Model

Figure 7.17: Crack Pattern for Column CS60 for Rotated and Fixed Crack Models (Cyclic)

Once the crack has formed in a column with a fixed crack model, the crack direction is fixed and shear stress are developed along the crack which prompts sliding. When changing the loading direction during cyclic loading, the cracks do not close. This results in significant crack widths that enable splitting and therefore pinching in the cyclic response. The ability of the rotated crack model to change the crack direction once developed prompts splitting after larger numbers of cycles compared to the fixed crack model.

The experimental analysis does not show any pinching in the cyclic response of the column. A comparison between the fixed, rotated and experimental maximum lateral resistance and the corresponding rotation are shown in Table 7.3.

Table 7.3: Comparison between the Fixed and Rotated Crack Models and the Experimental Analysis

	Rotated Crack Model	Fixed Crack Model	Experimental Analysis
Maximum Lateral Resistance (kips)	191.5	156.7	176
Drift Ratio Corresponding to the Maximum Lateral Resistance (%)	3	1.9	2.9

The experimental lateral resistance shows satisfactory agreement with the lateral resistance of the column with the fixed and rotated crack model. Better correlation in the corresponding drift ratio is present in the column with the rotated crack model. Therefore, the rotated crack model is the suitable model for column CS60.

7.5 Results of Experimental and Finite Element Model

The column specimens of Sokoli and Ghannoum (2016) were modelled using ATENA GiD 15.0.1 interface and the were analysed using ATENA Studio. This Section will present the results of the finite element model and compare them with the experimental values.

7.5.1 Column CS60

Figure 7.18 depicts the resistance curve of the analytical results for column CS60. Table 7.4 depict the milestone events for the experimental and analytical results.

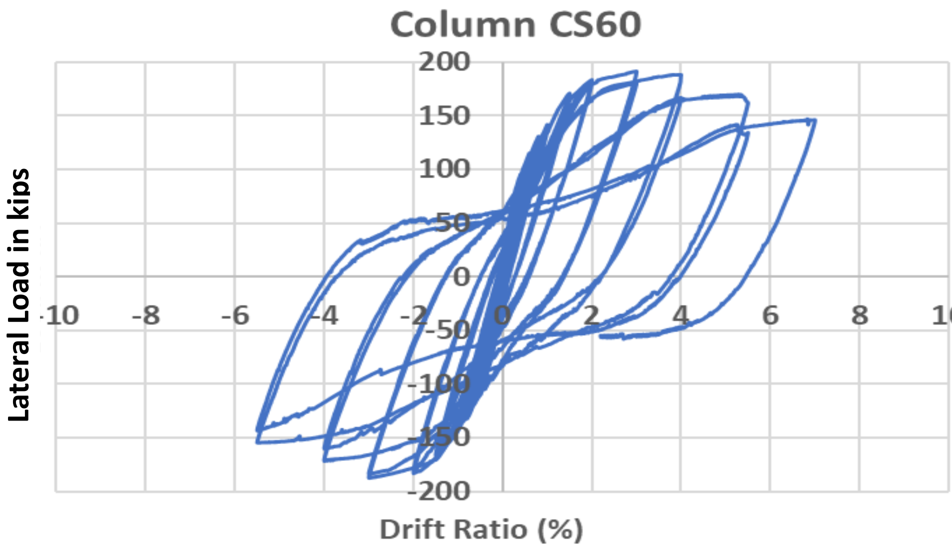

Figure 7.18: Analytical Resistance Curve of Column CS60

Table 7.4: Comparison Between analytical and Experimental Analysis for CS60

	Experimental		Analytical	
	V in kips	Drift Ratio %	V in kips	Drift Ratio %
First Longitudinal Reinforcement Yield	164	1.6	140	1.0
First Transverse Reinforcement Yield	159	3.10	170	1.5
First Flexural Crack	-76	-0.3	-100	-0.299
First Inclined Crack	104	0.6	93	0.38
Peak Lateral Load	176	2.9	192	3
Initiation of Lateral Strength Loss	144	5.2	153	5.43
Initiation of Axial Failure	135	5.8	145	5.5

The analytical model generally exhibits each milestone event described in the first column of Table 7.4. Good agreement between the experimental and analytical columns is evident, with regards to determining the first flexural crack, the first inclined crack, the peak lateral load and initiation of lateral shear strength loss. The analytical model however underestimates the occurrence of the first transverse and longitudinal reinforcement yield point. The analytical resistance curve also exhibits pinching in the last cycle, where shear failure has occurred earlier in the analytical model. Figure 7.19 depicts the lateral drift ratio vs. the vertical displacement at a distance of d/2 from the critical section at the top and bottom of the column.

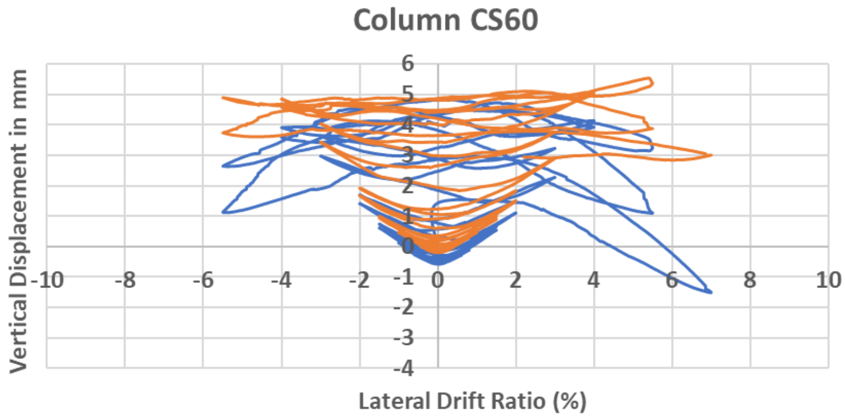

Figure 7.19: Vertical displacement Vs. Lateral drift Ratio for Column CS60

From Figure 7.19 it was concluded that the initiation of axial failure occurs at a drift ratio of 5.5%. The complete axial failure occurs at a displacement of 7%.

The crack patterns for the analytical column is shown in Figure 7.20. The minimum crack width is 1 mm for the analytical column.

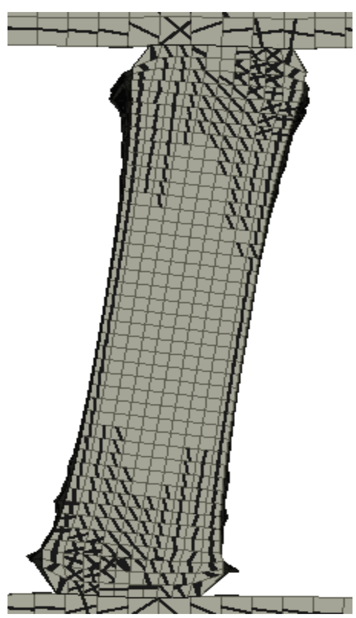

Figure 7.20: Crack pattern for Column CS60.

Similar flexural and shear cracks were observed for the column CS60 as shown in Figure 7.19. The cover on both sides of the critical section of the column has spalled off in both experimental and analytical analysis.

7.5.2 Column CS80

Figure 7.21 depicts the resistance curve of the analytical results for column CS80. Table 7.5 depict the milestone events on the experimental and analytical response curves.

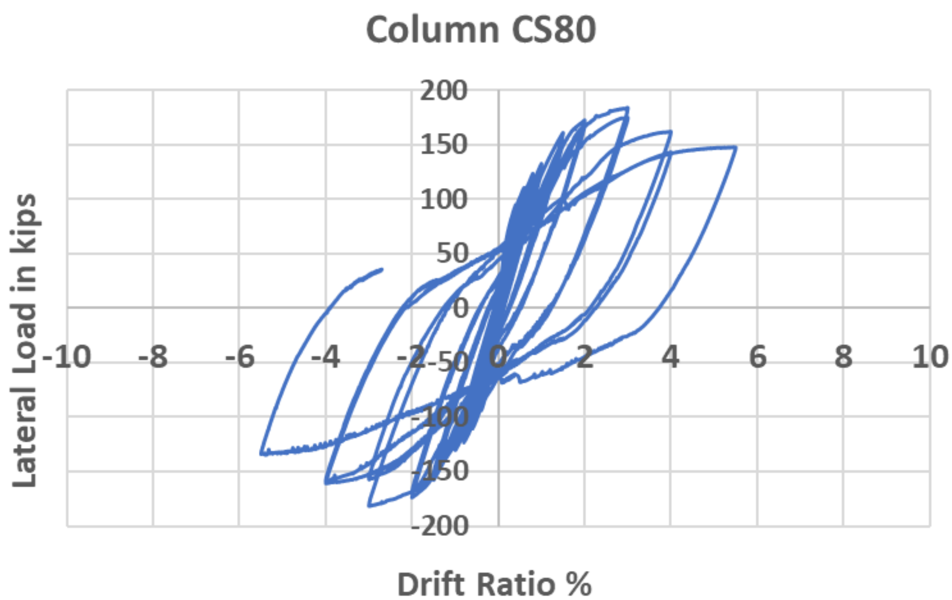

Figure 7.21: Analytical Resistance Curve of Column CS80

Table 7.5: Comparison Between Analytical and Experimental Analysis for CS80

	Experimental		Analytical	
	V in kips	Drift Ratio %	V in kips	Drift Ratio %
First Longitudinal Reinforcement Yield	148	1.0	132	1.0
First Transverse Reinforcement Yield	-170	-2.0	172	2.0
First Flexural Crack	98	0.4	87	0.3
First Inclined Crack	101	0.6	97	0.4
Peak Lateral Load	178	1.9	184	2.9
Initiation of Lateral Strength Loss	150	4.6	147	5.0
Initiation of Axial Failure	-112	-5.5	-120	-5.5

Better correlation for the points of transverse and longitudinal reinforcement yielding is found as compared to column CS60. The differences in the drift ratio corresponding to the lateral load in analytical and experimental column is larger in this case compared to column CS60. Figure 7.22 plots the vertical displacement against the lateral drift ratio at a distance of d/2 from the critical section at the top and bottom of the column.

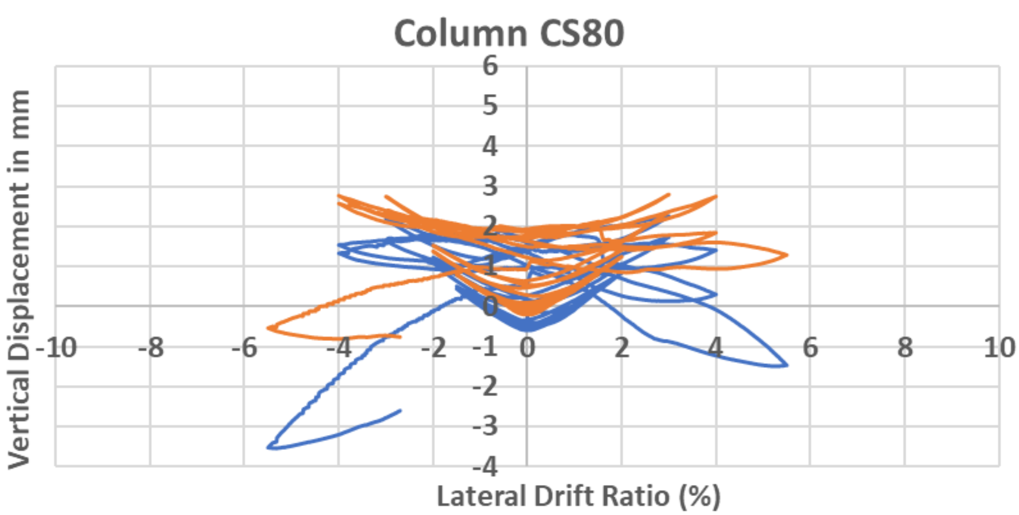

Figure 7.22: Vertical Displacement vs. Lateral Drift Ratio for Column CS80

The axial failure in column CS80 according to Figure 7.21 occurs at a drift ratio of +/- 5.5%.

The crack pattern for the analytical column is shown in Figure 2.23. The minimum crack width is 1 mm for the analytical column.

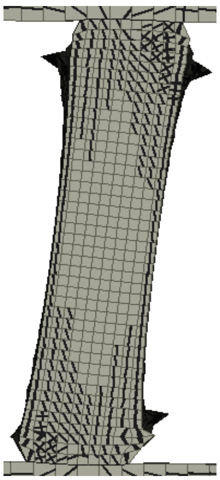

Figure 7.23: Crack pattern for Column CS80.

The analytical crack pattern is similar to the crack pattern observed in column CS60.

7.5.3 Column CS100

Figure 7.24 depicts the resistance curve of the analytical results for column CS100. Table 7.6 depict the milestone events on the experimental and analytical response curves.

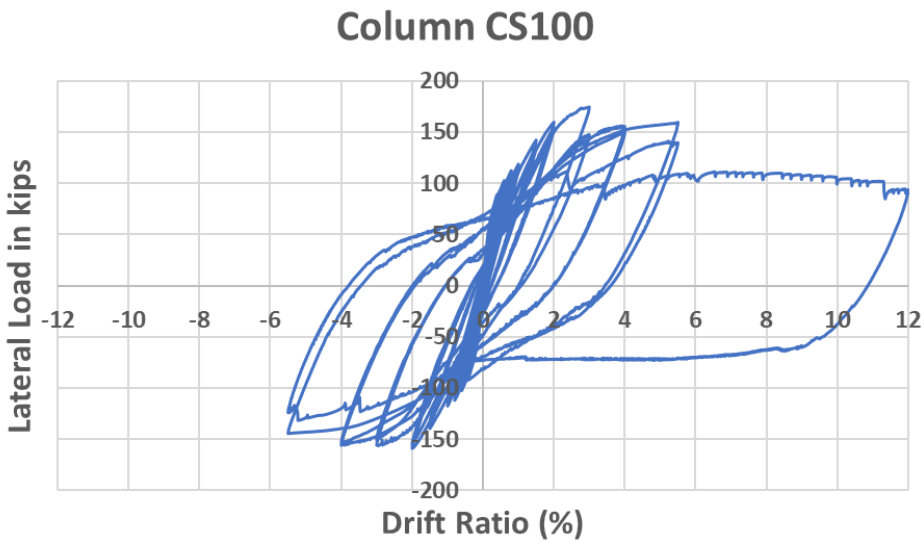

Figure 7.24: Analytical Resistance Curve of Column CS100

Table 7.5: Comparison Between analytical and Experimental Analysis for CS100

	Experimental		Analytical	
	V in kips	Drift Ratio %	V in kips	Drift Ratio %
First Longitudinal Reinforcement Yield	150	1.23	159	2.0
First Transverse Reinforcement Yield	-98	-4.0	159	2.3
First Flexural Crack	-85	-0.4	80	0.3
First Inclined Crack	103	0.6	-93	-0.4
Peak Lateral Load	169	1.9	174	2.9
Initiation of Lateral Strength Loss	158	-3.0	150	5.5
Initiation of Axial Failure	NA	12	140	-5.8

The model overestimates most of the events in this Column case. Pinching observed in the experimental column was not observed until 5% drift ratio in the analytical column case. The pinching in the experimental analysis was due to apparent bond splitting. Therefore, the analytical bond model should be adjected in the finite element model to capture an accurate bond failure as found in the experimental resistance curve. The vertical displacement at a distance of d/2 from the top and bottom column critical section vs. the drift ratio is depicted in Figure 7.25.

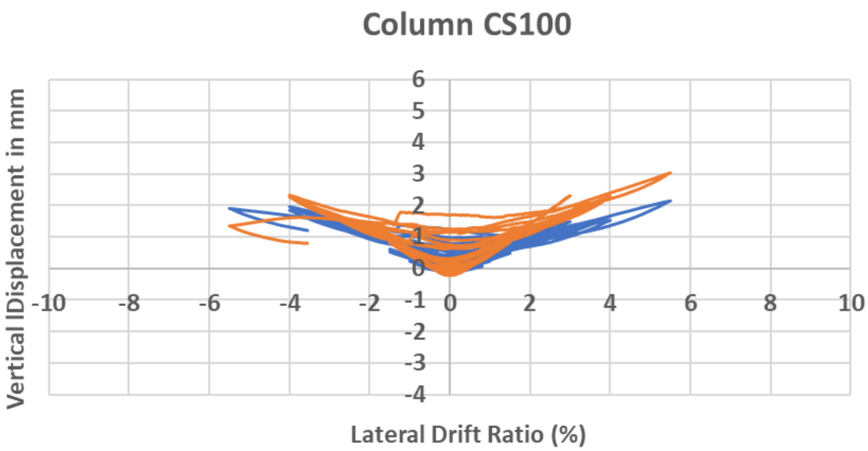

Figure 7.25: Vertical displacement Vs. Lateral drift Ratio for Column CS100

The axial failure occurred at a drift ratio of -5.8% whereas the experimental analysis does not exhibit axial failure. Significant differences are observed between analytical and experimental responses in this particular case; the experimental response curve shows intense pinching at the transition from positive to negative displacement, a feature that has not been captured in the analytical model considered. The pinching in the experimental analysis was due to bond failure that was not capture correctly in the analytical response. Therefore, to enhance the correlation between the analytical and experimental results the bond model in the analytical column should be revised to better correlate the experimental pinching. The crack patterns for the analytical column are shown in Figure 2.26. The minimum crack width is 1 mm for the analytical column. Clearly there is evidence of bar buckling and cover spalling in the critical regions, however the strength degradation that ensues is not as successfully captured as in the preceding cases.

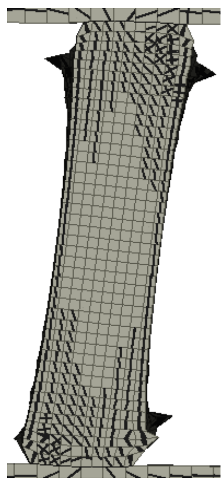

Figure 7.26: Crack pattern for Column CS100.

8. Conclusions and Recommendations

8.1 Summary of Study

This study investigated the seismic performance of reinforced concrete columns using nonlinear finite element analysis (ATENA Engineering 3D). The study was divided mainly into four parts. The first part investigated the effect of several design variables on the seismic performance of 60 cantilever lateral swaying columns (length of the cantilever is half the length of a laterally swaying full-column so there is a static equivalence between the cantilever and the full column, with one to one correspondence in the shear force, axial load, moment at the critical section, and lateral drift ratio). The columns were modelled using advanced nonlinear numerical simulation. All column models consisted of similar material properties and testing methods to determine the significance of the effect of a certain design variable relative to others. The study variables were the following five: (a) Longitudinal reinforcement detailing. 4 different patterns of reinforcement were considered, namely, continuous reinforcement connection between the shear span and the foundation with a 90° hook and ample anchorage, lap splice at the critical section over a length of 270 mm or 15 times the bar diameter, an anchorage length of 270 mm into the foundation and a fabricated structural hinge detail. (b) The second variable was the transverse reinforcement spacing; the two different spacing arrangements considered were, 100 mm and 200 mm. (c) The third variable was the axial load. Axial loads of 10%, 35% and 50% of crushing load $\left(\frac{P}{A_g f_c}\right)$ were applied to the columns. (d) The fourth variable was the aspect ratio of the column. Columns with aspect ratios of 4.2 and 2.3 (a/d) were modelled. The lower aspect ratio was represented by increasing the depth of the cross section from 400 mm to 700 mm. (e) The final variable studied was the longitudinal reinforcement ratio. Half of the columns modelled had 4Φ18 reinforcement bars per face and the other half had 2Φ18. Several material models were studied and prepared for concrete and bond and implemented in the finite element program. The deformation capacities at yielding and ultimate and the shear base of the columns were recorded and compared. The bond failure in the cases failing due to bond splitting and pull out were investigated and the development length specification of the two codes ACI 318M-19 and ACI 408R-03 were compared to the development lengths of the column.

The second part of this study was to investigate the validity of the assumption that the cantilever column can be used to estimate the deformation capacity of a full column based on the static similarities in the two cases. Finite element analysis was used to study the response of 16 full scale column with symmetrical boundary conditions at the top and bottom. Eight of the full scale columns had continuous reinforcement through the shear span and the beam cap and the foundation. The other eight had continuous reinforcement through the beam cap and lap splice connection at the bottom critical section. The full-scale columns were modelled using the same material properties of the cantilever case. The deformation capacities at yield and ultimate, the base shear and the longitudinal strains in the reinforcement were studied to investigate similarities and differences between the cantilever and full-scale columns.

The third part of the study was a review of the international assessment codes of existing structures (ASCE-SEI 41 17 and EUROCODE 8 Part III 2005). The deformation capacities of the columns modelled in the first part of the study was calculated using the assessment codes. The aspects that may cause uncertainties in the deformation capacity calculation were studied such as the curvatures and depth of the compression zone. The depth of the compression zone was found from two approaches, i.e., using the Response2000 software (Bentz 2001) and the proposal of Panagiotakos and Fardis (2001) which is the basic method used in Eurocode 8-III (2005). The curvatures were also found from the three approaches; Panagiotakos and Fardis (Eurocode 8-III 2005) Model (2001), from the Response2000 software and the method of Priestly et al. (2001). The column's performance levels from the finite element analysis were plotted against the performance levels calculated from the international assessment codes for existing structures in order to determine the efficiency of the codes in estimating the deformation capacities. The shear strength of the columns specified from the assessment codes were also plotted against the finite element base shear in order to examine the efficiency of the code expressions in determining the shear failure in columns.

The fourth part of this study, which is also the last part, examined the efficiency of concrete and bond models in finite element analysis in accurately reproducing the response of experimental columns. The column specimens of Ghannoum and Sokoli (2016) were used for this investigation. The application of different concrete crack models were discussed and their effectiveness and relevance was assessed from the correlation between experimental and analytical (calculated) responses.

8.2 Conclusions

From the results of finite element cantilever models it was concluded:

1- The columns with 100 mm stirrup spacing provide high core confinement and therefore provide larger deformation capacities relative to column with 200 mm stirrup spacing. This finding was compatible with Lynn (2001), Sezen (2002) and Elwood (2007) and other column tests in the experimental database.

2- Columns with low axial loads (10% of concrete crushing load) experienced bond failure which was either due to pullout from the foundation or due to splitting along the shear span of the column. Shear failure may also be present at low axial load with poor confinement accompanied with splitting along the shear span when the reinforcement is anchored properly into the foundation.

3- Columns with moderate axial load (35% of concrete crushing) fail due to shear and stirrup yielding. The ultimate failure in these columns was accompanied with concrete crushing. Initiation of buckling failure occurred at 35% of axial load was also present in the case of poor confinement. Buckling of compression reinforcement was also present in the case of 100 mm stirrup spacing, however this occurred after yielding of the stirrups wrapping the compression reinforcement.

4- At high axial loads (50% of concrete crushing), the main source of yielding and ultimate failure was concrete crushing. Additionally, columns with low confinement did not experience yielding in the longitudinal reinforcement as it was limited due to the concrete crushing. Stirrup yielding and shear failure were present in most of the columns cases.

5- Columns with low reinforcement ratios and low confinement (Flexure-Shear critical columns) exhibited the poorest response in all columns. These columns yielded at an approximate drift ratio of 0.46% and a maximum ultimate displacement of 2.5% for low axial loads.

6- Columns with low reinforcement ratios and high confinement (Flexural columns) are the most ductile columns. Such columns at low axial load yield at a drift ratio 0.46% and develop an ultimate drift ratio of 3.6%. For higher axial loads, poor lateral response was found relative to columns with good confinement but with higher reinforcement ratio. This is because columns with lower reinforcement ratio provide less core confinement at therefore less deformability if concrete crushing controls. No stirrup yielding or shear cracking is observed in this case.

7- Columns with high reinforcement ratio and high confinement (Flexural columns) provide better response at yielding but less ultimate deformability relative to columns with less reinforcement ratio at low axial loads. Yielding in these such columns occur at a drift ratio of 0.6%, while ultimate drift rotation was at 2.8%. Stirrup yielding and shear cracking were observed in low axial loads however they were not the main source of failure. At high axial loads such columns become (Flexural- shear columns) shear critical and this leads to axial failure.

8- Columns with high reinforcement ratios and low transverse reinforcement ratios were shear critical columns. Shear failure occurred at low axial loads. Splitting along the longitudinal reinforcement occurred at low axial loads as well.

9- If the column is subjected to low axial loads, no axial failure occurs even with the presence of shear failure such as column C10-1-20. Axial failure occurs immediately after shear failure or occurs simultaneously with shear failure with the increase of axial load.

10- The lateral load degradation in flexural columns was due to P-Δ effects only. These columns mainly failed due to bond splitting or pullout and were subjected to axial loads of (10%).

11- With the reduction of the aspect ratio the ultimate and yield drift ratio decrease, and the base shear increases, especially at high axial loads. The shear failure is the main mode of failure in these columns even at low axial load.

12- The columns with a fabricated structural hinge, all exhibit the same mode of failure regardless the reinforcement ratio or stirrup spacing. Bond pullout failure is found at low axial load and concrete crushing is the main mode of failure at high axial loads.

13- In the case of lap splice, the slip at yielding dominated the deformation capacity over the contribution of flexural rotation to the total drift, and therefore yielding of the reinforcement was delayed. At higher axial loads, the controlling mode of failure in the lap splice case was concrete splitting rather than reinforcement pullout.

14- In the case of short anchorages, pullout failure occurred only at low axial loads and high reinforcement ratios. In this case no delay in the reinforcement yielding occurred as was seen in the case of lap splice. However, as the pull out of the reinforcement in the short anchorage length occurred after yielding, the maximum lateral resisting load corresponded to a higher drift ratio as compared to the column with continuous reinforcement. With the reduction in the reinforcement ratio, flexural yielding controlled and therefore the columns failed due to splitting instead of pullout.

15- The confinement factors ($(k_{tr}+c_b)/d_b$, $(k_{tr}+cw)/d_b$) solely should not be used as an indication of the likelihood of bond failure. Pullout failure was also found in the column with high reinforcement ratio even though the k_{tr} values were more than the upper limit of 2.5 and the available development length was larger than the specified according to the ACI 318M 19. When the confinement of the cross section is such that the bond-confinement calculated from the factors $(k_{tr}+c_b)/d_b$ in the ACI 318M 19 code is less than 3, then the available development length determined from code equations should be multiplied by a factor ranging between 1 and 1.5, with the factor $(k_{tr}+c_b)/d_b$ equal to 1. The ACI 408R-03 provided better estimates for the failure mode.

From the results of finite element full scale models it was concluded:

1- The full column and the cantilever column do not provide the same ultimate rotations at low axial loads for column with continuous reinforcement at the top and bottom shear span-foundation/beam connection. This is because more reinforcement pullout demand was found at the top connection. The ultimate displacements in these cases were equal for the full and cantilever column. At higher axial loads (when the pull out failure is suppressed due to shear failure), strain penetration to the midpoint of the shear span in the full column resulted in the formation of a shear critical crack that was at a higher angle with the vertical axis. This pattern contributed to accelerating the shear failure and therefore providing less ultimate rotations as compared to the cantilever column (the full column approximately provided 0.8 of the ultimate drift ratio of the half column). By reducing the confinement of the section, the difference between the ultimate rotation for full and half columns reduced, because concrete crushing controls the ultimate failure. (At that limit, the full column approximately provided 0.9 of the ultimate drift ratio of the half column).

2- In the case of the lap splice, strain penetration in the full column offered a higher length for the lap splice to develop yield strains on the lapped bar extending along the shear span. Therefore, the difference in the yield displacement for the two cases was present at low axial loads (the yield displacement of the full column is approximately 0.8 percent of the cantilever column). Due to the same mechanism the cantilever column may slightly underestimate the lateral resisting load in the cantilever case. For columns with a low axial load and low reinforcement ratio, the cantilever column and the full column provided the same displacement because of pull out and splitting failure occurring at the top connection at ultimate. Other modes of failure at the top may limit the deformation capacity of the full column.

From the seismic assessment of existing structures it was concluded that:

1- Uncertainties in yield rotations arise when using curvatures from different approaches especially at higher axial loads. The empirical equations by Priestley et al. (1996) overestimated the yield rotations at higher axial load compared to the results from Response2000 full sectional analysis. This overestimation can affect the classification of performance level of a component and therefore the assessment results and the recommended retrofit strategy. Curvatures therefore should be calculated using full sectional analysis.

2- The ASCE-SEI 41/17 and the EUROCODE 8 Part III (2005) were overly conservative in calculating the deformation capacities at different performance levels for the case of the lap splice and short anchorage length. The ASCE-SEI 41/17 estimated more accurately the deformation capacities of columns failing in shear and compression bar buckling whereas EUROCODE 8 Part III (2005) provided more accurate estimates of deformation capacity for columns failing in flexure.

From model correlation it was concluded that:

1- The finite element analysis showed fair agreement with the experimental evidence in estimating the response of columns under cyclic loading. Differences in the rotated crack and fixed crack models under cyclic loading were identified. The fixed crack model underestimated the maximum lateral resisting load and the deformation capacities under cyclic loading. Once the crack was formed in the fixed crack model is would not close again and its angle would be fixed for the remainder of the analysis.

2- The finite element models also showed occurrence of shear failure earlier (i.e., at a lower drift ratio) than the experimental model.

8.3 Recommendations for Future Research

The following recommendations for further investigation are proposed based on the findings from this thesis:

1- The benchmark columns in the study contained stirrups with closed hook arrangements (135°). A next step in the investigation would be to study the effect of 90o hooks, which is a common occurrence in older construction around the world. Different stirrup arrangements (apart from perimeter stirrups considered here) would warrant further investigation.

2- The columns presented in this study were subjected to reversed cyclic displacement history and monotonically lateral displacement (pushover analysis) without accounting for force redistribution through the frame and the effects it would have on the columns, particularly in terms of the fluctuation of the overbearing axial load with the superposition of the earthquake overturn. The dynamic response of the columns should be investigated and the redistribution of forces in a frame with real time histories of real earthquakes should be considered with proper reference to column tests conducted on shake tables.

3- All columns in the present study were subjected to the same loading history. The effect of different cyclic load histories on the extent and severity of strain penetration and the validation of certain proposed models in literature regarding the onset of axial load failure after shear failure, such as that proposed by Elwood (2007) would be the next needed step in the simulation.

References

ACI 318. (2011). “Building Code Requirements for Structural Concrete and Commentary”. ACI, American Concrete Institute, Farmington Hills, MI.

ACI 318. (2014). “Building Code Requirements for Structural Concrete and Commentary”. ACI, American Concrete Institute, Farmington Hills, MI.

ACI 318. (2019). “Building Code Requirements for Structural Concrete and Commentary”. ACI, American Concrete Institute, Farmington Hills, MI.

ACI 408. (2003). “Bond and Development of Straight Reinforcing Bars in Tension”. ACI, American Concrete Institute, Farmington Hills, MI.

ASCE-41-17. (2017). ASCE Standard, ASCE/SEI, 41–17: “Seismic Evaluation and Retrofit of Existing Buildings”. Reston, VA: American Society of Civil Engineers.

Augenti, N. and Parisi, F. (2010). “Learning from Construction Failures Due to the 2009 L’Aquila, Italy, earthquake”. J Perform Construct Facilities. 24(6) :55-536.

Bazant, Z. and Oh, B. H. (1983). “Crack Band Theory for Fracture of Concrete”. Mat. Construction Journal. 16:155-177

Bentz, E.C., Collins, M.P. (2001). Response2000© User Manual. University of Toronto, Toronto, Ontario Canada

Berry, M. P., (2006). “Performance Modeling Strategies for Modern Reinforced Concrete Bridge Columns”. PhD dissertation, University of Washington, Seattle, WA.

Cervenka, V., Jendele, L., Cervenka, J. (2020). “Theory”. ATENA Program documentation Part 1. Prague (Czech Republic): Cervenka Consulting.

Chasioti, S. G., Syntzirma, D. V., and Pantazopoulou, S. J. (2010). “Codes of assessment of buildings: A comparative study”. In 9th US National and 10th Canadian Conference on Earthquake Engineering 2010, Including Papers from the 4th International Tsunami Symposium. 2: 1192–1201).

Ciampi, V., Eligehausen, R., Popov, E. P., and Bertero, V. V. (1982). "Analytical Model for Concrete Anchorages o f Reinforcing Bars under Generalized Excitations." UCB/EERC, 82/23, University o f California, Berkeley.

Collins, M. P., and Mitchell, D. (1991). Prestressed Concrete Structures, Prentice Hall, Englewood Cliffs, New Jersey.

CSA A.23.3. (2014). “Design of Concrete Structures”. Canadian Standards Association, CSA, Mississauga, Ontario, Canada.

Dogangun, A. (2004). “Performance of reinforced concrete buildings”. Eng. Struct. 26(6): 841–56.

Eligehausen, R., Popov, E. P., and Bertero, V. V. (1983). "Local Bond Stress-Slip Relationships of Deformed Bars under Generalized Excitations." UCB/EERC, 83/23, University of California, Berkeley.

Elwood, K. J., and Eberhard, M.O., (2006). “Effective Stiffness of Reinforced Concrete Columns”, PEER Research Digest No. 2006-1

Elwood, K. J. and Meohle, J. P. (2003). “Shake Table Tests and Analytical Studies on the Gravity Load Collapse of Reinforced Concrete Frames”. PEER Report 2003/01, Pacific Earthquake Engineering Research Center, University of California, Berkeley.

Elwood, K. J. and Moehle J. P. (2004). “Evaluation of Existing Reinforced Concrete Columns”. 13th World Conference on Earthquake Engineering. Vancouver, BC, Canada, August 1-6, No. 579.

Elwood, K. J. and Moehle J. P. (2005). “Axial Capacity Model for Shear Damaged Columns”. ACI Structural Journal. 102(4):578- 587.

Elwood, K. J., Matamoros, A., Wallace, J., Lehman, D., Heintz, J., Mitchell, A., Moore, M., Valley, M., Lowes, L., Comartin, C., Moehle, J. P. (2007). “Update to ASCE/SEI 41 Concrete Provisions”. Earthquake Spectra. 23(3): 493-523.

Elwood, K. (2007). “Shake Table Tests and Analytical Studies on the Gravity Load Collapse of Reinforced Concrete Frame”. PhD Dissertation, University of California, Berkeley.

EN 1992-1-1. (2003). Eurocode 2 – Design of Concrete Structures - Part 1–1: General Rules and Rules for Buildings. European Committee for Standardization (CEN), Brussels.

EN 1998-3. (2005). Eurocode 8 – Design of Structures for Earthquake Resistance - Part 3: Assessment and Retrofitting of Buildings. Brussels: European Committee for Standardization (CEN).

Esaki, F. (1996). “Reinforcing Effect of Steel Plate Hoops on Ductility of R/C Square Columns.” Proc., 11th World Conf. on Earthquake Engineering, Elsevier, New York.

Fajfar, P. (2018), "Analysis in Seismic Provisions for Buildings: Past, Present and Future. Geotechnical, Geological and Earthquake Engineering". 46:1-46.

FEMA 273. (1997). NEHRP Guidelines for the Seismic Rehabilitation of Buildings. Report No. FEMA-273, Federal Emergency Management Agency, Washington D.C.

FEMA 356. (2000). “Pre-standard and Commentary for the Seismic Rehabilitation of Buildings”

Ghannoum, W. M., (2007). “Experimental and Analytical Dynamic Collapse Study of a Reinforced Concrete Frame with Light Transverse Reinforcement”. PhD dissertation, University of California, Berkeley, CA.

Ghannoum, W. M, and Moehle, J. P. (2012). "Dynamic Collapse Analysis of a Concrete Frame Sustaining Column Axial Failures". ACI Structural Journal, 109(3):393-402

Goodnight, J.C., Kowalsky, M. J., and Nau, J. M. (2013). "Effect of Load History on Performance Limit States of Circular Bridge Columns". Journal of Bridge Engineering. ASCE, 18(12), ISSN 1084-0702/2013/ 12-1383–1396/

Hoehler M., (2002). "Formulation and Implementation of the Menegotto-Pinto Cyclic Steel Model for the Finite Element Program MASA".

Henkhuas, K. (2010). "Axial Failure of Vulnerable Reinforced Concrete Columns Damaged by Shear Reversals". PhD Dissertation, Purdue University, West Lafayette, Indiana.

Hognestad, E. (1951). "A study of Combined Bending and Axial Load in R.C. Members". University of Illinois Engineering Exp. Sta. Bull. no.399.

Jeong, SH. and Elnashai, AS. (2004). "Analytical and experimental seismic assessment of irregular RC buildings". In: 13th World Conference on Earthquake Engineering, Vancouver, Canada.

Kato, D., and Ohnishi, K., (2002). "Axial Load Carrying Capacity of R/C Columns under Lateral Load Reversals", Third US-Japan Workshop on Performance-Based Earthquake Engineering Methodology for Reinforced Concrete Building Structures, Seattle, WA, PEER Report 2002/02, Pacific Earthquake Engineering Research Center, University of California, Berkeley, :247-255.

Kent, D.C. and Park, R. (1971). "Flexural Members with Confined Concrete". Journal of the Structural Division. ASCE, 97(ST7): 1969-1990.

Kuo, W. W., Hwang, S. J., and Chen, Y. Z. (2006). "Force transfer mechanisms and shear strength of reinforced concrete beam-column elements," Proc. 4th International Conference on Earthquake Engineering, Taipei, Taiwan, :12–13.

Kupfer, H., Hilsdorf, H.K., and Rusch, H. (1969)."Behavior of Concrete Under Biaxial Stresses". ACI Journal Proceedings. 66(8): 656-666

Lam, S.S.E., Wu, B., Wong, Y.L., Wang, Z.Y., Liu, Z.Q., and Li, C.S. (2003). Drift Capacity of Rectangular Reinforced Concrete Columns with Low Lateral Confinement and High-Axial Load, Journal o f Structural Engineering, ASCE, 129(6):733-742

Lang, AF. and Marshall, JD. (2011). "Devil in the details: success and failure of Haiti's non engineered structures". Earthquake Spectra, 27(S1): 72-345.

Lehman D.E., Calderone, A.J. and Moehle, J. P. (1998). "Behavior and design of slender columns subjected to lateral loading". 6th US National Conference on Earthquake Engineering, EERI, Seattle, Washington, May 31-June 04.

Lehman, D and Moehle, J. P (2000). "Seismic Performance of Well-Confined Concrete Bridge Columns". 1988/01, UCB/PEER, University of California, Berkley, CA.

Li, X., Park, R., and Tanaka, H. (1991). “Effects of Variations in Axial Load Level on the Strength and Ductility of Reinforced Concrete Columns”. Proc., Pacific Conference on Earthquake Engineering, New Zealand National Society for Earthquake Engineering, Auckland, New Zealand, 147–158.

Lynn, A. C. (2001). “Seismic Evaluation of Existing Reinforced Concrete Building Columns”. PhD Dissertation, University of California, Berkeley.

Machulat, L. (2009). “Mitigation of Collapse Risk in Vulnerable Concrete Buildings”. The Pacific Earthquake research Centre, The University of Kanas for Research.

Masaya, H. (1973). “A List of Past Experimental Results of Reinforced Concrete Columns, Building Research Institute, Ministry of Construction, Tsukuba, Japan.

Matamoros, A. and Woods, C. (2010). “Drift at Axial Failure of R/C columns most vulnerable to collapse,” Structures Congress 2010, American Society of Civil Engineers, Orlando, Florida.

Matamoros, A.B., and von Ramin, M. (2005). “Estimating the Drift Ratio at Axial Load Failure of Reinforced Concrete Columns on the Basis of a Model to Calculate Shear Strength”, Proceedings o f the First NEE S/E-Defense Workshop on Collapse Simulation o f Reinforced Concrete Building Structures, Berkeley, CA, PEER Report 2005/10, Pacific Earthquake Engineering Research Center, University of California, Berkeley, pp. 261-274.

Matamoros, A. B. (2006). “Degrading Slope for Post-Peak Response of RC Columns Subjected to Load Reversals”. Proceedings, The Second NEES/E-Defense Workshop on Collapse Simulation of Reinforced Concrete Building Structures, October 31-November 1, E-Defense, Kobe, Japan, pp. 267-280.

Mehrabian A, Haldar A. (2005). “Some Lessons Learned from Post-Earthquake Damage Survey of Structures in Bam, Iran Earthquake of 2003. Struct Survey, 23(3):180–92.

Menegotto, M., and Pinto, P. E. (1973). "Method o f Analysis for Cyclically Loaded Reinforced Concrete Plane Frames Including Changes in Geometry and Nonelastic Behavior of Elements under Combined Normal Force and Bending". Proceedings of IABSE Symposium on Resistance and Ultimate Deformability of Structures Acted on by Well-Defined Repeated Loads, Lisbon

Mitchell, D. (2007). “Reducing Urban Seismic Risk”. Proposed Canadian Seismic Research Network, Montreal, Canada.

Model Code (2010). final draft, fib – Bulletin 65. Vol. 1. //www.fib-international.org.

Mostafaei, H., Vecchio, F. J., and Kabeyasawa, T. (2009). “Deformation Capacity of Reinforced Concrete Columns”. ACI Structural Journal, 106(2):187–195

National Research Council of Canada. (1995). “Guideline for Seismic Upgrading of Building Structures Upgrading of Building Rehabilitation”. Institute for Research and Construction NRC Publications Archive.

Ohue, M., Morimoto, H., Fujii, S., and Morita, S. (1985). “Behavior of R.C. Short Columns Failing in Splitting Bond-Shear under Dynamic Lateral Loading”. Trans. Jap. Concrete Inst., 7: 293–300

OpenSees. (2006). Open System for Earthquake Engineering Simulation, ('http://QpenSees.berkelev.edu')' Pacific Earthquake Engineering Research Center, University of California, Berkeley.

Otani, S., and Sozen, M. A. (1972). “Behavior of Multistory Reinforced Concrete Frames During Earthquakes”. Strucutral Research Series No. 392. University of Illinois Urbana-Champaihn, Urbana, IL, 551.

Ousalem, H., Kabeyasawa, T., and Tasai, A. (2004). “Evaluation of Ultimate Deformation Capacity at Axial Load Collapse of Reinforced Concrete Columns”, Proceedings o f 13th World Conference on Earthquake Engineering, Vancouver, B.C., Canada, Paper No. 370.

Panagiotakos T., and Fardis M. N. (2001). “Deformation of R.C. Members at Yielding and Ultimate". ACI Structural J., 98(2):135-148.

Pantazopoulou, S.J. (1998). “Detailing for Reinforcement Stability in RC Members. J. Struct. Eng. 124(6):623–632.

Pantazopoulou, S.J. (2003). “Strength and Deformation Capacity of Non-seismically Detailed Components”. Seismic Assessment and Retrofit of Reinforced Concrete Buildings, fib Bulletin No. 24: 91-150.

Park, R., and Paulay, T. (1975). Reinforced concrete structures. J. Wiley and Son, Inc., N. York, pp.769.

Park, R., Priestley, M.J.N. and Gill, W.D. (1982). “Ductility of Square-Confined Concrete Columns”. J. Struct. Division. 108(4): 929-950.

Priestley, M.J.N., Seible F., and Calvi M. (1996). Seismic Design and Retrofit of Bridges. J. Wiley & Sons Inc., N. York.

Priestley, M.J.N., Verma, R., and Xiao, Y. (1994). “Seismic Shear Strength of Reinforced Concrete Columns”, Journal of Structural Engineering, ASCE, 120(8):2310-2329.

Pujol, S., Ramirez, J.A. and Sozen, M.A. (1999). “Drift Capacity of Reinforced Concrete Columns Subjected to Cyclic Shear Reversals. Seismic Response of Concrete Bridges, American Concrete Institute, Farmington Hills, MI, 187(SP): 255-274.

Saatcioglu, M., and Ozcebe, G. (1989). “Response of reinforced concrete columns to simulated seismic loading.” ACI Struct. J., 86(1):3–12

Sasani, M., (2004). “Shear Strength and Deformation Capacity Models for RC Columns”, Proceedings o f 13th World Conference on Earthquake Engineering, Vancouver, B.C., Canada, Paper No. 1838.

Sasani, M., (2007). “Life Safety and Near Collapse Capacity Models for Seismic Shear Behavior of Reinforced Concrete Columns”. ACI Structural Journal, 104(1): 30-38.

Scott, B. D., Park, R., and Priestley, M. J. N. (1982). “Stress-strain behavior of concrete confined by overlapping hoops at low and high strain rates.” J. Am. Concr. Inst., 79(1): 13–27.

Sezen, H. and Moehle, J. P. (2006). “Seismic tests of concrete columns with light transverse reinforcement,” ACI Structural Journal 103(6): 842–849.

Sezen, H. (2002). “Seismic Response and Modeling of Reinforced Concrete Building Columns,” PhD dissertation, Department of Civil and Environmental Engineering, University of California, Berkeley, Berkeley, Calif.

Sezen, H., and Setzler, E. (2008). “Reinforcement Slip in Reinforced Concrete Columns”. ACI Structural Journal, 105(3): 280-289.

Shin, Y. B. (2011). “Dynamic Response o f Ductile and Non-Ductile Reinforced Concrete Columns”. PhD Dissertation, University of California, Berkeley.

Shoraka, B.M., Elwood, K.J,. (2013). “Mechanical Model for Non Ductile Reinforced Concrete Columns”. Journal of Earthquake Engineering, 17(7):937–957

Sokoli, D. and Ghannoum, W. M. (2016). “High-Strength Reinforcement in Columns under High Shear Stresses”. ACI Structural Journal, 113(3)

Spacone, E., Filippou, F. C., and Taucer, F. F. (1996). “Fibre beam-column model for non-linear analysis of R/C frames: Part I. Formulation”. Earthquake Engineering and Structural Dynamics, 25(7): 711–725

Syntzirma, D.V, Pantazopoulou, S.J and Aschheim, M.(2010). “Load History Effects on Deformation Capacity of Flexural Members Limited by Bar Buckling”. ASCE Journal of Structural Engineering, 136(1):1−11.

Taylor, A. W., Kuo, C., Wellenius, K., and Chung, D. (1997). ‘‘A Summary of Cyclic Lateral Load Tests on Rectangular Reinforced Concrete Columns’’. NISTIR 5984, Building and Fire Research Laboratory, National Institute of Standards and Technology, Gaithersburg, Md. 20899.

Terzic, V., Schoettler, M.J., Restrepo, J.I.(2015). "Mahin SA Concrete Column Blind Prediction Contest 2010" : Outcomes and Observations. PEER Report 2015/01. Pacific Earthquake Engineering Center, Berkeley.

Varum, H. (2003). “ Seismic Assessment, Strengthening and Repair of Existing Buildings. Dissertation, Universidadede Aveiro.

Vecchio F.J., and Collins M.P. (1986). "The Modified Compression Field Theory for R.C. Elements Subjected to Shear". ACI Structural, (83)2: 219-231.

Walraven, J. C. (1981). "Fundamental Analysis of Aggregate Interlock". Journal of the Structural Division.107(11):2245–2270.

Wight, J. K., and Sozen, M. A. (1973). "Shear Strength Decay in Reinforced Concrete Columns Subjected to Large Deflection Reversals". Structural Research Series No. 403, Univ. of Illinois, Urbana-Champaign, IL

Wight, James K., Jirsa, James O. and Corley, Gene W. (1984). "SP-084: Earthquake Effects on Reinforced Concrete Structures -- U S Japan Research". Vol. 84

Woods, C. (2010) Mitigation of Collapse Risk in Vulnerable Concrete Buildings. M.S. Thesis, University of Kansas, Lawrence.

Wu, C.L., Su, R.S., Hwang , S.J. and Yang Y.S. (2008). "Shake Table Tests on Reinforced Concrete short Columns Failing in Shear". The 14 the World Conference on Earthquake Engineering October 12-17, Beijing, China

Yalcin, C., and Saatcioglu, M. (2000). "Inelastic Analysis of Reinforced Concrete Columns." Comput. Struc., 77(5): 539–555.

Yavari, S. (2011). "Shaking Table Tests on the Response of Reinforced Concrete Frames with Non-Seismic Detailing". PhD Dissertation, The University of British Columbia, Vancouver.

Yoshimura, M., Takaine, Y., and Nakamura, T. (2003). "Collapse of reinforced concrete columns." Proc., 5th U.S.-Japan Workshop on Performance-Based Earthquake Engineering Methodology for Reinforced Concrete Building Structures, Pacific Earthquake Engineering Research Center, Berkeley, CA,pp. 239–253.

Zhao, J. and Sritharan, S., (2007). "Modeling of Strain Penetration Effects in Fiber-Based Analysis of Reinforced Concrete Structures". ACI Structural Journal, 104(2):133-141.

Appendix

Appendix A:Concrete Stress strain Calculations for Column Sections

Concrete Stress Strain Calculations for Section 1 (Section 400 mm Deep)

For 100 mm stirrup spacing:

$\rho_{s,tr}= \frac{50.2(2\cdot 292+2\cdot 342)}{292\cdot 342\cdot 100} = 0.006374$

$K_e = \left(1-\frac{100}{2\cdot 292}\right)\left(1-\frac{100}{2\cdot 342}\right)\left(1-\frac{6\cdot 70^2+2\cdot 298^2}{6\cdot 292\cdot 342}\right) = 0.463$

$\rho_{s,tr}$ =0.006374 · 0.463 =0.00295

K= 1+(0.00295 · (276/30)) = 1.027

f_{cc}= 30·1.027= 30.8 MPa

$\varepsilon_{cc,0=}$ 0.002·1.027= 0.002054

$\varepsilon_{c,50} = \frac{3+0.29\cdot f_c}{145\cdot f_c-1000} + 0.75\cdot \rho_{s,tr} \cdot \left(\frac{b_c}{s}\right)^{0.5} = \frac{3+0.29\cdot 30}{145\cdot 30-1000} + 0.75\cdot 0.00295 \cdot \left(\frac{292}{100}\right)^{0.5} = 0.00727$

For 200 mm stirrup spacing:

$\rho_{s,tr}= \frac{50.2\cdot(2\cdot 292+2\cdot 342)}{292\cdot 342\cdot 200} = 0.003187$

$K_e = \left(1-\frac{200}{2\cdot 292}\right)\left(1-\frac{200}{2\cdot 342}\right)\left(1-\frac{6\cdot 70^2+2\cdot 298^2}{6\cdot 292\cdot 342}\right) = 0.304$

$\rho_{s,tr}$ =0.003187·0.304 =0.000968

K= 1+0.000968 ·276/30= 1.0089

f_{cc}= 30·1.0089= 30.26 MPa

$\varepsilon_{cc,0=}$ 0.002·1.0089= 0.002017

f_{cc}, residual= 0.2·30.26= 6.052 MPa

$\varepsilon_{c,50} = \frac{3+0.29\cdot f_c}{145\cdot f_c-1000} + 0.75\cdot \rho_{s,tr} \cdot \left(\frac{b_c}{s}\right)^{0.5} = \frac{3+0.29\cdot 30}{145\cdot 30-1000} + 0.75\cdot 0.001037 \cdot \left(\frac{292}{200}\right)^{0.5} = 0.00437$

Concrete Stress-Strain Calculations for Section 2 (400 mm Deep cross section):

For 100 mm stirrup spacing:

$K_e = \left(1 - \frac{100}{2\cdot292}\right)\cdot\left(1 - \frac{100}{2\cdot342}\right)\cdot\left(1 - \frac{2\cdot248^2+2\cdot298^2}{6\cdot292\cdot342}\right)$= 0.35

$\rho_{s,tr}$ = 0.006·0.258 =0.0022474

K= 1+(0.002247 · (276/30))= 1.02

f_{cc}= 30·1.01= 30.6 MPa

$\varepsilon_{cc,0=}$ 0.002·1.020= 0.00204

$\varepsilon_{c,50} = \frac{3+0.29\cdot f_c}{145\cdot f_c-1000} + 0.75\cdot\ \rho_{s,tr}\cdot\left(\frac{b_c}{s}\right)^{0.5} = \frac{3+0.29\cdot30}{145\cdot30-1000} + 0.75\cdot\ 0.0022\cdot\left(\frac{292}{100}\right)^{0.5} = 0.00637$

For 200 mm stirrup spacing:

$K_e = \left(1 - \frac{200}{2\cdot292}\right)\left(1 - \frac{200}{2\cdot342}\right)\left(1 - \frac{2\cdot248^2+2\cdot298^2}{6\cdot292\cdot342}\right)$= 0.2318

$\rho_{s,tr}$ =0.0031·0.187 =0.0007389

K= 1+(0.0004693 · (276/30))= 1.006

f_{cc}= 30·1.006= 30.2 MPa

$\varepsilon_{cc,0=}$ 0.002·1.006= 0.002013

$\varepsilon_{c,50} = \frac{3+0.29\cdot f_c}{145\cdot f_c-1000} + 0.75\cdot\ \rho_{s,tr}\cdot\left(\frac{b_c}{s}\right)^{0.5} = \frac{3+0.29\cdot30}{145\cdot30-1000} + 0.75\cdot\ 0.000738\cdot\left(\frac{292}{200}\right)^{0.5} = 0.00416$

Concrete Stress-Strain Calculations for Section 1 (For the 700 mm deep section):

For 100 mm stirrup spacing:

$K_e = \left(1 - \frac{100}{2\cdot292}\right)\left(1 - \frac{100}{2\cdot642}\right)\left(1 - \frac{2\cdot70^2+2\cdot598^2}{6\cdot292\cdot642}\right)$= 0.258

$\rho_{s,tr}$ =0.005·0.258 =0.001292

K= 1+(0.00129 · (276/30))= 1.01

f_{cc}= 30·1.01= 30.35 MPa

$\varepsilon_{cc,0=}$ 0.002·1.020= 0.00202

$$\varepsilon_{c,50} = \frac{3+0.29\cdot f_c}{145\cdot f_c - 1000} + 0.75\cdot\ \rho_{s,tr}\cdot\left(\frac{b_c}{s}\right)^{0.5} = \frac{3+0.29\cdot 30}{145\cdot 30 - 1000} + 0.75\cdot\ 0.0012921\cdot\left(\frac{292}{100}\right)^{0.5} = 0.0051$$

For 200 mm stirrup spacing:

$$K_e = \left(1-\frac{200}{2\cdot 292}\right)\left(1-\frac{200}{2\cdot 642}\right)\left(1-\frac{2\cdot 70^2+2\cdot 598^2}{6\cdot 292\cdot 642}\right) = 0.352$$

$\rho_{s,tr}$ =0.0025·0.187 =0.0004693

K= 1+(0.0004693 · (276/30))= 1.004317

f_{cc}= 30·1.004317= 30.129 MPa

$\varepsilon_{cc,0=}$ 0.002·1.020= 0.0020086

$$\varepsilon_{c,50} = \frac{3+0.29\cdot f_c}{145\cdot f_c - 1000} + 0.75\cdot\ \rho_{s,tr}\cdot\left(\frac{b_c}{s}\right)^{0.5} = \frac{3+0.29\cdot 30}{145\cdot 30 - 1000} + 0.75\cdot\ 0.0004693\cdot\left(\frac{292}{200}\right)^{0.5} = 0.0039$$

Concrete Stress-Strain Calculations for Section 2 (For the 700 mm deep section):

For 100 mm stirrup spacing:

$$K_e = \left(1-\frac{100}{2\cdot 292}\right)\left(1-\frac{100}{2\cdot 642}\right)\left(1-\frac{2\cdot 248^2+2\cdot 598^2}{6\cdot 292\cdot 642}\right) = 0.1947$$

$\rho_{s,tr}$ =0.005·0.1947 =0.000974

K= (1+0.000974 · (276/30))= 1.0089

f_{cc}= 30·1.0089= 30.26 MPa

$\varepsilon_{cc,0=}$ 0.002·1.020= 0.00202

$$\varepsilon_{c,50} = \frac{3+0.29\cdot f_c}{145\cdot f_c - 1000} + 0.75\cdot\ \rho_{s,tr}\cdot\left(\frac{b_c}{s}\right)^{0.5} = \frac{3+0.29\cdot 30}{145\cdot 30 - 1000} + 0.75\cdot\ 0.000974\cdot\left(\frac{292}{100}\right)^{0.5} = 0.0047$$

For 200 mm stirrup spacing:

$$K_e = \left(1-\frac{200}{2\cdot 292}\right)\left(1-\frac{200}{2\cdot 642}\right)\left(1-\frac{2\cdot 248^2+2\cdot 598^2}{6\cdot 292 * 642}\right) = 0.141$$

$\rho_{s,tr}$ =0.0025·0.141 =0.000353

K= 1+(0.0004693 · (276/30))= 1.003

f_{cc}= 30·1.003= 30.09 MPa

$\varepsilon_{cc,0=}$ 0.002·1.003= 0.0020065

$$\varepsilon_{c,50} = \frac{3+0.29\cdot f_c}{145\cdot f_c - 1000} + 0.75\cdot \rho_w \cdot \left(\frac{b_c}{s}\right)^{0.5} = \frac{3+0.29\cdot 30}{145\cdot 30 - 1000} + 0.75\cdot 0.00035 \cdot \left(\frac{292}{200}\right)^{0.5} = 0.0038$$

Table A.1: Section1/ 200 mm stirrups spacing.

σ_c/f_c	ε
0	0
0.247989	1.77971E-05
0.44678	6.62309E-05
0.645838	0.000165395
0.846003	0.000372443
1	0.001008929
0.5	0.00393993
0.2	0.005698531
0	0.006870931

Table A.2: Section 1/ 100 mm stirrups spacing.

σ_c/f_c	ε
0	0
0.244075	1.74812E-05
0.44032	6.50554E-05
0.637704	0.00016246
0.838041	0.000365833
1	0.001027917
0.5	0.006762689
0.2	0.010203552
0	0.012497461

Table A.3: Section 2/200 mm stirrups spacing.

σ_c/f_c	ε
0	0
0.248476	1.78348E-05
0.447586	6.63711E-05
0.646857	0.000165746
0.84701	0.000373232
1	0.001006798
0.5	0.003713798
0.2	0.005337998
0	0.006420798

Table A.4: Section 2/ 100 mm stirrups spacing.

σ_c/f_c	ε
0	0
0.24544	1.75923E-05
0.442574	6.54686E-05
0.640544	0.000163492
0.840825	0.000368157
1	0.001021113
0.5	0.005862726
0.2	0.008768434
0	0.010704339

Table A.5: Section 1/200 mm stirrups spacing (h=700 mm)

σ_c/f_c	ε
0	0
0.249046	1.78788E-05
0.448529	6.6535E-05
0.648047	0.000166155
0.848184	0.000374154
1	0.001004317
0.5	0.003415652
0.2	0.004862453
0	0.005826987

Table A.6: Section 1/100 mm stirrups spacing (h=700 mm)

σ_c/f_c	ε
0	0
0.24735	1.77451E-05
0.445728	6.60372E-05
0.644519	0.000164912
0.844725	0.000371355
1	0.00101203
0.5	0.004642626
0.2	0.006820984
0	0.008273222

Table A.7: Section 2/200 mm stirrups spacing (h=700 mm)

σ_c/f_c	ε
0	0
0.249291	1.78978E-05
0.448934	6.66055E-05
0.648558	0.000166331
0.848688	0.00037455
1	0.001003254
0.5	0.003311472
0.2	0.004696402
0	0.005619689

Table A.8: Section 2/100 mm stirrups Spacing (h=700 mm)

σ_c/f_c	ε
0	0
0.248001	1.77965E-05
0.446804	6.62288E-05
0.645875	0.00016539
0.846056	0.000372432
1	0.001009041
0.5	0.004236323
0.2	0.006172693
0	0.007463605

Table A.9: Unconfined Cover

σ_c/f_c	ε
0	0
0.250044	0.000017956
0.450178	6.68222E-05
0.650128	0.000166872
0.850231	0.000375769
1	0.001
0.5	0.002992537
0.2	0.0041888
0	0.004985075

Appendix B : Bond Strength Calculations

Fib Model Code (2010) design Equation

K_{tr} Calculations: $K_{tr} = \frac{n_t A_{st}}{n_b d_b s_h}$

For Section 1, Stirrup Spacing of 200 mm

$$K_{tr} = \frac{\left(\frac{\pi}{4}\right)(2)(8)^2}{(4)(18)(200)} = 0.00698$$

For Section 1, Stirrup Spacing of 100 mm

$$K_{tr} = \frac{\left(\frac{\pi}{4}\right)(2)(8)^2}{(4)(18)(100)} = 0.0139$$

For Section 2, Stirrup Spacing of 200 mm

$$K_{tr} = \frac{\left(\frac{\pi}{4}\right)(2)(8)^2}{(2)(18)(200)} = 0.0139$$

For Section 2, Stirrup Spacing of 100 mm

$$K_{tr} = \frac{\left(\frac{\pi}{4}\right)(2)(8)^2}{(2)(18)(100)} = 0.0279$$

c_{min} and c_{max} Calculations:

For Section 1

c_x= 25+8 = 33 mm, c_y= 25+8= 33 mm, c_{si}= 70 mm

c_{min}= min (c_x, c_y, c_{si}/2)= min(33 mm, 33 mm, 35 mm) = 33 mm

c_{max}= max(c_x, c_{si}/2)= max (33 mm, 35 mm) = 35 mm

For Section 2

c_x= 25+8 = 33 mm , c_y= 25+8= 33 mm, c_{si}= 248 mm

c_{min}= min (c_x, c_y, c_{si}/2)= min(33 mm, 33 mm, 248 mm) = 33 mm

c_{max}= max (c_x, c_{si}/2)= max (33 mm, 124 mm) = 124 mm

$\propto_2 + \propto_1$ Calculations:

$\propto_2$ for Section 1 = $[(c_{min}/d_b)^{0.5} (c_s/2c_{min})^{0.15}] = [(33/18)^{0.5} (70/2\cdot 33)^{0.15}] = 1.36$

$\propto_2$ for Section 2 = $[(c_{min}/d_b)^{0.5} (c_s/2c_{min})^{0.15}] = [(33/18)^{0.5} (248/2\cdot 48)^{0.15}] = 1.56$

For Section 1, 20 cm spacing: $\propto_3 = 20\cdot (0.00698-0.5/50) = -0.0604$ the minimum specified limit is 0; therefore, $\propto_3 = 0$.

For section 1, 10 cm spacing: $\propto_3 = 20\cdot (0.0139-0.5/50) = 0.078$

For section 2, 20 cm spacing: $\propto_3 = 20\cdot (0.0139-0.5/50) = 0.078$

For section 2, 10 cm spacing: $\propto_3 = 20\cdot (0.0279-0.5/50) = 0.358$

Bond Strength Calcultions: $f_{bd} = (\acute{\eta}_1\ \acute{\eta}_2\ \acute{\eta}_3\ \acute{\eta}_4\ (f_{ck}/25)^{0.5}/\gamma_{cb})(\propto_2 + \propto_3)$

For Section 1, Stirrup Spacing of 200 mm

$f_{bd} = (1.75\cdot 1\cdot 1\cdot 1.17\cdot (30/25)^{0.5}) \cdot (1.36+0) = 2.91$ MPa

For Section 1, Stirrup Spacing of 100 mm

$f_{bd} = (1.75\cdot 1\cdot 1\cdot 1.17\cdot (30/25)^{0.5}) \cdot (1.36+0.078) = 3.22$ MPa

For Section 2, Stirrup Spacing of 200 mm

$f_{bd} = (1.75\cdot 1\cdot 1\cdot 1.17\cdot (30/25)^{0.5}) \cdot (1.56+0.078) = 3.67$ MPa

For Section 2, Stirrup Spacing of 100 mm

$f_{bd} = (1.75\cdot 1\cdot 1\cdot 1.17\cdot (30/25)^{0.5}) \cdot (1.56+0.358) = 4.3$ MPa

ACI-CODE 318M -11,14,19 Calculations:

For tension reinforcement:

K_{tr} Calculations: $K_{tr} = \frac{40A_{tr}}{s_h n}$

For Section 1, 200 mm Stirrup Spacing

$$K_{tr} = \frac{40 \cdot 2 \cdot \left(\frac{\pi}{4}\right) \cdot (8)^2}{200 \cdot 4} = 5.02$$

c_b= min((25+8+(18/2), (400-25(2)-8(2)-18)/2)= 42

$\frac{c_b+K_{tr}}{d_b} = \frac{42+5}{18} = 2.61 > 2.5\ (Pullout)$

For Section 1, 100 mm Stirrup spacing

$$K_{tr} = \frac{40 \cdot 2 \cdot \left(\frac{\pi}{4}\right) \cdot (8)^2}{100 \cdot 4} = \ 10.05$$

$$\frac{c_b + K_{tr}}{d_b} = \frac{42 + 10.05}{18} = 2.89 > 2.5\ (Pullout)$$

For Section 2, 20 mm Stirrup Spacing

$$K_{tr} = \frac{40 \cdot 2 \cdot \left(\frac{\pi}{4}\right) \cdot (8)^2}{100 \cdot 4} = \ 10.05$$

$$\frac{c_b + K_{tr}}{d_b} = \frac{42 + 5.02}{18} = 2.89 > 2.5\ (Pullout)$$

For Section 2, 100 mm Stirrup Spacing

$$K_{tr} = \frac{40 \cdot 2 \cdot \left(\frac{\pi}{4}\right) \cdot (8)^2}{100 \cdot 4} = \ 20.1$$

$$\frac{c_b + K_{tr}}{d_b} = \frac{42 + 20.1}{18} = 3.45 > 2.5\ (Pullout)$$

Bond Strength Calculations: $l_d = \frac{f_{yl}}{1.1\ \lambda f_c^{0.5}} \frac{\Psi_e \Psi_t \Psi_s}{\frac{c_b+K_{tr}}{d_b}} d_b$

Ψ_e= 1, Ψ_t= 1, Ψ_s= 0.8, Ψ_s (for the 19th version) =1.0

For all Sectional Geometry: $l_d = \frac{414}{1.1\ (1)(30)^{0.5}} \frac{1 \cdot 1 \cdot 0.8}{(2.5)} (18) = 395.8\ mm$

$$Bond\ Strenght\ (MPa) = \ \frac{d_b f_{yl}}{4 l_d}$$

$$Bond\ Strenght\ (MPa) = \ \frac{18(414)}{4(395.8)} = 4.6\ MPa$$

For Bars in Compression:

Taking the largest between the two equations $\left(\frac{0.24 f_{yl} \Psi_r}{\lambda \sqrt{f_c}}\right) d_b$ and $0.043 f_y \Psi_r d_b$

$$\left(\frac{0.24(414)(1)}{1\sqrt{30}}\right)(18) = 326.5 \text{ mm}$$

$0.043(414)(1)(18) = 320.436$

$$Bond\ Strength\ (MPa) = \frac{18(414)}{4(326.5)} = 5.7\ MPa$$

For standard hooks in tension:

Take the largest of 8d$_b$, 150, $l_d = \frac{0.24 f_{yl} \Psi_e}{\lambda f_c^{0.5}} d_b$

$$l_d = \frac{0.24(414)(1)}{(1)(30)^{0.5}}(18) = 326.53$$

In the 11th version :

$$Bond\ Strength\ (MPa) = \frac{18(414)}{4(326.5)} = 5.7\ MPa$$

In the 14th version Ψ_c= 0.7, Ψ_r=1.0 : 326.53(0.7) =228.571 mm, bond strength = 8.2 MPa

In the 19th version Ψ_c= 0.7, Ψ_r=1.0, Ψ_o=1.0: 326.53(0.7)= 228.517, bond strength = 8.2 MPa

For headed bars

for headed bars in tension, it is taken the larger of 150 mm, 8d$_b$ and $l_d = \frac{0.19 f_{yl} \Psi_e}{\lambda f_c^{0.5}} d_b$

$$l_d = \frac{0.19(414)(1)}{(30)^{0.5}}(18) = 258.58$$

For the 11th and the 14th version :

$$Bond\ Strength\ (MPa) = \frac{18(414)}{4(258.58)} = 7.2\ MPa$$

For the 19th version, Ψ_c= 0.7, Ψ_o=1.0, Ψ_p =1.6= $258.50\ (0.7)(1.6) = 289.52$, Bond strength= 6.43 MPa

ACI 408R-03 calculations:

c_b= smaller of a) distance from center of bar to nearest concrete edge; and b) one-half center to-center spacing between reinforcing bars. For Section 1 min {1.65 in , 1.74 in}, for Section 2 min {1.65 in, 5.22 in}.

C_s = minimum of (side cover, one-half clear spacing + 0.25)= for Section 1 min{ 0.98 inches, 1.39+0.25=1.64). C$_s$ for section 1 = 0.98 inches. For Section 2 (0.98 inches , 4.88+0.25 inches=5.13). C$_s$ for Section 2= 0.98 inches

C_{max} = maximum of (c_b, C_s).

C_{min} = minimum of (c_b, C_s).

w= $(0.1C_{max}/C_{min}) + 0.9 \leq 1.25$

c=C_{min} + $0.5D_b$

C_{max} Calculations:

C_{max} for Section 1 max[1.65, 0.98] = 1.65 inches
C_{max} for Section 2 max[1.65 , 0.98] = 1.65 inches

C_{min} Calculations:

C_{min} for Section 1 min[1.96, 0.98] = 0.98 inches.
C_{min} for Section 2 min[6.11, 0.98] = 0.98 inches

w Calculations:

w for Section 1 =(0.1(1.65) /0.98) +0.9 = 1.06
w for Section 2 =(0.1(1.65) /0.98) +0.9 = 1.06

C calculations:

C for Section 1 = 0.98+(0.5(0.70866))= 1.33
C for Section 2 = 0.98+(0.5(0.70866))= 1.33

t_d calculations:

t_d= 0.78(0.70866)+0.22= 0.77275 inches.

K_{tr} calculations: $K_{tr} = \frac{0.5A_{tr}t_d f_c^{0.5}}{s_h n}$

For Section 1, 200 mm Stirrup Spacing

$$K_{tr} = \frac{0.5(0.319)^2\left(\frac{\pi}{4}\right)(0.77275)(4351.1321)^{0.5}}{(7.874)(4)} = 0.128$$

$$\frac{cw+K_{tr}}{d_b} = \frac{1.33(1.06)+0.128}{0.70866} = 2.17 < 4.0$$

For Section 1, 100 mm Stirrup Spacing

$$K_{tr} = \frac{0.5(0.319)^2\left(\frac{\pi}{4}\right)(0.77275)(4351.1321)^{0.5}}{(3.937)(4)} = 0.252$$

$$\frac{cw+K_{tr}}{d_b} = \frac{1.33(1.06)+0.252}{0.70866} = 2.3 < 4.0$$

For Section 2, 200 mm Stirrup Spacing

$$K_{tr} = \frac{0.5(0.319)^2\left(\frac{\pi}{4}\right)(0.77275)(4351.1321)^{0.5}}{(7.874)(2)} = 0.252$$

$$\frac{cw+K_{tr}}{d_b} = \frac{1.33(1.06)+0.252}{0.70866} = 2.3 < 4.0$$

For section 2, 100 mm Stirrup Spacing

$$K_{tr} = \frac{0.5(0.319)^2\left(\frac{\pi}{4}\right)(0.77275)(4351.1321)^{0.5}}{(3.937)(2)} = 0.5$$

$$\frac{cw+K_{tr}}{d_b} = \frac{1.33(1.06)+0.5}{0.70866} = 2.69 < 4.0$$

Bond Strength Calculations: $l_d = \frac{\left(\frac{f_{yl}}{f_c^{0.25}} - 2500\Phi w\right)\lambda}{76.3\Phi\frac{((c)(w)+k_{tr})}{d_b}} d_b$

note: Φ is a strength reduction factor and will not be included in the calculations.

For section 1, 200 mm Stirrup Spacing:

$$l_d = \frac{\left(\frac{60045}{4351^{0.25}} - 2500(1.06)\right)}{76.3(2.17)} 0.70877 = 20.3\ in = 515.6\ mm$$

$$Bond\ Strength\ (MPa) = \frac{18(414)}{4(515.6)} = 3.4\ MPa$$

For Section 1, 100 mm Stirrup Spacing:

$$l_d = \frac{\left(\frac{60045}{4351^{0.25}} - 2500(1.06)\right)}{76.3(2.3)} 0.70877 = 19.1\ in = 486mm$$

$$Bond\ Strength\ (MPa) = \frac{18(414)}{4(486)} = 3.6\ MPa$$

For Section 2, 200 mm stirrup spacing:

$$l_d = \frac{\left(\frac{60045}{4351^{0.25}} - 2500(1.06)\right)}{76.3(2.3)} 0.70877 = 19.1\ in = 486\ mm$$

$$Bond\ Strength\ (MPa) = \frac{18(414)}{4(486)} = 3.6\ MPa$$

For Section 2, 100 mm Stirrup Spacing:

$$l_d = \frac{\left(\frac{60045}{4351^{0.25}} - 2500(1.06)\right)}{76.3(2.69)} 0.70877 = 16.3\ in = 416\ mm$$

$$Bond\ Strength\ (MPa) = \frac{18(414)}{4(486)} = 3.8\ MPa$$

CSA A23.3-14 calculations

K factors: K_1=1, K_2=1, K_3=1, K_4=0.8

d_{cs}: for Section 1 dsc= 42 mm , for Section 2 =42 mm

K_{tr} *Calcultions:* $K_{tr} = \frac{A_{tr} f_{yt}}{10.5 s_h n}$

For Section 1, 200 mm Stirrup Spacing

$$K_{tr} = \frac{(8)^2 \left(\frac{\pi}{4}\right)(2)(276)}{10.5(200)(4)} = 3.3$$

$$(d_{cs} + K_{tr}) = (42 + 3.3) = 45.3 > 2.5(18)\ (Pullout)$$

For Section 1, 100 mm Stirrup Spacing

$$K_{tr} = \frac{(8)^2 \left(\frac{\pi}{4}\right)(2)(276)}{10.5(100)(4)} = 6.6$$

$$(d_{cs} + K_{tr}) = (42 + 6.6) = 50.25 > 2.5(18)\ (Pullout)$$

For Section 2, 200 mm Stirrup Spacing

$$K_{tr} = \frac{(8)^2 \left(\frac{\pi}{4}\right)(2)(276)}{10.5(200)(2)} = 6.6$$

$$(d_{cs} + K_{tr}) = (42 + 6.6) = 50.25 > 2.5(18)\ (Pullout)$$

For Section 2, 100 mm Stirrup Spacing

$$K_{tr} = \frac{(8)^2\left(\frac{\pi}{4}\right)(2)(276)}{10.5(100)(2)} = 13.2$$

$$(d_{cs} + K_{tr}) = (42 + 13.2) = 55.212 > 2.5(18)\ (Pullout)$$

Bond Strength Calculations for Tension Reinforcement: $l_d = 1.15\frac{K_1K_2K_3K_4}{d_{cs}+K_{tr}}\frac{f_{yl}}{f_c^{0.5}}A_b$

$$l_d = 1.15\frac{0.8(1)(1)(1)}{45}\frac{141}{(30)^{0.5}}\left(\frac{\pi}{4}\right)(18)^2 = 393.23\ mm$$

$$Bond\ Strength\ (MPa) = \frac{18(414)}{4(393.23)} = 4.7\ MPa$$

Bond Strength Calculations for Compression Reinforcement:

$$l_d = \frac{0.24(18)(414)}{30^{0.5}} \geq 0.044(18)(414)$$

$$l_d = 326.53\ mm \geq 327.88\ mm$$

$$l_d = 326.53$$

$$Bond\ Strength\ (MPa) = \frac{18(414)}{4(326.53)} = 5.68\ MPa$$

Tension Reinforcement with Standard Hooks:

$$l_d = \frac{100d_b}{f_c^{0.5}}\frac{f_{yl}}{400}k_2k_1 = \frac{100(18)}{30^{0.5}}\left(\frac{414}{400}\right)(0.8)(0.9) = 190.47\ mm$$

$$Bond\ Strength\ (MPa) = \frac{18(414)}{4(190.47)} = 9.78\ MPa$$

Appendix C: Curvatures and Rotation Calculations

Depth of compression Zone at Ultimate and Yielding

Table C1: Depth of Compression Zone Values at Ultimate and Yielding

Longitudinal Reinforcement	Axial load %	X_y Response2000 (mm)	X_y From Panagiotakos and Fardis (2001)	X_u Response2000 At Max. Moment (mm)	X_u (Respon2000) At 85% Maximum Moment (mm)	X_u From Pantazopoulou 1998 (mm)
Cross section dimensions = 400 x 350 mm						
4 Φ18	10	131	122.7985	70	138.23	100.5867734
4 Φ 18	35	234	169.51041	185	201	189.3528139
4 Φ 18	50	298	216.35681	250	265.95	242.263804
2 Φ 18	10	120	113.24528	60	79	79.34689057
2 Φ 18	35	234	164.05498	188	200	182.7813584
2 Φ 18	50	298	218.87668	255	264	244.5911909
Cross section dimensions = 700 x 350 mm						
4 Φ18	10	209	204.75190	105	208	145.1837971
4 Φ 18	35	457	288.69672	340	359	335.7474731
4 Φ 18	50	574	382.32863	450	482.8	449.1188673
2 Φ 18	10	212	193.58942	100	180	120.6162323
2 Φ 18	35	297	281.63814	350	354.84	328.1464586
2 Φ 18	50	612	385.33197	470	479.5	452.0531553
Cross section dimensions = 400 x 350 mm – Lapped splice/ f_y reduced based on Eurocode Part 3						
4 Φ18	10	158	134.3663611	60	109	79.15485922
4 Φ 18	35	233	188.1209055	190	197.7	182.7219454
4 Φ 18	50	310	216.35681	260	264	243.7541998
2 Φ 18	10	140	127.2648601	60	72	65.74344866
2 Φ 18	35	228	187.374553	180	192	178.5725587
2 Φ 18	50	340	218.87668	265	262	245.5776357
Cross section dimensions = 400 x 350 mm – Lapped splice/ fy reduced based on ACSE SE 41-17						
4 Φ18	10	133	138.8793782	60	104	76.1411599
4 Φ 18	35	248	195.340276	180	195	181.7895301
4 Φ 18	50	332	216.3585842	260	264	244.1539418
2 Φ 18	10	144	132.586697	60	95	63.97124648
2 Φ 18	35	252	195.0671495	190	193	178.0242531
2 Φ 18	50	354	218.8778388	270	262	245.8274314

Sample of Calculations:

Longitudinal reinforcement = 4 Φ18, axial load = 10 % of crushing load , Concrete cover= 25 mm, b= 350 mm, h= 400mm and stirrups = Φ 8/100 mm.

For depth of compression zone at Yielding (Panagiotakos and Fardis 2001) :

$$\xi_y = (\alpha^2 A^2 + 2\alpha B)^{0.5} - \alpha A$$

$$\rho_1 = \frac{\frac{\pi}{4}\cdot(d_b{}^2)\cdot 4}{bd} = \frac{\frac{\pi}{4}\cdot(18^2)\cdot 4}{350(358)} = 0.008123511$$

$$\rho_2 = \frac{\frac{\pi}{4}\cdot(d_b{}^2)\cdot 4}{bd} = \frac{\frac{\pi}{4}\cdot(18^2)\cdot 4}{350(358)} = 0.008123511$$

If tension steel yielding controls →

$A = \rho_1 + \rho_2 + \rho_v + \frac{N}{bdf_y}$

$A = 0.0081235 + 0.0081235 + 0 + \frac{0.42}{0.35(0.358)(414)} = 0.02387488852$

$B = \rho_1 + \rho_2\delta_2 + 0.5\rho_v(1 + \delta_2) + \frac{N}{bdf_y}$

$$\delta_2 = \left(\frac{42}{358}\right) = 0.1173184358$$

$B = 0.0081235 + 0.0081235(0.1173) + 0 + \frac{0.42}{0.35(0.358)(414)} = 0.01717$

$\alpha = E_s/E_c = 200000/30000 = 6.66$

$\xi_y = (6.66^2\ (0.02387^2) + 2\ (6.66)\ (0.01717))^{0.5} - 6.66(0.023874) = 0.3429$

$C_y = 0.3429(358) = 122.8$ mm

If nonlinearity of concrete controls →

$A = \rho_1 + \rho_2 + \rho_v - \frac{N}{\varepsilon_c bdE_s}$

$A = 0.0081235 + 0.0081235 + 0 - \frac{0.42}{0.35(0.358)(200000)\left(1.8.\frac{30}{30000}\right)} = 0.00693$

$B = \rho_1 + \rho_2\ \delta_2 + 0.5\rho_v(1 + \delta_2)$

$B = 0.0081235 + 0.0081235(0.1173) = 0.00907638$

$\xi_y = (6.66^2\ (0.00693^2) + 2\ (6.66)\ (0.00907638))^{0.5} - 6.66(0.00693) = 0.3046$

C_y= 0.3046(358)= 109.05 mm

Depth of compression Zone at Ultimate (Pantazopoulou 1998)

1) $for\ x = d_2\ and\ \xi = d_2,\ \frac{N_{min}}{A_c f_c} = 0.72\delta_2 - \frac{f_y}{(1-\alpha)f_c}[\rho_1 + \rho_v(1-\delta_2)]$

N_{min}= $\left(0.72\ (0.1173) - \frac{414}{\left(1-\frac{552-414}{414}\right)(30)}(0.00812)\right)(0.4)(0.35)(30) = -0.273\ Mn$

2) $for\ x = x_{balance}\ and\ \xi_{balanced} = 0.64,\ \frac{N_{balanced}}{A_c f_c} = (\rho_2 - \rho_1)\frac{f_y}{f_c} + 0.275\frac{f_y}{f_c}\rho_v + 0.462$

$N_{balanced} = \left((0.00812 - 0.00812)\left(\frac{414}{30}\right) + 0.275\ \left(\frac{414}{30}\right)(30) + 0.462\right)(\ 0.4)(0.35)30 =$
$1.9404\ MPa$

3) $for\ x = d, \xi = 1,\ \frac{N_{max}}{A_c f_c} = 0.85^2 + \frac{f_y}{f_c}[\rho_2 + 0.8\ \rho_v],$

$$N_{max} = (0.85^2 + \left(\frac{414}{30}\right)\left(0.00812 + 0.8(0)\right)(0.4)(0.35)30 = 3.5\ MPa$$

If $N_{min} < N < N_{balanced}$

$$\xi_u = \frac{42}{358} + \left(\frac{\left(0.64 - \frac{42}{358}\right)(0.42 - -0.27)}{1.9404 - -0.27}\right) = 0.2804$$

C_u =0.2804(358) = 100.3 mm

➔ $\frac{f_y}{E_s}\left(\frac{1}{d-x_y}\right) = \frac{414}{200000}\left(\frac{1}{358-122.8}\right) = 8.8E-06$

➔ $\frac{\varepsilon_{cy}}{x_y} = \frac{0.75(0.00205)}{109.8} = 1.4E-05$

$8.8 \cdot 10^{-6} < 1.4 \cdot 10^{-5}$ therefore, steel yielding controls the failure of the section.

When doing the calculations for the column with the lap splice, f_{yl} is used as the reduced (According to EUROCODE 8 III 2005) steel strength with no ultimate strength.

Curvatures at Yielding and Ultimate

Panagiotakos and Fardis 2001 Curvatures:

(The depth of the compression Zone is from Response2000)

Table C2: Curvature Values at Yielding and Ultimate from Panagiotakos and Fardis (2001)-Depth of the Compression Zone from Response 2000

Column Set	Column Name	Yield Curvatures	Ultimate Curvatures (Depth of Compression Zone at 85% Maximum Moment)	Ultimate Curvatures (Depth of Compression Zone at Maximum Moment)
Section = 350 mm x 400 mm and Continuous Reinforcement	C10-1-10	9.12E-06	2.30E-05	5.14E-05
	C35-1-10	7.01E-06	1.66E-05	1.95E-05
	C50-1-10	5.50E-06	1.30E-05	1.44E-05
	C10-2-10	9.16E-06	1.64E-05	3.86E-05
	C35-2-10	6.70E-06	1.27E-05	1.38E-05
	C50-2-10	5.12E-06	9.66E-06	1.06E-05
	C10-1-20	8.70E-06	1.97E-05	5.50E-05
	C35-1-20	6.26E-06	1.59E-05	1.76E-05
	C50-1-20	4.95E-06	1.19E-05	1.29E-05
	C10-2-20	8.88E-06	1.90E-05	3.71E-05
	C35-2-20	6.08E-06	1.18E-05	1.37E-05
	C50-2-20	4.88E-06	9.55E-06	9.63E-06
Section = 350 mm x 400 mm and Lap Splice	C10-1-10	6.85E-06	2.88E-05	6.00E-05
	C35-1-10	6.94E-06	1.72E-05	1.89E-05
	C50-1-10	5.21E-06	1.33E-05	1.38E-05
	C10-2-10	6.37E-06	1.88E-05	4.35E-05
	C35-2-10	6.86E-06	1.24E-05	1.08E-05
	C50-2-10	4.85E-06	9.44E-06	1.00E-05
	C10-1-20	6.28E-06	2.48E-05	5.50E-05
	C35-1-20	7.08E-06	1.63E-05	1.83E-05
	C50-1-20	4.75E-06	1.21E-05	1.25E-05
	C10-2-20	6.31E-06	2.18E-05	4.33E-05
	C35-2-20	6.80E-06	1.19E-05	1.33E-05
	C50-2-20	4.56E-06	9.09E-06	9.45E-06

Table C2: Continued

Section = 350 mm x 700 mm and Continuous Reinforcement	C10-1-10	4.61E-06	1.25E-05	2.82E-05
	C35-1-10	3.54E-06	8.00E-06	8.71E-06
	C50-1-10	2.82E-06	5.99E-06	6.58E-06
	C10-2-10	4.69E-06	1.07E-05	2.46E-05
	C35-2-10	3.49E-06	6.70E-06	7.37E-06
	C50-2-10	2.77E-06	5.19E-06	5.49E-06
	C10-1-20	4.64E-06	1.16E-05	2.83E-05
	C35-1-20	5.43E-06	7.73E-06	8.09E-06
	C50-1-20	2.64E-06	5.72E-06	6.02E-06
	C10-2-20	4.54E-06	1.34E-05	2.54E-05
	C35-2-20	3.22E-06	6.73E-06	7.26E-06
	C50-2-20	2.46E-06	5.12E-06	5.29E-06

Sample of Calculations:

Longitudinal reinforcement = 4 Φ18, axial load = 10 % of crushing load , Concrete cover= 25 mm, b= 350 mm, h= 400mm and stirrups = Φ8/100 mm.

➔ $\frac{f_y}{E_s}\left(\frac{1}{d-x_y}\right) = \frac{414}{200000}\left(\frac{1}{358-131}\right) = 9.12E-06$

➔ $\frac{\varepsilon_{cy}}{x_y} = \frac{0.75(0.00205)}{131} = 1.156E-06$

$9.2 \cdot 10^{-6} < 1.156 \cdot 10^{-5}$, therefore, steel yielding controls the behaviour.

In the case of Lap Splice For lap splice case:

➔ $\frac{f_y}{E_s}\left(\frac{1}{d-x_y}\right) = \frac{273}{200000}\left(\frac{1}{358-158}\right) = 6.85E-06$

➔ $\frac{\varepsilon_{cy}}{x_y} = \frac{0.75(0.00205)}{153} = 1.156E-06$ therefore, Steel yielding controls.

Ultimate Curvatures

➔ $\frac{\varepsilon_{cu}}{x_u} = \frac{0.0036}{70} = 5.14E-05$

Panagiotakos and Fardis 2001 Curvatures:

(The depth of the compression Zone is from Panagiotakos and Fardis 2001)

Table C3: Curvature Values at Yielding and Ultimate from Panagiotakos and Fardis (2001)-Depth of the Compression Zone from Panagiotakos and Fardis (2001)

Column Set	Column Name	Yield Curvatures	Ultimate Curvatures
Cross Section = 350 x 400 mm and Continuous Reinforcement	C10-1-10	8.80E-06	3.58E-05
	C35-1-10	9.68E-06	1.90E-05
	C50-1-10	7.58E-06	1.49E-05
	C10-2-10	8.80E-06	2.68E-05
	C35-2-10	9.52E-06	1.43E-05
	C50-2-10	7.46E-06	1.11E-05
	C10-1-20	8.46E-06	4.16E-05
	C35-1-20	9.95E-06	1.81E-05
	C50-1-20	7.46E-06	1.35E-05
	C10-2-20	8.46E-06	3.28E-05
	C35-2-20	9.82E-06	1.42E-05
	C50-2-20	7.36E-06	1.06E-05
Cross Section = 350 x 400 mm and Lap Splice	C10-1-10	6.12E-06	4.55E-05
	C35-1-10	8.06E-06	1.97E-05
	C50-1-10	7.11E-06	1.48E-05
	C10-2-10	6.12E-06	3.41E-05
	C35-2-10	8.06E-06	1.48E-05
	C50-2-10	6.99E-06	1.11E-05
	C10-1-20	5.93E-06	5.02E-05
	C35-1-20	8.03E-06	1.85E-05
	C50-1-20	6.99E-06	1.34E-05
	C10-2-20	5.93E-06	3.95E-05
	C35-2-20	8.03E-06	1.46E-05
	C50-2-20	6.90E-06	1.06E-05
Cross Section = 350 x 700 mm and Continuous Reinforcement	C10-1-10	6.12E-06	4.55E-05
	C35-1-10	8.06E-06	1.97E-05
	C50-1-10	7.11E-06	1.48E-05
	C10-2-10	6.12E-06	3.41E-05
	C35-2-10	8.06E-06	1.48E-05
	C50-2-10	6.99E-06	1.11E-05
	C10-1-20	5.93E-06	5.02E-05
	C35-1-20	8.03E-06	1.85E-05
	C50-1-20	6.99E-06	1.34E-05
	C10-2-20	5.93E-06	3.95E-05
	C35-2-20	8.03E-06	1.46E-05
	C50-2-20	6.90E-06	1.06E-05

Sample of Calculations:

Longitudinal reinforcement = 4Φ18, axial load = 10 % of crushing load , Concrete cover= 25 mm, b= 350 mm, h= 400mm and stirrups = Φ8/100 mm.

➔ $\frac{f_y}{E_s}\left(\frac{1}{d-x_y}\right) = \frac{414}{200000}\left(\frac{1}{358-122.7}\right) = 8.8E-06$

➔ $\frac{\varepsilon_{cy}}{x_y} = \frac{0.75(0.00205)}{109} = 1.41E-06$

$9.2E-10^{-6} < 1.156E-05$, therefore, steel yielding controls the behaviour.

For Ultimate Curvatures :

➔ $\frac{\varepsilon_{cu}}{x_u} = \frac{0.0036}{100.58} = 3.58E-05E$

Curvatures from Response2000

Table C.4: Yield and Ultimate Curvatures Using Response2000

Column Set	Column Name	Yield Curvatures	Ultimate Curvatures φu (at 85% maximum Moment)	Ultimate Curvatures φu (at maximum Moment)
Cross Section = 350 x 400 mm and Continuous Reinforcement	C10-1-10	9.50E-06	1.48E-04	1.13E-04
	C35-1-10	6.90E-06	4.42E-05	1.53E-05
	C50-1-10	5.80E-06	2.78E-05	1.53E-05
	C10-2-10	9.50E-06	8.70E-05	7.03E-05
	C35-2-10	6.50E-06	2.50E-05	1.39E-05
	C50-2-10	5.60E-06	1.85E-05	1.14E-05
	C10-1-20	9.50E-06	1.30E-04	1.03E-04
	C35-1-20	5.40E-06	3.75E-05	1.53E-05
	C50-1-20	4.80E-06	2.30E-05	1.26E-05
	C10-2-20	9.50E-06	8.05E-05	4.79E-05
	C35-2-20	5.10E-06	2.42E-05	1.39E-05
	C50-2-20	4.40E-06	1.58E-05	9.40E-06
Cross Section = 350 x 400 mm and Lap Splice	C10-1-10	5.40E-06	1.68E-04	5.27E-05
	C35-1-10	7.10E-06	4.35E-05	1.52E-05
	C50-1-10	4.80E-06	2.60E-05	1.26E-05
	C10-2-10	5.30E-06	9.50E-05	3.96E-05
	C35-2-10	7.10E-06	2.45E-05	1.26E-05
	C50-2-10	4.50E-06	1.62E-05	1.04E-05
	C10-1-20	5.40E-06	1.40E-04	5.25E-05
	C35-1-20	7.20E-06	3.65E-05	1.53E-05
	C50-1-20	4.00E-06	2.20E-05	1.14E-05
	C10-2-20	5.90E-06	8.65E-05	3.96E-05

Table C.4: Continued

	C35-2-20	7.10E-06	2.35E-05	1.26E-05
	C50-2-20	4.90E-06	1.50E-05	9.50E-06
Cross Section = 350 x 700 mm and Continuous Reinforcement	C10-1-10	4.90E-06	5.80E-05	4.41E-05
	C35-1-10	3.10E-06	1.70E-05	7.90E-06
	C50-1-10	2.80E-06	1.08E-05	6.56E-06
	C10-2-10	4.90E-06	4.15E-05	3.01E-05
	C35-2-10	3.00E-06	1.28E-05	6.50E-06
	C50-2-10	2.60E-06	8.10E-06	5.40E-06
	C10-1-20	4.50E-06	5.50E-05	3.65E-05
	C35-1-20	2.50E-06	1.52E-05	7.22E-06
	C50-1-20	2.10E-06	9.50E-06	5.40E-06
	C10-2-20	4.90E-06	4.10E-05	3.32E-05
	C35-2-20	2.50E-06	1.18E-05	6.60E-06
	C50-2-20	2.30E-06	7.80E-06	4.90E-06

Priestley et al. 1996 Curvatures

Table C.4: Yield and Ultimate Curvatures Using Priestley et at. (1996)

Column Set	Column Name	Yield Curvatures	Ultimate Curvatures
Cross Section = 350 x 400 mm and Continuous Reinforcement	C10-1-10	1.09E-05	6.84E-05
	C35-1-10	1.09E-05	2.96E-05
	C50-1-10	1.09E-05	2.46E-05
	C10-2-10	1.09E-05	6.84E-05
	C35-2-10	1.09E-05	2.96E-05
	C50-2-10	1.09E-05	2.46E-05
	C10-1-20	1.09E-05	8.34E-05
	C35-1-20	1.09E-05	2.96E-05
	C50-1-20	1.09E-05	2.46E-05
	C10-2-20	1.09E-05	8.34E-05
	C35-2-20	1.09E-05	2.94E-05
	C50-2-20	1.09E-05	2.46E-05
Cross Section = 350 x 400 mm and Lap Splice	C10-1-10	7.19E-06	6.47E-05
	C35-1-10	7.19E-06	2.59E-05
	C50-1-10	7.19E-06	2.09E-05
	C10-2-10	7.19E-06	6.47E-05
	C35-2-10	7.19E-06	2.59E-05
	C50-2-10	7.19E-06	2.09E-05
	C10-1-20	7.19E-06	7.97E-05
	C35-1-20	7.19E-06	2.59E-05
	C50-1-20	7.19E-06	2.09E-05

	C10-2-20	7.19E-06	7.97E-05
	C35-2-20	7.19E-06	2.58E-05
	C50-2-20	7.19E-06	2.09E-05
Cross Section = 350 x 700 mm and Continuous Reinforcement	C10-1-10	7.19E-06	6.47E-05
	C35-1-10	7.19E-06	2.59E-05
	C50-1-10	7.19E-06	2.09E-05
	C10-2-10	7.19E-06	6.47E-05
	C35-2-10	7.19E-06	2.59E-05
	C50-2-10	7.19E-06	2.09E-05
	C10-1-20	7.19E-06	7.97E-05
	C35-1-20	7.19E-06	2.59E-05
	C50-1-20	7.19E-06	2.09E-05
	C10-2-20	7.19E-06	7.97E-05
	C35-2-20	7.19E-06	2.58E-05
	C50-2-20	7.19E-06	2.09E-05

Sample of Calcutions

$$\varphi_y = \frac{\frac{2.1 f_y}{E_s}}{h}$$

$$\varphi_y = \frac{\frac{2.1(414)}{200000}}{400}$$

$\varphi_u \rightarrow$

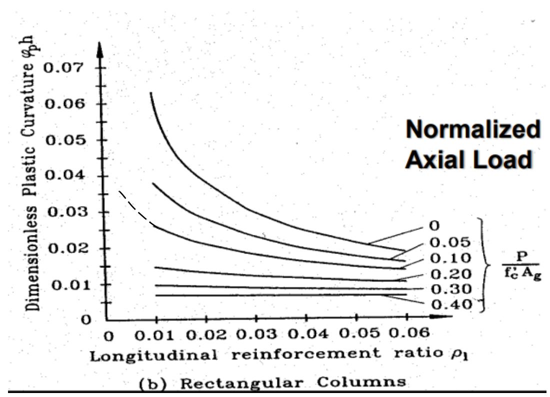

Figure C.1: Plastic Curvatures

For Cross Section = 350 x 400 mm and Continuous Reinforcement

$$For\ Section\ 1 \left(\frac{4\Phi 18}{\text{Face}}\right): \rho_1 = \frac{8\left(\frac{\pi}{4}\right)(18)^2}{358 \cdot 350} = 0.0162$$

$$For\ Section\ 2 \left(\frac{2\Phi 18}{\text{Face}}\right) \rho_1 = \frac{4\left(\frac{\pi}{4}\right)(18)^2}{358 \cdot 350} = 0.00812$$

For 0.1 Normalized Axial Load Ratio:

For Section 1, from Figure C.1a: φ_{pl}h = 0.023 → φ_{pl}= 5.75(10)$^{-5}$ rad/mm

For Section 2, from Figure C.1a: φ_{pl}h = 0.029 → φ_{pl}= 7.25(10)$^{-5}$ rad/mm

For 0.35 Normalized Axial Load Ratio:

For Section 1 and 2, From Figure C.1a: φ_{pl}h= 0.0075 → φ_{pl}= 1.875(10)$^{-5}$ rad/mm

For 0.5 Normalized Axial Load Ratio:

For Section 1 and 2, From Figure C.1a: φ_{pl}h= 0.0055→ φ_{pl}= 1.375(10)$^{-5}$

For Cross Section = 350 x 700 mm and Continuous Reinforcement

$$For\ Section\ 1\left(\frac{4\Phi 18}{\text{Face}}\right): \rho_1 = \frac{8\left(\frac{\pi}{4}\right)(18)^2}{658 \cdot 350} = 0.008839$$

$$For\ Section\ 2\ \left(\frac{2\Phi 18}{\text{Face}}\right): \rho_1 = \frac{4\left(\frac{\pi}{4}\right)(18)^2}{658 \cdot 350} = 0.0044197$$

For 0.1 normalized axial load ratio:

For Section 1, from Figure C.1a: φ_{pl}h = 0.0275 → φ_{pl}= 4.0(10)$^{-5}$ rad/mm

For Section 2, from Figure C.1a: φ_{pl}h = 0.0325 → φ_{pl}= 4.6428(10)$^{-5}$ rad/mm

For 0.35 Normalized Axial Load Ratio

φ_{pl}h= 0.0075 → φ_{pl}= 1.07(10)$^{-5}$ rad/mm

For 0.5 Normalized Axial Load Ratio:

φ_{pl}h= 0.0055→ φ_{pl}= 7.8(10)$^{-6}$ rad/mm

The f_{yl} used must account for the presences of the lapped bars at the critical region of the section.

φ_y(for 400 x 350 mm cross section) = $\frac{2.1\frac{414}{200000}\left(\frac{270}{408.16}\right)}{400}$ = 7.188 (10^{-6})

Rotation According to EUROCODE 8-III 2005

Damage limitation Rotation State calculations

Table C.5: Yield Rotations According to Damage Limitation State (Slip Rotations $=0.13\varphi_y\frac{d_b f_y}{\sqrt{f_c}}$)

Column Set	Column Name	Θ_{y1}	Θ_{y2}	Θ_{y3}	Θ_{y4}
Columns Set 1: Continuous Reinforcement	C10-1-10	8.06E-03	7.85E-03	8.32E-03	9.25E-03
	C35-1-10	6.63E-03	8.44E-03	6.56E-03	9.25E-03
	C50-1-10	5.62E-03	7.02E-03	5.82E-03	9.25E-03
	C10-2-10	8.09E-03	7.85E-03	8.32E-03	9.25E-03
	C35-2-10	6.42E-03	8.33E-03	6.29E-03	9.25E-03
	C50-2-10	5.36E-03	6.94E-03	5.68E-03	9.25E-03
	C10-1-20	7.78E-03	7.61E-03	8.32E-03	9.25E-03
	C35-1-20	6.12E-03	8.63E-03	5.55E-03	9.25E-03
	C50-1-20	5.24E-03	6.94E-03	5.14E-03	9.25E-03
	C10-2-20	7.90E-03	7.61E-03	8.32E-03	9.25E-03
	C35-2-20	6.00E-03	8.53E-03	5.34E-03	9.25E-03
	C50-2-20	5.19E-03	6.87E-03	4.87E-03	9.25E-03
Columns Set 2: Lap splice (270 mm)	C10-1-10	6.07E-03	5.59E-03	5.09E-03	6.30E-03
	C35-1-10	6.27E-03	7.04E-03	6.38E-03	6.44E-03
	C50-1-10	5.22E-03	6.74E-03	4.94E-03	6.55E-03
	C10-2-10	5.77E-03	5.61E-03	5.05E-03	6.33E-03
	C35-2-10	6.30E-03	7.13E-03	6.46E-03	6.52E-03
	C50-2-10	5.07E-03	6.81E-03	4.83E-03	6.65E-03
	C10-1-20	5.78E-03	5.55E-03	5.18E-03	6.39E-03
	C35-1-20	6.51E-03	7.16E-03	6.59E-03	6.58E-03
	C50-1-20	5.00E-03	6.78E-03	4.50E-03	6.65E-03
	C10-2-20	5.84E-03	5.59E-03	5.57E-03	6.44E-03
	C35-2-20	6.40E-03	7.25E-03	6.61E-03	6.67E-03
	C50-2-20	4.82E-03	6.38E-03	5.05E-03	6.60E-03
Columns Set 3: Short Anchorage length	C10-1-10	6.07E-03	5.59E-03	5.09E-03	6.30E-03
	C35-1-10	6.27E-03	7.04E-03	6.38E-03	6.44E-03
	C50-1-10	5.22E-03	6.74E-03	4.94E-03	6.55E-03
	C10-2-10	5.77E-03	5.61E-03	5.05E-03	6.33E-03
	C35-2-10	6.30E-03	7.13E-03	6.46E-03	6.52E-03
	C50-2-10	5.07E-03	6.81E-03	4.83E-03	6.65E-03
	C10-1-20	5.78E-03	5.55E-03	5.18E-03	6.39E-03
	C35-1-20	6.51E-03	7.16E-03	6.59E-03	6.58E-03
	C50-1-20	5.00E-03	6.78E-03	4.50E-03	6.65E-03
	C10-2-20	5.84E-03	5.59E-03	5.57E-03	6.44E-03
	C35-2-20	6.40E-03	7.25E-03	6.61E-03	6.67E-03
	C50-2-20	4.82E-03	6.38E-03	5.05E-03	6.60E-03

Column Set 4: Deep Cross Section (700 mm)	C10-1-10	6.36E-03	6.32E-03	6.62E-03	7.77E-03
	C35-1-10	5.41E-03	7.23E-03	5.03E-03	7.77E-03
	C50-1-10	4.78E-03	6.02E-03	4.77E-03	7.77E-03
	C10-2-10	6.44E-03	6.32E-03	6.62E-03	7.77E-03
	C35-2-10	5.30E-03	6.40E-03	4.30E-03	7.36E-03
	C50-2-10	4.63E-03	3.86E-03	3.53E-03	7.04E-03
	C10-1-20	5.44E-03	5.31E-03	5.34E-03	6.50E-03
	C35-1-20	7.09E-03	7.34E-03	4.50E-03	7.77E-03
	C50-1-20	4.08E-03	5.13E-03	3.72E-03	7.77E-03
	C10-2-20	5.37E-03	5.31E-03	5.61E-03	6.50E-03
	C35-2-20	5.06E-03	6.46E-03	3.89E-03	7.64E-03
	C50-2-20	6.36E-03	6.32E-03	6.62E-03	6.84E-03
Column Set 5: Hinge Fabrication at the critical Section	C10-1-10	6.22E-03	5.99E-03	6.40E-03	7.20E-03
	C35-1-10	6.18E-03	5.99E-03	4.87E-03	7.20E-03
	C50-1-10	4.87E-03	6.42E-03	4.22E-03	7.20E-03
	C10-2-10	4.00E-03	5.21E-03	6.40E-03	7.20E-03
	C35-2-10	6.20E-03	5.99E-03	4.63E-03	7.20E-03
	C50-2-10	4.73E-03	6.39E-03	4.11E-03	7.20E-03
	C10-1-20	3.81E-03	5.18E-03	6.40E-03	7.20E-03
	C35-1-20	5.93E-03	6.09E-03	3.99E-03	7.20E-03
	C50-1-20	4.45E-03	6.10E-03	3.63E-03	7.20E-03
	C10-2-20	3.69E-03	4.97E-03	6.40E-03	7.20E-03
	C35-2-20	6.04E-03	6.09E-03	3.81E-03	7.20E-03
	C50-2-20	4.37E-03	6.08E-03	3.40E-03	7.20E-03

Θ_{y1}: Yielding Curvatures= $\min\left\{\frac{f_y}{E_s}\left(\frac{1}{d-x_y}\right), \frac{\varepsilon_{cy}}{x_y}\right\}$, where x_y is the depth of the compression zone at yielding from Response2000

Θ_{y2}: Yielding Curvatures= $\min\left\{\frac{f_y}{E_s}\left(\frac{1}{d-x_y}\right), \frac{\varepsilon_{cy}}{x_y}\right\}$, where x_y is the depth of the compression zone at yielding from Panagiotakos and Fardis 2001.

Θ_{y3}: Yielding Curvatures are from Response2000.

Θ_{y4}: Yielding Curvatures are from Priestley et al. (1996) equation.

Sample of Calculations

➔ For Case 1 Continuous Reinforcement

Longitudinal reinforcement = 4Φ18, axial load = 10 % of crushing load , Concrete cover= 25 mm, b= 350 mm, h= 400mm and stirrups = Φ8/100 mm.

For θ_{y1}

$$\theta_y = \varphi_y \frac{L_v + a_v z}{3} + 0.00135\left(1 + 1.5\frac{h}{L_v}\right) + 0.13\varphi_y \frac{d_b f_y}{\sqrt{f_c}}$$

From Table C.2: φ_y = 9.12E-06

For a_v →

$$V_{Rd,c} = \left[C_{Rd,c} k (100\rho_l f_{ck})^{\frac{1}{3}} + K_1 \sigma_{cp}\right] b_w d \ \ (N)$$

$C_{Rd,c}$ =0.18/γ_c= 0.18 (the partial factor of concrete material is assumed =1 for assessment purposes)

$$k = 1 + \sqrt{\frac{200}{d}} = 1 + \sqrt{\frac{200}{358}} = 1.747435093$$

$$\rho_1 = \frac{A_{s1}}{bd} = \frac{\frac{\pi}{4}.(18)^2.(4)}{350(358)} = 0.008123$$

K_1= 0.15 (Recommended Value)

σ_{cp}= $\frac{N_{Ed}}{A_c} = \frac{420000}{350(400)} = 3 < 0.2 f_{cd}$

$V_{Rd,c}$ =[0.18 (1.747435093)(100(0.008123)· 30)$^{(1/3)}$ +0.5(3)]·350(358) = 170647.53 N = 170.64 kN

M_y From sectional analysis from Response2000 = 196 kN.m, V_y= 196/1.5= 130.66 kN

170.64< 130.66 kN, therefore a_v= 0

$$\theta_y = 9.12\text{E}-06\,.\frac{1500+0(316)}{3} + 0.00135\left(1+1.5\frac{400}{1500}\right) + 0.13(9.12\text{E}-06)\frac{18(414)}{\sqrt{30}}$$
$$= 8.06E-03$$

For θ_{y2}

$$\theta_y = 8.80\text{E}-06.\frac{1500+0(316)}{3} + 0.00135\left(1+1.5\frac{400}{1500}\right) + 0.13(8.80\text{E}-06)\frac{18(414)}{\sqrt{30}}$$
$$= 7.846 * 10^{-3}$$

For θ_{y3}

$$\theta_y = 9.5\text{E}-06.\frac{1500+0(316)}{3} + 0.00135\left(1+1.5\frac{400}{1500}\right) + 0.13(9.5\text{E}-06)\frac{18(414)}{\sqrt{30}}$$
$$= 8.320E-03$$

For θ_{y4}

$$\theta_y = 1.09\mathrm{E}-05.\frac{1500+0(316)}{3}+0.00135\left(1+1.5\frac{400}{1500}\right)+0.13(1.09\mathrm{E}-05)\frac{18(414)}{\sqrt{30}}$$
$$= 9.25E-03$$

- Same calculations for the Case 4: Deep Cross Section

➔ Lap Splice Case:

For a_v →

$$V_{Rd,c} = \left[C_{Rd,c}k(100\rho_l f_{ck})^{\frac{1}{3}} + K_1\sigma_{cp}\right] b_w d \ \ (N)$$

$C_{Rd,c}$ =0.18/γ_c= 0.18 (the partial factor of concrete material is assumed =1 for assessment purposes)

$$k = 1+\sqrt{\frac{200}{d}} = 1+\sqrt{\frac{200}{358}} = 1.747435093$$

$$\rho_1 = \frac{A_{s1}}{bd} = \frac{2.\frac{\pi}{4}.(18)^2.(4)}{350(358)} = 0.016246$$

K_1= 0.15 (Recommended Value)

$\sigma_{cp} = \frac{N_{Ed}}{A_c} = \frac{420000}{350(400)} = 3 < 0.2f_{cd}$

$V_{Rd,c}$ =[0.18 (1.747435093)(100(0.016246) 30)$^{(1/3)}$ +0.5(3)]350(358) = 200369.1121 N = 200.36kN

M_y From sectional analysis from Response2000 after reducing M_y= 149 kN.m, V_y= 149/1.5= 99.33 kN

99.33 < 200.33 kN, therefore a_v= 0

For θ_{y1}

$$\theta_y = 6.85\mathrm{E}-06\frac{1500+0(316)}{3}+0.00135\left(1+1.5\frac{400}{1500}\right)\left(\frac{149}{196}\right)+0.13(6.85\mathrm{E}-06)\frac{18(414)}{\sqrt{30}} = 6.07E-03$$

For θ_{y2}

$$\theta_y = 6.13\mathrm{E}-06\frac{1500+0(316)}{3}+0.00135\left(1+1.5\frac{400}{1500}\right)\left(\frac{149}{196}\right)+0.13(6.13\mathrm{E}-06)\frac{18(414)}{\sqrt{30}} = 5.59*10^{-3}$$

For θ_{y3}

$$\theta_y = 5.4\mathrm{E}-06\frac{1500+0(316)}{3}+0.00135\left(1+1.5\frac{400}{1500}\right)\left(\frac{149}{196}\right)+0.13(5.4\mathrm{E}-06)\frac{18(414)}{\sqrt{30}} = 5.09*10^{-3}$$

For θ_{y3}

$$\theta_y = 7.19\mathrm{E}-06\,\frac{1500+0(316)}{3} + 0.00135\left(1+1.5\frac{400}{1500}\right)\left(\frac{149}{196}\right) + 0.13(7.19\mathrm{E}-06)\frac{18(414)}{\sqrt{30}} = 6.30 * 10^{-3}$$

➔ For Case 3: Short Anchorage Length:

For a_v calcutions, A_{s1} is equal to the case with continuous reinforcement. Where, 99.3 < 170 kN, therefore a_v= 0

The rotation calculations are done the same as the lap splice case.

➔ Fabricated Hinge at the critical Section Case:

For a_v →

$$V_{Rd,c} = \left[C_{Rd,c}k(100\rho_l f_{ck})^{\frac{1}{3}} + K_1\sigma_{cp}\right] b_w d \ \ (N)$$

$C_{Rd,c}$ =0.18/γ_c= 0.18 (the partial factor of concrete material is assumed =1 for assessment purposes)

$$k = 1 + \sqrt{\frac{200}{d}} = 1 + \sqrt{\frac{200}{358}} = 1.747435093$$

$$\rho_1 = \frac{A_{s1}}{bd} = \frac{2\frac{\pi}{4}(18)^2(4)}{350(358)} = 0.016246$$

K_1= 0.15 (Recommended Value)

σ_{cp}= $\frac{N_{Ed}}{A_c} = \frac{420000}{350(400)} = 3 < 0.2 f_{cd}$

$V_{Rd,c}$ =[0.18 (1.747435093)(100(0.016246).30)$^{(1/3)}$ +0.5(3)]350(358) = 200369.1121 N = 200.36kN

M_y From sectional analysis from Response2000 after reducing M_y= 196 kN.m, V_y= 196/1.5= 99.33 kN

130.66 < 200.33 kN, therefore a_v= 0

For θ_{y1}

$$\theta_y = 9.12\mathrm{E}-06\,\frac{3000+0(316)}{3} + 0.00135\left(1+1.5\frac{400}{3000}\right) + 0.13(9.12\mathrm{E}-06)\frac{18(414)}{\sqrt{30}} = (1.24E-02)(0.5) = 6.2E-03$$

For θ_{y2}

$$\theta_y = 8.80E-06\,\frac{3000+0(316)}{3} + 0.00135\left(1+1.5\frac{400}{3000}\right) + 0.13(8.80E-06)\frac{18(414)}{\sqrt{30}} = 1.20E-02(0.5)$$
$$= 6E-03$$

For Θ_{y3}

$$\theta_y = 9.5E-06\,\frac{3000+0(316)}{3} + 0.00135\left(1+1.5\frac{400}{3000}\right) + 0.13(9.5E-06)\frac{18(414)}{\sqrt{30}} = 1.27E-02(0.5)$$
$$= 6.35E-03$$

For Θ_{y3}

$$\theta_y = 1.09E-05.\frac{3000+0(316)}{3} + 0.00135\left(1+1.5\frac{400}{3000}\right) + 0.13(1.09E-05)\frac{18(414)}{\sqrt{30}} = 1.44E-02(0.5)$$
$$= 7.2E-03$$

Table C.6: Yield Rotations According to Damage Limitation State (Slip Rotations $=\frac{\varepsilon_y}{d-d\prime}\frac{d_b f_y}{6\sqrt{f_c}}$)

Column Set	Column Name	Θ_{y1}	Θ_{y2}	Θ_{y3}	Θ_{y4}
Columns Set 1: Continuous Reinforcement	C10-1-10	7.93E-03	7.78E-03	8.08E-03	8.81E-03
	C35-1-10	6.88E-03	8.21E-03	8.53E-03	8.81E-03
	C50-1-10	6.13E-03	7.17E-03	7.78E-03	8.81E-03
	C10-2-10	7.96E-03	7.78E-03	7.93E-03	8.81E-03
	C35-2-10	6.72E-03	8.14E-03	8.38E-03	8.81E-03
	C50-2-10	5.94E-03	7.10E-03	7.38E-03	8.81E-03
	C10-1-20	7.72E-03	7.60E-03	7.58E-03	8.81E-03
	C35-1-20	6.50E-03	8.35E-03	7.88E-03	8.81E-03
	C50-1-20	5.85E-03	7.11E-03	7.03E-03	8.81E-03
	C10-2-20	7.82E-03	7.60E-03	7.38E-03	8.81E-03
	C35-2-20	6.41E-03	8.28E-03	7.58E-03	8.81E-03
	C50-2-20	5.82E-03	7.05E-03	6.78E-03	8.81E-03
Columns Set 2: Lap splice (270 mm)	C10-1-10	5.84E-03	5.48E-03	5.09E-03	6.01E-03
	C35-1-10	6.02E-03	6.59E-03	6.38E-03	6.15E-03
	C50-1-10	5.28E-03	6.40E-03	4.94E-03	6.26E-03
	C10-2-10	5.63E-03	5.51E-03	5.05E-03	6.04E-03
	C35-2-10	6.07E-03	6.68E-03	6.46E-03	6.24E-03
	C50-2-10	5.19E-03	6.48E-03	4.83E-03	6.36E-03
	C10-1-20	5.65E-03	5.48E-03	5.18E-03	6.10E-03
	C35-1-20	6.24E-03	6.72E-03	6.59E-03	6.30E-03
	C50-1-20	5.14E-03	6.46E-03	4.50E-03	6.37E-03
	C10-2-20	5.71E-03	5.53E-03	5.57E-03	6.15E-03
	C35-2-20	6.18E-03	6.81E-03	6.61E-03	6.38E-03
	C50-2-20	4.99E-03	6.15E-03	5.05E-03	6.31E-03

Columns Set 3: Short Anchorage length	C10-1-10	5.84E-03	5.48E-03	5.09E-03	6.01E-03
	C35-1-10	6.02E-03	6.59E-03	6.38E-03	6.15E-03
	C50-1-10	5.28E-03	6.40E-03	4.94E-03	6.26E-03
	C10-2-10	5.63E-03	5.51E-03	5.05E-03	6.04E-03
	C35-2-10	6.07E-03	6.68E-03	6.46E-03	6.24E-03
	C50-2-10	5.19E-03	6.48E-03	4.83E-03	6.36E-03
	C10-1-20	5.65E-03	5.48E-03	5.18E-03	6.10E-03
	C35-1-20	6.24E-03	6.72E-03	6.59E-03	6.30E-03
	C50-1-20	5.14E-03	6.46E-03	4.50E-03	6.37E-03
	C10-2-20	5.71E-03	5.53E-03	5.57E-03	6.15E-03
	C35-2-20	6.18E-03	6.81E-03	6.61E-03	6.38E-03
	C50-2-20	5.16E-03	6.32E-03	5.05E-03	6.31E-03
Column Set 4: Deep Cross Section (700 mm)	C10-1-10	6.31E-03	6.28E-03	6.58E-03	7.44E-03
	C35-1-10	5.55E-03	7.01E-03	6.51E-03	7.44E-03
	C50-1-10	5.04E-03	6.04E-03	6.09E-03	7.44E-03
	C10-2-10	6.37E-03	6.28E-03	6.30E-03	7.44E-03
	C35-2-10	5.42E-03	6.08E-03	6.04E-03	7.04E-03
	C50-2-10	4.84E-03	3.70E-03	5.39E-03	6.74E-03
	C10-1-20	5.38E-03	5.29E-03	5.26E-03	6.16E-03
	C35-1-20	6.89E-03	7.09E-03	5.95E-03	7.44E-03
	C50-1-20	4.38E-03	5.15E-03	5.74E-03	7.44E-03
	C10-2-20	5.33E-03	5.29E-03	4.96E-03	6.16E-03
	C35-2-20	5.23E-03	6.11E-03	5.92E-03	7.31E-03
	C50-2-20	6.31E-03	6.28E-03	4.92E-03	6.54E-03
Column Set 5: Hinge Fabrication at the critical Section	C10-1-10	6.11E-03	5.95E-03	6.25E-03	6.99E-03
	C35-1-10	5.01E-03	6.32E-03	6.70E-03	6.99E-03
	C50-1-10	4.26E-03	5.29E-03	5.95E-03	6.99E-03
	C10-2-10	6.13E-03	5.95E-03	6.10E-03	6.99E-03
	C35-2-10	4.89E-03	6.29E-03	6.55E-03	6.99E-03
	C50-2-10	4.10E-03	5.27E-03	5.55E-03	6.99E-03
	C10-1-20	5.90E-03	6.04E-03	5.75E-03	6.99E-03
	C35-1-20	4.64E-03	6.05E-03	5.75E-03	6.99E-03
	C50-1-20	4.00E-03	5.09E-03	5.20E-03	6.99E-03
	C10-2-20	5.99E-03	6.04E-03	4.90E-03	6.99E-03
	C35-2-20	4.58E-03	6.03E-03	5.40E-03	6.99E-03
	C50-2-20	3.83E-03	4.85E-03	4.95E-03	6.99E-03

Θ_{y1}: Yielding Curvatures= $\min\left\{\frac{f_y}{E_s}\left(\frac{1}{d-x_y}\right), \frac{\varepsilon_{cy}}{x_y}\right\}$, where x_y is the depth of the compression zone at yielding from Response2000.

Θ_{y2}: Yielding Curvatures= $\min\left\{\frac{f_y}{E_s}\left(\frac{1}{d-x_y}\right), \frac{\varepsilon_{cy}}{x_y}\right\}$, where x_y is the depth of the compression zone at yielding from Panagiotakos and Fardis 2001.

Θ_{y3}: Yielding Curvatures are from Response2000.

Θ_{y4}: Yielding Curvatures are from Priestley et al. (1996) equation.

Sample of Calculations

➔ For Continuous Reinforcement:

Longitudinal reinforcement = 4φ18, axial load = 10 % of crushing load , Concrete cover= 25 mm, b= 350 mm, h= 400mm and stirrups = φ18/100 mm.

For Θ_{y1}

$$\theta_y = 9.12\mathrm{E}-06\ \frac{1500+0(316)}{3} + 0.00135\left(1+1.5\frac{400}{1500}\right) + \frac{\frac{414}{200000}}{358-42}\frac{18(414)}{6\sqrt{30}} = 7.93E-03$$

For Θ_{y2}

$$\theta_y = 8.80\mathrm{E}-06\ \frac{1500+0(316)}{3} + 0.00135\left(1+1.5\frac{400}{1500}\right) + \frac{\frac{414}{200000}}{358-42}\frac{18(414)}{6\sqrt{30}} = 7.78E-03$$

For Θ_{y3}

$$\theta_y = 9.50\mathrm{E}-06.\frac{1500+0(316)}{3} + 0.00135\left(1+1.5\frac{400}{1500}\right) + \frac{\frac{414}{200000}}{358-42}\frac{18(414)}{6\sqrt{30}} = 8.08\mathrm{E}-03$$

For Θ_{y3}

$$\theta_y = 1.086\mathrm{E}-05.\frac{1500+0(316)}{3} + 0.00135\left(1+1.5\frac{400}{1500}\right) + \frac{\frac{414}{200000}}{358-42}\frac{18(414)}{6\sqrt{30}} = 8.81\mathrm{E}-03$$

➔ Lap Splice Case:

For a_v →

$$V_{Rd,c} = \left[C_{Rd,c}k(100\rho_l f_{ck})^{\frac{1}{3}} + K_1\sigma_{cp}\right]b_w d\ \ (N)$$

$C_{Rd,c}$ =0.18/γ_c= 0.18 (the partial factor of concrete material is assumed =1 for assessment purposes)

$$k = 1+\sqrt{\frac{200}{d}} = 1+\sqrt{\frac{200}{358}} = 1.747435093$$

$$\rho_1 = \frac{A_{s1}}{bd} = \frac{2\frac{\pi}{4}(18)^2(4)}{350(358)} = 0.016246$$

K_1= 0.15 (Recommended Value)

$\sigma_{cp} = \frac{N_{Ed}}{A_c} = \frac{420000}{350(400)} = 3 < 0.2 f_{cd}$

$V_{Rd,c}$ =[0.18 (1.747435093)(100(0.016246) 30)$^{(1/3)}$ +0.5(3)]350(358) = 200369.1121 N = 200.36kN

M_y From sectional analysis from Response2000 after reducing M_y= 149 kN.m, V_y= 149/1.5= 99.33 kN

99.33 < 200.33 kN, therefore a_v= 0

For θ_{y1}

$$\theta_y = 6.85\mathrm{E}-06\ \frac{1500+0(316)}{3} + 0.00135\left(1+1.5\frac{400}{1500}\right)\left(\frac{149}{196}\right) + \frac{\frac{414}{200000}\left(\frac{270}{408}\right)}{358-42}\frac{18\cdot 414}{6\sqrt{30}} = 5.82E-03$$

For θ_{y2}

$$\theta_y = 6.13\mathrm{E}-06\ \frac{1500+0(316)}{3} + 0.00135\left(1+1.5\frac{400}{1500}\right)\left(\frac{149}{196}\right) + \frac{\frac{414}{200000}\left(\frac{270}{408}\right)}{358-42}\frac{18\cdot 414}{6\sqrt{30}} = 5.48E-03$$

For θ_{y3}

$$\theta_y = 5.4\mathrm{E}-06\ \frac{1500+0(316)}{3} + 0.00135\left(1+1.5\frac{400}{1500}\right)\left(\frac{149}{196}\right) + \frac{\frac{414}{200000}\cdot\left(\frac{270}{408}\right)}{358-42}\frac{18\cdot 414}{6\sqrt{30}} = 5.09E-03$$

For θ_{y3}

$$\theta_y = 7.19\mathrm{E}-06\ \frac{1500+0(316)}{3} + 0.00135\left(1+1.5\frac{400}{1500}\right)\left(\frac{149}{196}\right) + \frac{\frac{414}{200000}\left(\frac{270}{408}\right)}{358-42}\frac{18\cdot 414}{6\sqrt{30}} = 6.01E-03$$

➔ For short anchorage Length:

For a_v calcutions, A_{s1} is equal to the case with continuous reinforcement. Where, 99.3 < 170 kN, therefore a_v= 0

The rotation calculations are done the same as the lap splice case.

➔ Fabricated Hinge at the critical Section Case:

For a_v →

$$V_{Rd,c} = \left[C_{Rd,c}k(100\rho_l f_{ck})^{\frac{1}{3}} + K_1\sigma_{cp}\right]b_w d\ \ (N)$$

$C_{Rd,c}$ =0.18/γ_c= 0.18 (the partial factor of concrete material is assumed =1 for assessment purposes)

$$k = 1 + \sqrt{\frac{200}{d}} = 1 + \sqrt{\frac{200}{358}} = 1.747435093$$

$$\rho_1 \frac{A_{s1}}{bd} = \frac{2\frac{\pi}{4}(18)^2(4)}{350(358)} = 0.016246$$

K_1= 0.15 (Recommended Value)

$\sigma_{cp}= \frac{N_{Ed}}{A_c} = \frac{420000}{350(400)} = 3 < 0.2f_{cd}$

$V_{Rd,c}$ =[0.18 (1.747435093)(100(0.016246)30)$^{(1/3)}$ +0.5(3)]350(358) = 200369.1121 N = 200.36kN

M_y From sectional analysis from Response2000=196 kN, V_y= 196/1.5= 99.33 kN

130.66 < 200.33 kN, therefore a_v= 0

For θ_{y1}

$$\theta_y = \left(9.12\text{E}-06\,\frac{3000+0(316)}{3} + 0.00135\left(1+1.5\frac{400}{3000}\right) + \frac{\frac{414}{200000}}{358-42}\frac{18\cdot 414}{6\sqrt{30}}\right)(0.5) = 6.11E-03$$

For θ_{y2}

$$\theta_y = \left(8.80\text{E}-06\,\frac{3000+0(316)}{3} + 0.00135\left(1+1.5\frac{400}{3000}\right) + \frac{\frac{414}{200000}}{358-42}\frac{18\cdot 414}{6\sqrt{30}}\right)0.5 = 5.95E-03$$

For θ_{y3}

$$\theta_y = \left(9.5\text{E}-06\,\frac{3000+0(316)}{3} + 0.00135\left(1+1.5\frac{400}{3000}\right) + \frac{\frac{414}{200000}}{358-42}\frac{18\cdot 414}{6\sqrt{30}}\right)0.5 = 6.25E-03$$

For θ_{y3}

$$\theta_y = \left(1.086\text{E}-05\,\frac{3000+0(316)}{3} + 0.00135\left(1+1.5\frac{400}{3000}\right) + \frac{\frac{414}{200000}}{358-42}\frac{18\cdot 414}{6\sqrt{30}}\right)0.5 = 6.99E-03$$

Near Collapse Rotation State

Table C.7: Ultimate Plastic Rotations According to EUROCODE 8 III 2005

Column Set	Column Name	Θ_{pl}	Θ_{um}
Columns Set 1: Continuous Reinforcement	C10-1-10	2.28E-02	3.34E-02
	C35-1-10	1.61E-02	2.48E-02
	C50-1-10	1.31E-02	2.07E-02
	C10-2-10	1.84E-02	2.69E-02
	C35-2-10	1.30E-02	1.99E-02
	C50-2-10	1.05E-02	1.66E-02
	C10-1-20	2.26E-02	3.31E-02
	C35-1-20	1.60E-02	2.45E-02
	C50-1-20	1.30E-02	2.05E-02
	C10-2-20	1.83E-02	2.69E-02
	C35-2-20	1.29E-02	1.99E-02
	C50-2-20	1.05E-02	1.66E-02
Columns Set 2: Lap splice (270 mm)	C10-1-10	5.44E-03	3.23E-02
	C35-1-10	3.85E-03	2.39E-02
	C50-1-10	3.13E-03	1.99E-02
	C10-2-10	4.91E-03	3.15E-02
	C35-2-10	3.47E-03	2.33E-02
	C50-2-10	2.82E-03	1.95E-02
	C10-1-20	6.01E-03	3.19E-02
	C35-1-20	4.25E-03	2.36E-02
	C50-1-20	3.45E-03	1.97E-02
	C10-2-20	5.09E-03	3.14E-02
	C35-2-20	3.60E-03	2.32E-02
	C50-2-20	2.92E-03	1.94E-02
Columns Set 3: Short Anchorage length	C10-1-10	4.51E-03	2.76E-02
	C35-1-10	3.19E-03	2.04E-02
	C50-1-10	2.59E-03	1.70E-02
	C10-2-10	4.02E-03	2.69E-02
	C35-2-10	2.84E-03	1.99E-02
	C50-2-10	2.31E-03	1.66E-02
	C10-1-20	4.31E-03	2.73E-02
	C35-1-20	3.05E-03	2.02E-02
	C50-1-20	2.48E-03	1.69E-02
	C10-2-20	3.95E-03	2.69E-02
	C35-2-20	2.79E-03	1.99E-02
	C50-2-20	2.27E-03	1.66E-02

Table C.7: Continued

Column Set 4: Deep Cross Section (700 mm)	C10-1-10	1.84E-02	2.71E-02
	C35-1-10	1.30E-02	2.00E-02
	C50-1-10	1.06E-02	1.67E-02
	C10-2-10	1.50E-02	2.21E-02
	C35-2-10	1.06E-02	1.63E-02
	C50-2-10	8.63E-03	1.36E-02
	C10-1-20	1.83E-02	2.69E-02
	C35-1-20	1.30E-02	1.99E-02
	C50-1-20	1.05E-02	1.66E-02
	C10-2-20	1.50E-02	2.20E-02
	C35-2-20	1.06E-02	1.63E-02
	C50-2-20	8.61E-03	1.36E-02
Column Set 5: Hinge Fabrication at the critical Section	C10-1-10	1.77E-02	2.55E-02
	C35-1-10	1.25E-02	1.89E-02
	C50-1-10	1.02E-02	1.58E-02
	C10-2-10	1.42E-02	2.06E-02
	C35-2-10	1.01E-02	1.52E-02
	C50-2-10	8.18E-03	1.27E-02
	C10-1-20	1.42E-02	2.17E-02
	C35-1-20	1.01E-02	1.60E-02
	C50-1-20	8.17E-03	1.34E-02
	C10-2-20	1.15E-02	1.76E-02
	C35-2-20	8.16E-03	1.30E-02
	C50-2-20	6.63E-03	1.08E-02

Sample of calculations:

➔ For Continuous Reinforcement:

Longitudinal reinforcement = 4 Φ18, axial load = 10 % of crushing load , Concrete cover= 25 mm, b= 350 mm, h= 400mm and stirrups = Φ 8/100 mm.

$$\Theta_{um} = \frac{1}{\gamma_{el}} 0.016(0.3^{v}) \left[\frac{\max(0.01;w')}{\max(0.01;w)} f_c\right]^{0.225} \left(\frac{L_v}{h}\right)^{0.35} 25^{\left(\alpha\rho_{sx}\frac{f_{wy}}{f_c}\right)}(1.25^{100\rho_d})$$

ρ'= 0.8126% ,w' = 0.008126(414/30) = 0.11213, ρ = 0.8126 % , w = 0.008126 (414/30) = 0.11213,

$$\rho_{sx} = \frac{2\left(\frac{\pi}{4}\right)(8)^2}{350 \cdot 100} = 2.871E-03$$

$$\alpha = \left(1 - \frac{100}{2(342)}\right)\left(1 - \frac{100}{2(292)}\right)\left(1 - \frac{6(88.6)^2+2(316)^2}{6(292)342}\right) = 0.4161$$

$$\Theta_{um} = \frac{1}{1.5} 0.016(0.3^{0.1}) \left[\frac{\max(0.01; 0.11213)}{\max(0.01; 0.11213)} 30 \right]^{0.225} \left(\frac{1500}{400} \right)^{0.35} 25^{\left(0.414(0.00287123)\frac{276}{30}\right)}$$

$$\Theta_{um} = \frac{1}{1.5} 0.016(0.3^{0.1})[30]^{0.225} \left(\frac{1500}{400} \right)^{0.35} 25^{\left(0.4161(0.00287123)\frac{276}{30}\right)} = 0.0334419$$

$$\Theta_{um}{}^{pl} = \Theta_{um} - \Theta_y = \frac{1}{\gamma_{el}} 0.0145(0.25^{v}) \left[\frac{\max(0.01; w')}{\max(0.01; w)} \right]^{0.3} \left(\frac{L_v}{h} \right)^{0.35} 25^{\left(\alpha \rho_{sx} \frac{f_{wy}}{f_c}\right)} (1.275^{100\rho_d}) f_c{}^{0.2}$$

$$\Theta_{um}{}^{pl} = \Theta_{um} - \Theta_y = \frac{1}{1.8} 0.0145(0.25^{0.1})[1]^{0.3} \left(\frac{1500}{400} \right)^{0.35} 25^{\left(0.4161(0.00287123)\frac{276}{30}\right)} 30^{0.2}$$
$$= 0.0227819$$

For columns with 200 mm stirrup spacing the ultimate and plastic rotations are multiplied by 0.825.

$$\Theta_{um} = 0.0334419(0.825) = 0.275895675$$

$$\Theta_{um}{}^{pl} = 0.0227819\ (0.825) = 0.0187950675$$

(Same Calculations are for the column with deep cross section. For the Fabricated hinge, same calculations are done as well but divided over 2).

➔ For Lap splice Case :

Longitudinal reinforcement = 4Φ18, axial load = 10 % of crushing load , Concrete cover= 25 mm, b= 350 mm, h= 400mm and stirrups = Φ 8/100 mm.

$$\Theta_{um} = \frac{1}{1.5} 0.016(0.3^{0.1})[30 \cdot 2]^{0.225} \left(\frac{1500}{400} \right)^{0.35} 25^{\left(0.4161(0.00287123)\frac{276}{30}\right)} = 0.0390931 \cdot 0.825$$
$$= 0.0322518$$

$$\Theta_{um}{}^{pl} = \Theta_{um} - \Theta_y = \frac{1}{1.8} 0.0145(0.25^{0.1})[2]^{0.3} \left(\frac{1500}{400} \right)^{0.35} 25^{\left(0.4161(0.00287123)\frac{276}{30}\right)} 30^{0.2}$$
$$= 0.028047 \cdot 0.825 \cdot \left(\frac{270}{1147.6} \right) = 5.44E - 03$$

➔ For short Anchorage Reinforcement

Longitudinal reinforcement = 4φ18, axial load = 10 % of crushing load , Concrete cover= 25 mm, b= 350 mm, h= 400mm and stirrups = φ18/100 mm.

$$\Theta_{um} = \frac{1}{1.5} 0.016(0.3^{0.1})[30]^{0.225} \left(\frac{1500}{400} \right)^{0.35} 25^{\left(0.4161(0.00287123)\frac{276}{30}\right)} = 0.0334419 \cdot 0.825$$
$$= 0.027589(0.5) = 0.01379$$

$$\Theta_{um}{}^{pl} = \Theta_{um} - \Theta_y = \frac{1}{1.8}0.0145(0.25^{0.1})[1]^{\,0.3}\left(\frac{1500}{400}\right)^{0.35}\ 25^{\left(0.4161(0.00287123)\frac{276}{30}\right)}30^{0.2}$$
$$= 0.0227819 \cdot 0.825 \cdot \left(\frac{270}{1125}\right) = (4.5108E-03)(0.5) = 2.255E-03$$

Table C8: Ultimate Rotation Capacity (Near Collapse- EUROCODE 8 Part III 2005) $0.13 \cdot \varphi_y \cdot \frac{d_b f_y}{\sqrt{f_c}}$

Column Set	Column Name	Θ_{u1}	Θ_{u2}	Θ_{u3}	Θ_{u4}
Columns Set 1: Continuous Reinforcement	C10-1-10	3.08E-02	3.06E-02	3.20E-02	3.08E-02
	C35-1-10	2.27E-02	2.41E-02	2.54E-02	2.35E-02
	C50-1-10	1.87E-02	1.98E-02	2.23E-02	1.94E-02
	C10-2-10	2.64E-02	2.62E-02	2.76E-02	2.63E-02
	C35-2-10	1.94E-02	2.09E-02	2.22E-02	2.00E-02
	C50-2-10	1.59E-02	1.72E-02	1.98E-02	1.67E-02
	C10-1-20	3.03E-02	3.02E-02	3.18E-02	3.05E-02
	C35-1-20	2.21E-02	2.42E-02	2.52E-02	2.29E-02
	C50-1-20	1.82E-02	1.96E-02	2.22E-02	1.91E-02
	C10-2-20	2.62E-02	2.59E-02	2.75E-02	2.63E-02
	C35-2-20	1.89E-02	2.11E-02	2.22E-02	1.97E-02
	C50-2-20	1.57E-02	1.71E-02	1.98E-02	1.65E-02
Columns Set 2: Lap splice (270 mm)	C10-1-10	1.15E-02	1.10E-02	1.09E-02	1.17E-02
	C35-1-10	1.01E-02	1.09E-02	1.04E-02	1.03E-02
	C50-1-10	8.34E-03	9.61E-03	9.74E-03	9.67E-03
	C10-2-10	1.07E-02	1.05E-02	1.03E-02	1.12E-02
	C35-2-10	9.78E-03	1.06E-02	9.98E-03	9.98E-03
	C50-2-10	7.89E-03	9.28E-03	9.29E-03	9.41E-03
	C10-1-20	1.18E-02	1.15E-02	1.10E-02	1.24E-02
	C35-1-20	1.08E-02	1.14E-02	1.05E-02	1.08E-02
	C50-1-20	8.45E-03	9.97E-03	9.91E-03	1.01E-02
	C10-2-20	1.09E-02	1.06E-02	1.01E-02	1.15E-02
	C35-2-20	1.00E-02	1.08E-02	9.90E-03	1.02E-02
	C50-2-20	7.74E-03	9.30E-03	9.03E-03	9.50E-03
Columns Set 3: Short Anchorage length	C10-1-10	1.06E-02	1.01E-02	1.05E-02	1.00E-02
	C35-1-10	9.46E-03	1.02E-02	9.62E-03	9.71E-03
	C50-1-10	7.81E-03	9.08E-03	7.92E-03	9.21E-03
	C10-2-10	9.79E-03	9.62E-03	1.00E-02	9.40E-03
	C35-2-10	9.14E-03	9.94E-03	8.87E-03	9.35E-03
	C50-2-10	7.37E-03	8.77E-03	7.61E-03	8.77E-03
	C10-1-20	1.01E-02	9.84E-03	1.04E-02	9.28E-03
	C35-1-20	9.56E-03	1.02E-02	9.15E-03	9.35E-03
	C50-1-20	7.48E-03	9.00E-03	7.83E-03	8.94E-03
	C10-2-20	9.80E-03	9.47E-03	9.71E-03	8.77E-03
	C35-2-20	9.20E-03	9.99E-03	8.77E-03	9.10E-03

	C50-2-20	7.09E-03	8.65E-03	7.37E-03	8.38E-03
Column Set 4: Deep Cross Section (700 mm)	C10-1-10	2.48E-02	2.48E-02	2.51E-02	2.62E-02
	C35-1-10	1.85E-02	2.03E-02	1.81E-02	2.08E-02
	C50-1-10	1.54E-02	1.66E-02	1.54E-02	1.84E-02
	C10-2-10	2.15E-02	2.13E-02	2.16E-02	2.28E-02
	C35-2-10	1.59E-02	1.70E-02	1.49E-02	1.74E-02
	C50-2-10	1.33E-02	1.25E-02	1.22E-02	1.46E-02
	C10-1-20	2.38E-02	2.36E-02	2.37E-02	2.48E-02
	C35-1-20	2.00E-02	2.03E-02	1.75E-02	2.07E-02
	C50-1-20	1.46E-02	1.56E-02	1.42E-02	1.70E-02
	C10-2-20	2.04E-02	2.03E-02	2.06E-02	2.15E-02
	C35-2-20	1.57E-02	1.71E-02	1.45E-02	1.73E-02
	C50-2-20	1.29E-02	1.28E-02	1.16E-02	1.40E-02
Column Set 5: Hinge Fabrication at the critical Section	C10-1-10	2.39E-02	2.37E-02	2.41E-02	2.49E-02
	C35-1-10	1.74E-02	1.89E-02	1.74E-02	1.97E-02
	C50-1-10	1.42E-02	1.54E-02	1.44E-02	1.74E-02
	C10-2-10	2.04E-02	2.02E-02	2.06E-02	2.15E-02
	C35-2-10	1.48E-02	1.65E-02	1.47E-02	1.73E-02
	C50-2-10	1.20E-02	1.34E-02	1.23E-02	1.54E-02
	C10-1-20	2.02E-02	2.03E-02	2.06E-02	2.14E-02
	C35-1-20	1.45E-02	1.62E-02	1.40E-02	1.73E-02
	C50-1-20	1.19E-02	1.31E-02	1.18E-02	1.54E-02
	C10-2-20	1.76E-02	1.76E-02	1.79E-02	1.87E-02
	C35-2-20	1.25E-02	1.42E-02	1.20E-02	1.54E-02
	C50-2-20	1.01E-02	1.13E-02	1.00E-02	1.38E-02

Θ_{u1}: Yielding Curvatures= $\min\left\{\frac{f_y}{E_s}\left(\frac{1}{d-x_y}\right), \frac{\varepsilon_{cy}}{x_y}\right\}$, where x_y is the depth of the compression zone at yielding from Response2000.

Θ_{u2}: Yielding Curvatures= $\min\left\{\frac{f_y}{E_s}\left(\frac{1}{d-x_y}\right), \frac{\varepsilon_{cy}}{x_y}\right\}$, where x_y is the depth of the compression zone at yielding from Panagiotakos and Fardis 2001.

Θ_{u3}: Yielding Curvatures are from Response2000.

Θ_{u4}: Yielding Curvatures are from Priestley et al. (1996) equation.

Table C9: Ultimate Rotation Capacity (Near Collapse- EUROCODE 8 Part III 2005) Slip Rotations $= \frac{\varepsilon_y}{d-d\prime}\frac{d_b f_y}{6\sqrt{f_c}}$

Column Set	Column Name	Θ_{u1}	Θ_{u2}	Θ_{u3}	Θ_{u4}
Columns Set 1: Continuous Reinforcement	C10-1-10	3.08E-02	3.06E-02	3.09E-02	3.16E-02
	C35-1-10	2.35E-02	2.40E-02	2.46E-02	2.49E-02
	C50-1-10	1.94E-02	2.00E-02	2.09E-02	2.19E-02
	C10-2-10	2.63E-02	2.61E-02	2.63E-02	2.72E-02
	C35-2-10	2.00E-02	2.08E-02	2.14E-02	2.18E-02
	C50-2-10	1.67E-02	1.74E-02	1.79E-02	1.94E-02
	C10-1-20	3.05E-02	3.02E-02	3.01E-02	3.14E-02
	C35-1-20	2.29E-02	2.40E-02	2.38E-02	2.48E-02
	C50-1-20	1.91E-02	1.98E-02	2.00E-02	2.18E-02
	C10-2-20	2.63E-02	2.59E-02	2.57E-02	2.71E-02
	C35-2-20	1.97E-02	2.09E-02	2.05E-02	2.17E-02
	C50-2-20	1.65E-02	1.73E-02	1.73E-02	1.93E-02
Columns Set 2: Lap splice (270 mm)	C10-1-10	1.12E-02	1.09E-02	1.15E-02	1.09E-02
	C35-1-10	9.99E-03	1.01E-02	1.00E-02	1.04E-02
	C50-1-10	8.48E-03	9.44E-03	9.38E-03	9.34E-03
	C10-2-10	1.07E-02	1.03E-02	1.09E-02	1.04E-02
	C35-2-10	9.34E-03	9.69E-03	9.69E-03	1.01E-02
	C50-2-10	8.17E-03	9.03E-03	9.12E-03	9.03E-03
	C10-1-20	1.19E-02	1.11E-02	1.21E-02	1.15E-02
	C35-1-20	1.02E-02	1.03E-02	1.05E-02	1.09E-02
	C50-1-20	8.85E-03	9.67E-03	9.82E-03	9.72E-03
	C10-2-20	1.07E-02	1.02E-02	1.12E-02	1.05E-02
	C35-2-20	9.46E-03	9.70E-03	9.94E-03	1.04E-02
	C50-2-20	8.12E-03	8.87E-03	9.21E-03	9.06E-03
Columns Set 3: Short Anchorage length	C10-1-10	1.03E-02	9.93E-03	1.05E-02	9.99E-03
	C35-1-10	9.33E-03	9.40E-03	9.34E-03	9.78E-03
	C50-1-10	7.95E-03	8.90E-03	8.84E-03	8.80E-03
	C10-2-10	9.80E-03	9.36E-03	1.01E-02	9.52E-03
	C35-2-10	8.71E-03	9.06E-03	9.06E-03	9.49E-03
	C50-2-10	7.66E-03	8.52E-03	8.61E-03	8.51E-03
	C10-1-20	1.02E-02	9.36E-03	1.04E-02	9.78E-03
	C35-1-20	8.98E-03	9.13E-03	9.32E-03	9.74E-03
	C50-1-20	7.88E-03	8.70E-03	8.84E-03	8.74E-03
	C10-2-20	9.58E-03	8.88E-03	1.00E-02	9.40E-03
	C35-2-20	8.65E-03	8.89E-03	9.14E-03	9.56E-03
	C50-2-20	7.47E-03	8.21E-03	8.55E-03	8.41E-03

Column Set 4: Deep Cross Section (700 mm)	C10-1-10	2.48E-02	2.47E-02	2.50E-02	2.59E-02
	C35-1-10	1.89E-02	1.98E-02	1.96E-02	2.05E-02
	C50-1-10	1.57E-02	1.64E-02	1.67E-02	1.80E-02
	C10-2-10	2.15E-02	2.13E-02	2.13E-02	2.25E-02
	C35-2-10	1.63E-02	1.70E-02	1.67E-02	1.77E-02
	C50-2-10	1.37E-02	1.35E-02	1.40E-02	1.54E-02
	C10-1-20	2.37E-02	2.36E-02	2.36E-02	2.45E-02
	C35-1-20	1.87E-02	1.98E-02	1.89E-02	2.04E-02
	C50-1-20	1.57E-02	1.63E-02	1.63E-02	1.80E-02
	C10-2-20	2.04E-02	2.03E-02	1.99E-02	2.11E-02
	C35-2-20	1.62E-02	1.73E-02	1.65E-02	1.79E-02
	C50-2-20	1.36E-02	1.37E-02	1.35E-02	1.51E-02
Column Set 5: Hinge Fabrication at the critical Section	C10-1-10	2.38E-02	2.36E-02	2.39E-02	2.47E-02
	C35-1-10	1.81E-02	1.86E-02	1.92E-02	1.95E-02
	C50-1-10	1.46E-02	1.53E-02	1.61E-02	1.71E-02
	C10-2-10	2.04E-02	2.02E-02	2.04E-02	2.12E-02
	C35-2-10	1.52E-02	1.61E-02	1.66E-02	1.71E-02
	C50-2-10	1.25E-02	1.32E-02	1.37E-02	1.52E-02
	C10-1-20	2.04E-02	2.03E-02	2.00E-02	2.12E-02
	C35-1-20	1.52E-02	1.59E-02	1.58E-02	1.70E-02
	C50-1-20	1.25E-02	1.31E-02	1.34E-02	1.52E-02
	C10-2-20	1.77E-02	1.76E-02	1.64E-02	1.85E-02
	C35-2-20	1.31E-02	1.39E-02	1.36E-02	1.51E-02
	C50-2-20	1.08E-02	1.15E-02	1.16E-02	1.36E-02

Θ_{u1}: Yielding Curvatures= min $\left\{\frac{f_y}{E_s}\left(\frac{1}{d-x_y}\right), \frac{\varepsilon_{cy}}{x_y}\right\}$, where x_y is the depth of the compression zone at yielding from Response2000.

Θ_{u2}: Yielding Curvatures= min $\left\{\frac{f_y}{E_s}\left(\frac{1}{d-x_y}\right), \frac{\varepsilon_{cy}}{x_y}\right\}$, where x_y is the depth of the compression zone at yielding from Panagiotakos and Fardis 2001.

Θ_{u3}: Yielding Curvatures are from Response2000.

Θ_{u4}: Yielding Curvatures are from Priestley et al. (1996) equation.

Rotations -ASCE SEI 41-17

Rotation Calculations:

Yield Rotations According to Lehman et al. (1998) Equation:

Table C10: Yield Rotation Calculations (Lehman et al. (1998))

Column Set	Column Name	Θ_{y1}	Θ_{y2}	Θ_{y3}	Θ_{y4}
Columns Set 1: Continuous Reinforcement	C10-1-10	6.31E-03	6.10E-03	6.56E-03	7.48E-03
	C35-1-10	5.01E-03	6.80E-03	4.94E-03	7.60E-03
	C50-1-10	3.99E-03	5.38E-03	4.19E-03	7.59E-03
	C10-2-10	6.33E-03	6.09E-03	6.56E-03	7.48E-03
	C35-2-10	4.79E-03	6.68E-03	4.65E-03	7.58E-03
	C50-2-10	3.72E-03	5.28E-03	4.04E-03	7.57E-03
	C10-1-20	5.96E-03	5.80E-03	6.50E-03	7.41E-03
	C35-1-20	4.43E-03	6.91E-03	3.86E-03	7.52E-03
	C50-1-20	3.56E-03	5.24E-03	3.46E-03	7.52E-03
	C10-2-20	6.08E-03	5.80E-03	6.50E-03	7.41E-03
	C35-2-20	4.30E-03	6.81E-03	3.65E-03	7.51E-03
	C50-2-20	3.50E-03	5.16E-03	3.18E-03	7.51E-03
Columns Set 2: Lap splice (270 mm)	C10-1-10	4.73E-03	3.81E-03	3.76E-03	4.96E-03
	C35-1-10	4.90E-03	5.09E-03	5.01E-03	5.07E-03
	C50-1-10	3.75E-03	4.73E-03	3.48E-03	5.08E-03
	C10-2-10	4.40E-03	3.80E-03	3.68E-03	4.95E-03
	C35-2-10	4.83E-03	5.07E-03	4.99E-03	5.05E-03
	C50-2-10	3.49E-03	4.68E-03	3.25E-03	5.05E-03
	C10-1-20	4.31E-03	3.66E-03	3.72E-03	4.91E-03
	C35-1-20	4.94E-03	5.02E-03	5.03E-03	5.02E-03
	C50-1-20	3.39E-03	4.63E-03	2.89E-03	5.03E-03
	C10-2-20	4.32E-03	3.66E-03	4.05E-03	4.91E-03
	C35-2-20	4.76E-03	5.02E-03	4.96E-03	5.02E-03
	C50-2-20	3.26E-03	4.33E-03	3.49E-03	5.02E-03
Columns Set 3: Short Anchorage length	C10-1-10	4.73E-03	3.81E-03	3.76E-03	4.96E-03
	C35-1-10	4.90E-03	5.09E-03	5.01E-03	5.07E-03
	C50-1-10	3.75E-03	4.73E-03	3.48E-03	5.08E-03
	C10-2-10	4.40E-03	3.80E-03	3.68E-03	4.95E-03
	C35-2-10	4.83E-03	5.07E-03	4.99E-03	5.05E-03
	C50-2-10	3.49E-03	4.68E-03	3.25E-03	5.05E-03
	C10-1-20	4.31E-03	3.66E-03	3.72E-03	4.91E-03
	C35-1-20	4.94E-03	5.02E-03	5.03E-03	5.02E-03
	C50-1-20	3.39E-03	4.63E-03	2.89E-03	5.03E-03
	C10-2-20	4.32E-03	3.66E-03	4.05E-03	4.91E-03
	C35-2-20	4.76E-03	5.02E-03	4.96E-03	5.02E-03

	C50-2-20	3.26E-03	4.33E-03	3.49E-03	5.02E-03
Column Set 4: Deep Cross Section (700 mm)	C10-1-10	3.35E-03	3.32E-03	3.55E-03	4.42E-03
	C35-1-10	2.83E-03	4.21E-03	2.53E-03	4.62E-03
	C50-1-10	2.36E-03	3.30E-03	2.35E-03	4.63E-03
	C10-2-10	3.40E-03	3.32E-03	3.54E-03	4.42E-03
	C35-2-10	2.78E-03	4.17E-03	2.45E-03	4.60E-03
	C50-2-10	2.30E-03	3.26E-03	2.19E-03	4.61E-03
	C10-1-20	3.30E-03	3.18E-03	3.21E-03	4.35E-03
	C35-1-20	4.01E-03	4.21E-03	2.05E-03	4.53E-03
	C50-1-20	2.16E-03	3.20E-03	1.80E-03	4.55E-03
	C10-2-20	3.22E-03	3.17E-03	3.47E-03	4.34E-03
	C35-2-20	2.53E-03	4.19E-03	2.05E-03	4.53E-03
	C50-2-20	2.03E-03	3.00E-03	1.92E-03	4.54E-03
Column Set 5: Hinge Fabrication at the critical Section	C10-1-10	5.38E-03	5.20E-03	5.61E-03	6.41E-03
	C35-1-10	4.12E-03	5.66E-03	4.12E-03	6.44E-03
	C50-1-10	3.25E-03	4.45E-03	3.47E-03	6.43E-03
	C10-2-10	5.41E-03	5.20E-03	5.61E-03	6.41E-03
	C35-2-10	3.97E-03	5.62E-03	3.88E-03	6.43E-03
	C50-2-10	3.05E-03	4.42E-03	3.35E-03	6.43E-03
	C10-1-20	5.12E-03	5.28E-03	5.59E-03	6.39E-03
	C35-1-20	3.68E-03	5.32E-03	3.22E-03	6.42E-03
	C50-1-20	2.92E-03	4.19E-03	2.87E-03	6.42E-03
	C10-2-20	5.23E-03	5.28E-03	5.59E-03	6.39E-03
	C35-2-20	3.60E-03	5.29E-03	3.04E-03	6.41E-03
	C50-2-20	2.73E-03	3.91E-03	2.63E-03	6.42E-03

Θ_{y1}: Yielding Curvatures= $\min\left\{\frac{f_y}{E_s}\left(\frac{1}{d-x_y}\right), \frac{\varepsilon_{cy}}{x_y}\right\}$, where x_y is the depth of the compression zone at yielding from Response2000.

Θ_{y2}: Yielding Curvatures= $\min\left\{\frac{f_y}{E_s}\left(\frac{1}{d-x_y}\right), \frac{\varepsilon_{cy}}{x_y}\right\}$, where x_y is the depth of the compression zone at yielding from Panagiotakos and Fardis 2001.

Θ_{y3}: Yielding Curvatures are from Response2000.

Θ_{y4}: Yielding Curvatures are from Priestley et al. (1996) equation.

Sample of calculations:

➔ For Continuous Reinforcement:

Longitudinal reinforcement = 4φ18, axial load = 10 % of crushing load , Concrete cover= 25 mm, b= 350 mm, h= 400mm and stirrups = φ18/100 mm.

$$\Theta_y = \frac{1}{3}L_v\varphi_y + \frac{V_y}{0.4E_{sec}(0.8A_g)} + \frac{\varphi_y f_y d_b}{8\sqrt{f_c}}$$

$$\theta_{y1} = \frac{1}{3}(1500)(9.12 \cdot 10^{-6}) + \frac{\frac{0.196}{1.5}}{0.4(15000)(0.8 \cdot 0.35 \cdot 0.4)} + \frac{9.2 \cdot 10^{-6}(414)(18)}{8\sqrt{30}} = 6.31E - 03$$

$$\theta_{y2} = \frac{1}{3}(1500)(8.8 \cdot 10^{-6}) + \frac{\frac{0.196}{1.5}}{0.4(15000)(0.8 \cdot 0.35 \cdot 0.4)} + \frac{8.8 \cdot 10^{-6}(414)(18)}{8\sqrt{30}} = 6.1E - 03$$

$$\theta_{y3} = \frac{1}{3}(1500)(9.5 \cdot 10^{-6}) + \frac{\frac{0.196}{1.5}}{0.4(15000)(0.8 \cdot 0.35 \cdot 0.4)} + \frac{9.5 \cdot 10^{-6}(414)(18)}{8\sqrt{30}} = 6.56E - 03$$

$$\theta_{y4} = \frac{1}{3}(1500)(1.086 \cdot 10^{-5}) + \frac{\frac{0.196}{1.5}}{0.4(15000)(0.8 \cdot 0.35 \cdot 0.4)} + \frac{1.086 \cdot 10^{-5}(414)(18)}{8\sqrt{30}} = 7.4E - 03$$

Same Calcutions are done for the rest of the column cases, the curvatures for the columns with Lap splice are found using the reduced strength of the reinforcement.

The maximum strength the reinforcement in a member can reach with lapped bars at the critical cross section is:

$$f_s = 1.25\left(\frac{l_b}{l_d}\right)^{\frac{2}{3}} f_{yl}$$

$l_{d\ available}$ =0.27 m

l_d is the required development length required by ACI standards and is found as following:

l_d required using ACI Standards and is found as following:

$\frac{l_d}{D_b} = \frac{1.25 \cdot f_y}{B \cdot \sqrt{f_c}}$, where B=2.0 for bars less than No.7

$l_d = \frac{1.25 \cdot 414}{2 \cdot \sqrt{30}} \cdot 18 = 850.33918 = 850.339$ mm

$$f_s = 1.25\left(\frac{270}{850.34}\right)^{\frac{2}{3}} 414 = 241\ MPa$$

Plastic Rotation Calculations:

Immediate Occupancy

Table C11: Yield Rotation Calculations (Lehman et al. (1996))

Column Set	Column Name	Θ_1	Θ_2	Θ_3	Θ_4
Columns Set 1: Continuous Reinforcement	C10-1-10	9.85E-03	9.63E-03	1.01E-02	1.10E-02
	C35-1-10	6.57E-03	8.35E-03	6.49E-03	9.15E-03
	C50-1-10	4.87E-03	6.27E-03	5.07E-03	8.47E-03
	C10-2-10	9.20E-03	8.96E-03	9.42E-03	1.03E-02
	C35-2-10	5.85E-03	7.74E-03	5.72E-03	8.64E-03
	C50-2-10	4.26E-03	5.82E-03	4.58E-03	8.11E-03
	C10-1-20	1.02E-02	1.01E-02	1.08E-02	1.17E-02
	C35-1-20	6.58E-03	9.06E-03	6.01E-03	9.67E-03
	C50-1-20	4.90E-03	6.59E-03	4.81E-03	8.87E-03
	C10-2-20	9.88E-03	9.59E-03	1.03E-02	1.12E-02
	C35-2-20	6.08E-03	8.59E-03	5.43E-03	9.29E-03
	C50-2-20	4.53E-03	6.19E-03	4.21E-03	8.54E-03
Columns Set 2: Lap splice (270 mm)	C10-1-10	4.73E-03	3.81E-03	3.76E-03	4.96E-03
	C35-1-10	4.90E-03	5.09E-03	5.01E-03	5.07E-03
	C50-1-10	3.75E-03	4.73E-03	3.48E-03	5.08E-03
	C10-2-10	4.40E-03	3.80E-03	3.68E-03	4.95E-03
	C35-2-10	4.83E-03	5.07E-03	4.99E-03	5.05E-03
	C50-2-10	3.49E-03	4.68E-03	3.25E-03	5.05E-03
	C10-1-20	4.31E-03	3.66E-03	3.72E-03	4.91E-03
	C35-1-20	4.94E-03	5.02E-03	5.03E-03	5.02E-03
	C50-1-20	3.39E-03	4.63E-03	2.89E-03	5.03E-03
	C10-2-20	4.32E-03	3.66E-03	4.05E-03	4.91E-03
	C35-2-20	4.76E-03	5.02E-03	4.96E-03	5.02E-03
	C50-2-20	3.26E-03	4.33E-03	3.49E-03	5.02E-03
Columns Set 3: Short Anchorage length	C10-1-10	4.73E-03	3.81E-03	3.76E-03	4.96E-03
	C35-1-10	4.90E-03	5.09E-03	5.01E-03	5.07E-03
	C50-1-10	3.75E-03	4.73E-03	3.48E-03	5.08E-03
	C10-2-10	4.40E-03	3.80E-03	3.68E-03	4.95E-03
	C35-2-10	4.83E-03	5.07E-03	4.99E-03	5.05E-03
	C50-2-10	3.49E-03	4.68E-03	3.25E-03	5.05E-03
	C10-1-20	4.31E-03	3.66E-03	3.72E-03	4.91E-03
	C35-1-20	4.94E-03	5.02E-03	5.03E-03	5.02E-03
	C50-1-20	3.39E-03	4.63E-03	2.89E-03	5.03E-03
	C10-2-20	4.32E-03	3.66E-03	4.05E-03	4.91E-03
	C35-2-20	4.76E-03	5.02E-03	4.96E-03	5.02E-03
	C50-2-20	3.26E-03	4.33E-03	3.49E-03	5.02E-03

Column Set 4: Deep Cross Section (700 mm)	C10-1-10	7.06E-03	7.03E-03	7.26E-03	8.13E-03
	C35-1-10	4.49E-03	5.87E-03	4.20E-03	6.28E-03
	C50-1-10	3.24E-03	4.19E-03	3.23E-03	5.52E-03
	C10-2-10	6.69E-03	6.60E-03	6.83E-03	7.71E-03
	C35-2-10	4.14E-03	5.53E-03	3.81E-03	5.96E-03
	C50-2-10	2.99E-03	3.95E-03	2.88E-03	5.29E-03
	C10-1-20	7.55E-03	7.42E-03	7.45E-03	8.60E-03
	C35-1-20	6.11E-03	6.30E-03	4.15E-03	6.63E-03
	C50-1-20	3.41E-03	4.45E-03	3.05E-03	5.81E-03
	C10-2-20	7.22E-03	7.16E-03	7.46E-03	8.34E-03
	C35-2-20	4.31E-03	5.97E-03	3.83E-03	6.31E-03
	C50-2-20	3.05E-03	4.02E-03	2.94E-03	5.56E-03
Column Set 5: Hinge Fabrication at the critical Section	C10-1-10	7.51E-03	7.32E-03	7.73E-03	8.53E-03
	C35-1-10	5.25E-03	6.79E-03	5.25E-03	7.57E-03
	C50-1-10	3.98E-03	5.18E-03	4.20E-03	7.17E-03
	C10-2-10	7.19E-03	6.98E-03	7.39E-03	8.19E-03
	C35-2-10	4.80E-03	6.44E-03	4.70E-03	7.25E-03
	C50-2-10	3.55E-03	4.91E-03	3.84E-03	6.93E-03
	C10-1-20	7.49E-03	7.65E-03	7.96E-03	8.76E-03
	C35-1-20	5.02E-03	6.67E-03	4.57E-03	7.76E-03
	C50-1-20	3.83E-03	5.10E-03	3.78E-03	7.32E-03
	C10-2-20	7.36E-03	7.41E-03	7.72E-03	8.52E-03
	C35-2-20	4.71E-03	6.41E-03	4.15E-03	7.53E-03
	C50-2-20	3.42E-03	4.61E-03	3.33E-03	7.11E-03

Life Safety Limit Sate

Table C12: Rotation at Life Safety

Column Set	Column Name	Θ_1	Θ_2	Θ_3	Θ_4
Columns Set 1: Continuous Reinforcement	C10-1-10	1.81E-02	1.79E-02	1.83E-02	1.93E-02
	C35-1-10	1.02E-02	1.20E-02	1.01E-02	1.28E-02
	C50-1-10	6.93E-03	8.32E-03	7.13E-03	1.05E-02
	C10-2-10	1.59E-02	1.56E-02	1.61E-02	1.70E-02
	C35-2-10	8.32E-03	1.02E-02	8.19E-03	1.11E-02
	C50-2-10	5.51E-03	7.08E-03	5.83E-03	9.36E-03
	C10-1-20	2.02E-02	2.00E-02	2.07E-02	2.16E-02
	C35-1-20	1.16E-02	1.41E-02	1.10E-02	1.47E-02
	C50-1-20	8.05E-03	9.73E-03	7.95E-03	1.20E-02
	C10-2-20	1.87E-02	1.84E-02	1.91E-02	2.01E-02
	C35-2-20	1.02E-02	1.27E-02	9.58E-03	1.34E-02
	C50-2-20	6.92E-03	8.58E-03	6.60E-03	1.09E-02
Columns Set 2: Lap splice (270 mm)	C10-1-10	1.13E-02	1.04E-02	1.03E-02	1.15E-02
	C35-1-10	8.43E-03	8.62E-03	8.54E-03	8.60E-03
	C50-1-10	7.29E-03	8.27E-03	7.01E-03	8.61E-03
	C10-2-10	1.10E-02	1.04E-02	1.02E-02	1.15E-02
	C35-2-10	8.37E-03	8.61E-03	8.53E-03	8.59E-03
	C50-2-10	7.02E-03	8.22E-03	6.79E-03	8.59E-03
	C10-1-20	1.14E-02	1.07E-02	1.08E-02	1.20E-02
	C35-1-20	1.20E-02	1.21E-02	1.21E-02	1.21E-02
	C50-1-20	1.05E-02	1.17E-02	9.96E-03	1.21E-02
	C10-2-20	1.14E-02	1.07E-02	1.11E-02	1.20E-02
	C35-2-20	1.18E-02	1.21E-02	1.20E-02	1.21E-02
	C50-2-20	1.03E-02	1.14E-02	1.06E-02	1.21E-02
Columns Set 3: Short Anchorage length	C10-1-10	1.13E-02	1.04E-02	1.03E-02	1.15E-02
	C35-1-10	8.43E-03	8.62E-03	8.54E-03	8.60E-03
	C50-1-10	7.29E-03	8.27E-03	7.01E-03	8.61E-03
	C10-2-10	1.10E-02	1.04E-02	1.02E-02	1.15E-02
	C35-2-10	8.37E-03	8.61E-03	8.53E-03	8.59E-03
	C50-2-10	7.02E-03	8.22E-03	6.79E-03	8.59E-03
	C10-1-20	1.14E-02	1.07E-02	1.08E-02	1.20E-02
	C35-1-20	1.20E-02	1.21E-02	1.21E-02	1.21E-02
	C50-1-20	1.05E-02	1.17E-02	9.96E-03	1.21E-02
	C10-2-20	1.14E-02	1.07E-02	1.11E-02	1.20E-02
	C35-2-20	1.18E-02	1.21E-02	1.20E-02	1.21E-02
	C50-2-20	1.03E-02	1.14E-02	1.06E-02	1.21E-02

Column Set 4: Deep Cross Section (700 mm)	C10-1-10	1.37E-02	1.35E-02	1.38E-02	1.44E-02
	C35-1-10	6.70E-03	7.81E-03	6.70E-03	8.37E-03
	C50-1-10	4.23E-03	5.09E-03	4.39E-03	6.52E-03
	C10-2-10	1.20E-02	1.18E-02	1.21E-02	1.27E-02
	C35-2-10	5.57E-03	6.75E-03	5.50E-03	7.34E-03
	C50-2-10	3.49E-03	4.46E-03	3.70E-03	5.91E-03
	C10-1-20	1.66E-02	1.65E-02	1.69E-02	1.75E-02
	C35-1-20	8.69E-03	1.02E-02	8.36E-03	1.07E-02
	C50-1-20	5.76E-03	6.81E-03	5.73E-03	8.27E-03
	C10-2-20	1.54E-02	1.52E-02	1.57E-02	1.63E-02
	C35-2-20	7.90E-03	9.46E-03	7.50E-03	9.92E-03
	C50-2-20	4.97E-03	5.94E-03	4.90E-03	7.62E-03
Column Set 5: Hinge Fabrication at the critical Section	C10-1-10	1.25E-02	1.23E-02	1.27E-02	1.35E-02
	C35-1-10	7.89E-03	9.43E-03	7.89E-03	1.02E-02
	C50-1-10	5.69E-03	6.89E-03	5.91E-03	8.88E-03
	C10-2-10	1.13E-02	1.11E-02	1.15E-02	1.23E-02
	C35-2-10	6.72E-03	8.36E-03	6.62E-03	9.17E-03
	C50-2-10	4.71E-03	6.07E-03	5.00E-03	8.08E-03
	C10-1-20	1.30E-02	1.32E-02	1.35E-02	1.43E-02
	C35-1-20	8.16E-03	9.81E-03	7.71E-03	1.09E-02
	C50-1-20	5.94E-03	7.21E-03	5.89E-03	9.44E-03
	C10-2-20	1.23E-02	1.24E-02	1.27E-02	1.35E-02
	C35-2-20	7.31E-03	9.00E-03	6.75E-03	1.01E-02
	C50-2-20	5.05E-03	6.24E-03	4.96E-03	8.74E-03

Collapse Prevention Limit Sate

Table C13: Collapse Prevention Rotations

Column Set	Column Name	Θ_1	Θ_2	Θ_3	Θ_4
Columns Set 1: Continuous Reinforcement	C10-1-10	2.28E-02	2.26E-02	2.31E-02	2.40E-02
	C35-1-10	1.23E-02	1.41E-02	1.22E-02	1.49E-02
	C50-1-10	8.10E-03	9.49E-03	8.30E-03	1.17E-02
	C10-2-10	1.97E-02	1.95E-02	1.99E-02	2.08E-02
	C35-2-10	9.74E-03	1.16E-02	9.61E-03	1.25E-02
	C50-2-10	6.23E-03	7.80E-03	6.55E-03	1.01E-02
	C10-1-20	2.59E-02	2.57E-02	2.64E-02	2.73E-02
	C35-1-20	1.45E-02	1.69E-02	1.39E-02	1.75E-02
	C50-1-20	9.85E-03	1.15E-02	9.75E-03	1.38E-02
	C10-2-20	2.38E-02	2.35E-02	2.42E-02	2.51E-02
	C35-2-20	1.26E-02	1.51E-02	1.20E-02	1.58E-02
	C50-2-20	8.29E-03	9.95E-03	7.97E-03	1.23E-02
Columns Set 2: Lap splice (270 mm)	C10-1-10	1.39E-02	1.30E-02	1.29E-02	1.41E-02
	C35-1-10	9.84E-03	1.00E-02	9.95E-03	1.00E-02
	C50-1-10	8.70E-03	9.68E-03	8.42E-03	1.00E-02
	C10-2-10	1.36E-02	1.30E-02	1.29E-02	1.41E-02
	C35-2-10	9.78E-03	1.00E-02	9.94E-03	1.00E-02
	C50-2-10	8.44E-03	9.63E-03	8.20E-03	1.00E-02
	C10-1-20	1.42E-02	1.36E-02	1.36E-02	1.48E-02
	C35-1-20	1.48E-02	1.49E-02	1.49E-02	1.49E-02
	C50-1-20	1.33E-02	1.45E-02	1.28E-02	1.49E-02
	C10-2-20	1.42E-02	1.36E-02	1.39E-02	1.48E-02
	C35-2-20	1.47E-02	1.49E-02	1.49E-02	1.49E-02
	C50-2-20	1.32E-02	1.42E-02	1.34E-02	1.49E-02
Columns Set 3: Short Anchorage length	C10-1-10	1.39E-02	1.30E-02	1.29E-02	1.41E-02
	C35-1-10	9.84E-03	1.00E-02	9.95E-03	1.00E-02
	C50-1-10	8.70E-03	9.68E-03	8.42E-03	1.00E-02
	C10-2-10	1.36E-02	1.30E-02	1.29E-02	1.41E-02
	C35-2-10	9.78E-03	1.00E-02	9.94E-03	1.00E-02
	C50-2-10	8.44E-03	9.63E-03	8.20E-03	1.00E-02
	C10-1-20	1.42E-02	1.36E-02	1.36E-02	1.48E-02
	C35-1-20	1.48E-02	1.49E-02	1.49E-02	1.49E-02
	C50-1-20	1.33E-02	1.45E-02	1.28E-02	1.49E-02
	C10-2-20	1.42E-02	1.36E-02	1.39E-02	1.48E-02
	C35-2-20	1.47E-02	1.49E-02	1.49E-02	1.49E-02
	C50-2-20	1.32E-02	1.42E-02	1.34E-02	1.49E-02

Column Set 4: Deep Cross Section (700 mm)	C10-1-10	2.07E-02	2.06E-02	2.09E-02	2.17E-02
	C35-1-10	1.06E-02	1.20E-02	1.03E-02	1.24E-02
	C50-1-10	6.49E-03	7.44E-03	6.48E-03	8.77E-03
	C10-2-10	1.87E-02	1.87E-02	1.89E-02	1.98E-02
	C35-2-10	9.13E-03	1.05E-02	8.80E-03	1.10E-02
	C50-2-10	5.51E-03	6.47E-03	5.40E-03	7.82E-03
	C10-1-20	2.31E-02	2.30E-02	2.30E-02	2.42E-02
	C35-1-20	1.38E-02	1.40E-02	1.18E-02	1.43E-02
	C50-1-20	8.01E-03	9.05E-03	7.65E-03	1.04E-02
	C10-2-20	2.19E-02	2.18E-02	2.21E-02	2.30E-02
	C35-2-20	1.08E-02	1.25E-02	1.04E-02	1.28E-02
	C50-2-20	6.78E-03	7.75E-03	6.68E-03	9.30E-03
Column Set 5: Hinge Fabrication at the critical Section	C10-1-10	1.53E-02	1.51E-02	1.55E-02	1.63E-02
	C35-1-10	9.40E-03	1.09E-02	9.40E-03	1.17E-02
	C50-1-10	6.67E-03	7.87E-03	6.89E-03	9.86E-03
	C10-2-10	1.37E-02	1.35E-02	1.39E-02	1.47E-02
	C35-2-10	7.81E-03	9.46E-03	7.71E-03	1.03E-02
	C50-2-10	5.37E-03	6.73E-03	5.67E-03	8.75E-03
	C10-1-20	1.62E-02	1.63E-02	1.67E-02	1.75E-02
	C35-1-20	9.96E-03	1.16E-02	9.50E-03	1.27E-02
	C50-1-20	7.15E-03	8.42E-03	7.10E-03	1.06E-02
	C10-2-20	1.52E-02	1.52E-02	1.55E-02	1.63E-02
	C35-2-20	8.80E-03	1.05E-02	8.24E-03	1.16E-02
	C50-2-20	5.98E-03	7.17E-03	5.89E-03	9.67E-03

Θ_{y1}: Yielding Curvatures= $\min\left\{\frac{f_y}{E_s}\left(\frac{1}{d-x_y}\right), \frac{\varepsilon_{cy}}{x_y}\right\}$, where x_y is the depth of the compression zone at yielding from Response2000.

Θ_{y2}: Yielding Curvatures= $\min\left\{\frac{f_y}{E_s}\left(\frac{1}{d-x_y}\right), \frac{\varepsilon_{cy}}{x_y}\right\}$, where x_y is the depth of the compression zone at yielding from Panagiotakos and Fardis 2001.

Θ_{y3}: Yielding Curvatures are from Response2000.

Θ_{y4}: Yielding Curvatures are from Priestley et al (1996) equation.

Sample of Calculations

$$a = 0.42 - 0.043\frac{N_{UD}}{A_g \cdot f_c} + 0.63\rho_t - 0.023\frac{V_y}{V_{Col}}$$

$$a = 0.42 - 0.043\frac{0.42}{358(350)30} + 0.63(0.000802) - 0.023\frac{130}{205} = 0.023$$

$$b = \frac{0.5}{5+\frac{N_{UD}}{0.8A_g F_{CE}} \cdot \frac{1}{\rho_t} \cdot \frac{f_{CE}}{f_{yt}}} - 0.1$$

$$b = \frac{0.5}{5+\frac{0.42}{0.8(358)350(30)} \cdot \frac{1}{0.000802} \cdot \frac{30}{276}} - 0.1 < a \text{ , } b = 0.023$$

Θ at Immediate Occupancy= 0.15a+ θ_y

$0.15(0.23)+ 6.26(10)^{-3}= 9.23(10)^{-3}$

Θ at life safety = 0.5(b)+θ_y, where b is the plastic rotation and is equal to

$0.5(0.023) + 6.26(10)^{-3}= 1.80(10)^{-2}$

Θ at Collapse Prevention = 0.7(b)+θ_y, where b is the plastic rotation and is equal to

$0.5(0.023) + 6.26(10)^{-3}= 2.28(10)^{-3}$

Appendix D: Shear Strength Calculations

EUROCODE 8 Part III 2005

Table D1: Shear Strength EUROCODE 8 Part III

Column Set	Column Name	Shear Strength in kN
Columns Set 1: Continuous Reinforcement	C10-1-10	250.3955
	C35-1-10	314.8579
	C50-1-10	328.4321
	C10-2-10	176.7377
	C35-2-10	241.2001
	C50-2-10	254.7743
	C10-1-20	216.8917
	C35-1-20	282.5155
	C50-1-20	292.2314
	C10-2-20	143.2339
	C35-2-20	208.8577
	C50-2-20	218.5736
Columns Set 2: Lap splice (270 mm)	C10-1-10	248.9873
	C35-1-10	306.9282
	C50-1-10	328.4321
	C10-2-10	175.3295
	C35-2-10	233.2704
	C50-2-10	254.7743
	C10-1-20	215.1849
	C35-1-20	272.5793
	C50-1-20	292.2314
	C10-2-20	141.5271
	C35-2-20	198.9215
	C50-2-20	218.5736
Columns Set 3: Short Anchorage length	C10-1-10	248.9873
	C35-1-10	306.9282
	C50-1-10	328.4321
	C10-2-10	175.3295
	C35-2-10	233.2704
	C50-2-10	254.7743
	C10-1-20	215.1849
	C35-1-20	272.5793
	C50-1-20	292.2314
	C10-2-20	141.5271
	C35-2-20	198.9215
	C50-2-20	218.5736
Column Set 4: Deep Cross Section (700 mm)	C10-1-10	439.3292
	C35-1-10	640.5090
	C50-1-10	672.2089
	C10-2-10	326.6455
	C35-2-10	527.8253
	C50-2-10	559.5252
	C10-1-20	394.5997
	C35-1-20	598.6647
	C50-1-20	621.9021
	C10-2-20	281.9171
	C35-2-20	485.9810
	C50-2-20	509.2184
Column Set 5: Hinge Fabrication at the critical Section	C10-1-10	198.8555
	C35-1-10	231.0867
	C50-1-10	237.8738
	C10-2-10	125.1977
	C35-2-10	157.4289
	C50-2-10	164.2160
	C10-1-20	182.1036
	C35-1-20	214.9155
	C50-1-20	219.7735
	C10-2-20	108.4458
	C35-2-20	141.2577
	C50-2-20	146.1157

Shear Strength Calculations

$$\mathrm{V}_r = \frac{1}{\gamma_{el}}\left[\frac{h-x}{2\cdot L_v}\cdot \min(N; 0.55\cdot A_c\cdot f_c) + \left(1-0.05\cdot min\left(5;\mu_\Delta{}^{pl}\right)\right)\right.$$
$$\left.\cdot\left[0.16\cdot max(0.5; 100\cdot\rho_{tot})\cdot\left(1-0.16\cdot\min\left(5;\frac{L_v}{h}\right)\right)\cdot\sqrt{f_c}\cdot A_c + \rho_{sx}b_w z f_{y,tr}\right)\right]$$

$$\mathrm{V}_r = \frac{1}{1.15}\left[\frac{400-122.8}{2(1500)}\cdot\min(0.420; 0.55(350\cdot 400)30)\right.$$
$$+\left[0.16\cdot max(0.5; 100\cdot 0.01624)\cdot\left(1-0.16\cdot\min\left(5;\frac{1500}{400}\right)\right)\cdot\sqrt{30}\cdot(400\cdot 350)\right.$$
$$\left.+(0.006382343)350(316)276\right)\Bigg] = 205.4\ kN$$

ASCE SEI 41-17 Calculations

Table D2: Shear Strength ASCE SEI 41-17

Column Set	Column Name	V_c kN
Columns Set 1: Continuous Reinforcement	C10-1-10	205.3415
	C35-1-10	260.3246
	C50-1-10	285.6820
	C10-2-10	155.6552
	C35-2-10	210.6382
	C50-2-10	235.9957
	C10-1-20	205.3415
	C35-1-20	260.3246
	C50-1-20	285.6820
	C10-2-20	155.6552
	C35-2-20	210.6382
	C50-2-20	235.9957
Columns Set 2: Lap splice (270 mm)	C10-1-10	205.3415
	C35-1-10	260.3246
	C50-1-10	285.6820
	C10-2-10	155.6552
	C35-2-10	210.6382
	C50-2-10	235.9957
	C10-1-20	205.3415
	C35-1-20	260.3246
	C50-1-20	285.6820
	C10-2-20	155.6552
	C35-2-20	210.6382
	C50-2-20	235.9957
Columns Set 3: Short Anchorage length	C10-1-10	205.3415
	C35-1-10	260.3246
	C50-1-10	285.6820
	C10-2-10	155.6552
	C35-2-10	210.6382
	C50-2-10	235.9957
	C10-1-20	205.3415
	C35-1-20	260.3246
	C50-1-20	285.6820
	C10-2-20	155.6552
	C35-2-20	210.6382
	C50-2-20	235.9957
Column Set 4: Deep Cross Section (700 mm)	C10-1-10	523.4927
	C35-1-10	700.3446
	C50-1-10	781.9065
	C10-2-10	432.1698
	C35-2-10	609.0218
	C50-2-10	690.5836
	C10-1-20	523.4927
	C35-1-20	700.3446
	C50-1-20	781.9065
	C10-2-20	432.1698
	C35-2-20	609.0218
	C50-2-20	690.5836
Column Set 5: Hinge Fabrication at the critical Section	C10-1-10	152.3570
	C35-1-10	179.8486
	C50-1-10	192.5273
	C10-2-10	102.6707
	C35-2-10	130.1623
	C50-2-10	142.8410
	C10-1-20	152.3570
	C35-1-20	179.8486
	C50-1-20	192.5273
	C10-2-20	102.6707
	C35-2-20	130.1623
	C50-2-20	142.8410

Sample of Calculations:

Longitudinal reinforcement = 4Φ18, axial load = 10 % of crushing load , Concrete cover= 25 mm, b= 350 mm, h= 400mm and stirrups = Φ8/100 mm.

For Column shear strength calcutions:

A_v =2(π/4) $(8)^2$ = 100.53 mm^2, f_c =30 kN, N_{UG}=0.42 MN

$(\frac{100.53(276)358}{100}) + \ 1\left(\frac{0.5\sqrt{30}}{\frac{1500}{358}}\sqrt{1+\frac{0.42}{0.5(400)350\sqrt{30}}}\right)(0.8)400(350)$ = 93.37+ 105.96 = 205 kN